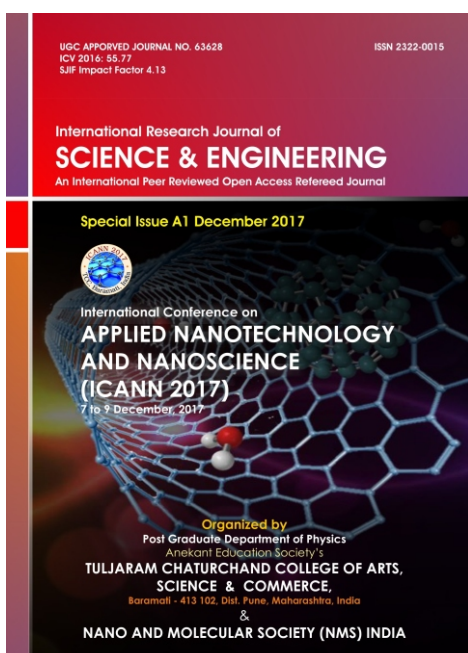


UGC Approved Journal No. 63628
ICV 2016 : 55.77
SJIF Impact Factor 4.11

ISSN: 2322-0015

International Research Journal of
SCIENCE & ENGINEERING
An International Peer Reviewed Open Access Refereed Journal

Special Issue A1 December 2017



International Conference on
**APPLIED
NANOTECHNOLOGY
AND NANOSCIENCE
(ICANN 2017)**

Chief Editor : Dr. Arvind B. Chavhan

STATUTORY WARNING

Articles, data, figures, scientific contents and its interpretation and authenticity reported by author(s) and published in IJLSCI are the exclusive views of author(s). The editorial board, IJLSCI is not responsible for any controversies arising out of them. In case of any plagiarism found, author(s) will have to face its consequences.

Organized by
Post Graduate Department of Physics
Anekant Education Society's
TULJARAM CHATURCHAND COLLEGE OF ARTS, SCIENCE & COMMERCE
Baramati Dist. Pune, Maharashtra, India
and
NANO AND MOLECULAR SOCIETY (NMS) INDIA

All the materials in this journal is copyright and may not be reproduced except with the return permission of the publisher
2013-18 © Copyright International Research Journal of Science & Engineering

ABOUT IRJSE

IRJSE is a peer-reviewed journal, which aims to provide the most complete and reliable source of information on current developments in the field. The emphasis will be on publishing quality research papers rapidly and freely available to researchers worldwide. IRJSE serves an important role by encouraging, fostering and promoting developments in Science & Engineering areas. It is an open access journal, which publishes original research articles, reviews and short communication in all areas of Sciences and Engineering and Technology at the interface of related disciplines.

Science Discipline Viz. Mathematics, Statistics, Physics, Chemistry, Geology & Earth Science, Environmental Science, Life Sciences, etc.

Engineering sciences and technology discipline Viz. Mechanical Engineering, Civil Engineering, Electrical Engineering, Electronics & Telecommunication Engineering, Computer Engineering, Chemical Engineering, Biotechnology, Information Technology, Architecture Engineering, Artificial Intelligence, Computer Software and Application, Computing, Data Mining, Design. Energy, Image Processing, Internet and World wide web, manufacturing, military, mining, Nanotechnology and smart materials, Networking, Polymers and Plastics, Renewable Energy, Robotics, Space environment and Aviation Technology, Systems Engineering transport, etc. RJET publishes Original research Articles, Short Communications, Review Articles in all areas of Engineering and Technology. The subject covered is Engineering Mechanics, Construction Materials, Surveying, Fluid Mechanics and Hydraulics, Modeling and Simulations, Thermodynamics, Refrigeration & Air-conditioning, Metallurgy, Electronic Communication Systems, Agricultural Machinery & Equipment, Applied Sciences, Chemical Engineering, etc.

TYPES OF RESEARCH PAPER

Original Articles:

These should describe new and carefully confirmed findings, and experimental methods should be given in sufficient detail for others to verify the work. The length of an original article is the minimum required to describe and interpret the work clearly.

Short Communications:

Short communication also contain abstract. The list of references should not exceed 15. The presentation of Short Communications should contain headings such as Introduction, Materials and Methods, Results and Discussion, etc.

Reviews Articles:

Submissions of review articles and perspectives covering topics of current interest are welcome and encouraged.

The journal is published in online version only which is free access and downloads.

This Journal is circulated / Distributed Through Subscription only

Submission of Paper: Submission of paper is encouraged by e-mail to editorirjse@gmail.com OR editor@irjse.in

Subscription Plan: Rs. 3500 /- or 250 US\$ (Individual Annual); Rs. 4500/- or 350 US\$ (Institutional)

Life Membership: Rs. 15000/- or 550 US\$ (Individual) Rs. 25000/- or 850 US\$ (Institutional)

Fellow Membership: Rs. 25000/- or 850 US\$ (Individual) Rs. 35000/- or 1700 US\$ (Institutional)

Publisher and Owner: Dr. Arvind Chavhan, Published from IRJSE, 46, Guruwandan, Jawahar Nagar VMV Road, Amravati- 444604. India

Editor in Chief: Arvind Chavhan, D.B. College, Bhokar, Nanded, India

Publisher, Editorial Board and Editor in Chief take no responsibilities for the inaccurate, misleading data, opinion and statement appeared in the articles published in this journal. All responsibilities of the contents rest upon the authors (especially upon the corresponding author).

Indexing:

INNOSPACE (SJIF), ROAD, OAJI, Academic Keys, J-index.net, Scholar Steer, Research Bible, Google Scholar, DAIJ, DRIJ, DIIF, SIS, ISI, ASI.

No Part of the this Journal can be reproduced without written permission of the publisher © Copyright 2013-18 By International Research Journal of Science & Engineering

All the Articles are freely accessible on the website of the International Research Journal of Science & Engineering <http://www.irjse.in>, As well as some of the Indexing agencies website via., oaji.net, [research bible](http://research.bible), Cite factors, ISI, etc.

Editorial Board

Editor-in-Chief

Dr. Arvind Chavhan

D. B. College, Bhokar, Nanded MS, India.

Co-Editor in Chief

Dr. Satish B. Chavhan

Department of Mathematics
D.B. College, Bhokar, Nanded

Dr. B. G. Nemmaniwar

Department of Physics
D.B. College, Bhokar,
Nanded, India.

Managing Editor

Prof. B.B. Chavhan

G.H.Raisoni Institute of Engg &
Computer Application, Amravati,
MS, India.

Executive Editor

Prof. Vivek Rathod

S.N. Institute of Pharmacy, Pusad
Yavatmal, MS, India.

Advisory Board

Dr. K.M. Kulkarni,

Ex- Director, Higher Education MS,
Amravati, Maharashtra, India

Dr. Prabha Bhogaokar,

Ex- Director, GVISH, Amravati,
Maharashtra, India

Dr. B.N. Pandey,

Professor in Human Genetics, Purnia
University, Purnia, Bihar, India

Dr. V.G. Thakare,

Principal, Shri Shivaji Science
College, Amravati, India

Dr. V.N. Kadam,

G.S. Gawande College,
Umardhed, Maharashtra, India

Dr. Ratnakar B. Lanjewar,

Nagpur, Maharashtra, India.

Dr. Satish A. Bhalerao,

Department of Botany,
Wilson College, Mumbai, India

Associate Editor

Dr. S. B. Zade,

Rashtrasant Tukadoji Maharaj
Nagpur University, Nagpur,
Maharashtra, India

Dr. Moinuddin Sarker

Natural State Research (NSR) Inc.,
37 Brown House Road, Stamford,
CT 06902, USA

Ravishankar N. Chityala

University Of California,
Santa Cruz, (UCSC) 1156 High
Street, Santa Cruz, CA 95064.

FatehMebarek-Oudina

Département des Sciences de la
Matière, Faculté des Sciences,
Université 20 Août, Skikda, Algeria.

Dr. H. S. Lunge,

Department of Statistics,
Shri Shivaji Science College,
Amravati, MS, India

Dr. K. Nagmani,

Scientist -C , Sathyabama
University Remote sensing and
Geoinformatics Centre,
Sathyabama University, Rajiv
Gandhi Road, Sholinganallur,
Chennai - 600119, TN, India.

Dr. M. N. Bhajbhuj

Department of Botany,
Jawaharlal Nehru Mahavidyalaya,
Wadi, Nagpur, MS, India

Dr.Sanyogita Shrikant Deshmukh

J.D.Patil Sangludkar
Mahavidyalaya,Daryapur
Amravati, MS India

Dr. Santosh S. Pawar,

Institute of Forensic Science,
Nagpur, MS, India

Dr. Kishor G. Patil,

Institute of Sciences,
Nagpur,MS, India

Dr. Piyush Gupta

Department of Chemistry
SRM University, NCR Campus,
Modinagar, Ghaziabad, U.P.

Dr. Selby Jose

Department of Mathematics,
Govt. Institute of Science, Mumbai.

Dr. Laxmikant Basavraj Dama

Department of Zoology,
D.B.F. Dayanand College of Arts
and Science, Solapur MS, India

Dr. Ashok Eknath Kalange

P.G. & Research Center in Physics
T.C.College of ASC, Baramati, Pune
MS, India

Dr. Rajusing G. Jadhao,

Department of Zoology,
Shri Shivaji Science College,
Amravati, MS, India

Dr. Shailendra D. Deo,

Department of Mathematics,
N. S. Science & Arts College,
Bhadrawati, Maharashtra, India.

Dr. Sangita P. Ingole,

Department of Environmental
Science, Shri Shivaji Science College,
Amravati, MS, India

Dr. Masrat Sulfana,

Department of Environmental
Engineering,M.G.M. College of
Engineering, Auragabad, India

Dr. Sachin Tawade

Department of Botany
D.B. College, Bhokar,Nanded

Dr. Revati R.Khokale

Department of Library & Information
Sciences, Shri Shivaji Science
College, Amravati- India

Member of Editorial Board

Prof. Pradeep M. Ingole,

Department of Mechanical
Engineering, Prof. Ram Meghe
Institute of Technology and
Research, Badnera, Amravati.

Prof. U. N. Rathod,

Department of Chemistry,
Shri Shivaji Science College,
Amravati, India

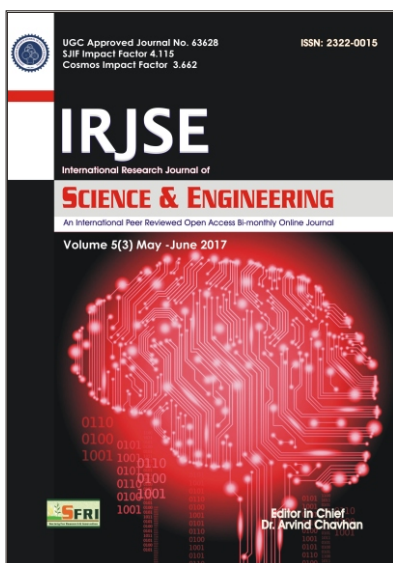
Prof. K. J. Gawai,

Department of Environmental
Science, Shri Shivaji Science College,
Amravati, India

Prof. D. M. Chavhan,

Department of Chemistry,
Sharadchandra Pawar
Mahavidyalaya, Lonand,

IRJSE CALL FOR CONFERENCE SPECIAL ISSUE



ISSN: 2322-0015
UGC Approved Journal No. 63628)
ICV 2016 55.77

Conferences organiser are welcome to publish their Research articles with IRJSE.

The conference organizers are requested to provide the manuscripts in .doc format to the editor of IRJSE. The conference organizers are also requested to submit the review comments and the list of reviewers to IJLSCI along with the set of manuscripts. The manuscripts must be categorized according to the topics addressed by them. Conferences interested to publish their selected manuscripts with **International Research Journal of Sciences & Engineering** are requested to use the copyright forms provided in the download section. Compliance with the documents is a necessity for publication in IRJSE.

All correspondence concerning publication should be addressed to the

Editor in Chief

Dr. Arvind Chavhan

46, Guruvandan, Jawahar Nagar, Amravati- 444604

Email: editorirjse@gmail.com

Cell : (+91) 9970559438 | 9420775527

“Applied Nanotechnology and Nanoscience” (ICANN 2017)

CONTENTS	
1	Effect of precipitation conditions on crystallization of TiO ₂ nanoparticles in acidic route Wani PN, Ekar SU, Kangude BU, Shelke PN, Chaudhari SR, Chaskar MG, Chabukswar VV and Kholam YB
8	Synthesis and Dielectric properties of nanocrystalline Gd ³⁺ substituted Nickel-Cadmium ferrites More RM, Chaudhari ND, and Vasambekar PN
15	Study of Variation of Bandgaps of Pure and Doped Nickel Oxide Nanoparticles (NiO) prepared in different environments Kaushik Baishya and Karmakar Sanjib
21	Clinical applications of ZnO nanoparticles Khater MS, Kulkarni GR, Talathi P and Karnik R
29	Green Synthesis and Characterization of Nanocrystalline Graphene Oxide Gijare Medha, Chaudhari Sharmila and Garje Anil
35	Fabrication and Characteristics of Nano Sized ZnSe Thin Films by Chemical Bath Deposition Pingale PC, Kale RD and Kalange AE
39	The effect sintering temperature on structural and magnetic properties of Nano-crystalline Al ³⁺ doped Magnesiumcopper ferrites synthesized by Sol-gel method Lagad SB and Gaikwad SV
44	Screening of silver nanoparticles producing cyanobacteria and its characterization Pawar Sunil, Bhosale Amarsinh, Mulani Parvin, Patekar Panchratna and Shaha Swarali.
55	Synthesis of ZnO:TiO ₂ Nanocomposite Thin Films by Spraypyrolysis Waghmode JV, Bhosale SE, Shinde TB, Mohite VR and Sapkal RT
59	Nanomaterial applications as radiosensitizer in radiation therapy for cancer treatment Singh Lalit Mohan, Singh KY and Kumar Dinesh
64	Innovative applications of Nanophase alumina as dehydration catalyst and as humidity sensor Sali Nitin, Gandhe Shrikant, Dighe Pradeep, Bhoraskar SV
69	Structural and dielectric properties of Nd Substituted Ni-Co Nanoferrites by autocombustion route Kokare MK and Rathod SM

73	Synthesis and Characterization of Spray Deposited Lithium Ferrite Thin Film Chilwar Rahul R, Somvanshi Sandeep B, Chavan Apparao R, Kharat Prashant B, Babrekar MK and Jadhav KM
77	Structural and Magnetization Behaviour in Magnetically Diluted Nickel Ferrite at Nanoscale Deshmukh SS, Humbe Ashok, Keche Atul, Patil Manisha, More SD, Shukla SJ and Jadhav KM
81	Selective low-temperature chlorine gas sensing properties of bio-inspired nanocrystalline TiO ₂ Ekar SU, Wani PN, Shaikh SF, Nakate UT, Ghule BG, Shinde PV, Raut SD, Jadhav VV, Jadhav SS, Kholam YB and Mane RS
87	Synthesis and Characterization of Gd doped Y ₂ O ₃ Phosphor Material Kale Sanjay R and Thube Dilip R
91	Preparation of MnS thin films by chemical bath deposition and effect of bath temperature on their optical properties Sonavane DK, Jare SK, Suryawanshi RV, Kathare RV, Bulakhe RN
95	Study of electrical properties of semiconducting nanocomposites Tiwari KP and Pandey Anand
99	Study of temperature change on ultrasonic velocity and some acoustic parameters of binary liquid mixture of DMSO+ Chlorobenzene Kolhe RK and Bhosale BB
103	Novel synthesis of Cu ₂ CoSnS ₄ thin films for photovoltaic application Maldar PS, Mane AA, Nikam SS, Mohite VS, Giri SD, Sarkar A, Moholkar AV
109	Study of chromium atom adsorption on single wall carbon nanotube using first-principles density functional theory Nirmal Sangeeta A, Sonawane MR and Atram RG
117	Synthesis and Characterization of Polyaniline-SnO ₂ Composite for Volatile Organic Compounds (VOCs) Detection Varade PS, Gangal SA, Shaligram AD
123	Band Gap Energy of Ni _{1-x} Cd _x Y _y Fe _{2-y} O ₄ by Sol-gel Method Bhise RB and Rathod SM
128	Elemental and Compositional Studies on Hg _x Pb _{1-x} S Nanoparticle Films Grown from an Alkaline Chemical Bath Chattarki AN,
133	Empirical mathematical model based on Moisture Diffusion and its Activation Energy in nAg/PVP nanocomposite Mahapure Poonam D, Gangal SA, Aiyer RC and Gosavi SW
143	Author Index

Effect of precipitation conditions on crystallization of TiO₂ nanoparticles in acidic route

Wani PN^{1,2}, Ekar SU³, Kangude BU¹, Shelke PN⁴, Chaudhari SR⁵, Chaskar MG⁶, Chabukswar VV⁷ and Kholam YB^{1*}

¹Department of Physics, Baburaoji Gholap College, Sangvi, Pune 411 027, M.S., India.,²Department of Physics, Prof. Ramkrishna More College, Akurdi, Pune 411 044, M.S., India.,³Centre for Nano-materials and Energy Devices, School of Physical Sciences, Swami Ramanand Teerth Marathwada University, Nanded 431606, M.S., India.,⁴Department of Physics, Annasaheb Waghire College, Otur, Junnar, Pune 412 409, M.S., India.,⁵Department of Physics, Annasaheb Magar College, Hadapsar, Pune 411 028, M.S., India.,⁶Department of Chemistry, Prof. Ramkrishna More College, Akurdi, Pune 411 044, M.S., India.,⁷Department of Chemistry, Nowrosjee Wadia College, Pune 411 001, M.S., India.,

*Corresponding author Email : ykhollam@yahoo.co.in

Manuscript Details

Available online on <http://www.irjse.in>
ISSN: 2322-0015

Editor: Dr. Arvind Chavhan

Cite this article as:

Wani PN, Ekar SU, Kangude BU, Shelke PN, Chaudhari SR, Chaskar MG, Chabukswar VV and Kholam YB. Effect of precipitation conditions on crystallization of TiO₂ nanoparticles in acidic route, *Int. Res. Journal of Science & Engineering*, December 2017; Special Issue A1 : 1-7.

© The Author(s). 2017 Open Access

This article is distributed under the terms of the Creative Commons Attribution 4.0 International License

(<http://creativecommons.org/licenses/by/4.0/>), which permits unrestricted use, distribution, and reproduction in any medium, provided you give appropriate credit to the original author(s) and the source, provide a link to the Creative Commons license, and indicate if changes were made.

ABSTRACT

Herein, the crystallization of anatase TiO₂ particles under the different precipitation conditions in acidic route is reported. The nanocrystalline TiO₂ particles are prepared by using simple precipitation route with titanium tetra isopropoxide (TTIP) and sodium hydroxide as precursor materials. The Ti-hydroxide precipitation at ice bath and hot conditions followed by annealing of as-dried precipitate in a temperature zone between 350 - 450 °C leads the formation of nanocrystalline TiO₂ particles. The OH/TTIP molar ratio for all preparations is kept nearly equal to 5.0. The as-annealed powders are characterized by using X-ray diffraction, field emission scanning electron microscopy, and UV-Visible spectroscopy. The structural characterization results revealed the crystallization of nanocrystalline TiO₂ particles. The morphological characterization results indicated nearly uniform size distribution of softly agglomerated spherical particles in as-prepared phase pure TiO₂ powders. The energy dispersive X-ray analysis confirmed the purity of material of resultant powders. It is noted that precipitation conditions play vital role on crystallinity, morphological nature and band gap energy of resultant TiO₂ particles.

Keywords: TTIP, Acidic route, X-ray diffraction, FESEM.

INTRODUCTION

Titanium oxide (TiO_2) is very useful material for large number of applications such as solar cells, sensors, ceramic membrane, catalyst for photocatalytic decomposition, textiles, pigments, cosmetics and optoelectronics [1-10] owing to its better biocompatibility, non-toxicity, better thermal stability long term photostability and strong oxidized stability. The various methods like anodization, vapor deposition sol-gel, hydrothermal, emulsion, microwave, electrochemical, homogeneous precipitation at low temperatures, ionized cluster beam deposition, aerosol process, mechano-chemical, mechanical milling, combustion synthesis, chemical vapor deposition, glycothermal and precipitation are reported for the synthesis of TiO_2 [11-26] particles of different morphologies like nanoparticles, nanotubes, nanowires, nanorods, nanosheets, nanoribbons, nanoflakes, nanofibers, spheres, needles, cubes, star shapes etc. The experimental conditions and phase symmetry of material play an important role in deciding the properties of the material. The properties of the materials are also depending upon the materials purity and crystallinity.

In present work, the TiO_2 powders with anatase phase symmetry are generated by using simple method of precipitation-followed by annealing at elevated temperatures. The titanium tetraisopropoxide is used as Ti-precursor. Herein, the TiO_2 nanoparticles (NPs) are prepared by using acidic route under both ice bath and hot conditions. The precipitation of Ti-hydroxide is carried out at ice bath temperature as well as at 70 °C (hot condition). The effects of hot and ice bath conditions during the processing by acidic route on the crystallization of TiO_2 NPs are studied in present work. The data obtained pertaining to this is presented in this communication.

METHODOLOGY

Initially, 0.2 M solution of titanium tetra isopropoxide (TTIP) was prepared by adding 2.27 ml of TTIP in 40 ml isopropyl alcohol. Similarly, 1 M solution of NaOH was prepared by dissolving 1 gm of it in 40 ml double distilled water (DDW). In acidic route, the TTIP

solution was added in NaOH solution drop by drop at a temperature of 70 °C and resultant mixture was stirred for 5 hr. The precipitation reaction was started within half an hour. The precipitate obtained was filtered and thoroughly washed with 0.1 N HCl. Finally, the precipitate was again washed for several times with DDW and then dried at room temperature. The as-dried precipitate was then annealed at 350 and 450 °C for 2 hr. to obtain TiO_2 nanoparticles (NPs). The powders prepared by using acidic route at temperature of 70 °C were identified as AH. The above mentioned precipitation reaction was also repeated in ice bath conditions. The precipitate obtained was filtered and thoroughly washed with 0.1 N HCl. Finally, the precipitate was again washed for several times with DDW and then dried at room temperature. The as-dried precipitate was then annealed at 350 and 450 °C for 2 hr. to obtain TiO_2 nanoparticles. The powders prepared by using acidic route at ice bath temperature were identified as AI. For both reactions the OH/TTIP ratio was kept nearly equal to 5.0. The resultant powders were characterized by using different physical techniques. The X-ray diffraction patterns of resultant powders were recorded by using Bruker D8 Advance (filtered $\text{CuK}\alpha$ radiation, $\lambda = 1.5406 \text{ \AA}$) machine. The morphological analysis was done by using scanning electron microscope [JEOL JSM-6360-LA and Philips XL-30]. The optical spectra of powders were recorded by using the UV-Visible spectrophotometer [V-670, JASCO UV-VIS-NIR spectrometer].

RESULTS AND DISCUSSION

The figure -1 gives the X-ray diffraction (XRD) patterns of as-prepared powders obtained under different processing conditions in acidic route. The powders: AH350 and AI350 prepared by using the acidic route at hot as well as ice bath conditions and annealed at 350 °C for 2 hr. show clearly the amorphous nature. The XRD patterns of both the powders clearly show only a broad hump around the position of anatase TiO_2 reflection having 100 % relative intensity. However, the powders: AH350 prepared by using the acidic route under the hot conditions and annealed at 350 °C for 2 hr show much better crystallinity as compared to the

powders: AI350 prepared by using the acidic route under the ice bath conditions and annealed at 350 °C for 2 hr. The powder: AH350 show the slight evolution of (101), (200) and (204) reflections of TiO₂ with anatase symmetry. Further, the powders: AI450 and AH450 prepared by using the acidic route under the ice bath and hot conditions respectively and annealed at 450 °C display much better crystalline nature. The different observed reflections are indexed to TiO₂ phase. The diffraction peaks: (101), (103), (004), (112), (200), (105), (211), (204), (116), (220) and (215) observed in both XRD patterns are found to be perfectly matching with the the JCPDS data [JCPDS card no.: 71 - 1166] given for TiO₂ with anatase symmetry.

This clearly indicates the formation TiO₂ with anatase symmetry in resultant AI450 and AH450 powders. However, powder: AI450 prepared by using acidic route under ice bath condition and annealed at 450 °C shows very good crystallinity as compared to the powder: AH450 prepared at hot bath conditions.

The large difference in the relative intensities of various corresponding peaks is observed in XRD patterns of two powders: AI450 and AH450. The relative intensity ratio of peaks is found to be ~ 3.03 for two powders: AI450 and AH450.

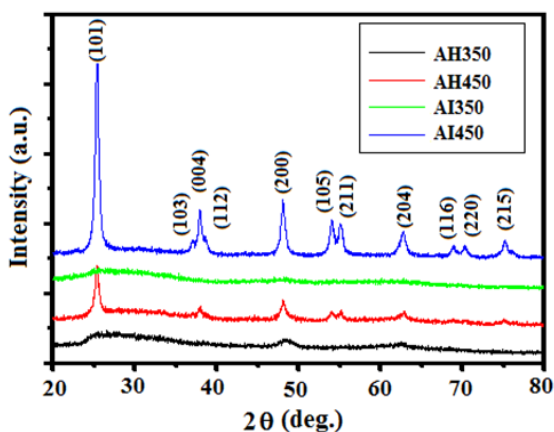


Fig. 1. The X-ray diffraction (XRD) patterns of pure TiO₂ prepared under different processing conditions

Thus, the powder AI450 is more crystalline as compared to the powder AH450. From all these observations, it is clear that the powders obtained by using the acidic route at the ice bath precipitation temperature are highly crystalline as compared to the

powders obtained at ~ 70 °C hot precipitation temperature. Thus, acidic route processing at ice bath precipitation temperature followed by annealing at 450 °C generates the well crystalline TiO₂ powders with anatase symmetry. The values for crystallite size (D) for the powders: AI450 and AH450 are obtained by using Scherrer's formula:

$$D = \frac{0.9\lambda}{\beta \cos\theta} \quad (1)$$

where, $\lambda = 1.54 \text{ \AA}$, β = full width at half maximum and θ = Bragg's diffraction angle. The values for crystallite size for the powders: AI450 and AH450, are found to be 14.77 nm and 16.49 nm respectively. The higher value of crystallite size in case of AH450 powder might be due to the sintering effect in primary particles leading to bigger TiO₂ particles. The sintering of the of primary particles is due to the processing of precipitation reaction at 70 °C.

Thus, the crystallite size for powders processed at ice bath condition is smaller as compared to crystallite size for powders processed at hot condition. Thus the ice bath processing helps in keeping lower crystallite size and limits the particle growth. The field emission scanning electron microscopy (FESEM) and scanning electron microscopy (SEM) images for AI450, and AH450 powders are shown in figure - 2. both images show the following general observations. The primary particles are nearly spherical. The primary spherical particles are agglomerating to form the soft / hard agglomerates. The agglomeration nature in case of AI450 powder is soft. However, primary particles are fusing to form hard agglomerates in case of AH450 powders. The evolution of hard agglomerates in case of AH450 powder might be due to the processing of these powders under hot condition during the precipitation reaction. This observation is consistent with crystallite data obtained from X-ray diffraction studies. Further, figure-2 also gives the particle size distribution data in terms of histograms alongwith corresponding microscopy images. From histograms, the particle size for both powders are obtained. The particle size distribution for both powders: AI450 and AH450 is almost nearly uniform.

The average particle/agglomerate size for AI450 and AH450 powders are found to be ~ 34 nm and 69 nm respectively. From all above morphological

observations, it is clear that the TiO₂ powders prepared in present work are nanocrystalline in nature. Further, the synthesis of TiO₂ powders: AI450 by using the acidic route at ice bath temperature leads the generation of spherical particles with lower average particle size. All these observations are consistent with results obtained during X-ray diffraction studies of these powders. Figure - 3 (left) gives the UV-Visible absorbance spectra for the resultant powders: AI450 and AH450. The absorbance spectra are used for finding the energy band gap (E_g) values in resultant powders : AI450 and AH450. The optical band gap value of resultant powder is estimated from Tauc plot. The Tauc's relation of photon energy (hν) with absorption coefficient (α) is given as:

$$\alpha = \frac{\alpha_0 (h\nu - E_g)^n}{h\nu} \quad (2)$$

where, E_g = band gap energy, α = absorption coefficient, α₀ = constant. Tauc's plots generated from

the UV-visible spectra for resultant AI450 and AH450 powders are given in figure -3 (right). The value of band gap energy (E_g) is obtained by extrapolation of straight-line portion of the plot to zero absorption edge. The values for band gap energies for the AI450 and AH450 powders are found to be 3.38 and 3.31 eV respectively. The band gap values are found to be matching with the reported data. The higher band gap energy for powder AI450 as compared to band gap energy for AH450 powder is due to increase in average particle size in case of AH450 powder.

In present work, the TiO₂ powders are prepared by using the method consisting of two steps: precipitation of Ti-hydroxide and annealing of this hydroxide at elevated temperatures. In first step, the precipitation of Ti-hydroxide is carried out by using acidic route under two different conditions of temperatures: ice bath and 70 °C. In second step, the annealing of thoroughly washed as-dried Ti-hydroxide is done at two different temperatures: 350 and 450 °C for 2 hr.

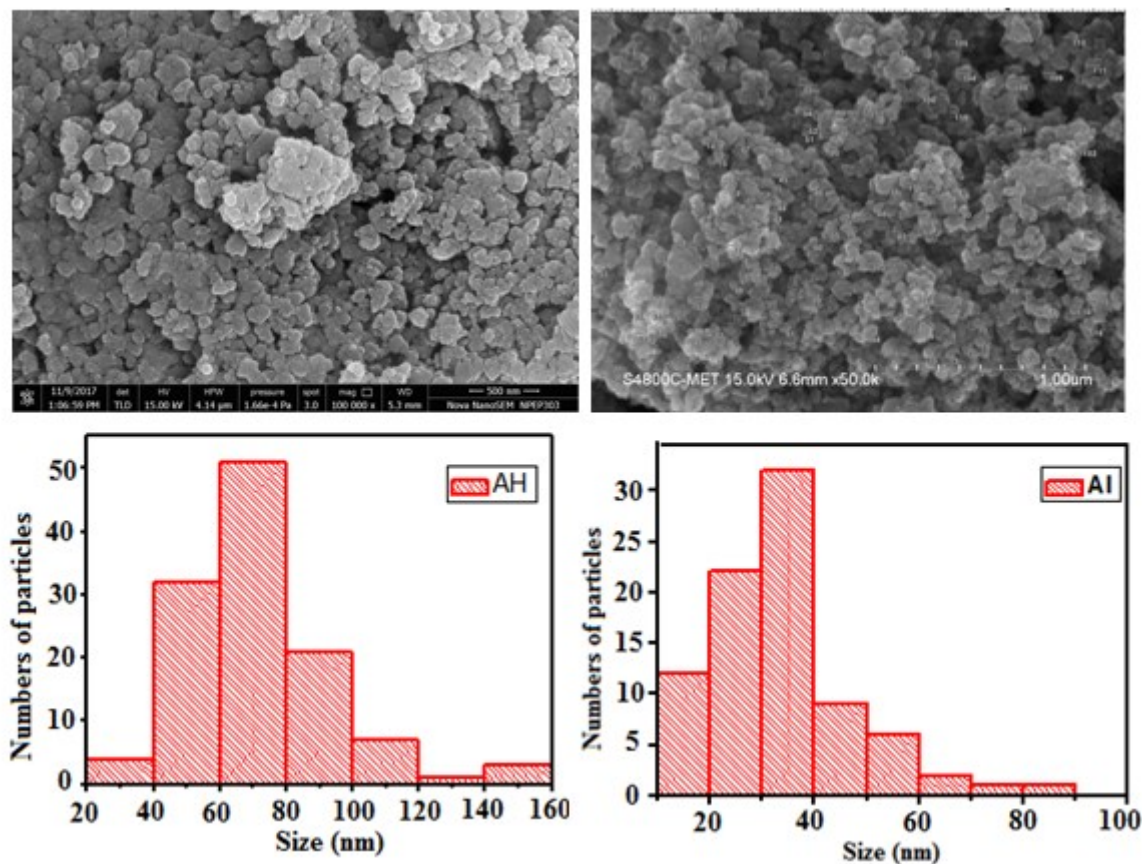


Fig. 2. The microphotographs and corresponding particle size distribution for AH450 (left) and AI450 (right) TiO₂ powders

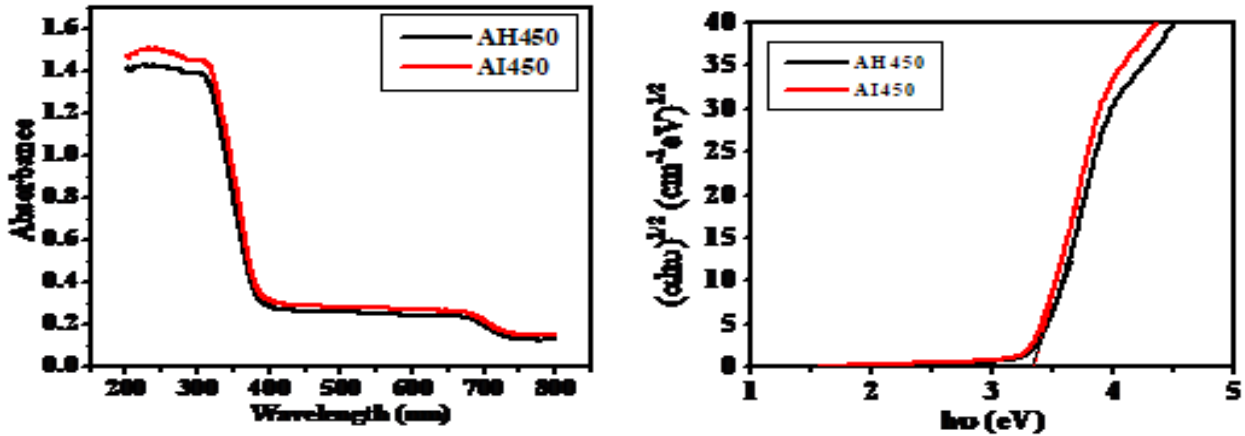


Fig 3. UV-Visible spectra and corresponding Tauc plots for AH450 and AI450 TiO₂ powders

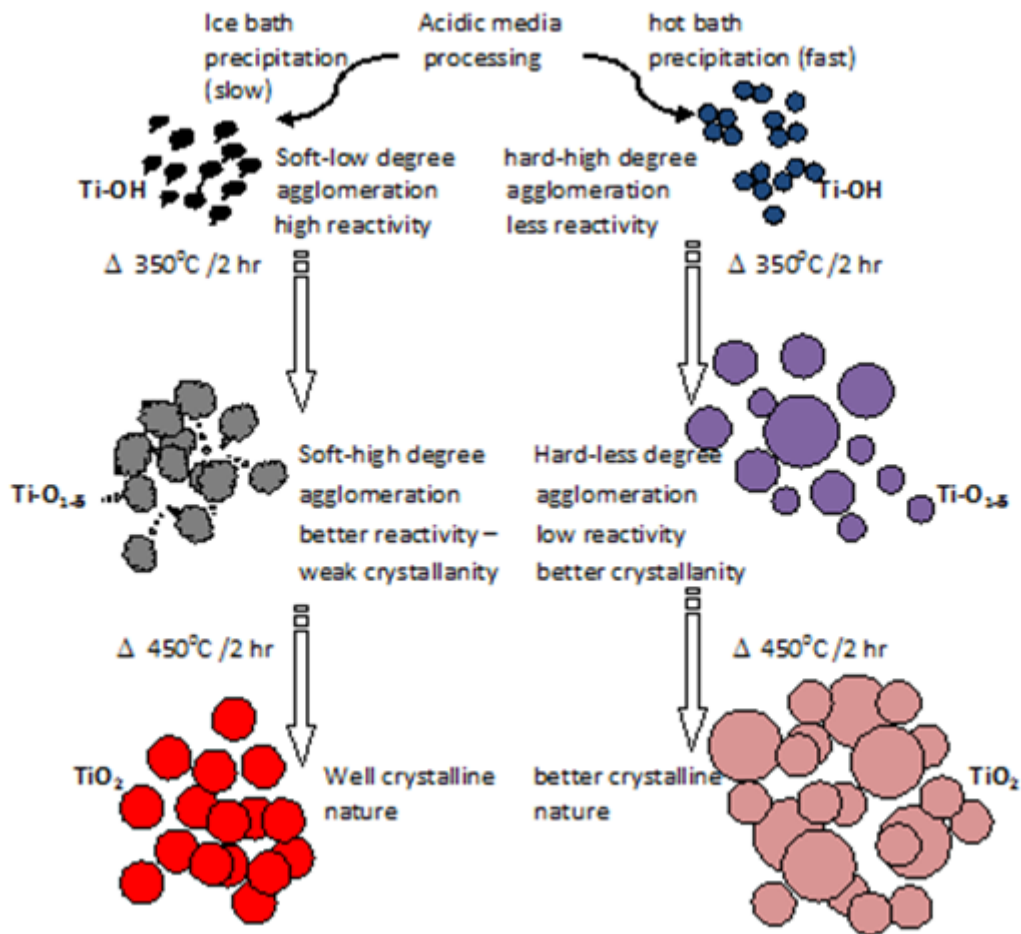


Fig. 4. The mechanism for processing of TiO₂ powder with anatase symmetry by using the acidic route

The results presented in this communication showed well crystalline nature of powders processed under ice bath temperature as compared to the powders generated by using precipitation at hot condition (at 70 °C). The mechanism for this could be as follows. The figure - 4 illustrates the said mechanism of

processing of anatase TiO₂ powder by using the acidic route. In case of the Ti-hydroxide precipitation at ice bath temperature, the hydrolysis of Ti-precursor occurs slowly. The slow hydrolysis favours the precipitation of Ti-hydroxide particles with low degree of agglomeration.

Further, processing at low i.e. ice bath temperature gives rise soft agglomerates with high degree of reactivity. The annealing of such as-prepared Ti-hydroxide particles having soft agglomeration nature with low degree of agglomeration and high degree of reactivity at moderate temperature i.e. 350 °C leads Ti-oxide powder with very weak crystallinity.

The weak crystallinity might be realized because of lower rate of reaction and hence crystallization of soft agglomerates due to insufficient thermal energy gained at moderate temperature of annealing (350 °C). On further processing i.e. annealing at higher temperature of 450 °C, due to availability of sufficient thermal energy and higher degree of reactivity of soft agglomerates leads the TiO₂ powder with very well crystallinity.

In another case, the Ti-hydroxide precipitation is carried out at higher temperature of 70 °C. This increases the rate of hydrolysis as compared to the hydrolysis at ice bath temperature. The hydrolysis at 70 °C leads the precipitation of Ti-hydroxide particles with increased level of agglomeration. Further, the agglomeration nature is hard. The hard agglomerates decrease the reactivity of corresponding particles. On annealing of the such agglomerates at moderate temperature, 350 °C leads Ti-oxide powder with better crystallinity due to sintering effect as compared to the oxide powder obtained at 350 °C during ice bath processing. Furthermore, the annealing of this Ti-oxide powder at higher temperature of 450 °C do not increase the crystallinity much further because of less reactivity of sintered hard agglomerates as compared to the crystallinity of oxide powder obtained at 450 °C during the ice bath processing. The above mentioned mechanism generates well crystalline TiO₂ powders with anatase symmetry in case of acidic route under ice bath temperature precipitation of Ti-hydroxide.

CONCLUSION

In present work, TiO₂ powders are prepared by using simple precipitation reaction by using acidic route at hot and ice bath conditions. In a acidic route, ice bath conditions are found to be more effective for

preparation of well nanocrystalline TiO₂ particles with nearly uniform size distribution. This might be due to the controlled hydrolysis-precipitation of Ti-hydroxide particles leading into soft - less agglomeration with high degree of reactivity. Further, annealing of such precipitate at high temperature generates well crystalline anatase TiO₂ nanoparticles due to soft agglomeration of intermediate product with high reactivity and smaller average particle size.

Conflicts of interest: The authors stated that no conflicts of interest.

REFERENCES

1. Li Dand, and Xia Y. *Nano Lett.*, 2003; 3: 555.
2. Kwon CH, Shin H, and Kim JH. *Mater. Chem. & Phys.*, 2004; 86: 78.
3. Viswanathamurthi P, Bhattarai N, and Kim CK. *Inorg. Chem. Commun.*, 2004; 7: 679.
4. Stathatos E, Tsiourvas D, and Lianos P, *Colloids Surf A*, 1999; 149: 49.
5. Ohenoja K, Illikainen M, and Niinimäki J, Effect of operational parameters and stress energies on the particle size distribution of TiO₂ pigment in stirred media milling, *Powder Technol.*, 2013; 234: 91-96.
6. Wang Z, Shi L, Wu F, Yuan S, Zhao Y, and Zhang M, The sol-gel template synthesis of porous TiO₂ for a high performance humidity sensor, *Nanotechnology*, 2011; 22: 275502.
7. Liu G, Hoivik N, and Wang K, Small diameter TiO₂ nanotubes with enhanced photo-responsivity, *Electrochem. Commun.*, 2013; 28: 107 - 110.
8. Han C-H, Lee H-S, and Han S-D, Synthesis of nanocrystalline TiO₂ by sol-gel combustion hybrid method and its application to dye solar cells, *Bull. Korean Chem. Soc.*, 2008; 29: 1495 - 1498.
9. Radeti_c M, Functionalization of textile materials with TiO₂ nanoparticles, *J. Photochem. Photobiol. C: Photochem. Rev.* 2013; 16: 62-76.
10. Chen J, Wang H, Wei X, and Zhu L, Characterization, properties and catalytic application of TiO₂ nanotubes prepared by ultrasonic-assisted sol-hydrothermal method, *Mater. Res. Bull.*, 2012; 47: 3747 - 3752.
11. Lim G-T, Kim KH, Park J, Ohk S-H, Kim J-H, and Cho DL, *J. Ind. Eng. Chem.*, 2010; 16: 723.

12. Takeuchi M, Sakamoto K, Tsujimaru K, and Anpo M, *Catal. Lett.*, 2009; 131: 189.
13. Kitamura Y, Okinaka N, Shibayama T, Mahaney OOP, Kusano D, Ohtani B, and Akiyama T. *Powder Technol.*, 2007; 176: 93.
14. Billik P, and Plesch G. *Mater. Lett.*, 2007; 61: 1183.
15. Chen K-Y, and Chen Y-W, *J. Sol-Gel Sci. Technol.*, 2003; 27: 111.
16. Shahruz N, and Hossain MM, *World Appl. Sci. J.*, 2011; 12: 1981.
17. Patil KC, Aruna ST, and Mimani T. *Curr. Opin. Solid State Mater.*, 2002; 6: 507.
18. Li H, Cao L, Liu W, Su G, and Dong B. Synthesis and investigation of TiO₂ nanotube arrays prepared by anodization and their photocatalytic activity, *Ceram. Int.*, 2012; 38: 5791 - 5797.
19. Moore JJ, and Feng HJ. *Prog. Mater. Sci.*, 1995; 39: 243.
20. Kolenko YV, Churagulov BR, Kunst M, Mazerolles L, and Colbeau-Justin C. *Appl. Catal. B: Environ.*, 2004; 54: 51.
21. Musić S, Gotić M, Ivanda M, Popović S, Turković A, Trojko R, Sekulić A, and Furić A. Chemical and micro structural properties of TiO₂ synthesized by solgel procedure, *Mater. Sci. Eng. B*, 1997; 47: 33 - 40.
22. Mali SS, Shinde PS, Betty C, Bhosale PN, Lee WJ, and Patil PS, Nanocoral architecture of TiO₂ by hydrothermal process: synthesis and characterization, *Appl. Surf. Sci.*, 2011; 257: 9737-9746.
23. Lu C-H, and Wen M-C. Synthesis of nanosized TiO₂ powders via a hydrothermal microemulsion process, *J. Alloys Compd.*, 2008; 448: 153 -158.
24. Suprabha T, Roy HG, Thomas J, Kumar KP, and Mathew S. Microwave-assisted synthesis of titania nanocubes, nanospheres and nanorods for photocatalytic dye degradation, *Nanoscale Res. Lett.*, 2009; 4: 144 - 152.
25. Ito A, Sato T, and Goto T. Transparent anatase and rutile TiO₂ films grown by laser chemical vapor deposition, *Thin Solid Films*, 2014; 551: 37 - 41.
26. Akhavan Sadr F, Montazer M, In situ sonosynthesis of nano TiO₂ on cotton fabric, *Ultrason. Sonochemistry*, 2014; 21: 681 - 691.

Synthesis and Dielectric properties of nanocrystalline Gd³⁺ substituted Nickel-Cadmium ferrites

More RM¹, Chaudhari ND², and Vasambekar PN³

¹Department Physics, D.B.J. College, Chiplun, Ratnagiri, MS., ²Department of Physics, Pratishthan Mahavidyalaya, Paithan, Aurangabad, MS., ³Department of Electronics Science, Shivaji University, Kolhapur, MS. Email: rajendrammore@gmail.com, nk.dchaudhari@gmail.com

Manuscript Details

Available online on <http://www.irjse.in>
ISSN: 2322-0015

Editor: Dr. Arvind Chavhan

Cite this article as:

More RM, Chaudhari ND, and Vasambekar PN. Synthesis and Dielectric properties of nanocrystalline Gd³⁺ substituted Nickel-Cadmium ferrites, *Int. Res. Journal of Science & Engineering*, December 2017; Special Issue A1 : 8-14.

© The Author(s). 2017 Open Access

This article is distributed under the terms of the Creative Commons Attribution 4.0 International License

(<http://creativecommons.org/licenses/by/4.0/>), which permits unrestricted use, distribution, and reproduction in any medium, provided you give appropriate credit to the original author(s) and the source, provide a link to the Creative Commons license, and indicate if changes were made.

ABSTRACT

Nanocrystalline Gd³⁺ substituted Ni-Cd spinel ferrites having general formula Cd_xNi_{1-x}Gd_yFe_{2-y}O₄ with x = 0.0, 0.2, 0.4, 0.6, 0.8, 1.0 and y = 0.00, 0.05 and 0.1 were synthesized by oxalate co-precipitation method using Sulphates. XRD analysis confirms that all the composition exhibits a single phase cubic spinel structure excluding the presence of any intermediate phase. Room temperature dielectric properties such as dielectric constant, dielectric loss factor, loss tangent, ac conductivity for all samples were investigated as a function of composition and frequency range between 20 Hz to 1 MHz. These dielectric studies indicates that the dielectric constant, dielectric loss and loss tangent for all composition shows usual dielectric dispersion which is due to Maxwell-Wagner type interfacial polarization.

Key Words: Dielectric constant, loss tangent, loss factor, co precipitation, Gd³⁺ substitution.

INTRODUCTION

Spinel ferrites have attracted a lot of attention of researchers due to their wide range of technological applications. Ferrite materials are widely used in many technical fields such as telecommunication, digital memories, multilayer chip inductor, radar and satellite communication, gas sensors, photoelectric devices, microwave devices and biomedical applications [1, 2, 3].

They have good dielectric properties and large number of application from microwave to radio frequency. The dielectric properties of ferrites are depend upon the method of preparation, sintering time and sintering temperature, chemical composition, type and quantity of substituent [4,5]. For high frequency applications, the knowledge of dielectric properties of ferrites is necessary and the parameters such as dielectric constant, dielectric loss, loss tangent and AC conductivity could be evaluated. These dielectric properties provide information about the behavior of localized electric charge carriers leading to greater understanding of mechanism of dielectric polarization in the sample [6]. Generally the ferrite materials were synthesized using conventional ceramic oxide method which suffers from many drawbacks such as requirement of high sintering temperature and more time. The particles obtained from ceramic method are large and non uniform in size resulting in the formation of voids and low density material [7]. To overcome these limitations of ceramic methods, many chemical methods such as co-precipitation, sol-gel, combustion, hydrothermal, oxalate precursor, microwave syntheses have been used for the preparation of high density ferrites [9–14]. The objective of the present work is to synthesize the Ni-Cd and Gd³⁺ substituted Ni-Cd ferrites using co-precipitation method and to study the effect of Gd³⁺ substitution on the dielectric properties.

METHODOLOGY

The ferrite system CdxNi_{1-x}GdyFe_{2-y}O₄ (x = 0.0, 0.2, 0.4, 0.6, 0.8 and 1.0 with y = 0.0, 0.05, 0.10) was prepared by oxalate co-precipitation method. The high purity AR grade nickel sulphate, cadmium sulphate, gadolinium sulphate and ferrous sulphate were weighed carefully on single pan microbalance to have proper stoichiometric proportion required in the final product. The oxalate co-precipitation method for the preparation of present ferrite system is discussed elsewhere [15]. The dry powder was presintered at 600°C for one hour in air. The pellets of 10 mm diameter were formed with hydraulic press by applying the pressure of 5 tones inch⁻² for five minutes. Finally the prepared pellets were sintered at 1000°C for two hours.

The structural formation was confirmed by taking X-ray diffractograms of all the samples, recorded with Philips PW 3710 powder diffractometer by continuous scanning in the range of 0 to 100°. The dielectric measurements were carried out at room temperature in the frequency range 20 Hz to 1MHz with HEWLETT PACKARD, precision LCR meter model HP 4284A.

The dielectric constant (ϵ') of ferrite sample was calculated using a relation [8, 31].

$$\epsilon' = \frac{C_p \times t}{\epsilon_0 A} \text{ ----- [1]}$$

Where ϵ' is dielectric constant, ϵ_0 is free space permittivity, C_p is capacitance of sample, t is thickness of the sample and A is area of cross section. The dielectric loss tangent ($\tan\delta$) was calculated using a relation

$$\tan\delta = \frac{1}{Q} \text{ ----- [2]}$$

Where Q is the quality factor

The dielectric loss factor (ϵ'') of the ferrite samples is given by

$$\epsilon'' = \epsilon' \times \tan\delta \text{ ----- [3]}$$

The ac conductivity in the frequency range 1 KHz - 1MHz was determined using the values of dielectric constant and dielectric loss tangent in the relation [26]

$$\sigma_{ac} = \omega \epsilon_0 \epsilon' \tan\delta \text{ ----- [4]}$$

Where σ_{ac} is ac conductivity and ω is angular frequency.

RESULT AND DISCUSSION

X-RAY diffraction:

Fig. 1 shows a typical X - ray diffraction pattern for CdxNi_{1-x}GdyFe_{2-y}O₄ (x = 0.0, 0.2, 0.4, 0.6, 0.8 and 1.0 with y = 0.0, 0.05, 0.10) sintered at 1000°C for 2 hours. All the sintered compositions show all the characteristics reflections of cubic spinel ferrites with most intense [311] reflection which confirms the formation of cubic spinel structure without any signature of secondary phase in sintered ferrite compositions. An absence of any extra peak ensures that the synthesized products are phase pure. The crystallite size of all samples was calculated using the Debye-Scherrer formula and it was found to be in 40 to 50 nm regime.

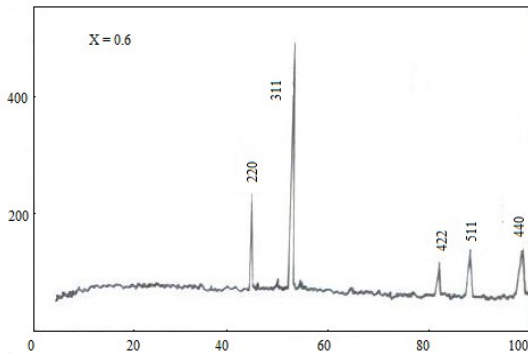


Fig. 1: Typical XRD pattern for $Cd_xNi_{1-x}Gd_{0.05}Fe_{1.95}O_4$ with $x = 0.6$

Compositional variation of ϵ' , ϵ'' , $\tan\delta$ AND σ_{ac} :

Table 1 represents the values of dielectric parameters as a function of composition at frequency 5 KHz for $y = 0.00, 0.05$ and 0.1 . It is observed that all the dielectric parameters show similar trend/ behaviour for all composition series. For $y = 0.00$, the dielectric parameters ϵ' , ϵ'' , $\tan\delta$ decreases with increase in x content. For Gd^{3+} substituted composition with $y = 0.05$, the ϵ' , ϵ'' , $\tan\delta$ increase initially up to $x = 0.2$, then reaches maximum thereafter decreases for its further substitution. For $y = 0.1$, they increase up to $x = 0.4$, thereafter again decrease. Jadhav et al [9] have observed an initial increase in dielectric constant with increase in Zn up to $x = 0.3$ and then decrease with further increase in Zn content for Ni-Zn ferrites and this behaviour is attributed to fluctuating in hopping mechanism between Fe^{3+} and Fe^{2+} ions. Kolekar [16] have investigated the dielectric studies of Gd^{3+} substituted Cu-Cd ferrites as function of

compositions. Iwachi [17] reported that the strong relation between the conduction mechanism and dielectric behaviour of ferrites starting with assumption that the conduction mechanism and polarization are quite similar processes to each other. They observed that an electronic exchange between $Fe^{2+} = Fe^{3+}$ results in local polarization and determines its dielectric behaviour. Hence, similar explanation may be proposed for the compositional variation of dielectric constant in present ferrite system. D. Ravinder [18] concluded that the number of ferrous ions on octahedral site plays a dominant role in the process of conduction mechanism and hence dielectric polarization. The high dielectric constant composition has maximum number of ferrous ions and thus it reveals maximum dielectric polarization in case of Erbium substituted Mn-Zn ferrites. Batoo [19] have observed the decrease in dielectric constant with increasing Al content and concluded that when Al is doped in Mn ferrite, it occupies the octahedral site resulting in decrease in number of Fe ions and is responsible for the polarization in the system. The value of $\tan\delta$ depends on many factors such as Fe^{2+} content, stoichiometry and sintering temperature [20]. Table 1 shows that dielectric loss tangent also depend on the composition. It is also observed that when Gd^{3+} is substituted in Ni-Cd ferrites the dielectric loss tangent decreases. For $y = 0.00$ ac conductivity decrease faster initially, from $x = 0.4$ it decrease very slowly and for $y = 0.05$ & 0.1 , there is no particular trend with composition. It is also observed that after substitution of Gd^{3+} in Ni-Cd ferrites the conductivity decreases.

Table 1: Data on dielectric constant (ϵ'), dielectric loss factor (ϵ''), dielectric loss tangent ($\tan\delta$) and AC conductivity σ_{ac} for $Cd_xNi_{1-x}Gd_yFe_{2-y}O_4$ ferrite system

$x \downarrow$	ϵ'			ϵ''			$\tan\delta$			$\sigma_{ac} \times 10^{-8}$ $\Omega^{-1}cm^{-1}$		
	0.00	0.05	0.1	0.00	0.05	0.1	0.00	0.05	0.1	0.00	0.05	0.1
0.00	269	395	351	121	67	59	0.45	0.17	0.17	33.8	18.6	16.7
0.2	235	459	237	91	94	45	0.38	0.20	0.18	25.2	26.2	12.4
0.4	177	438	339	29	66	56	0.16	0.15	0.16	8.16	18.4	15.6
0.6	150	408	250	20	67	33	0.13	0.16	0.13	5.54	18.7	9.2
0.8	101	381	280	21	42	40	0.20	0.11	0.14	5.79	11.7	11.2
1.0	76	265	255	18	35	47	0.23	0.09	0.18	4.98	9.9	13.1

FREQUENCY VARIATION OF ϵ' , ϵ'' , $\tan\delta$ AND σ_{ac} :

Figs. 2(a, b, c), 3(a, b, c) and 5(a, b, c) shows the variation of dielectric constant (ϵ'), dielectric loss factor (ϵ''), dielectric loss tangent ($\tan\delta$) and AC conductivity (σ_{ac}) as a function of frequency for the present ferrite system with $y = 0.00, 0.05$ and 0.1 respectively at room temperature in the frequency range 1 KHz to 1MHz. From Figs., it is clearly seen that ϵ' , ϵ'' and $\tan\delta$ decrease as the frequency increases showing usual dielectric dispersion. The dispersion is sharp at lower frequencies and almost level off at higher frequencies. This type of nature can be explained by Maxwell [21] Wagner [22] and Koops [28] phenomenological theory. The decrease in dielectric constant at higher frequency can be explained on the basis that the dielectric medium is assumed to be composed of well conducting grains which are separated by non-conducting grain boundaries. The grain boundaries are found to be more effective at lower frequency while ferrite grains are more effective at higher frequency [27]. When electrons reach non conducting grain boundaries through the hopping, the resistance of grain boundary is high; hence electrons pile up at grain boundaries and produce the polarization. At higher frequency, beyond a certain limit, the electron does not follow the alternating field. This decreases the possibility of electron reaching the grain boundary which results decrease in polarization (Maxwell-Wagner [21,22]). The explanation about the polarization process was given by Rabinkin and Novikova [30]. They pointed out that the polarization in ferrite is quite similar to the conduction process. The electron exchange between $Fe^{2+} \leftrightarrow Fe^{3+}$ results in local displacement of electron in the direction of applied field, hence determines the polarization. The polarization decreases with increase in frequency is due to the fact that beyond a certain frequency of external field the exchange between $Fe^{2+} \leftrightarrow Fe^{3+}$ does not follow the alternating field [29]. The high value of dielectric constant at low frequency is due to Fe^{2+} ions and grain boundary defects [21, 22].

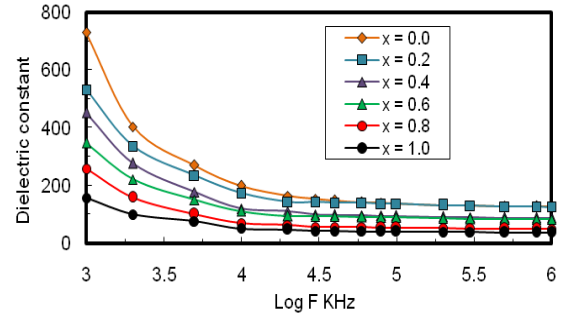


Fig. 2(a): Variation of Dielectric constant with frequency of $Cd_xNi_{1-x}Fe_{2-y}Gd_yO_4$. For $y = 0.00$.

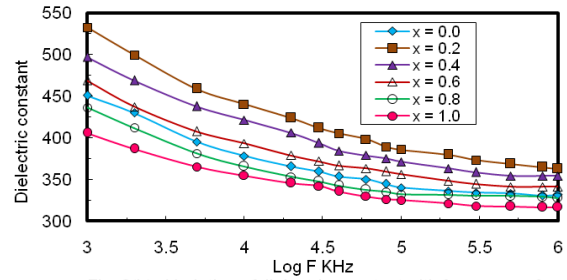


Fig. 2(b): Variation of dielectric constant with frequency of $Cd_xNi_{1-x}Fe_{2-y}Gd_yO_4$. For $y = 0.05$.

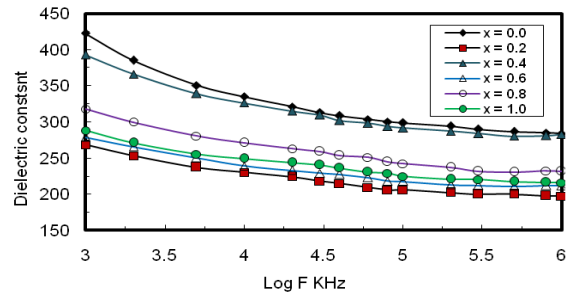


Fig. 2(c): Variation of Dielectric constant with frequency for $Cd_xNi_{1-x}Fe_{2-y}Gd_yO_4$ For $y = 0.10$.

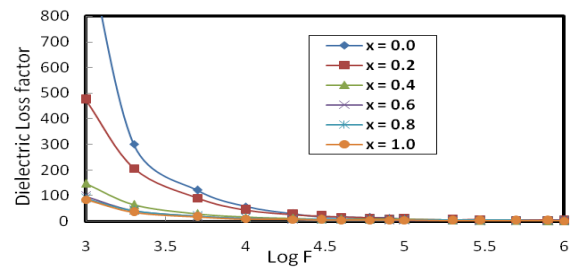


Fig. 3(a) Variation of dielectric loss factor with frequency for $Cd_xNi_{1-x}Fe_{2-y}Gd_yO_4$ for $y = 0.00$

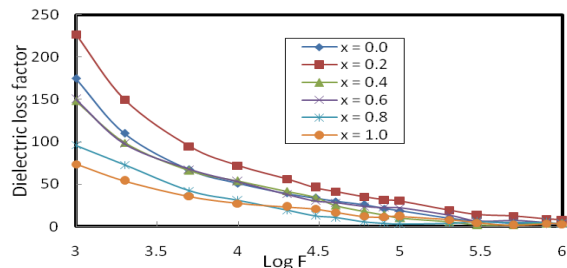


Fig. 3(b): Variation of dielectric loss factor with frequency for $Cd_xNi_{1-x}Fe_{2-y}Gd_yO_4$ for $y = 0.05$

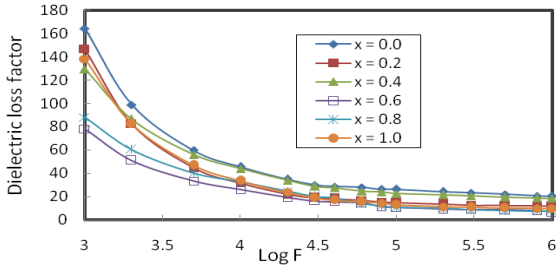


Fig. 3(c): Variation of dielectric loss factor with frequency for $Cd_xNi_{1-x}Fe_{2-y}Gd_yO_4$ for $y = 0.10$

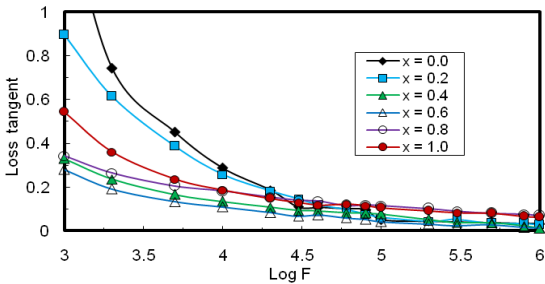


Fig. 4(a): Variation of Dielectric loss tangent with frequency of $Cd_xNi_{1-x}Fe_{2-y}Gd_yO_4$. For $y = 0.00$.

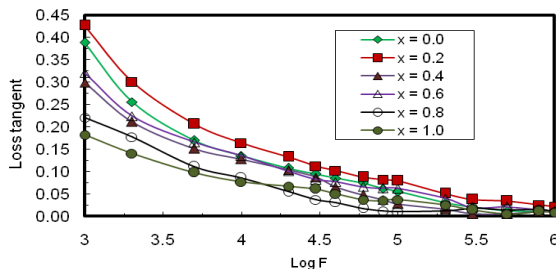


Fig. 4(b): Variation of Dielectric loss tangent with frequency, of $Cd_xNi_{1-x}Fe_{2-y}Gd_yO_4$. For $y = 0.05$.

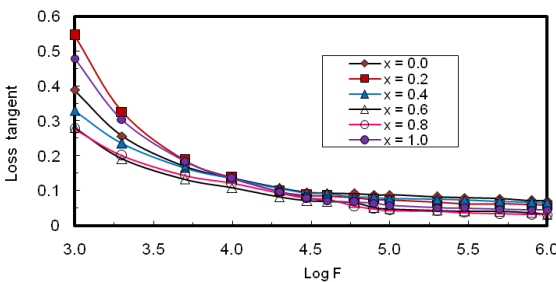


Fig. 4(c): Variation of dielectric loss tangent with frequency of $Cd_xNi_{1-x}Fe_{2-y}Gd_yO_4$. For $y = 0.10$.

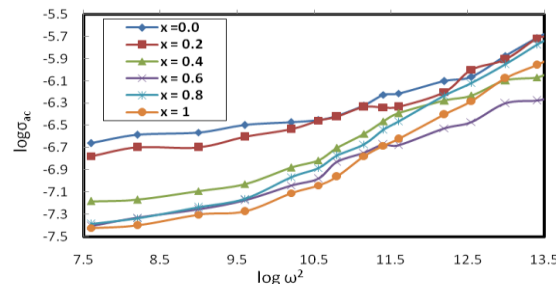


Fig. 5(a) Variation of ac conductivity with frequency for $Cd_xNi_{1-x}Fe_{2-y}Gd_yO_4$ for $y = 0.00$

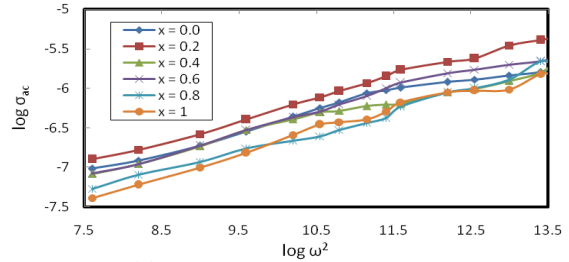


Fig. 5(b) Variation of ac conductivity with frequency for $Cd_xNi_{1-x}Fe_{2-y}Gd_yO_4$ for $y = 0.05$

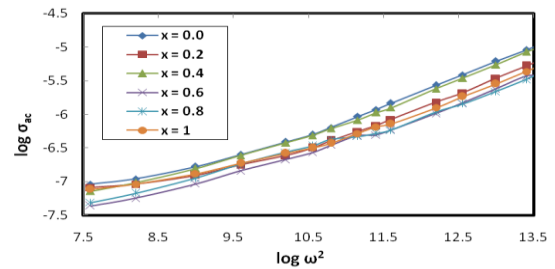


Fig. 5(c) Variation of ac conductivity with frequency for $Cd_xNi_{1-x}Fe_{2-y}Gd_yO_4$ for $y = 0.1$

It is necessary to understand the conduction mechanism and type of polarons responsible for the conduction. The variation of AC conductivity as a function of frequency for all compositions with $y = 0.00, 0.05$ and 0.1 is represented in Figs. 5(a, b, c). The frequency dependence of ac conductivity is given by Batoo [19]

$$\sigma_{tot.} = \sigma_B(T) + \sigma(\omega, t)$$

$\sigma_B(T)$ is the conductivity due to band conduction and frequency independent function and predominant in low frequency and at high temperature while $\sigma(\omega, t)$ is pure ac conductivity due to hopping process at octahedral site. It is frequency dependent function and predominant in high frequency region and at low temperature. The frequency dependence of the second term can be expressed as $\sigma_{AC} = A\omega^n$, where A is the constant having unit of conductivity, n is temperature dependent function, σ is real part of conductivity and ω is the angular frequency.

It is well known that in large polaron hopping ac conductivity decreases with frequency while in small polaron hopping it increases with frequency [23-25]. Austin and Mott [25] have explained the electrical conduction mechanism in terms of electron and polaron hopping. From the variation of $\log \sigma_{AC}$ versus $\log(\omega^2)$, it is seen that ac conductivity increases with increase in frequency which is a normal behavior for

ferrite materials. For the present ferrite system, the plots of ac conductivity measurement are observed to be linear and indicate the conduction is due to small polaron. The increase in ac conductivity can be explained, as the frequency of applied field increases the conductive grains becomes more active and promoting the electron hopping between two octahedral sites and a transition between Fe^{2+} and Fe^{3+} ions thereby increases the hopping conduction. R. C. Kambale et al [7] have reported a linear response in ac conductivity measurement and attributed to the small polaron type hopping mechanism in Ni-Zn ferrites.

CONCLUSION

The Ni-Cd-Gd ferrite nanoparticles having general formula $\text{Cd}_x\text{Ni}_{1-x}\text{Gd}_y\text{Fe}_{2-y}\text{O}_4$ ($x = 0.0, 0.2, 0.4, 0.6, 0.8$ and 1.0 with $y = 0.0, 0.05, 0.10$) were successfully synthesized by co-precipitation techniques using sulphates. The X-ray diffraction pattern reveals the formation of single phase cubic spinel structure excluding the presence of any undesirable secondary structure. The dielectric parameters such as dielectric constant (ϵ'), dielectric loss factor (ϵ''), dielectric loss tangent ($\tan\delta$) decrease as the frequency increases exhibiting a normal behaviour of ferrites. The dependence of dielectric properties on frequency of alternating applied field is in accordance with Maxwell-Wagner model and Koops phenomenological theory. AC conductivity (σ_{ac}) increases with increase in frequency. The plots of AC conductivity measurements are almost linear, indicating that the conduction is due to small polaron hopping.

REFERENCES

1. Pasquate M, Sasso CP, Velluto M, Lim SH. Stress sensing with Co based ferrite compositions. *J. Magn. Magn. Mater.* 2002; 242: 1460-1463.
2. Amin GR, Youseti MH, Abolhassani MR, Manouchehri S, Keshavarz MH, Fatahian S. Magnetic properties and microwave absorption in Ni-Zn and Mn-Zn ferrite nanoparticles synthesized by low temperature solid state reaction, *J. Magn. Magn. Mater.*, 2011; 323: 730-734.
3. Yallop MM, Othman SF, Curtis ET, Gupta B K, Jaggi M, Chauhan SC. Multifunctional magnetic nanoparticles for magnetic resonance imaging and cancer therapy, *Biomaterials.* 2011; 32: 1890-1905.
4. Zaki HM. AC conductivity and frequency dependence of dielectric properties of Copper doped magnetite, *Physica B. Condensed Matter.* 2005; 363: 232-244.
5. Kaur B, Bhat M, Licci F, Kumar R, Bamzui KK, Katru PN. *J. Mater. Chem. Phys.* 2007; 103:255.
6. Ghodake JS, Kambale RC, Salvi SV, Sawant SR, Suryawanshi SS. Electric properties of Co substituted Ni-Zn ferrites, *J. Alloys & Comp.* 2009; 486:830-834.
7. Kambale RC, Adhate NR, Chaugule BK, Kolekar YD. Magnetic and dielectric properties of mixed spinel Ni-Zn ferrites synthesized by citrate-nitrate combustion method, *J. Alloys & Comp.* 2010; 491: 372-377.
8. Kambale RC, Shaikh PA, Bhosale CH, Rajpure KY, Kolekar YD, Dielectric properties and complex dielectric impedance spectroscopy studies of mixed Ni-Co ferrites, *Smart Mater. Struct.*, 2009;18: 085014.
9. Jadhav SS, Shirsath SE, Toksha BG, Shengule DR, Jadhav KM. Structural and dielectric properties of Ni-Zn ferrites nanoparticles by co-precipitation method, *J. Optoelect. & Adv. Mater.* 2008;10(10):2644-2648.
10. Nasir S, Anis-ur Rehman M, Malik MA, Structural and dielectric properties of Cr doped Ni-Zn nano ferrites, *Phys. Scr.* 2011; 83: 025602.
11. Chen O, Du P, Huang W, Jin Lu, Weng W, Han G. Ferrite with extra ordinary electric and dielectric properties prepared from self combustion technique, *App. Phys. Letters.*, 2007;99:132907 (1-3)
12. Chaudhari ND, Kambale RC, Bhosale DN, Suryawanshi SS, Sawant S R, Thermal hysteresis and domain states in Ni-Zn ferrites synthesized by oxalate precursor's method, *J. Magn. Magn. Mater.*, 2010; 322:1999-2005.
13. Singh AK, Goel TC, Mendiratta RG, Thakur OP, Prakash C. Magnetic properties of Mn substituted Ni-Zn ferrites, *J. Appl. Phys.*, 2002 ;92(7): 3872-3876.
14. Koseoglu Y. Structural and magnetic properties of Cr doped Ni-Zn ferrites nanoparticles prepared by surfactant assisted hydrothermal technique, *Ceramic Inter.*, 2015; 41: 6417-6423.
15. More RM, Shinde TJ, Chaudhari ND, Vasambekar PN, . Effect of temperature on X-ray, IR and magnetic properties of nickel ferrite prepared by oxalate co-precipitation method, *J. Mater. Sci. Mater. In Elect.*,2005; 16: 721-724.

16. Kolekar CB, Kamble PN, Kulkarni SG, Vaingankar AS. Effect of Gd^{3+} substitution on dielectric behaviour of Copper-Cadmium ferrites, *J. Mater. Sci.*, 1995; 30: 5784-5788
17. Iwachi K. Dielectric properties of fine particles of Fe_3O_4 and some ferrites, *Jap. J. Appl. Phys.*, 1971; 10:1520.
18. Ravinder D, Vijaya Kumar K. Dielectric behavior of Erbium Substituted Mn-Zn ferrites, *Bull. Mater. Sci.*, 2001; 24(5): 505-509.
19. Batoo KM. Study of dielectric and impedance properties of Mn ferrites, *Physica B*, 2011; 406: 382-387
20. Verma A, Goel TC, Mendiratta RG, Kishan P. Magnetic properties of Nickel-Zinc ferrites prepared by citrate precursors method, *J. Magn. Mater.* 2000; 208: 13-19.
21. Maxwell JC. "A Treatise in Electricity and Magnetism", Oxford University Press, New York, 1973; 1: 828.
22. Wagner KW. Zur Theorie der Unvollkommenen Dielektrika, *Ann. Der. Physik*, 1913; 40: 817-855.
23. Devan RS, Chaugule BK. Effect of composition on coupled electric, magnetic and dielectric properties of two phase particulate magnetolectric composite, *J. Appl. Phys.*, 2007; 101: 014109
24. Mahajan RP, Patankar KK, Kothale MB, Patil SA. Conductivity, Dielectric behavior and magnetolectric effect in Copper Ferrite-barium titanate composites, *Bull. Mater. Sci.*, 2000; 23: 273-279
25. Austin LG, Mott NF. Polarons in crystalline and non-crystalline materials, *Adv. In Physics*, 1969; 18(71): 41-102.
26. Ajmal M, Maqsood A. AC conductivity and density related and magnetic properties of $Ni_{1-x}Zn_xFe_2O_4$ ferrites with variation of Zinc concentration, *Mater. Lett.*, 2008, 62: 2077.
27. Amed MA, El Hitti MA, El Nimr M, Amer M. Dielectric behavior in Co substituted NiSb ferrites, *J. Mater. Sci. Letters*, 1997; 16: 1076-1079.
28. Koops CG. On dispersion of resistivity and dielectric constant of some semiconductors at audio frequencies, *Phys. Rev.*, 1951; 83: 12
29. Popandian N, Balay P, Narayanasamy A. Electrical conductivity and dielectric behavior of nanocrystalline $NiFe_2O_4$ spinel, *J. Phys.:Condens. Matter*, 2002; 14: 3221.
30. Rabinkin LT, Novikova ZI. "Ferrites", (Minsk: Acad. Nauk, USSR), 1960:146.
31. Shaikh PA, Kambale RC, Rao AV, Kolekar YD. Studies on structural and electrical properties of $Co_{1-x}Ni_xFe_{1.9}Mn_{0.1}O_4$ ferrites, *J. Alloys & Comp.*, 2009; 482: 276-282.

Study of Variation of Bandgaps of Pure and Doped Nickel Oxide Nanoparticles (NiO) prepared in different environments

Kaushik Baishya¹ and Karmakar Sanjib*

¹Department of Instrumentation & USIC, Gauhati University, Guwahati-781014

*Corresponding author's email: sankarmakar@gauhati.ac.in

Manuscript Details

Available online on <http://www.irjse.in>
ISSN: 2322-0015

Editor: Dr. Arvind Chavhan

Cite this article as:

Kaushik Baishya and Karmakar Sanjib. Study of Variation of Bandgaps of Pure and Doped Nickel Oxide Nanoparticles (NiO) prepared in different environments, *Int. Res. Journal of Science & Engineering*, December 2017; Special Issue A1 : 15-20.

© The Author(s). 2017 Open Access

This article is distributed under the terms of the Creative Commons Attribution 4.0 International License

(<http://creativecommons.org/licenses/by/4.0/>),

which permits unrestricted use, distribution, and reproduction in any medium, provided you give appropriate credit to the original author(s) and the source, provide a link to the Creative Commons license, and indicate if changes were made.

ABSTRACT

We report synthesis and characterisation of Nickel Oxide (NiO) nanoparticles and Al doped Nickel Oxide (ANO) nanoparticles prepared by Chemical Bath Deposition (CBD) method. The nanoparticles of NiO and ANO are characterised by XRD (Philips, XPERT PRO) and UV-vis-absorption (Hitachi U-1800) techniques. The NiO nanoparticles are prepared from nickel nitrate and sodium hydroxide solutions. Similarly, the ANO nanoparticles are prepared from nickel nitrate and aluminium nitrate solutions with different Al percentages viz. 2.5, 4.5 and 6.5 as dopant. Both the nanoparticles of NiO and ANO are prepared at room temperature (RT) and subsequently calcined at 473 K and 673 K. At RT the nanoparticles are found to be amorphous in nature and after calcination the nanoparticles get crystallised which is confirmed by the XRD analysis. The direct band gaps calculated from the UV-vis absorption spectra of NiO nanoparticles prepared at RT and 473 K and 673 K temperatures are found to be of the order of 5.79 eV, 5.61 eV and 5.55 eV. But for ANO nanoparticles prepared at RT the direct band gaps are found to be of the order of 4.36 eV, 3.84 eV and 3.82 eV at doping percentage 2.5, 4.5 and 6.5 respectively. It is seen that when the calcination temperatures and doping percentage are increased, the band gaps decreases. Due to the increase in particle size at higher temperatures, the band gaps are reduced. Increase in doping percentages lead to increase in conductivity due to the higher concentration of carriers.

Keywords: NiO nanoparticles, Al doped NiO, Microstrain Band Gap

INTRODUCTION

Nanostructured materials have been showing increasing research interest due to their unique chemical and physical properties [4-7]. The size, shape and band gaps of nanomaterials are greatly affected by these properties. The nanoscale oxide particles of transition metals are gaining continuous importance for various applications such as catalysts, passive electronic components and ceramic devices. Nickel Oxide (NiO) is a wide band gap metal oxide ranging from 3.6 eV to 4.0eV [8-17] with wide range of applications like catalytic, magnetic and conductivity. When particle size decreases, nanoparticles show blue shift but in some reported work the values of optical band gap of nanostructure are found to be less than the optical band gap of bulk NiO nanoparticles [8].

In this work, NiO nanoparticles and ANO nanoparticles are prepared by CBD method. The ANO nanoparticles are prepared using different aluminium doping concentrations.

METHODOLOGY

Preparation of NiO nanoparticles by CBD method:

NiO nanoparticles are prepared by CBD method. 0.019M $\text{Ni}(\text{NO}_3)_2 \cdot 6\text{H}_2\text{O}$ (solution1) and 0.5M NaOH (solution2) are dissolved in ethanol under continuous stirring condition at 80°C. Solution1 is added drop wise to solution 2 under continuous stirring condition. The mixture is filtered and the precipitate obtained is allowed to dry for further characterizations.

Preparation of ANO nanoparticles by CBD method:

All chemicals are of analytical reagent grade and are used without further purification. ANO nanoparticles are prepared by chemical precipitation method. The reactants are $\text{NiNO}_3 \cdot 6\text{H}_2\text{O}$ and $\text{Al}(\text{NO}_3)_3 \cdot 9\text{H}_2\text{O}$. Ethanol is used as the reaction medium in all the synthesis steps. In a typical synthesis, desired molar proportions of $\text{NiNO}_3 \cdot 6\text{H}_2\text{O}$ (0.2M) and $\text{Al}(\text{NO}_3)_3 \cdot 9\text{H}_2\text{O}$ (2.5, 4.5 and 6.5 at.%) each in 100 ml ethanol are dissolved and stirred for 30 minutes. NaOH (0.25M) solution is added drop wise to the solution under continuous stirring for four hours to get fine precipitation. The obtained precipitate is

filtered and dried at room temperature to obtain Al doped NiO nanoparticles.

CHARACTERIZATION METHODS:

X-Ray Diffraction analysis:

The phase and the structure of NiO nanoparticles and ANO nanoparticles are identified by X-Ray Diffractometer (XRD) which is operated with generator setting of 35mA and 40kV with $\text{CuK}\alpha$ ($\lambda=1.5418 \text{ \AA}$) radiation. The XRD is calibrated with a standard silicon sample and broadening of peaks because of instrumental effect is also corrected by Warren rule. The scanning range is from 25-90° (2 θ) at a scan speed 1sec/step and 0.02° 2 θ is the step size. The diffraction patterns of the NiO nanoparticles and ANO nanoparticles prepared at RT and at different annealed temperatures of 473K and 673K are given in Fig1 and Fig2 respectively. The diffraction patterns of the nanoparticles corresponds to (111), (200), (220), (311) and (222) planes almost match with standard NiO powder (ICCD No. 78-0643). The prepared NiO nanoparticles are cubic with $a=4.176$ and space group $\text{Fm}\bar{3}\text{m}$ (225).

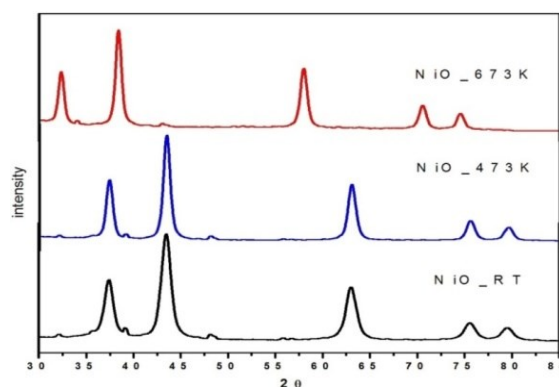


Figure 1: The XRD pattern of NiO nanoparticles prepared at temperatures RT, 473K and 673K

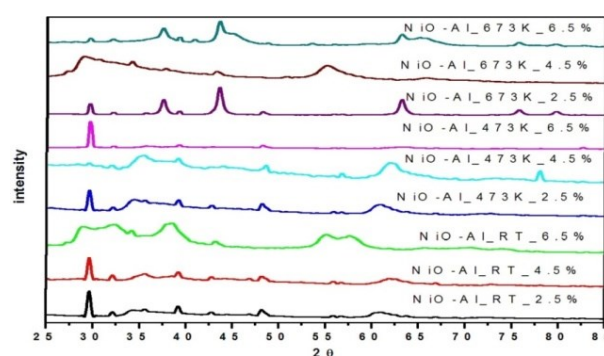


Figure 2: The XRD pattern of ANO nanoparticles

prepared at RT, 473K and 673K.

2.2.1 Microstrain analysis for NiO nanoparticles:

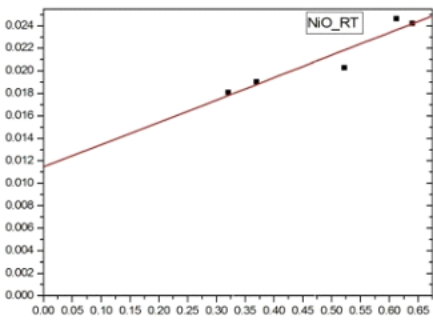


Figure 3

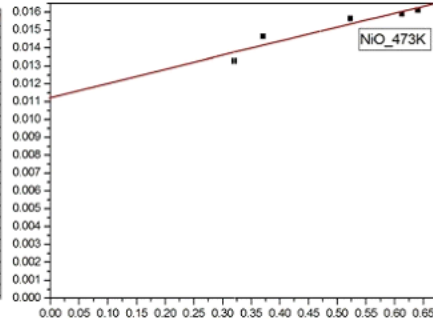


Figure 4

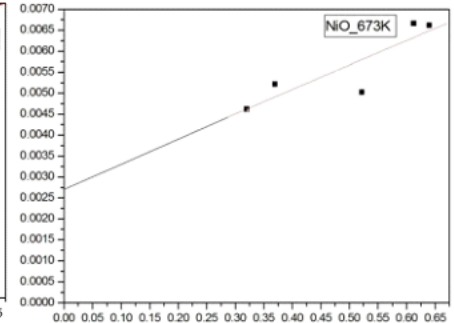


Figure 5

2.2.2 Microstrain analysis for ANO nanoparticles:

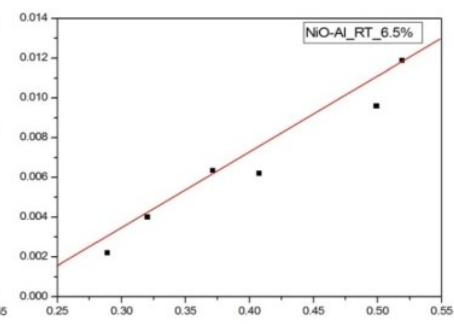
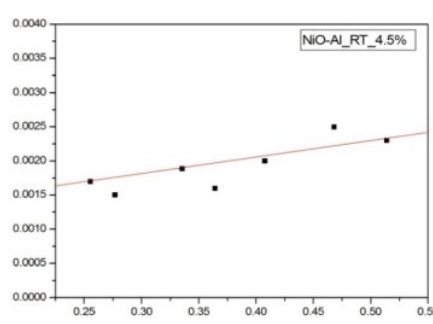
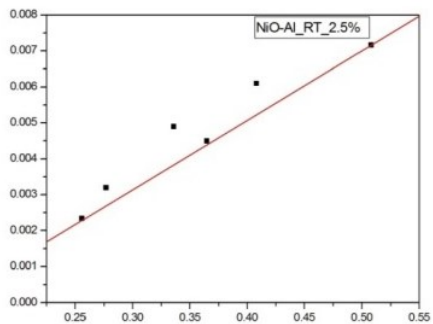


Figure 6: The W_Hall plot to determine grain size and strain of Al doped NiO nanoparticles (2.5%, 4.5% and 6.5%) prepared at RT.

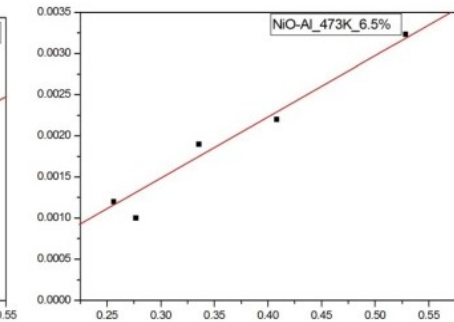
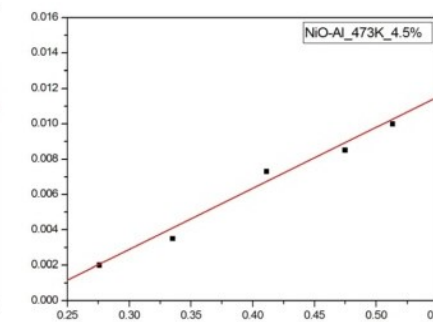
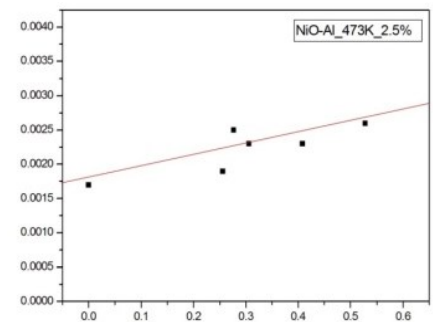


Figure 7: The W_Hall plot to determine grain size and strain of Al doped NiO nanoparticles (2.5%, 4.5% and 6.5%) prepared at 473K.

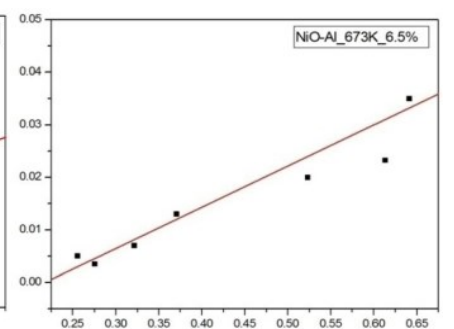
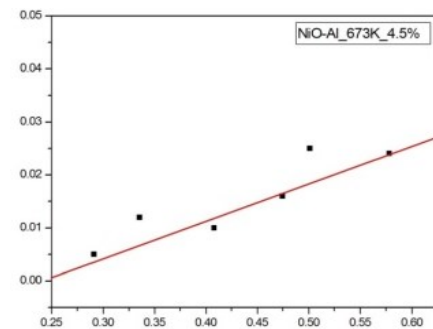
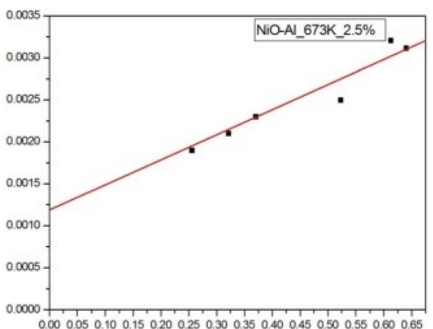


Figure 8: The W_H plot to determine grain size and strain of Al doped NiO nanoparticles (2.5%, 4.5% and 6.5%) prepared at 673K.

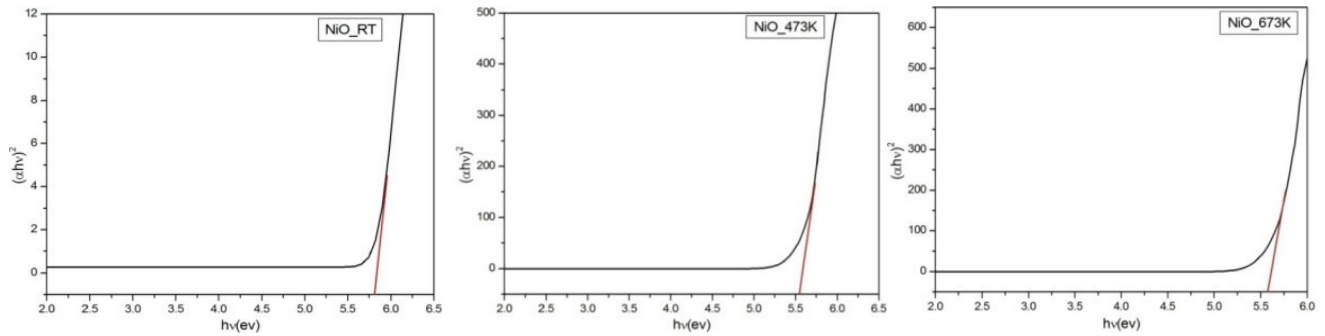


Figure 9: The direct band gaps of the NiO nanoparticles calculated from the UV-vis-absorption at temperatures RT, 473K and 673K.

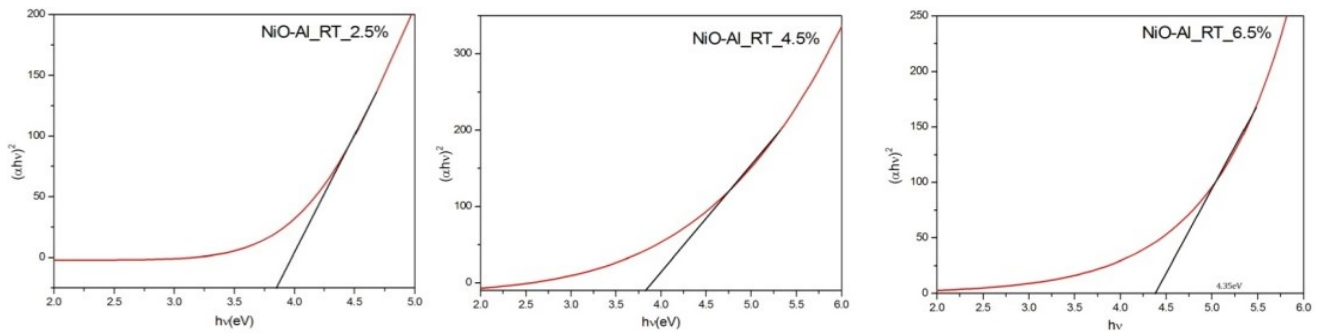


Figure 10: The direct band gaps calculated from the UV-vis-absorption of Al doped NiO nanoparticles prepared at RT.

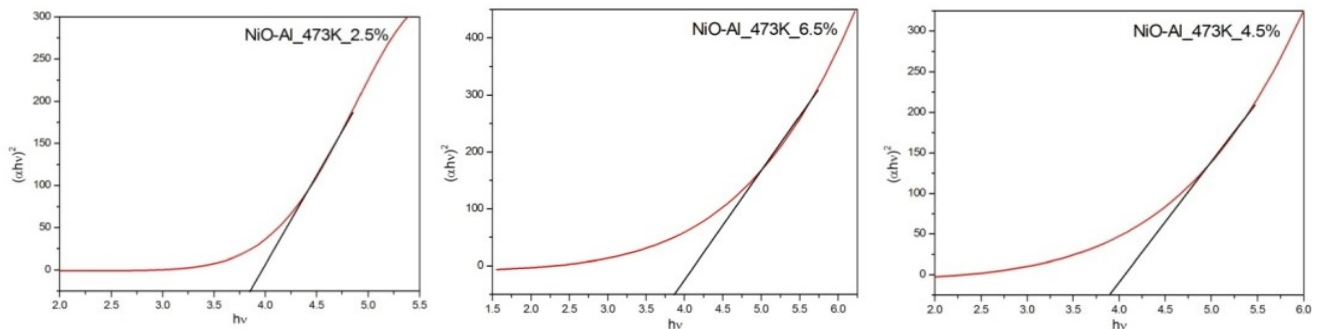


Figure 11: The direct band gaps calculated from the UV-vis-absorption of Al doped NiO nanoparticles prepared at 473K.

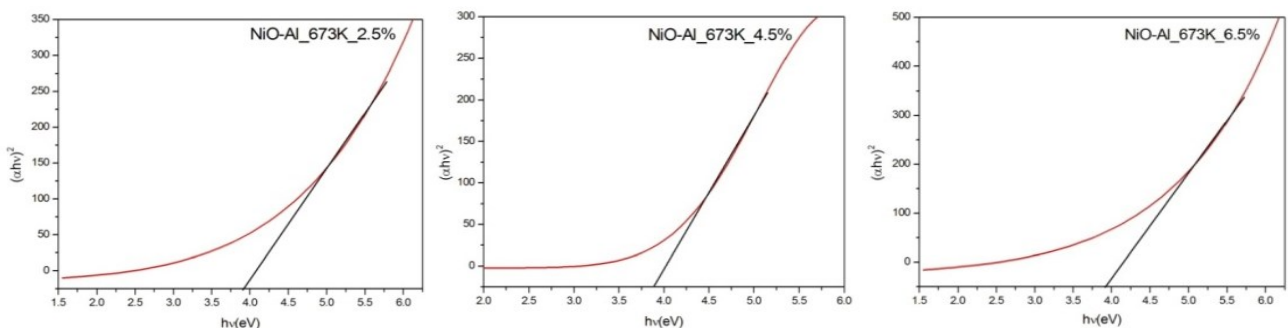


Figure 12: The direct band gaps calculated from the UV-vis-absorption of Al doped NiO nanoparticles prepared at 673K.

Table 1: Comparison of bandgaps, particle sizes and microstrains of NiO and ANO nanoparticles.

Sample code	Doping conc.	Band Gap (eV)			Particle size(nm)			Microstrain		
		RT	473K	673K	RT	473K	673K	RT	473K	673K
NiO		5.79	5.61	5.55	12.05	13.50	54.55	0.013	0.0052	0.0027
	2.5%	4.36	3.83	3.80	6.30	8.16	11.66	0.0075	0.0017	0.0031
	4.5%	3.84	3.81	3.79	8.67	12.61	13.87	0.0023	0.0135	0.0160
ANO	6.5%	3.82	3.80	3.75	9.25	15.41	17.82	0.0148	0.0029	0.0173

Microstrain analysis:

The observed peak shifts in the peaks of the nanoparticles are because of the development of defects in the nanoparticles at higher calcination temperatures. The broadening in the diffraction peaks occur due to inhomogeneous microstrain induced by strain broadening or because of shrinkage of coherent scattering volume (size broadening). The strain and size broadening can be separated by W_H plotting. The specimen broadening in XRD lines broaden due to small grain size and strain. The Williamson-Hall technique is adopted where microstrain ' ϵ ' and grain size is related as:

$$\beta \cos\theta = \epsilon \sin\theta + \lambda/D$$

β where is the full width at half maxima of the peak (in radians), θ is the diffraction angle, λ the wavelength of X-ray. The slope of the graph between $\beta \cos\theta$ and $\sin\theta$ gives the microstrain and the intercept on Y-axis gives λ/D . The particle sizes and microstrains of the NiO/ANO at RT and different calcination temperatures calculated from the W-H plots are given in the Table. 1. Figure 3: The W_Hall plot to determine grain size and strain of NiO nanoparticles prepared at RT. Figure 4: The W_H plot to determine grain size and strain of NiO nanoparticles prepared at 473K. Figure 5: The W_Hall plot to determine grain size and strain of NiO nanoparticles prepared at 673K.

2.3 UV-vis characterization:

UV-vis absorption spectroscopy is one of the most important techniques to investigate the energy structures and optical properties of nanocrystalline semiconductors and has widely been studied [22]. The strong absorption in the UV region can be assigned to the band gap absorption of nanostructured NiO. The plots of $(ah\nu)^2$ vs $h\nu$ for NiO and ANO nanoparticles corresponding to different annealing temperatures calculated from absorption data are shown in Fig 9,10

and 11. The linear nature of the plots indicate the involvement of direct transition and thus the prepared NiO nanoparticles fall on the group of direct band gap metal oxide [23]. UV-vis spectra are taken from the NiO nanoparticles and ANO nanoparticles (2.5%, 4.5% and 6.5%) at RT, 473K and 673K. The direct band gaps of NiO and ANO nanoparticles calculated from the UV-vis-absorption at RT, 473K and 673K are given in Table 1. UV-vis spectra are taken from the ANO nanoparticles (2.5%, 4.5% and 6.5%) at RT, 473K and 673K. The direct band gaps calculated from the UV-vis-absorption are given in Table 1.

CONCLUSIONS

1. ANO and CNO nanoparticles are prepared successfully and matched with the standard data.
2. With change in doping concentrations and temperatures, size of the nanoparticles increases.
3. With decrease in size, band gap and microstrain increases.

Acknowledgement

We express our sincere gratitude to DST (SERB) for financial support; SAIF, Dept. of Instrumentation & USIC, Gauhati University for providing XRD facilities and Dept. of Chemistry, Gauhati University for providing UV-vis spectroscopy facilities.

REFERENCES

1. Janssen GJM & Nieuwpoort WC, *Phys. Rev. B* 38, 3449.
2. Reddy B, Ramasubba, Harish,G.S., Reddy,Ch. Seshendra,Reddy,P.Shreedraha.2014; 4(6)
3. Alkahlout A, Dahoudi NAI, Grobelsek I, Jilavi M, De Oliviera PW. Vol. 2014, Article ID 235638.

4. Wang X, Ye LJ, Hu P, Yuan FL, *Cryst. Growth Des.* 2007;7:2415.
5. Huang CN, Chen SY, Shen P. *J. Phys. Chem.* 2007;C 111:3322.
6. Zhao B, Ke XK, Bao JH. *J. Phys. Chem.* 2009;C 113:14440.
7. Wu MS, Hsieh HH. *Electrochim. Acta* 2008;53: 3427.
8. Xu CK, Hong KQ, Liu S, Wang GH, Zhao XN. *J. Cryst. Growth* 2003;255: 308.
9. Xing W, Li F, Yan ZF, Cheng HM, Lu GQ. *Int. J. Nanosci.* 2004;3: 321.
10. Liu XM, Zhang XG, Fu SY. *Mater. Res. Bull.* 2006;41: 620.
11. Bai L, Yuan F, Hu P, Yan S, Wang X, Li S. *Mater. Lett.* 2007; 61: 1698.
12. Ni XM, Zhang YF, Tian DY, Zheng HG, Wang XW. *J. Cryst. Growth* 2007; 306: 418.
13. Al-Hajry A, Umar A, Vaseem M, Al-Assiri MS. *Superlattice Microstruct.* 2008;44:216.
14. Zhu LP, Liao GH, Yang Y, Zhao HM, Wang JG. *Nanoscale Res. Lett.* 2009;4: 550.
15. Wang HZ and Qian YT. *Cryst. Res. Technol.* 2010;45:545.
16. Yang H, Tao Q, Zhang X, Tang A, Ouyang J. *J. Alloys Compd.* 2008; 98: 459.
17. Varkey AJ and Fort AF. *Thin Solid Films.* 1993;47:235.
18. Kalam A, Ayed S, Al-Shihri M, Shakir AA, El-Bindary El Sayed S, Yousef Gaohui Du. *Synthesis and Reactivity in Inorganic, Metal-Organic, and Nano-Metal Chemistry.* 2008;41: 1324–1330.
19. Boschloo G and Hagfeldt A. *J. Phys. Chem. B.* 2001;105: 3039.
20. Wang X, Song J, Gao L, Jin J, Zheng H, Zhang Z. *Nanotechnology*, 2005;39:16.
21. Chakrabarty S and Chatterjee K. *J. Phys Sci.*, 2009; 13: 245.
22. Klug HP and Alexander LE. *X-ray Diffraction Procedures for Polycrystalline and Amorphous Material.* Second ed. New York: *John Wiley & Sons*; 1974.
23. Miah MAH, Begum J, Uddin MJ, Momin MA, Bhuiyan MRA. *J. Appl. Sci. Tech.*, 2010; 7(2): 27-32.

© 2017 | Published by IRJSE

Clinical applications of ZnO nanoparticles

Khater MS¹, Kulkarni GR², Talathi P³ and Karnik R⁴

1. Assistant Professor, Department of Biotechnology, Abasaheb Garware College, Karve Road, Pune 411004, MS, India. 2. Department of Physics, Savitribai Phule Pune University, Ganeshkhind, Pune 411007, India. 3 and 4. Department of Biotechnology, Abasaheb Garware College, Karve Road, Pune 411004, India
E-mail : d_maya19@yahoo.com

Manuscript Details

Available online on <http://www.irjse.in>
ISSN: 2322-0015

Editor: Dr. Arvind Chavhan

Cite this article as:

Khater MS, Kulkarni GR, Talathi P and Karnik R. Clinical applications of ZnO nanoparticles, *Int. Res. Journal of Science & Engineering*, December 2017; Special Issue A1 : 21-28.

© The Author(s). 2017 Open Access

This article is distributed under the terms of the Creative Commons Attribution 4.0 International License

(<http://creativecommons.org/licenses/by/4.0/>), which permits unrestricted use, distribution, and reproduction in any medium, provided you give appropriate credit to the original author(s) and the source, provide a link to the Creative Commons license, and indicate if changes were made.

ABSTRACT

Zinc oxide (ZnO) NPs have wide industrial and commercial applications. Due to their physical properties ZnO NP are also used in cosmetics for protection from UV radiation. However, ZnO NP are non toxic to upper epidermal layer (stratum corneum) but they are potential toxic to cancerous cells. The aim of this study is to assess the cytotoxicity of ZnO nanopowder (particle size 50 nm) to human skin fibroblasts and human embryonic kidney cells. ZnO NP show higher toxicity after 24 hrs exposure. Results of this study indicated that human skin fibroblasts and human embryonic kidney cells both are sensitive to ZnO nanoparticles through the viability assay. 2. PVC (Poly Vinyl Chloride) is a versatile plastic that has been used for medical applications including containers for blood, urine, IV solutions, catheters, tubing for dialysis, surgical gloves etc. This may lead to nosocomial infections. The aim of this study is to assess the ZnO coated PVC sheets for bacterial adhesion. ZnO films were coated on medical-grade PVC surface by the improved organic-inorganic interfacial adhesion method and its antibacterial property at different concentrations against *E.coli* and *S.aureus* were studied. The antibacterial properties of the THF-ZnO/PVC film are better than that of the ZnO/PVC and uncoated PVC. A ZnO molecule with smaller size, large surface area, higher polarity, exhibits higher antimicrobial activity. Under UV irradiation, the THF-ZnO/PVC film shows the best antibacterial properties with 80-90% bactericidal effect.

Keywords: ZnO, medical grade poly vinyl chloride (PVC), bactericidal, anti-cancer.

INTRODUCTION

Zinc oxide (ZnO) nanoparticles have their own importance due to their vast area of applications, for example, gas sensor, biosensor, cosmetics, storage, optical devices, window materials for displays, solar cells, and drug-delivery. Zinc oxide (ZnO) NPs have very wide industrial and commercial applications, particularly in pigments. Due to their physical properties ZnO NP are also used in cosmetics for protection from UV radiation. It has many clinical applications and two of them are studied in this work.

1. ZnO NP are non toxic to upper epidermal layer (stratum corneum) but they are potential toxic to cancerous cells. A limited number of in vitro studies have also been performed to assess the toxicities of the nanoparticles using different cellular systems and test methods [4,10,23,29]. However, published toxicity data are still considered inadequate to earn a full understanding of the potential toxicity of these nanoparticles. Further studies are needed to clarify the risk of these materials as well as their application for human use. The aim of this study is to assess the cytotoxicity of ZnO nanopowder (particle size 50 nm) to human skin fibroblasts and human embryonic kidney cells.

2. The increasing use of polymer materials such as polyethylene, polyurethanes, and poly vinyl chloride (PVC) in the hospital care has led to a concomitant increase in the incidence of biomaterial-related infections (BRI). Adhesion of bacteria to biomaterials led to the formation of biofilm on the surface, which plays a crucial role in the pathogenesis of the BRI [14]. The growth and production of biofilm protect the bacteria from the host defense mechanisms and external agents as the drug treatments [2,11], which makes the cure of the bacterial infections quite difficult and requires either higher doses or more potent antibiotics.

In order to efficiently prevent or reduce biofilm formation, many efforts have been done to enhance the anti-bacterial properties of biomaterials. Some efforts such as modifying the physicochemical properties of biomaterial surface, coating with silver, azidation treatment, antibiotic impregnation into the

polymer matrix, have been examined in recent years [7,24].

To increase the antibacterial efficiency of biomaterials, many studies have been done to coat ZnO NPs on many biomaterial's surface such as glass, ceramic, stainless steel, polymer, and so on. In this work, the ZnO PVC sheets were prepared by deep coating method and THF was used to pretreat the surface of PVC sheet similar to organic-in-organic interfacial adhesion method [16]. The bacterial adhesion and antibacterial activity of ZnO PVC sheets was analysed by total viable count of bacterial cells on the surface of PVC sheets as compared to plain PVC sheets under similar conditions.

METHODOLOGY

1 Cytotoxicity of ZnO against human skin fibroblasts and human embryonic kidney cells

1.1 Nano particles

Zinc oxide nanopowder, <50nm particle size was purchased from (Sigma-Aldrich, USA) CAS: 1314-13-2 MW: 81.39 g/mol, Titanium oxide nanopowder, <25nm particle size was obtained from (sigma-Aldrich, Bangalore) CAS:1317-70-0 MW: 79.87g/mol

1.2 Preparation of nanoparticles

ZnO nanoparticle were suspended in the culture medium at the concentration of 5000 ppm and dispersed by ultrasonic vibration for 15 min. In order to ensure the uniform suspension, they were stirred on vortex agitation (1 min) before every use.

1.3 Human skin fibroblasts and culture conditions

A431, and HEK 293 were obtained from NCCS (National Centre for Cell Science, Pune) in 25cm² flasks with good confluency were grown in MEM powder (Gibco life technologies), contents - Earle's salt, L-glutamine, non-essential amino acids (without sodium bicarbonate) Formula No-04-5045EF [lot no-1383815] Adult bovine serum 500ml (Bioscience, New Zealand). All cultures were maintained in a phenol red free culture medium DMEM/F12 (Dulbecco's modified essential medium/Ham's 12 nutrient mixture, Gibco), supplemented with 5% (v/v) fetal calf serum (JS Bioscience, Australia), and 1% (v/v)

antibiotic (2 mL-glutamine, 100 mg/mL Penicillin and 0.1 mg/mL Streptomycin; Gibco). Cultured cells were kept at 37°C in a humidified 5% CO₂ incubator

1.4 Viability assay

Once the cells reached confluence, the culture medium was removed from the flask and the cells were rinsed three times with sterile PBS. The confluent cell layers were enzymatically removed, using Trypsin/ EDTA (Gibco, USA), and resuspended in culture medium. Cell viability was assessed by vital staining with trypan blue (0.4% (w/v); Sigma, USA), and cell number was determined using a light microscope

2. ZnO coated medical grade PVC sheets for bacterial adhesion

2.1. Maintenance of bacterial culture

Pure culture of *E.coli* and *S.aureus* was maintained on sterile nutrient agar plate (Peptone, NaCl, agar, distilled water) and sterile nutrient agar slant. Streak plate technique is used for subculture and well grown culture is preserved in refrigerator at 4°C. Cultures are sealed with parafilm before storing. Bacteria grown on suitable agar slants and agar plates are transferred to fresh ones before they exhaust all nutrients or dry out. Subculture is performed once in a week for maintaining viability of bacterial culture.

2.2 Preparation of Zinc Oxide nanoparticle stock

Zinc Oxide nanoparticles from Sigma-Aldrichs (<50nm particle size) was dissolved in methanol. Stock prepared was 1mg/ml of methanol. This solution was dispersed for 30 minute in sonicator. From this stock 5µg/ml, 10µg/ml, 50µg/ml, and 100µg/ml concentrations of ZnO nanoparticles in methanol was prepared. These nanoparticles were also dispersed for 30 minute at RT in sonicator for its further use.

2.3 Coating of ZnO NPs on medical grade PVC Surface

The ZnO film was prepared by dip-coating method with ZnO suspension as precursor. The PVC sheets (1.5 × 0.7 cm) were pre-immersed in THF-PVC solution for 10s. Immediately, the PVC samples were dipped into different concentration of ZnO colloidal solution and were centrifuge at speed of 1200 rpm for 30 min. The ZnO gel film on PVC were dried in an oven at 60°C for 30 min. After seven such coating steps, the transparent ZnO film on PVC were

obtained. The PVC sheets without pretreatment were coated with ZnO under similar operating conditions for comparison. For ease of presentation the ZnO film with pretreatment were labelled as THF-ZnO/PVC and that without pretreatment were labelled as ZnO/PVC and it was characterized by SEM.

2.4 Bacterial Adhesion

The neat PVC, ZnO/PVC and THF-ZnO/PVC sheets were immersed in the aqueous solution of *E. coli* and kept at 37°C for 24 h. The sheets were taken out and rinsed gently with sterile phosphate buffered saline (PBS) to remove the non-adherent bacteria. Then, the bacteria adhered on the sheets were washed off into 5 ml of sterile PBS in an ultrasonic cleaner for 5 min. The number of the washed off bacteria was then determined by colony counts (CFU). The adherent number was expressed by the ratio of the total adherent bacterial to the area of the measured sample and represented as bacterial adhesion TVC/cm². The same process was carried out with *S. aureus*. PVC sheets were analyzed by SEM.

2.5 Antibacterial Property ZnO/PVC sheets

ZnO/PVC sheets (1.5 × 0.7cm) with different concentrations were placed on sterile plates, and then 0.5 ml broth inoculated with 10⁴ cfu/ml of *E. coli* was added onto the surfaces. The samples were irradiated with 8 W UV lamp (with wavelength at 365 nm) for 150 min. After irradiation, the sheets were rinsed with sterile phosphate buffered saline (PBS) and the number of viable bacteria was determined by colony counts (CFU). The plain PVC sheet sample was also tested for comparison. The antibacterial property of PVC, ZnO/ PVC and THF-ZnO/PVC was represented by the bacteriocidal percentage, a ratio of the dead number of the bacterial to the initial number of the bacterial cells. The same process was carried out with *S. aureus*

RESULTS AND DISCUSSION

3.1 Cytotoxicity of ZnO against human skin fibroblasts and human embryonic kidney cells

ZnO-NPs (50 nm sized) induced cytotoxicity in cultured human skin fibroblast (A431) and human embryonic kidney cells (HEK293) by elevating

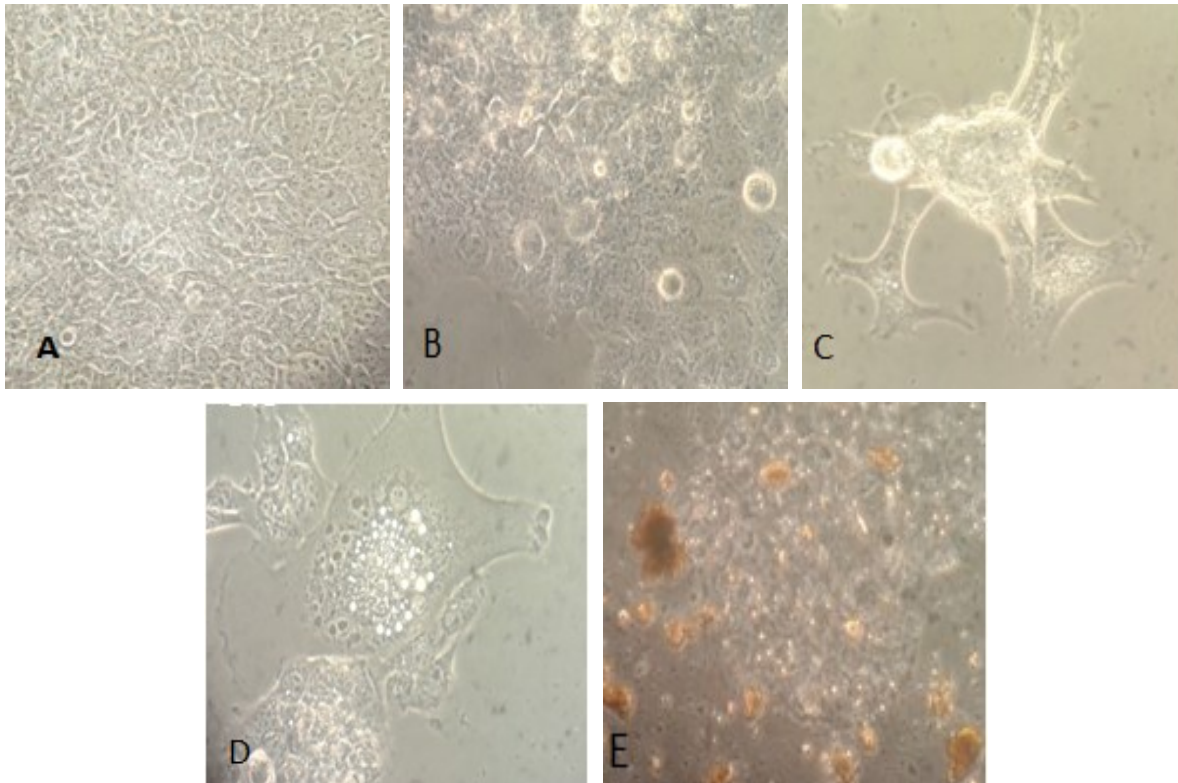


Fig 1 A normal human skin fibroblast A431 cells, B cells treated with ZnO NP 5 µg/ml for 24 hrs. C cells treated with ZnO NP 10 µg/ml for 24 hrs. D cells treated with ZnO NP 50 µg/ml for 24 hrs. E cells treated with ZnO NP 100 µg/ml for 24 hrs.

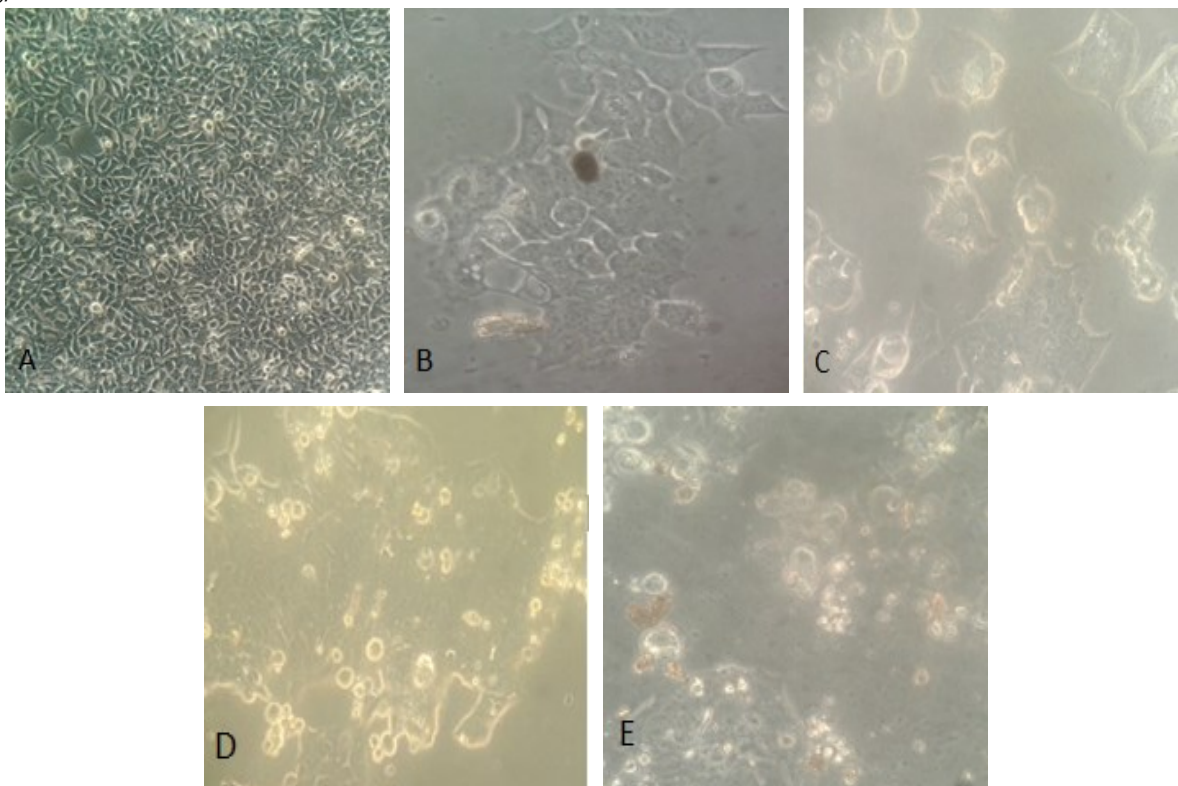
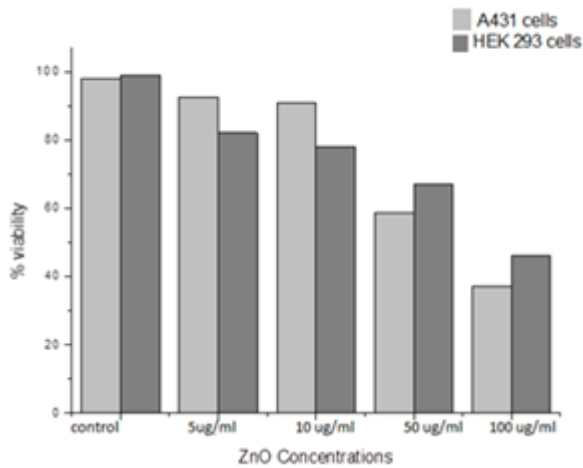


Fig 2 A normal human embryonic kidney HEK 293 cells cells, B cells treated with ZnO NP 5 µg/ml for 24 hrs. C cells treated with ZnO NP 10 µg/ml for 24 hrs. D cells treated with ZnO NP 50 µg/ml for 24 hrs. E cells treated with ZnO NP 100 µg/ml for 24 hrs.



Graph1: % Viability of human skin fibroblast (A431) and human embryonic kidney cells (HEK293) treated with ZnO NPs of different concentrations for 24 hrs..

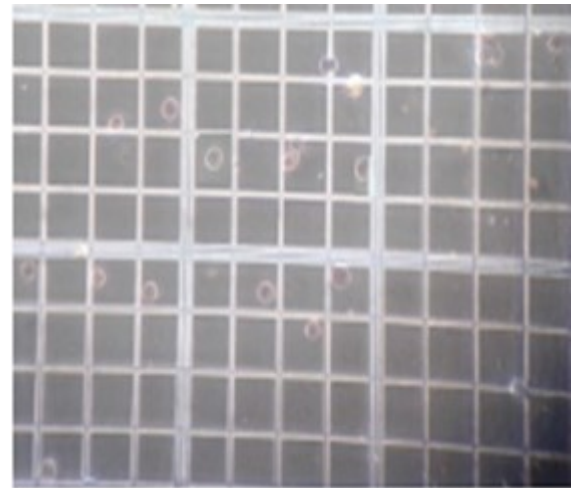


Fig 3 Viability was checked using trypan blue stain and cells were counted using haemocytometer. Dead cells appeared blue color whereas viable cells were unstained.

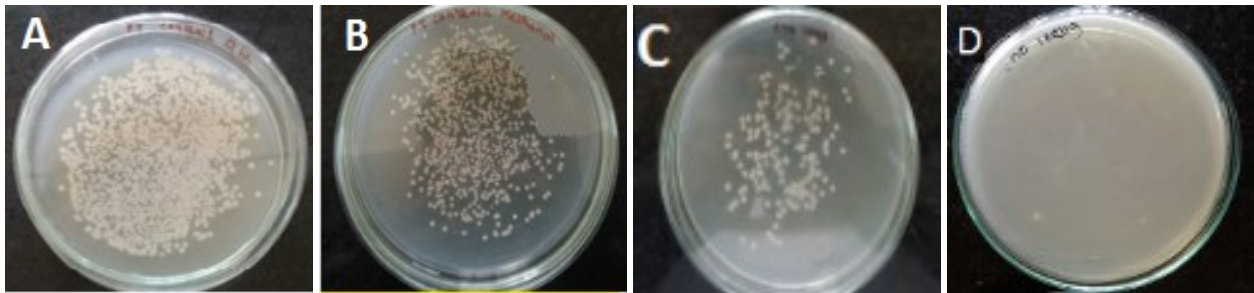


Fig:4: Bacterial (*S. aureus*) adhesion on medical grade PVC :A-Initial number, B-Plain PVC, C- ZnO(100µg/ml) PVC, D- ZnO(100µg/ml)+THF

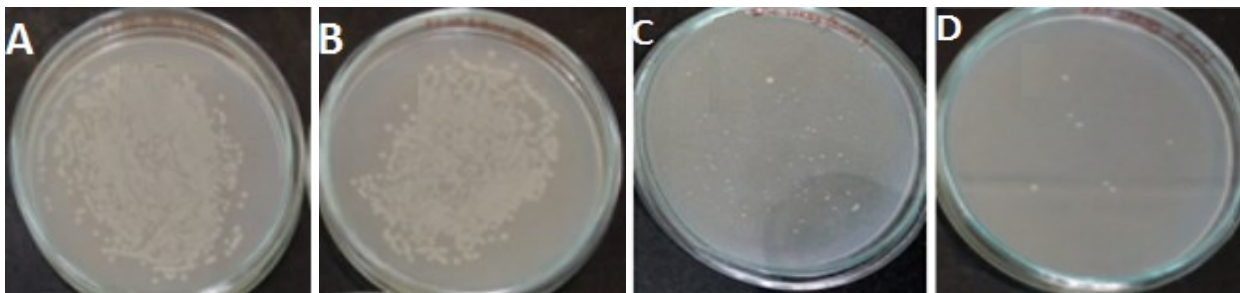


Fig:5: Bacterial (*E. coli*) adhesion on medical grade PVC :A-Initial number, B-Plain PVC, C- ZnO(100µg/ml) PVC, D- ZnO(100µg/ml)+THF

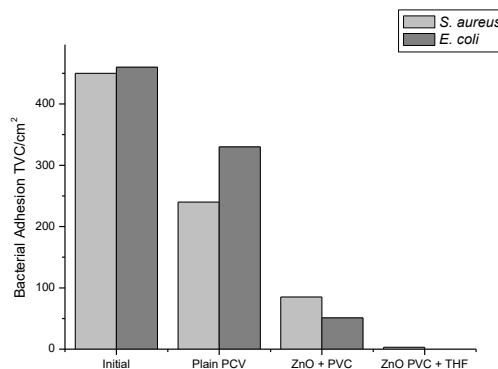
inflammatory response from morphological observations in a concentration-dependant fashion (Fig. 1 and 2). Cell viability was also confirmed by viability test with trypan blue dye staining. Death of the cells was confirmed by entry of dye in to cytoplasm of the cells, which stains cell blue (Figure-3) ZnO NPs also induced detachment of cells from the surface illustrating apoptotic type of cell death. Also it can be seen from our study that A 431 cells had high toxicity

response as compared to HEK 293 cells. The cytotoxicity of ZnO is concentration dependent (Graph 1). Similar results were observed in a study where it is shown that oxidative stress-induced apoptosis may be considered as one of the pathways of toxicity by ZnO-NPs [8]. In vitro toxicity assessment has become widely used for recent toxicity studies. Such assays provide rapid, cost effective and reliable results [13].

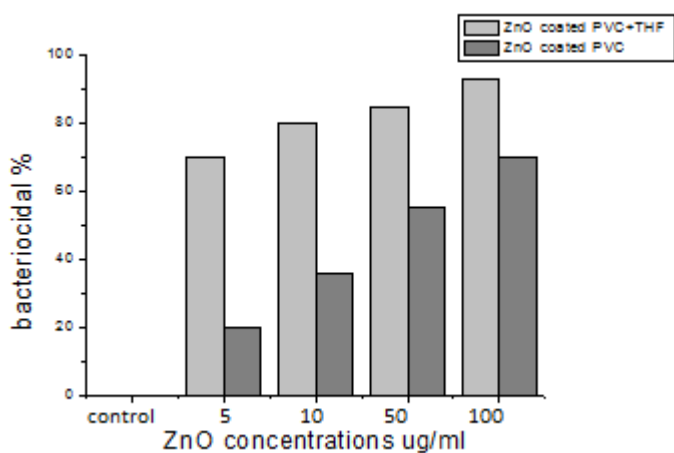
3.2 ZnO coated medical grade PVC sheets for bacterial adhesion

3.2.1 Bacterial adhesion

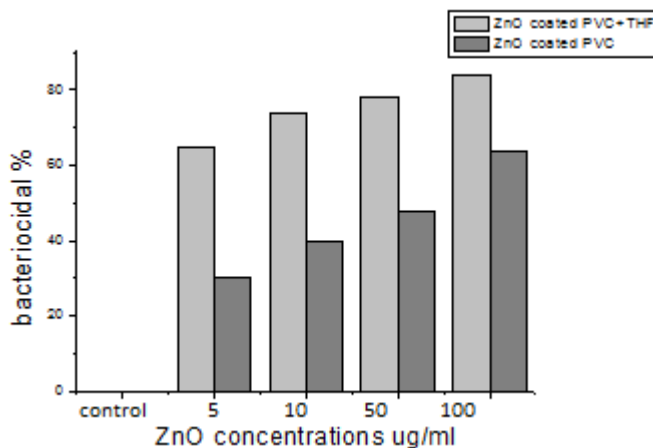
This work reveals that the antibacterial property of medical grade PVC sheets can be enhanced by ZnO coating where THF helps in good adhesion of NPs on the surface of PVC sheets. In bacterial adhesion studies, total viable count (TVC) of bacteria reduced substantially on the surface of ZnO + PVC and ZnO + PVC + THF sheets compared to plain PVC (Graph 2, Fig. 4 and 5). This observation is also supported by SEM observation where lysed cells were observed on the surface of ZnO + PVC and ZnO + PVC + THF sheets (Fig. -6).



Graph2: Effect of nanoparticles coated medical grade PVC sheets on bacterial adhesion



Graph3: Bacteriocidal % of of medical grade PVC Coated with ZnO NPs of different concentrations with and without THF against *E.coli*



Graph4: Bacteriocidal % of of medical grade PVC Coated with ZnO NPs of different concentrations with and without THF against *S.aureus*.

3.2.2 Antibacterial property of ZnO PVC sheets

The photocatalytic property of metal oxide that is responsible for the excellent sterilization properties [18]. Considering this ZnO coated medical grade PVC sheets immersed in bacterial suspension with or without THF were irradiated by UV light for 150 minutes. Then the number of viable bacteria was determined by TVC and plain PVC sheet was used for comparison. The antibacterial property of plain PVC, ZnO + PVC and ZnO + PVC + THF was estimated by bacteriocidal percentage as a ration of dead number of cells to the initial number of bacterial cells for different concentration of ZnO. The bacteriocidal percentage of of different concentration of ZnO NPs coated on PVC sheets with THF is in the

range 75% to 90% for and 20% to 65% without THF against *E. coli* compared to plain PVC. Similar results were obtained against *S. aureus* as 60% to 80% for with THF and 20% to 58% for without THF (Graph-3 and 4). Similar antibacterial effect is observed by Lin H. et. al. in 2013 [16] and they stated that the photocatalytic property and sterilization activity of THF-ZnO/PVC are much better than that of ZnO/PVC. The main reason is may be that the amount of ZnO on THF-ZnO/PVC is larger than that on ZnO/PVC. Under UV irradiation, the amount of electron and hole produced on THF-ZnO/PVC were higher than that on ZnO/PVC that resulted in higher concentration of radicals ($O_2\cdot$ and $HO\cdot$) on THF-ZnO/ PVC.

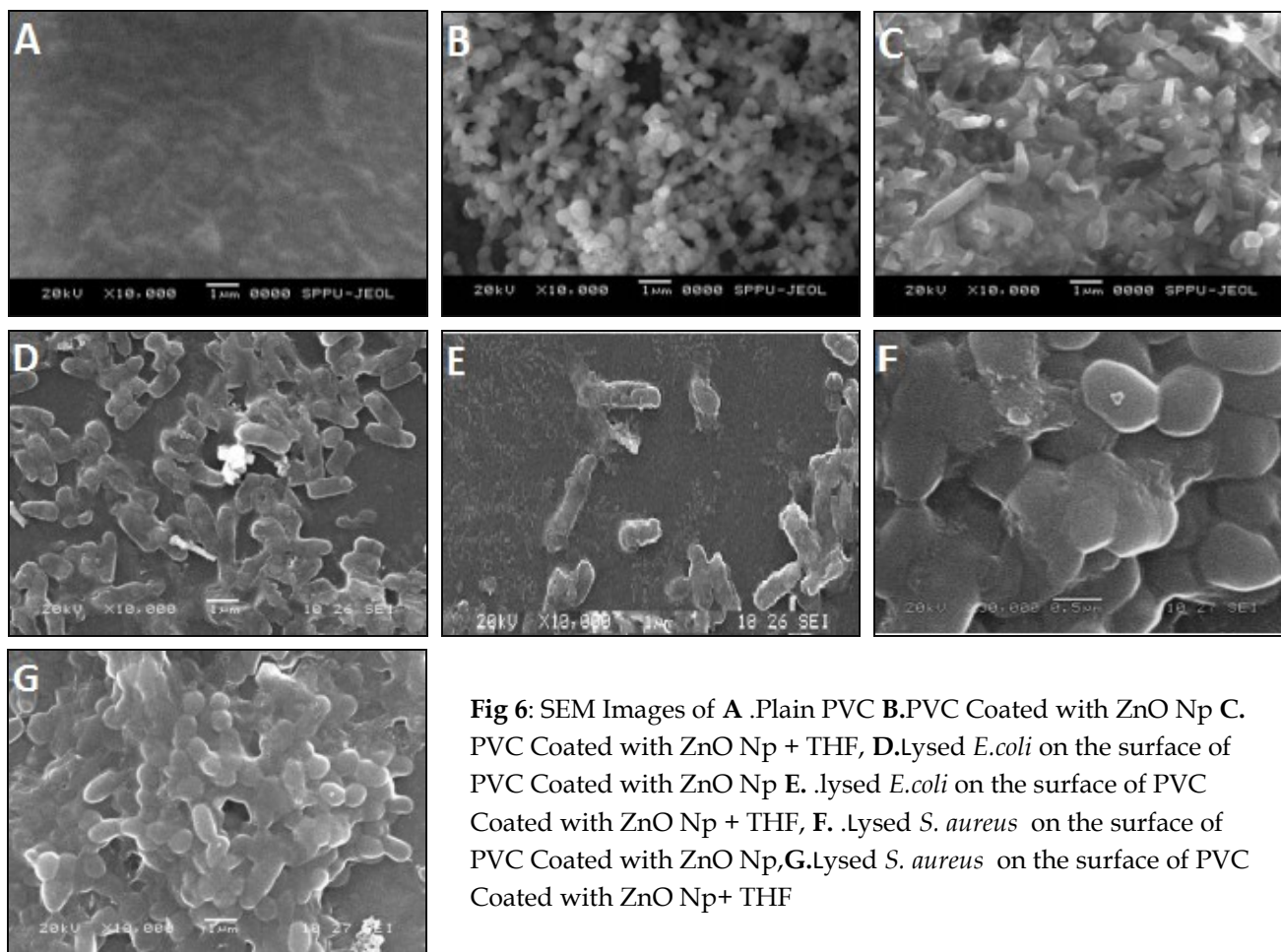


Fig 6: SEM Images of **A** .Plain PVC **B**.PVC Coated with ZnO Np **C**. PVC Coated with ZnO Np + THF, **D**.Lysed *E.coli* on the surface of PVC Coated with ZnO Np **E**. .lysed *E.coli* on the surface of PVC Coated with ZnO Np + THF, **F**. .lysed *S. aureus* on the surface of PVC Coated with ZnO Np,**G**.lysed *S. aureus* on the surface of PVC Coated with ZnO Np+ THF

CONCLUSION

Hence, we can conclude that ZnO-NPs are toxic to both skin fibroblast (A431) and human embryonic kidney cells (HEK293) hence care has to be taken while processing and formulating the nanoparticles till its final finished product and it. The antibacterial properties of medical-grade PVC material can be enhanced by coating by ZnO and THF helps in adhesion of ZnO NPs to PVC Sheets. The result provides a convenient method that can enhance the adhesive strength and amount of inorganic oxide film coated on organic materials. It is also easy to operate and can be applied on various biomaterials.

REFERENCES

1. An YH and Friedman JR. Concise Review of Mechanisms of Bacterial Adhesion to Biomaterial Surfaces. *Journal of Biomedical Materials Research* 1998; Vol. 43, No. 3:338-348.
2. An YH and Friedman JR. Prevention of Sepsis in Total Joint Arthroplasty. *Journal of Hospital Infection* 1996; Vol. 33, No. 2:93-108.
3. Bekbolet M. Photocatalytic Bactericidal Activity of TiO₂ in Aqueous Suspensions of *E. coli*, *Water Science and Technology*, 1997; Vol. 35, No. 11-12:95-100.
4. Cai R, Hashimoto K, Itoh K, Kubota Y and A, F Photokilling of malignant cells with ultrafine TiO₂ powder, *Bulletin of the Chemical Society of Japan*. 1991;64:1268-1273.
5. Damodara RA, Youa SJ and Chou HH. Study the Self Cleaning, Antibacterial and Photocatalytic Properties of TiO₂ Entrapped PVDF Membranes. *Journal of Hazardous Materials*. 2009; 172, No. 2-3,:1321-1328
6. Dechsakulthorn, Fin, In vitro cytotoxicity assessment of selected nanoparticles using human skin fibroblasts. 2007; AATEX 14. Special Issue 2007: 397-400.
7. Desai NP, Hossainy SFA and Hubbei JA Surface-Immobilized Polyethylene Oxide for Bacterial Repellence. *Biomaterials* 1992;Vol. 13, No. 7:417- 420 8
8. Dubey Akhilesh. Oxidative Stress and Nano-

- Toxicity Induced by TiO₂ and ZnO on WAG Cell Line. *PloS one* 2015;10.5: 127493)
9. Dufour EK, Kumaravel T, Nohynek GJ, Kirkland D and Toutain H. Clastogenicity, photo-clastogenicity or pseudo-photo-clastogenicity: Genotoxic effects of zinc oxide in the dark, in pre-irradiated or simultaneously irradiated Chinese hamster ovary cells, *Mutation Research*. 2006;Vol 607:215-224.
 10. Dunford R, Salinaro A, Cai L, Serpone N, Horikoshi, S., Hidaka, H., and Knowland, J., Chemical oxidation and DNA damage catalysed by inorganic sunscreen ingredients, *FEBS Letters*. 1997;418:87-90)
 11. Gristina AG, Hobgood CD and Webb LX, Adhesive Colonization of Biomaterials and Antibiotic Resistance. *Biomaterials* 1987; 8,6:423-426.
 12. Guan, Rongfa. Cytotoxicity, oxidative stress, and genotoxicity in human hepatocyte and embryonic kidney cells exposed to ZnO nanoparticles. *Nanoscale research letters* 2012 ;1:602
 13. Hayes A and Markovic B. Alternative to animal testing for determining the safety of cosmetics, *Cosmetics, Aerosols & Toiletries in Australia*. 1999; Vol.12:24-30.
 14. Jones N, Ray B, Ranjit KT and Manna AC, Antibacterial Activity of ZnO Nanoparticle Suspensions on a Broad Spectrum of Microorganisms, *FEMS Microbiology Letters* 2008;Vol. 279, No. 1: 71-76.
 15. Lakshmi S, Pradeep SS and Kumar JA, Bacterial Adhesion onto Azidated Poly (Vinyl Chloride) Surfaces, *Journal of Biomedical Materials Research* 2002;Vol. 61, No. 1:26-32.
 16. Lin H, Din L, Deng W, Wang X, Long J, Lin Q, Coating of Medical-Grade PVC Material with ZnO for Antibacterial Application *Advances in Chemical Engineering and Science* 2013; 3: 236-241.
 17. Lin, Weisheng. Toxicity of nano and microsized ZnO particles in human lung epithelial cells. *Journal of Nanoparticle Research*. 2009;11.1 : 25-39.
 18. Lin HX, Xu ZT and Wang XX. Photocatalytic and Antibacterial Properties of Medical-Grade PVC Material Coated With TiO₂ Film. *Journal of Biomedical Materials Research* 2008;Vol. 87, No. 2:425-431.
 19. Najim, Nigar, Effects of the absorption behaviour of ZnO nanoparticles on cytotoxicity measurements. *Journal of Nanomaterials*. 2014: 19.
 20. Park KD, Kim YS and Hun DK, Bacterial Adhesion on PEG Modified Polyurethane Surfaces, *Biomaterials* 1998;Vol. 19, No. 7-9:851-859.
 21. Saliyani, Mahsa, Razihi J., and Goharshadi E. K., Mechanism of oxidative stress involved in the toxicity of ZnO nanoparticles against eukaryotic cells. *Nanomedicine Journal* 2016; 3.1: 1-14.
 22. Saptarshi, Shruti R., Albert D., and Andreas LL. Biological reactivity of zinc oxide nanoparticles with mammalian test systems: an overview. *Nanomedicine* 2015;10.13: 2075-2092.
 23. Sayes CM, Wahi R, Kurian PA, Liu Y, West J. L, Ausman KD, Warheit DB and Colvin V L., Correlating Nanoscale Titania Structure with Toxicity: A Cytotoxicity and Inflammatory Response Study with Human Dermal Fibroblasts and Human Lung Epithelial Cells, *Toxicological Sciences* 2012;92, 174-185. America, Vol. 26, No. 1:173-186.
 24. Triandafillu K., Balazs D. J. and Aronsson B. D., Adhesion of Pseudo-Monas Aeruginosa Strains to Untreated and Oxygen-Plasma Treated Poly (Vinyl Chloride) (PVC) from Endotracheal Intubation Devices. *Biomaterials* 2003;Vol. 24, No. 8:1507-1518.
 25. Vergidis P and Patel R. Novel Approaches to the Diagnosis, Prevention, and Treatment of Medical Device-Associated Infection, *Infectious Disease Clinics of North America* 2012;26 (1): 173-186.
 26. Wang B, Feng WY, Wang TC, Jia G, Wang M, Shi JW, Zhang F, Zhao YL and Chai ZF. Acute toxicity of nano- and micro-scale zinc powder in healthy adult mice, *Toxicology Letters*. 2006; Vol.161:115-123.
 27. Wang J, et al. Acute toxicity and biodistribution of different sized titanium dioxide particles in mice after oral administration, *Toxicology Letters*. 2007; Vol. 168:176-185.
 28. Warheit, DB. Nanoparticles: Health impacts?, *Materials Today*. 2007; Vol. 7:32-35.
 29. Warheit, DB, Webb TR, Reed KL, Frerichs S and Sayes CM. Pulmonary toxicity study in rats with three forms of ultrafine-TiO₂ particles: Differential responses related to surface properties, *Toxicology*. 2007; Vol. 230:90-104.

Green Synthesis and Characterization of Nanocrystalline Graphene Oxide

Gijare Medha¹, Chaudhari Sharmila² and Garje Anil^{3*}

¹AISSMS's Polytechnic, Pune 411001, Maharashtra, India, ²Annasaheb Magar College, Hadapsar, Pune, Maharashtra, India, ³S.P. College, Pune 411030, Maharashtra, India,

*Corresponding author email: adgarje@gmail.com

Manuscript Details

Available online on <http://www.irjse.in>

ISSN: 2322-0015

Editor: Dr. Arvind Chavhan

Cite this article as:

Gijare Medha, Chaudhari Sharmila, Garje Anil. Green Synthesis and Characterization of Nanocrystalline Graphene Oxide, *Int. Res. Journal of Science & Engineering*, December 2017; Special Issue A1 : 29-34.

© The Author(s). 2017 Open Access

This article is distributed under the terms of the Creative Commons Attribution 4.0 International License

(<http://creativecommons.org/licenses/by/4.0/>), which permits unrestricted use, distribution, and reproduction in any medium, provided you give appropriate credit to the original author(s) and the source, provide a link to the Creative Commons license, and indicate if changes were made.

ABSTRACT

Green reduction of Graphene oxide (GO) using various natural materials including plant extracts has drawn significant attention among the scientist community. These methods are sustainable, cost effective and more ecofriendly than other standard methods of reduction of nanoparticles. In the present work, Graphene oxide (GO) was prepared using predefined Modified Hummer's method. Reduced Graphene oxide (RGO) is obtained using aqueous leaf extract of *Lantana camara* (Tantani) and aqueous peel extract of *Citrus limeta* (Sweet lime) using cold maceration, sonication and refluxing methods. Structural and Optical characteri-zation of graphene and reduced graphene oxide was carried out using XRD, UV-visible, FTIR, SEM and EDX. UV-visible spectroscopy was used to monitor the formation of reduced Graphene oxide. The crystalline size of Graphene nanoparticles was confirmed by XRD analysis. FTIR analysis showed the green reduction of Graphene oxide using phytochemicals. The morphology and elemental composition of synthesized Graphene was studied by SEM and EDX analysis. The production of graphene using phytoextracts as reducing agent emphasizes on facile method and future green technology for various applications such as water purifiers, super capacitors, biosensors, solar cells etc.

Keywords: green synthesis, graphene oxide, reduced graphene oxide, phytoextracts

INTRODUCTION

Nanoscience and nanotechnology mainly deal with the synthesis, characterization, study and use of non-material. Graphene is the world's thinnest, strongest, and stiffest material, as well as being an excellent conductor of heat and electricity. It is the basic building block of other important allotropes. Graphene oxide (GO) is of great interest due to its low cost, easy access, and extensive ability to convert to graphene. Graphene, a two dimensional mono atomic thick building block of a carbon allotrope has received world-wide attention due to its extraordinary thermal, optical, mechanical and transport properties. Recent progress has shown that the graphene-based materials can have a profound impact on electronic and optoelectronic devices, chemical sensors, biosensors, nanocomposites, and energy storage [1-3]. Researchers are taking into consideration two primary methods for the fabrication of graphene: a top-down (TD) and a bottom-up (BU) approach. In TD approach, there are reported methods on the production of graphene such as micromechanical cleavage, graphitization of SiC and solution exfoliation of graphite in organic solvents. However, these methods turn out a poor yield of graphene layers. Chemical reduction of graphite oxide colloidal suspensions has been considered as an effective route to synthesize graphene sheets due to its simplicity, reliability, ability for large-scale production and exceptionally low price. A number of reducing agents such as dimethyl hydrazine, hydroquinone, aluminum powder, sodium borohydride, sulfur containing compounds, hexamethylenetetramine, poly-electrolyte, Ethylene diamine (EDA), sodium citrate, carbon monoxide and norepinephrine have been experimented on and were found to have performed under various conditions i.e., acid/alkali, thermal treatment and others treatments such as laser, plasmas, microwave, sonochemical, electrochemical, two-step reduction and so on. These different reduction methods result in graphene with different properties. Even with the distinct advantages of chemical route for reduction of GO, the reduced GO (RGO) tends to form irreversible aggregation due to strong van der Waals attractive forces among the graphene planes which creates bottle neck and confines its process ability [4-6]. However, this can be eliminated by chemical modification of graphene using small

organic molecules, biomolecules etc. One more negative aspect of the chemical reduction method is the high toxic nature of the reducing agents (hydrazine, dimethyl hydrazine, sodium borohydride, hydroquinone, etc). The existence of such toxic agents could have harmful effect, particularly in cases of biorelated applications such as catalysis and drug delivery. Even in the case of metal/hydrochloric acid reduction of GO, particles/traces of metals may stay behind as impurities. In this context, use of green nanotechnology which reports on the reduction of GO to overcome the above problem by using reducing agents such as biomolecules, microbes and phytoextracts reduction has become extremely crucial. Green nanotechnology in which biomolecules, microbes and plant extracts are used as both reducing and capping agent has been widely explored in the synthesis of metal nanoparticles This method helps in bio-reduction of GO to graphene [7-9]. It has been discovered that various phytochemicals obtained from different parts of plants like leaves, peel, root etc. which mostly contains biomolecules including proteins, vitamins, amino acids, saccharides, alkaloids, pectin's, alcoholic compounds, flavonoids and enzymes have the potential to serve as reducing and capping agents in the bio-reduction and formation of functional graphene from GO. Apart from use of less toxic chemicals, other Salient feature of green technology is that most operates at mild conditions; room temperature & atmospheric pressure making it affordable & cost effective [10-12].

METHODOLOGY

Preparation of Graphene oxide

Graphene oxide powder was prepared by modified Hummer's method [13]. Graphite powder (2 gm), 2 gm NaNO_3 , 90 ml of conc. H_2SO_4 was added in 1000 ml beaker/ volumetric flask in ice bath and stirred continuously for 4 hrs. 12 gm of KMnO_4 was added very slowly (below 15°C) for 30 minutes. The mixture was diluted with 184 ml of DI water and stirred for 2 hrs continuously at 35°C . Further it is refluxed at 98°C (10-15 min) till brown color is obtained. The mixture was treated with 40 ml H_2O_2 till solution turned to bright yellow color and stirred with double distilled water for 1 hr. The mixture was centrifuged with 10% HCl and DI water. Gel like substance was vacuum dried at 60°C for 6-7 hrs.

Preparation of Phytoextracts

Fresh leaves of *Lantana camara* (Tantani), *Citrus limeta* (Sweet lime) fruit peel were collected from local area and washed with DI water to remove the dust particles. They were blended with domestic blender and kept in DI water for cold maceration overnight. The mixture was stirred for 30 min in 50 ml of DI water at 50°C and cooled the filtrate and store at 4°C.

Synthesis of reduced graphene oxide

60 mg GO was sonicated in DI for 45 min and 10 ml leaf extract of *Lantana camara* (Tantani) was added to it. The mixture was refluxed for 6 hrs at 50 °C, until color changes to brown-black. The mixture was centrifuged with water for several times. The reduction of GO is indicated from the color change of the solution before and after reaction (from yellow, brown to dark brown), which could serve as a piece of evidence for the conversion of GO to graphene. The color change is also due to the large number of hydrophilic functional groups, such as carboxyl, hydroxyl, and epoxy groups, on GO nano sheets. After reduction, a homogeneous yellow-brown GO dispersion was converted to black, indicated the conversion of GO to L-rGO. The process was repeated for the peel extract of *Citrus limeta* (Sweet lime). After reduction, a homogeneous yellow-brown GO dispersion was converted to black, indicated the conversion of GO to C-rGO [14-17].

Characterization of synthesized GO, L-rGO & C-rGO

Optical characterization

UV-Visible absorption spectroscopy, JASCO V-670 spectrophotometer in the operating range 200-800 nm was used. The prepared samples were exposed to UV-Vis radiation and the absorption wavelength was determined from the intensity of the transmitted light.

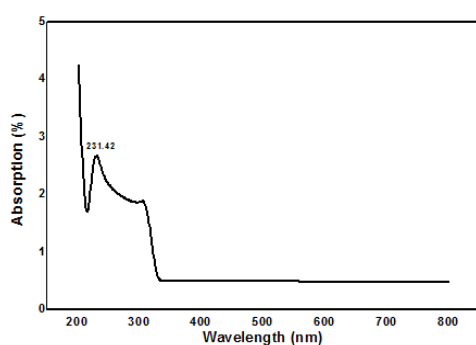


Fig. 1 a) UV-visible spectra of L-rGO

For FTIR study, we have employed FTIR-6100 spectrometer (JASCO) in the transmission (T) mode. Transmissions have taken in the wave number range 400-4000 cm^{-1} .

Structural characterization

XRD analysis for the synthesized GO, L-rGO and C-rGO powder was carried out with Bruker D8-Advanced Diffractometer using $\text{Cu K}\alpha$ radiation ($\lambda = 1.542 \text{ \AA}$) with an operating voltage of 40 kV and a current of 30 mA. The grain size measurement is carried out using Scherer formula. The surface morphology and elemental composition of rGO sample were studied with the help of Scanning Electron Microscope (SEM) (JEOL JSM 6360).

RESULTS AND DISCUSSION

Optical Characterization

UV-Visible Spectroscopy

The UV-visible spectrum for rGO is presented in Fig.1. The characteristic peak of L-rGO appears at 332 nm indicates that the formation of L-rGO. The band gap can be calculated using equation $E = hc / \lambda$, the band gap was found to be 5.36 eV. The characteristic peak of C-rGO appear at 332 nm indicates that the formation of C-rGO. The band gap was found to be 3.73 eV.

FTIR analysis

The stretching and vibrational studies of rGO were carried out using FTIR. Figure 2(a) shows the FTIR spectrum of L-rGO. The characteristic absorption band is observed at 1432.82 and 1094.4 cm^{-1} which is assigned to C-O stretching due to carboxyl / alkoxy functional groups. The band at 1734 .65 cm^{-1} shows

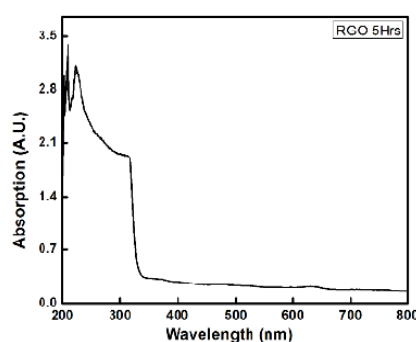


Fig 1. b) UV-visible spectra of C-rGO

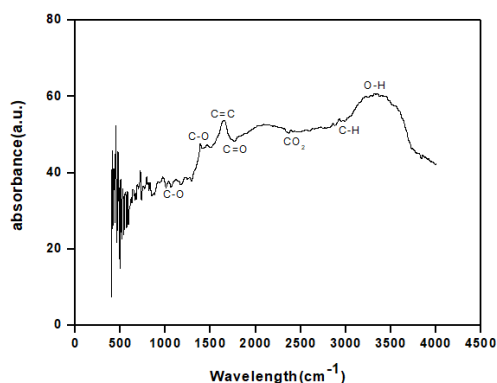


Figure 2 (a) FTIR spectrum of L-rGO

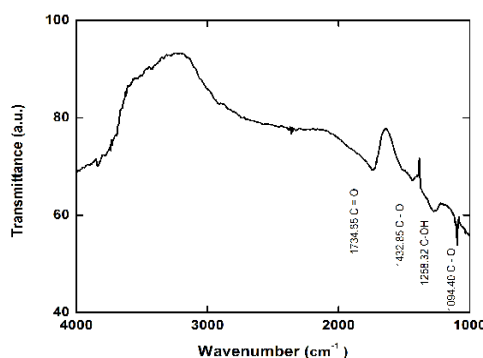


Figure 2 (b) FTIR spectrum of C-rGO

C=O (carbonyl/carboxyl functional group) stretching. The band observed at 1258.32 cm^{-1} shows C-OH stretching (epoxy functional group). Figure 4.4(b) shows the FTIR spectrum of C-rGO. The characteristic absorption band is observed at 1432.82 and 1094.4 cm^{-1} which is assigned to C-O stretching due to carboxyl / alkoxy functional groups. The band at 1734.65 cm^{-1} shows C=O (carbonyl/carboxyl functional group) stretching. The band observed at 1258.32 cm^{-1} shows C-OH stretching (epoxy functional group).

Structural characterization

XRD analysis

Pristine graphite exhibits a basal reflection (002) peak at $2\theta = 24.8^\circ$ (d-spacing = 0.358 nm). Compared with pristine graphite, the diffraction peak of synthesized GO appears at the lower angle from $2\theta = 12.3^\circ$ (d=0.718 nm) as shown in Fig. 3 (a). The intense crystalline peak of graphite occurs at 24.8° (d-spacing = 0.358 nm) was observed for the GO powder. This is the characteristic peak of hexagonal graphite with a d-spacing of 3.58 Å. Upon conversion of graphite into GO the peak position shifts to 12.3° . The interlayer spacing now increases to 7.18 Å. This increase in d-spacing is due to the intercalation of OH containing functional groups in between the graphene layers [18]. After reduction by *Lantana camara* leaf extract a broad peak appears, starting from 24 to 30° as shown in Fig. 3 (b). The characteristic XRD peaks appear at position $2\theta = 24.9^\circ$ (d= 3.58Å) and 26.6° which confirms the formation of L-rGO from GO as seen in Fig 3(b). The average crystallite size was estimated according to the Scherrer equation. The average crystallite size was found to be 2.71 nm. This broad

peak is also suggestive of a loss of the long range order in graphene and the great reduction of GO and formation of few-layer graphene. After reduction by *Citrus limeta* peel extract the 12.3° peak disappears and a broad peak appears. The characteristic XRD peaks appear at position $2\theta = 24.9^\circ$ which confirms the formation of C-rGO from

GO as seen in Fig 3 (c). The average crystallite size was estimated according to the Scherrer equation $D = \frac{0.9\lambda}{\beta \cos\theta}$. The average crystallite size of C-rGO was

found to be $\approx 17\text{nm}$.

Table showing calculation of average grain size of L-rGO

Peak no.	2θ (degree)	d (Å)	D grain size nm
1	12.39	7.13	2.64
2	15.83	5.59	2.84
3	24.75	3.59	3.05
4	26.59	3.34	2.88
5	21.03	2.88	2.47
6	41.45	2.18	3.20
7	52.39	1.74	2.57
8	60.29	1.53	2.64
9	72.49	1.30	2.77

The surface morphology and elemental composition of rGO sample were studied with the help of Scanning Electron Microscope (SEM) (JEOL JSM 6360). Figure 4 (a) shows the SEM images of synthesized L-rGO sample and Fig 4 (b) shows the SEM images of synthesized C-rGO sample. The SEM images clearly show that the multilayered sheets of rGO which conforms the formation of rGO. Number of rGO sheets are layered onto each other results agglomeration of rGO.

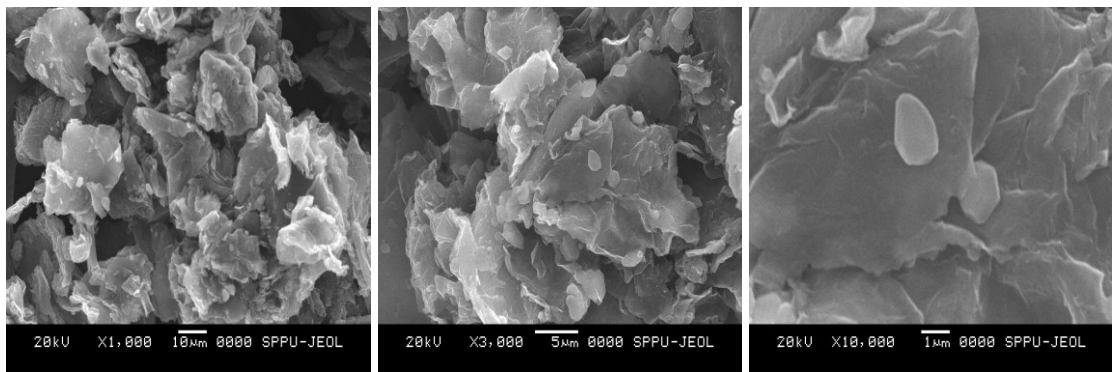
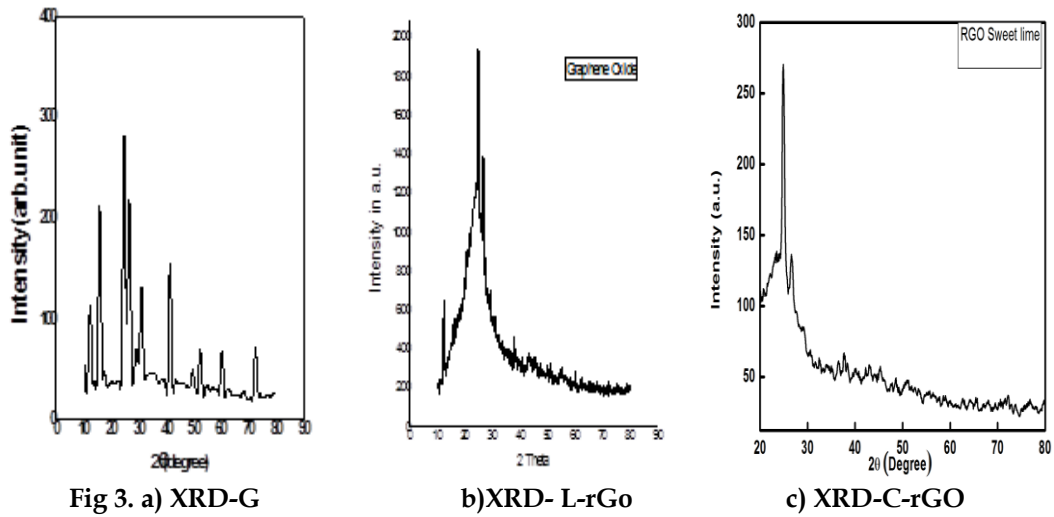


Fig. 4 a. SEM of image of L-rGO

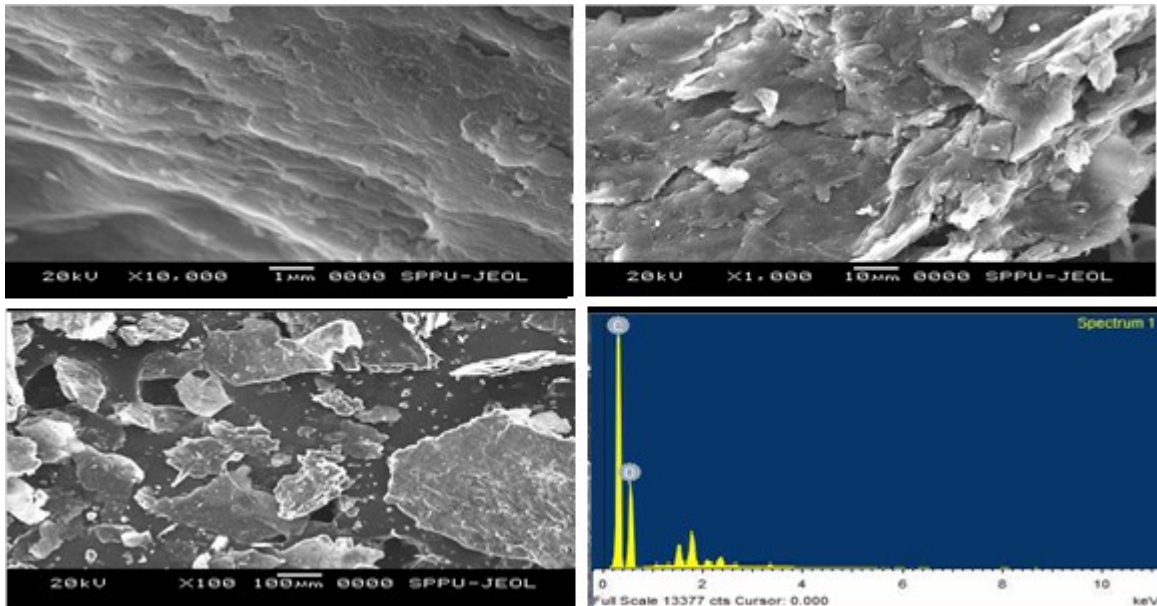


Fig 4 (b) SEM of image of C-rGO

EDX analysis

The EDX result also confirms and showing the elemental composition of elements C and O respectively.

CONCLUSIONS

Lantana camara, *Citrus limeta* can successfully reduce GO and forms graphene sheets which are

dispersible in water. Graphene obtained through such green routes could be of great importance in a countless industrial applications, especially in biologically sensitive areas.

Acknowledgments

The authors are thankful to AISSMS's college of pharmacy and engineering for facilitating characterization techniques.

REFERENCES

1. Geim K. Science. 2009;324: 1530
2. Daniel R. Dreyer, W. et al. The chemistry of graphene oxide", Chemical Society Reviews, *Chem. Soc. Rev.*2010;39: 228-240.
3. Dhand Vivek, et al. A Comprehensive Review of Graphene Nanocomposites: Research Status and Trends", *Journal of Nanomaterials*.2013;13:14.
4. Singh V, Joung D, et al. Graphene based materials: past, present and future," *Progress in Materials Science*.2011;56,8: 1178-1271.
5. Zhu Y, S. Murali, W. Cai et al. Graphene and graphene oxide: synthesis, properties, and applications," *Advanced Materials*.2010; 22, 35: 3906-3924.
6. Ramesha GK, Kumara AV, et al. Graphene and graphene oxide as effective adsorbents toward anionic and cationic dyes", *Journal of Colloid and Interface Science*.2011;361, 1:270-277.
7. Nikam Aarti P. et al. Nanoparticles - An Overview", *International Journal of Research and Development in Pharmacy and Life Sciences*, 2014;3, 5:1121-1127.
8. Malik Parth, et al. Green Chemistry Based Benign Routes for Nanoparticle Synthesis, *Journal of Nanoparticles*. 2014; 14.
9. Monaliben Shah et al. Green Synthesis of Metallic Nanoparticles via Biological Entities". 2015;8: 7278-7308.
10. Khana Mujeeb, et al. Pulicaria Glutinosa Plant Extract: A Green and Eco-Friendly Reducing Agent for the Preparation of Highly Reduced Graphene Oxide", *The Royal Society of Chemistry*, 2014; 4:24119-24125.
11. Rai M, Yadav A, and Gade A. CRC 675-current trends in phytosynthesis of metal nanoparticles," *Critical Reviews in Biotechnology*, 2008;28,4:277-284.
12. Jianchang Li, et al. The Preparation of Graphene Oxide and Its Derivatives and Their Application in Bio-Tribological Systems", *Lubricants*, 2014; 2: 137-161.
13. Paulchamy B, et al. A Simple Approach to Stepwise Synthesis of Graphene Oxide Nanomaterial. *J Nanomed Nanotechnol*, 2015; 6, 1:2157-7439
14. Jannathul Firdhouse M and Lalitha P. Eco-friendly synthesis of graphene using the aqueous extract of *Amaranthus dubius*", *Carbon - Sci. Tech.* 2013;5/2: 253 - 259.
15. Sangiliyandi Gurunathan et al. *Ginkgo biloba*: a natural reducing agent for the synthesis of cytocompatible graphene", *International Journal of Nanomedicine*, 2014;9: 363 - 377.
16. Mujeeb Khan et al. Green Approach for the Effective Reduction of Graphene Oxide Using *Salvadora persica* L.Root(Miswak) Extract "Nanoscale Research Letters 2015;10:281.
17. Sangiliyandi Gurunathan et al. Microbial reduction of graphene oxide by *Escherichia coli*: A green chemistry approach". 2013; 102: 772-777.
18. Kartick, et al. Green Synthesis of Graphene" *Journal of Nanoscience and nanotechnology*, 2013;13: 4320-4324.

Fabrication and Characteristics of Nano Sized ZnSe Thin Films by Chemical Bath Deposition

Pingale PC*, Kale RD and Kalange AE

Advanced Material Laboratory, Post Graduate Department of Physics, Tuljaram Chaturchand College of Arts, Science and Commerce, Baramati-413102, M. S., India.

*Email: pcpingale@gmail.com

Manuscript Details

Available online on <http://www.irjse.in>
ISSN: 2322-0015

Editor: Dr. Arvind Chavhan

Cite this article as:

Pingale PC, Kale RD and Kalange AE. Fabrication and Characteristics of Nano Sized ZnSe Thin Films by Chemical Bath Deposition, *Int. Res. Journal of Science & Engineering*, December 2017; Special Issue A1 : 35-38.

© The Author(s). 2017 Open Access

This article is distributed under the terms of the Creative Commons Attribution 4.0 International License

(<http://creativecommons.org/licenses/by/4.0/>), which permits unrestricted use, distribution, and reproduction in any medium, provided you give appropriate credit to the original author(s) and the source, provide a link to the Creative Commons license, and indicate if changes were made.

ABSTRACT

Zinc selenide is a potential candidate for use as an n-type window layer in thin film heterojunction solar cells due to its wide band gap of 2.7 eV. ZnSe thin films were therefore, chemically deposited onto glass microslides at 70°C. The deposition time and reaction pH were monitored as 180 min and 10±0.5 respectively. Film thickness of ZnSe thin films was measured by an interferometer technique and is found to be 544 nm. The films were then characterized by the XRD, optical and Raman techniques. Structural studies on ZnSe showed that the films exhibit hexagonal wurtzite structure with <100> preferred orientation. The d-value and intensity of reflection have excellent match with that of the JCPD data. The lattice parameter 'a' is found to be 3.990 Å and 'c' is 6.560 Å. The average crystallite size using Debye Shirrer's method is 52 nm. The surface features revealed by SEM showed uniformly distributed crystallites and their spherical shape. Broad absorption edge of thin films was revealed with high absorption coefficient ($\alpha = 10^4 - 10^5 \text{ cm}^{-1}$). The optical bandgap (E_g) of ZnSe thin films is 2.682 eV. Raman spectra showed presence of LO mode at 248 cm^{-1} and TO mode at 204 cm^{-1} .

Keywords: ZnSe, Chemical bath, Wurtzite, LO and TO modes.

INTRODUCTION

The II -VI polycrystalline semiconducting materials are under increased scrutiny because of their wider use in device cost reduction in the era of photovoltaics and high speed optoelectronics [1-2]. Due to non-toxicity, higher abundance, thermal and mechanical stability, zinc selenide is one of the most promising materials for the fabrication of the next generation of optoelectronic devices in the UV-Vis region [1-4]. Various deposition techniques have been widely used to produce zinc selenide thin films. However, seeking the most reliable and economic deposition technique is the main goal. The most intensively studied techniques include, chemical bath [1,5,6], RF magnetron sputtering, thermal evaporation [2], sol-gel method, pulsed laser deposition (PLD) and spray pyrolysis. Among these methods, chemical bath is the most useful technique for large area applications. This method is cheaper, simple and allows us to obtain films with high transparency and conductivity for optoelectronic applications [5]. Preparation of non-toxic, cost-effective and stable material is the need of society and its use in optoelectronic devices alternative to Cd free (eco-friendly) is necessity of nature [2,6].

METHODOLOGY

Preparation of the samples

ZnSe thin films were deposited by a chemical bath deposition on to glass substrate using AR grade zinc sulphate and sodiumselenosulphate as precursor. Glass substrates were ultrasonically cleaned by de-ionized water, acetone and methanol before the experiment. The volume of chemical bath contains zinc sulphate + ammonia + sodiumselenosulphate + water (10 + 10 + 20+60) ml solutions. The films were prepared at the deposition temperature 70°C, deposition time 180 min, pH 11 with equimolar (0.1 M) zinc sulphate and sodiumselenosulphate solutions.

Characterization of the samples

The film composition and surface morphologies were investigated by the EDS and SEM. A JEOL6360, JED2300 scanning electron microscope were used for

these studies. The structural properties were studied by Philips X- ray diffractometer PW - 1710 ($\lambda = 1.5405 \text{ \AA}$) using Cu - K_{α} radiation in the range 20° to 80° . Optical transmission at room temperature was recorded in the 200-900 nm wavelength range using a UV-Vis-NIR spectrophotometer. Raman spectra were obtained using Reinshaw microscope (514 nm He-Ne laser) in the spectral range from 150 to 320 cm^{-1} .

RESULT AND DISCUSSION

The ZnSe films obtained under the above conditions are homogeneous, tightly adherent with light brown colored tinge. Film thickness of ZnSe thin films is $\sim 544 \text{ nm}$.

The EDS Studies

An energy dispersive X-ray spectroscopy (EDS) was employed to determine the quantitative measure of ZnSe thin film samples. The atomic % of Zn^{2+} , Se^{2-} are 40.96 and 59.06 respectively. EDS analysis conferred presence of expected elements Zn and Se in the thin solid films. Fig 1 shows EDS spectra for ZnSe thin films.

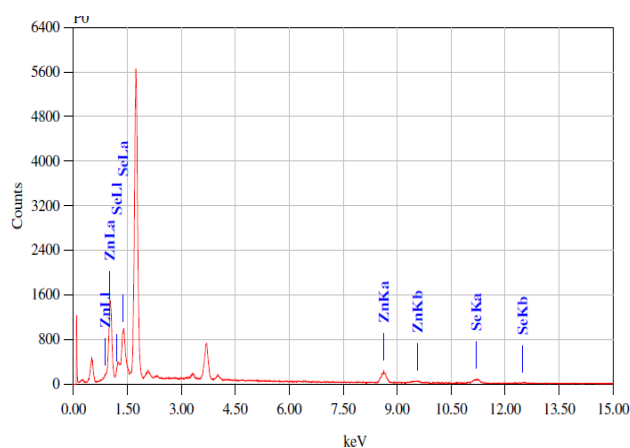


Figure 1. EDS Spectra of ZnSe Thin Films

Surface Microscopy

The surface morphology of the thin film layer was viewed through a scanning electron microscope at 20 KV is shown in Fig. 2. SEM micrograph showed that the crystallites are uniformly distributed and spherical in shape. A considerable fusing of crystallites has also been observed.

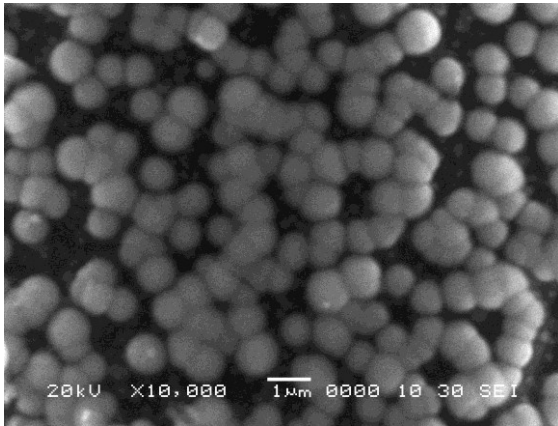


Figure 2 SEM Micrographs of ZnSe Thin Films

X-ray Diffraction

Structural characterization of the as-deposited samples was done using XRD analysis. Fig. 3 shows X-ray diffractogram of ZnSe sample. Structural studies showed that the polycrystalline nature of the material and films exhibit hexagonal wurtzite structure with <100> preferred orientation. The average crystallite size calculated using Debye-Shirrer Equation is 52 nm. The lattice parameter 'a' is found to be 3.990 Å and 'c' is 6.560 Å.

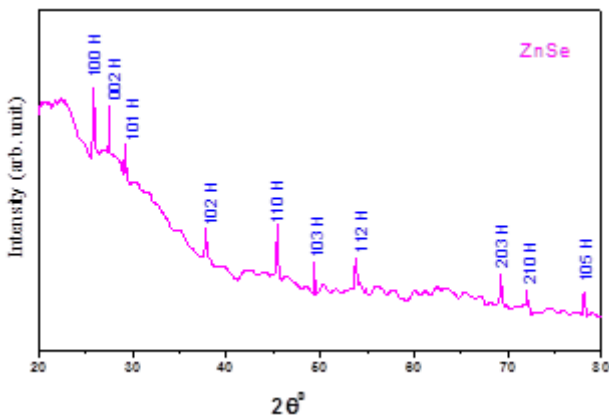


Figure 3. X-ray diffractogram of ZnSe Thin Film

Raman Studies

Fig. 4 shows Raman Spectra of ZnSe thin films. Raman spectra showed presence of LO mode at 248 cm⁻¹ and TO mode at 204 cm⁻¹. Existence of LO and TO modes confirmed formation of the ZnSe thin films. The presence of LO mode signify crystalline nature of the as-deposited ZnSe thin films.

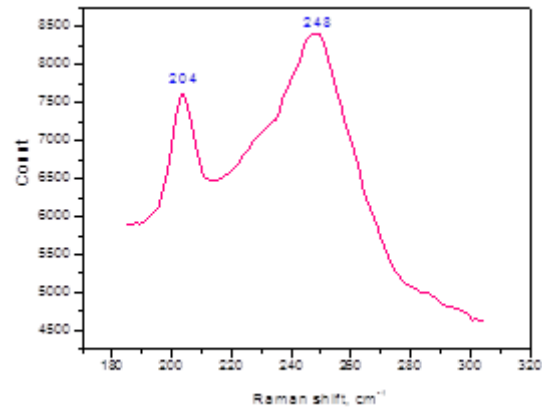


Figure 4. Raman Spectra of ZnSe Thin Films

Optical Studies

The optical band gap (E_g) was therefore determined for the film using $(\alpha h\nu) = A (h\nu - E_g)^m$, where m and A are constants, α is the absorption coefficient (cm⁻¹) and $h\nu$ is the photon energy (eV). The Variation of $(\alpha h\nu)^2$ vs $h\nu$ of ZnSe thin film is shown in of Fig. 5. The optical band gap (E_g) of ZnSe thin films is 2.682 eV.

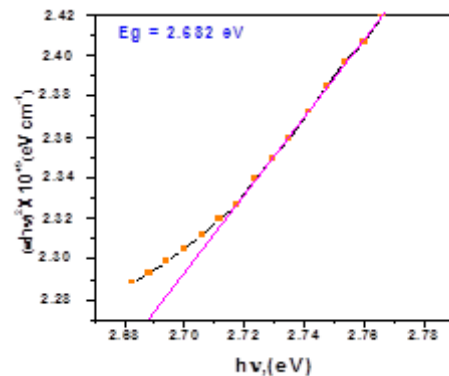


Figure 5. Variation of $(\alpha h\nu)^2$ vs $h\nu$ for ZnSe thin films.

CONCLUSION

ZnSe thin films were successfully deposited on glass substrates by a liquid phase chemical bath deposition. The formation of ZnSe thin film layers was confirmed by the EDS. ZnSe solid thin films are polycrystalline in nature and exhibit hexagonal phase with growth orientation <100>. Existence of LO and TO modes confirmed formation of the ZnSe thin films. The optical band gap of thin films is 2.682 eV and useful for photovoltaic studies.

Acknowledgement

I acknowledge BCUD, SPPU Pune for sanctioning the minor research project.

REFERENCES

1. Chen L, Zhang D, Zhai G, Zhang J, Mater. Chem. Phys. 2010;120: 456.
2. Murali KR, Thiakvathy K, Vasantha S, Oomen R, Chalco. Lett. 2008;5: 111.
3. Venkatachalm S, Mangalraj D, Narayandass K, Appl. Surf. Sci. 2007;253: 5137.
4. Khan TM, Mehemoood MF, Mahmood A, Shah A, Raza Q, Iqbal A, Aziz U, Thin Solid Films 2011;519: 5971.
5. Hodes G, Phys. Chem. Chem. Phys. 2007;9:2181.
6. Deshmukh LP, Pingale PC, Kamble SS, Lendave SA, Mane ST, Pirgonde BR, Sharon M, Mater. Lett. 2013;92: 308.
7. Pingale PC, Mane ST, Lendave SA, Kamble SS, Suryawanshi RV, Singh A, Kothari DC, Deshmukh LP, Sharon M, Nepal J. Chem. Soc.2012;30:130.

The effect sintering temperature on structural and magnetic properties of Nano-crystalline Al³⁺ doped Magnesium-copper ferrites synthesized by Sol-gel method

Lagad SB¹ and Gaikwad SV*

¹Research Scholar, JJT University, Jhunjhunu, Rajasthan and Anantrao Thopte College, Bhor, Dist- Pune, Maharashtra, India, *Reader, P. G. Department of Physics, Abasaheb Garware College, Pune, India.

Email Id: lagadshahu@gmail.com

Manuscript Details

Available online on <http://www.irjse.in>
 ISSN: 2322-0015

Editor: Dr. Arvind Chavhan

Cite this article as:

Lagad SB and Gaikwad SV. The effect sintering temperature on structural and magnetic properties of nanocrystalline Al³⁺ doped Magnesium-copper ferrites synthesized by Sol-gel method., *Int. Res. Journal of Science & Engineering*, December 2017; Special Issue A1 : 39-43.

© The Author(s). 2017 Open Access

This article is distributed under the terms of the Creative Commons Attribution 4.0 International License

(<http://creativecommons.org/licenses/by/4.0/>), which permits unrestricted use, distribution, and reproduction in any medium, provided you give appropriate credit to the original author(s) and the source, provide a link to the Creative Commons license, and indicate if changes were made.

ABSTRACT

Aluminium doped Mg-Cu ferrite (Mg_{0.5}Cu_{0.5}Fe_{1.7}Al_{0.3}O₄) nanoparticles were synthesized by sol gel auto combustion techniques using respective metal nitrates with citric acid as fuel for combustion process. The resulting sample annealed at 400°C and 700°C temperature. The formation of ferrite nanoparticles with single phase spinel structure is evident from X-ray diffraction analysis of the as-burnt, sintered sample at 400°C and 700°C temperature. An intense XRD peak indicates the formation of nanoparticles. Average crystallite size calculated from most intense reflection peak (311) using Debye-Scherrer's formula is found to be nanometer in range and that increases with increase in sintering temperature. The lattice constant and other structural parameters evaluated from XRD data are in reported range. EDS data confirms that the reactant have under gone complete reaction. Magnetic study of the prepared samples is carried out using vibrating sample magnetometer (VSM). VSM data shows that the prepared samples are soft ferromagnetic materials.

Key words: Ferrite, nanoparticles, magnetic, X-ray diffraction, SEM, VSM.

INTRODUCTION

Ferrite materials are special class among the numerous magnetic materials as they are widely used magnetic materials as they have excellent electrical and magnetic properties [1, 2]. The interesting physical properties of ferrites arise from their ability to distribution of the cations among the available sites. Now a days nano-magnetic materials have attained great interest because of their potential applications in many fields like high-density data storage, ferro-fluid, magneto-optical recording, magnetic resonance imaging, drug delivery, magneto-caloric refrigeration etc [3].

Among the different spinel type ferrite material Mg-Cu ferrites are great importance because of their excellent chemical stability, high electrical resistivity, low eddy current and dielectric losses, low coercivity, and moderate saturation magnetization [4]. Due to these important properties they are widely used as magnetic materials at high frequency applications.

The number of methods has been used to prepare nanosized ferrite particles. Fine particle nature of nanosize can be achieved through number of methods which include chemical precipitation [5], micro-emulsion [6], sol-gel [7], hydrothermal process [8] etc. The role of synthesis variables such as pH, fuel, fuel ratio, annealing temperature and time are also important in governing the size of the particles and hence the physical properties. Among the various fuels citric acid is commonly used for sol-gel synthesis. No more work reported about synthesis and magnetic properties of Aluminium doped magnesium-copper ferrite synthesized by various methods.

In this study, we report the synthesis of aluminium substituted for iron in magnesium- copper ferrite nanoparticles using sol-gel auto combustion technique and sintered at 400°C and 700°C. The characterizations of X-ray diffraction, scanning electron microscopy for structural and magnetic properties of ferrite were investigated. The structural, morphological and magnetic properties are presented.

METHODOLOGY

(A) Preparation method: A. R. grade precursors viz. aluminium nitrate $[Al(NO_3)_3 \cdot 9H_2O]$, magnesium nitrate $[Mg(NO_3)_2 \cdot 6H_2O]$, copper nitrate $[Cu(NO_3)_2 \cdot 3H_2O]$ and ferric nitrate $[Fe(NO_3)_3 \cdot 9H_2O]$ were used to synthesize the nanoparticles. Citric acid $[C_6H_8O_7 \cdot H_2O]$ was used as fuel. The stoichiometric amounts of nitrates were dissolved in de-ionized water with continuous magnetic stirring. Then the citric acid solution prepared separately was mixed in the metal nitrate solution. The molar ratio of acid to nitrates was maintained 1:1. The nitrate-citrate solution was neutralized by adding liquid ammonia to it and then allowed to evaporate till the formation of viscous gel by heating at 80°C on hot plate with continuous stirring. The gel is then burnt in to ashes of Al doped Mg-Cu ferrite nanoparticles by raising its temperature to 100°C.

The thermo-gravimetric analysis of the as prepared sample suggests the formation of spinel phase decomposition of all the precursors at about 400°C. Accordingly the as burnt powder was annealed at temperature 400°C and 700°C for 3 hour to obtain the spinel phase of the Al doped Mg-Cu ferrite nanoparticles.

(B) Measurements and Characterization: The sintered samples were analyzed by X-ray diffractometer (BRUKER AXS MODEL-D8 advance) using Cu-K α radiation at room temperature in 2 θ range from 20° to 80°. The lattice constant was determined from X-ray data analysis using formula.

$$\frac{\sin^2 \theta}{h^2 + k^2 + l^2} \dots 1$$

Where, 'a' is lattice constant, (hkl) represents Miller indices and ' λ ' is the wavelength of X-ray used and ' θ ' is the glancing angle.

The crystallite size 'D' was determined from the full width half maximum (β) of the strongest reflection (311) and by using the Scherrer's formula [9],

$$D = \frac{0.9\lambda}{\beta \cos \theta} \dots \dots 2$$

Where, ' λ ' is the wavelength of X-ray used and ' θ ' is the Bragg's angle.

The X-ray density was calculated from lattice parameter (a) using formula,

$$d_x = \frac{8M}{N_A a^3} \dots\dots 3$$

Where, M is molecular weight, N_A is the Avogadro's number and a is lattice constant.

The bulk density (d_b) samples were calculated by measuring mass and volume of pellet as

$$\text{Bulk density}(d_b) = \frac{\text{Mass of Pellet}}{\text{Thickness of pallet (h) X Cross section area } (\pi r^2)}$$

$$d_b = \frac{M}{h \pi r^2} \dots\dots 4$$

Where, r is radius of pellet and h is thickness of pellet. From the x-ray density (d_x) and bulk density (d_b) values, porosity was calculated using the relation.

$$\text{Porosity}(P) = 1 - \left(\frac{d_b}{d_x} \right) \dots\dots 5$$

Morphological study is carried out using scanning electron microscope (SEM). The magnetic properties were measured (Model- LAKESHORE Model-7307) at room temperature using vibrating sample magnetometer (VSM) technique.

RESULTS AND DISCUSSION

A) Structure properties: The structural analysis of $Mg_{0.5}Cu_{0.5}Fe_{1.7}Al_{0.3}O_4$ ferrite samples of as-burnt, sintered at 400°C and 700°C temperature was performed by powder XRD method. As-burnt, sintered at 400°C and 700°C temperature samples with sample code of ($Mg_{0.5}Cu_{0.5}Fe_{1.7}Al_{0.3}O_4$) is given in table 1. The X-ray diffraction (XRD) patterns of all above samples are as shown in figure 1.

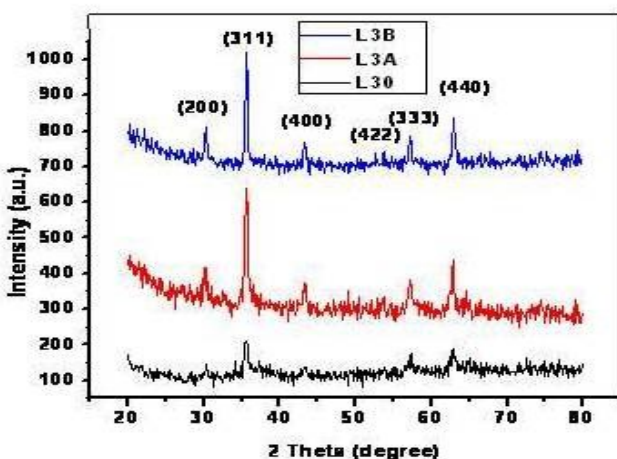


Figure 1: Powder X-ray diffraction (XRD) pattern of L30, L3A and L3B samples

Table1: Sample code of $Mg_{0.5}Cu_{0.5}Fe_{1.7}Al_{0.3}O_4$ sample as-burnt, sintered at 400°C and 700°C temperature

Temperature of sample	Sample code
As-burnt sample (27°C)	L30
400°C	L3A
700°C	L3B

Table 2: Various parameters of Aluminium doped Mg-Cu ferrites nanoparticle

Parameters	Unit	L30	L3A	L3B
Crystallite size(D) nm	Nm	20.4	32.53	48.62
Lattice constant (a)	Å	8.3532	8.3656	8.3949
Unit cell volume	(Å) ³	583	585	592
X-ray density (d_x)	g/cm ³	4.8072	4.7857	--
Bulk density (d_b)	g/cm ³	1.6457	1.8694	--
Porosity (P)	(%)	65.76	60.94	--

All observed peaks of XRD correspond to standard spinel diffraction patterns with no extra peak which confirmed single phase cubic structure. The prominent (hkl) planes (220), (311), (400) (422), (333) and (440) were indexed. The broader peaks observed in XRD pattern suggest the nano-crystalline nature of sample. The values of structural parameters obtained from XRD analysis are given in table 2. It's observed from table 2 that the crystallite size (D) as well as lattice constant (a) increases with sintering temperature of sample as shown in figure 2. X-ray density and porosity were decreases with sintering temperature. These structural parameters obtained for the present sample are good agreement with those reported in the literature [10]. Morphology study of the samples carried out by using SEM reveals the spherical shape of the particles and size of particle increases with increasing sintering temperature as shown in figure 3.

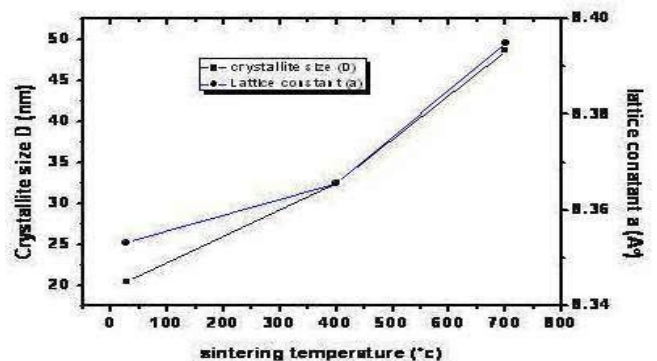


Figure 2: Variation of crystallite size with sintering temperature

In order to confirm the stoichiometry of the prepared nanocrystalline Al substituted Mg-Cu ferrites, energy dispersive spectroscopic (EDS) analysis carried out. Figure 4 shows EDS pattern nanocrystalline Al substituted Mg-Cu ferrite samples. It is clear that Mg^{2+} , Cu^{2+} , Al^{3+} , Fe^{3+} and O^{2-} are present in proper proportions. This suggests that the expected stoichiometry is maintained in the prepared samples. The EDS results also confirm that precursors used for the synthesis have fully undergone the chemical reaction to form the single phase aluminium doped Mg-Cu ferrite samples in Nano crystalline nature. Some of the samples showed impurities of Zn of about less than 1%, which might have crept into the samples due to contents of sample surface and porcelain boat and get loss due to sintering temperature. The important point is that EDS result pointed no loss of ingredients after high temperature sintering and results matched the expected values within the experimental error.

B) Magnetic properties: The room temperature measurement of magnetic properties of L30, L3A and L3B ($Mg_{0.5}Cu_{0.5}Fe_{1.7}Al_{0.3}O_4$) samples was carried out using vibrating sample magnetometer. Figure 5 shows the hysteresis loop of aluminium doped Mg-Cu ferrite nanoparticles at room temperature.

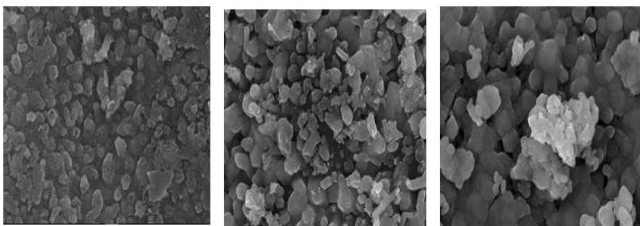


Figure 3 SEM image of L30, L3A and L3B samples

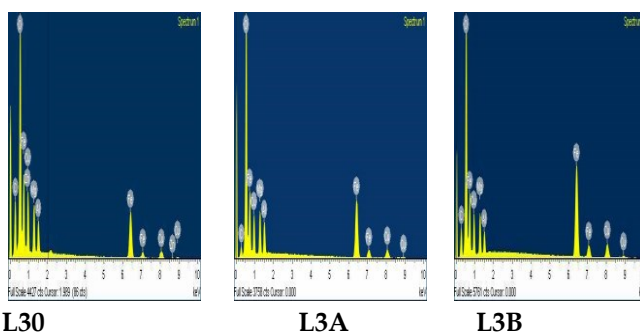


Figure 4: EDS pattern of L30, L3A and L3B samples

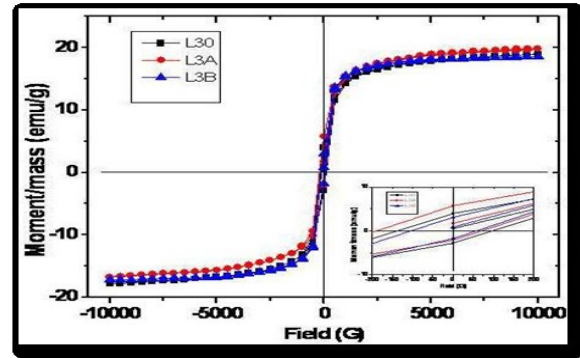


Figure 5: Hysteresis plot of L30, L3A and L3B samples measured at room temperature.

Table 3: Magnetic properties of $Mg_{0.5}Cu_{0.5}Fe_{1.7}Al_{0.3}O_4$

Parameter	Unit	L30	L3A	L3B
Saturation Magnetization (M_s)	emu/g	18.42	19.86	17.91
Coercivity (H_{ci})	G	119.15	130.25	80.35
Retentivity (M_r)	emu/g	3.99	5.76	5.05
Squareness (M_r/M_s)	--	0.1862	0.2147	0.1348

The saturation magnetization (M_s), coercivity (H_{ci}) and remanance magnetization (M_r) measured from hysteresis loop are listed in table 3. The saturation magnetization (M_s) initially increases with sintering temperature due to increase in particle size [11] and then decreases as given in table 3. Similar behavior for coercivity (H_{ci}) and retentivity (M_r) of samples. Compared with values of coercivity (H_{ci}) and retentivity (M_r) of all samples, sample L3B having least these values as given in table 3. This shows that sample is soft ferrite material.

CONCLUSIONS

The nano-crystalline aluminium doped Mg-Cu ferrite was successfully synthesized by sol-gel method. The X-ray diffraction results showed the formation of single phase cubic spinel structure with particle size in nanometer range. The EDS data shows that all elements present in aluminium doped Mg-Cu ferrite sample have maintained their stoichiometry proportions. The hysteresis pattern exhibits soft ferromagnetic nature of the samples.

Acknowledgements:

Author is very thankful to Director, Indian Institute of Technology Pawai, Mumbai for SEM and EDS

facilities, Department of Physics, Savitribai Phule Pune University, Pune for XRD facility. Department of Physics, C.T. Bora College, Shirur and Dr. Gaikwad S.V. Abasaheb Garware College, Pune for useful guidance.

REFERENCES:

1. Kurikka V.P.M. Shafi, Yuri Koitpin, Ahron Gedanken, Ruslan Prozorov, Janos Lendvai, Israel Felner, *J. Phys Chem.*1997;B 101:6409.
2. Lagarashi H, Okazaki K, *J Am. ceram. Soc.* 1977; 60: 51.
3. Muhammad Yashir Rafique, Liqing Pan, Qurat-al-ainJaved, Muhammad ZubairIqbal, Lihong Yang, *J. Nanopart Res.* 2012;14:1189.
4. SatoTurtello R, Giap V. Duong Nunes W, Grpssinger R, Knobel M, *J Magn. Magn. Mater* 2008;320:339.
5. Shenoy SD, Joy PA, Anantharam MR, *J. Magn. Magn Mater.* 2004; 269:217.
6. Nju XS, Du WP, Du WM, *Sensors Actuators B*, 2004;99:405.
7. Brown P, Hope-Weeks LJ, *J. Sol Gel Sci. Tech.* 2009; 51:238.
8. Rozman M and Drofenik M, *J. Am. Ceram. Soc.* 1995;78: 2449.
9. Anis-ur-Rehman M, Abdulla A, Ansari Mariam, Zeb-un-Nisa and Awan MS. *World Academy of Science, engineering and technology* 2011;52:679.
10. Sang-Hoon Park, Jeong-Keun Ji, Won-Ki Ahn, Jun-Sig Kum, *Electronic Materials Letters*, 2004;4(4): 175-179.
11. Chauhan BS, Kumar R, Jadhav KM, and Singh M, *Journal of Magnetism and Magnetic Materials*, (2004);283(1): 71-81.

Screening of silver nanoparticles producing cyanobacteria and its characterization

Pawar Sunil*, Bhosale Amarsinh, Mulani Parvin, Patekar Panchratna and Shaha Swarali.

Department of Microbiology, Tuljaram Chaturchand College, Baramati-413102, Dist-Pune, Maharashtra

*Corresponding author: E-mail: suniltppawar@yahoo.co.in | Contact: +91-9423251465

Manuscript Details

Available online on <http://www.irjse.in>
ISSN: 2322-0015

Editor: Dr. Arvind Chavhan

Cite this article as:

Pawar Sunil, Bhosale Amarsinh, Mulani Parvin, Patekar Panchratna and Shaha Swarali. Screening of silver nanoparticles producing cyanobacteria and its characterization, *Int. Res. Journal of Science & Engineering*, December 2017; Special Issue A1 : 44-54.

© The Author(s). 2017 Open Access

This article is distributed under the terms of the Creative Commons Attribution 4.0 International License

(<http://creativecommons.org/licenses/by/4.0/>), which permits unrestricted use, distribution, and reproduction in any medium, provided you give appropriate credit to the original author(s) and the source, provide a link to the Creative Commons license, and indicate if changes were made.

ABSTRACT

Biosynthesis of nanoparticles is the major division in the field of applicable nanoscience and nanotechnology. Nanoparticles can be synthesized using plant extracts, enzymes, bacteria, fungi and algae. Nanoparticles can be made of materials of diverse chemical nature, the most common being metals, metal oxides, silicates, non-oxide ceramics, polymers, organics, carbon and biomolecules. Silver nanoparticles are widely used particularly in textiles, plastics and medical industries, changing the pattern of silver emission as these technologies and products diffuse through the global economy. In the present investigation, twenty cyanobacterial isolates were screened for the synthesis of silver nanoparticles. Out of that *Oscillatoria* spp. was shown to be capable to biosynthesize Ag-NPs. Silver nano particles synthesis of has been shown from filamentous *Oscillatoria* sp. and it was confirmed using yellowish-brown color in aqueous solution along with the uv-vis spectroscopy. It was confirmed by scanning electron microscopy (SEM) which showed that Ag-NPs were present and evenly distributed throughout the cell free liquid culture of the AgNO₃-incubated culture. XRD X-ray diffraction (XRD) was carried out to confirm crystalline nature of the particles and it is concluded that the mix phase of AgNO₃ and silver nanoparticles is observed. FTIR was used to identify the biomolecules in *Oscillatoria* sp. responsible for the silver ions reduction and stabilization of reduced silver ions. The antibacterial activity of silver nanoparticles produced by *Oscillatoria* sp. was observed against pathogens, viz., *E. coli*, *Klebsiella* sp., *Salmonella* sp., *Pseudomonas* sp. using disc diffusion method. The bioactive-ty of the synthesized silver nanoparticles had inhibitory effect on important human pathogens. It would be desirable to develop a technology in which the specific size and shape of the particles could be obtained by the use of a specific strain of cyanobacteria.

Keywords: Silver nanoparticles, Cyanobacteria, Scanning electron microscopy, X-ray diffraction Antibacterial activity.

INTRODUCTION

Nanotechnology has a very important modern field concerns with the growth of new processes for the synthesis of nanoparticles of different sizes, shape and proscribed dispersity [1]. These particles can be made up with diverse chemical nature materials, the most common being metals, metal oxides, silicates, non-oxide ceramics, polymers, organics, carbon and biomolecules. Nanoparticles exist in several different morphologies [2]. Biosynthesis of nanoparticles is the major division in the field of applicable nanoscience and nanotechnology therefore there is a need for microbe mediated synthesis that includes a clean, nontoxic and ecofriendly method of nanoparticles synthesis [3].

Nanotechnology is enabling technology that deals with nanometer sized objects. The biosynthesis of silver nanoparticles of different sizes, ranging from 1-70nm, and shapes including spherical, triangular & hexagonal [4]. The mechanism for the bioreduction of silver by bacteria involves reducing & other proteins in which sulphur and carboxylate group from cell wall. The silver nitrate caused the reduction of silver through nitrate dependant reductase. Biosynthesis of nanoparticles is a kind of bottom up approach where the main reaction occurring is reduction/oxidation [5]. Silver nanoparticles are of interest for antimicrobial applications, biosensor materials, composite fibers, cryogenic superconducting materials, cosmetic products, and electronic components because of the unique properties and morphologies [7]. There is however various theories on the action of silver nanoparticles on microbes to cause the microbicidal effect [8].

The need for biosynthesis of nanoparticles rose as the physical and chemical processes were costly [9]. Microorganisms including bacteria, fungi and algae have been proposed as potential eco-friendly nanofactories for the synthesis of metal including silver [10,12]. A two step mechanism for synthesis of silver nanoparticles using microbes is, the first step involved trapping of Ag⁺ ions at the surface of biological cells & in the second step enzymes nanosilver particles. Silver ion, Ag⁺ has been reported to have high bio concentration factors (>10⁵), for freshwater green

algae and marine algae [13; 14]. Mubarak et al., [15] reported that the marine cyanobacterium *Oscillatoria willei* synthesized silver nanoparticles. They screened cyanobacteria & green algae as model biological system for their ability to form AgNPs. Nowadays, silver nanoparticles gain more attention by researchers not only because of their wide application and antimicrobial effects but also having potential risk in environmental and human health [16]. Against these backdrops the present study aimed at the synthesis of silver nanoparticles through biological methods using blue green algae and their application in inhibition of pathogenic bacteria and fungi [15,17].

The aim of the study is to isolate cyanobacteria from different locations & test the ability of synthesizing silver nanoparticles from cellular extracts of cyanobacterial isolates, the positive strain used for nanoconversion & also characterize the size of synthesized silver nanoparticles & study their antimicrobial property against various pathogenic bacteria.

METHODOLOGY

1. Collection of cyanobacterial samples:

Samples were collected from fresh water ponds, rivers, ditches and soils from Baramati region. Samples were collected in plastic bags or in bottles. The collected samples were brought in laboratory and used for isolation. The Cyanobacterial cultures were enriched in sterile BG-11 medium.

2. Isolation and identification of isolate:

The enriched samples showing blue-green, green coloration are inoculated in liquid medium for isolation of cultures. For unicellular cyanobacterial enriched samples were streaked on respective agar plates of growth medium. Visibly distinct cyanobacterial colonies are reinoculated for further purification. In case of filamentous cultures, selective inoculation of single filaments under aseptic conditions is the methods of isolation used. On the basis of morphological characteristics cyanobacterial cultures were identified as described by Rippka *et al.* [18] and Desikachary [19].

3. Screening of cyanobacteria for synthesis of silver nanoparticles:

Cyanobacterial isolates are inoculated in fresh BG-11 medium (100ml) and incubated at for 21 days under 1800-2000 lux light intensity. After the incubation, 20 ml each culture centrifuged at 10,000 rpm for 10 min at 4°C (Make- Remi Cooling centrifuge) and biomass were homogenized and again centrifuged. The supernatant and homogenized solution is used for the synthesis of the silver nanoparticles. The supernatant (5% of total volume) of cyanobacterial cultures are separately added to the flasks containing silver nitrate at a concentration of 0.1 g/L. The reaction between these supernatants and silver ions is carried out for 72 hrs. The bioreduction of silver ions in the solution is monitored by sampling the aqueous solution (2ml) and measuring the absorption spectrum of the solution using UV-Visible spectrophotometer (Shimadzu UV-1800) at a resolution of 1 nm [20].

3. Production of silver nanoparticles:

On the basis of preliminary detection using UV-Vis spectra the silver nanoparticles producing cyanobacterial cultures were selected for the further production. The supernatant (5% of total volume) of cyanobacterial cultures are separately added to the flasks containing silver nitrate at a concentration of 0.1 g/L. The reaction between these supernatants and silver ions is carried out for 72 hrs. The solution was centrifuged and the particles were separate out. These particles were used for further characterization.

5. Characterization of silver nanoparticles

5.1 UV-Visible spectra analysis: After 4 hrs of incubation of the above mixture, the preliminary detection of silver nanoparticles were carried out by visual observation of color change (white to brown) of the culture filtrate. The reduction of silver ions measured by using a UV-Visible spectrophotometer (Shimadzu UV-1800) at varying intervals (4hrs, 24 hrs, 48 hrs and 72 hrs) and scanning the spectra between 200-800 nm at the resolution of 1 nm[8].

5.2 Fourier Transform Infrared (FTIR) analysis: The silver nanoparticles analyzed by Fourier transform infrared (FTIR) analysis. The dried silver nanoparticles are analyzed using FTIR spectroscopy (Perkin Elmer Spectrum Version 10.03.06) between

frequency range 450 to 4000 cm^{-1} with resolution 4 cm^{-1} [20].

5.3 Scanning Electron Microscopy

A scanning electron microscope was used to record the micrograph images of synthesized silver nanoparticles [21].

5.4 X-Ray Diffraction (XRD) Analysis

The formation of silver nanoparticles was checked by X-ray diffraction (XRD) using an X-ray diffractometer. The supernatant treated with silver nitrate is evaporated to dryness under sunlight. The air dried biomass is analyzed. The full widths at half maximum (FWHM) values of X-ray diffractions were used to calculate particles size[20].

6. Antibacterial activity of silver nanoparticles: The silver nanoparticles synthesized from cyanobacterial isolates tested for antimicrobial activity by disc diffusion method against pathogenic microorganisms like *E. coli*, *Staphylococcus* sp., *Salmonella* sp., *Klebsiella* sp. and *Pseudomonas* sp. The pure cultures of these organisms were sub cultured on nutrient agar slants and incubated at 37°C for 24 hrs. Each strain having cell number $10^6/\text{ml}$ was spread uniformly on the nutrient agar plates and sterile paper discs dipped into the samples of nanoparticles solution were placed onto the nutrient agar plates. After incubation at 37°C for 24 hrs, the zones of inhibition of bacteria were measured.

RESULTS AND DISCUSSION

3.1. Isolation and identification of cyanobacteria:

Cyanobacteria were inoculated in BG11 medium. The flasks were incubated at $25\pm 2^\circ\text{C}$ at 1800-2000 lux light intensity for 21 days. After 21 days incubation, enriched samples showing blue-green, coloration were inoculated in medium for isolation of cultures. The data of isolation and identification of cultures enriched in sterile BG₁₁ medium are presented in Figure 1. It could be seen that a total 20 isolates were obtained and identified from enriched flasks. The isolated and laboratory set of cyanobacterial cultures were identified as per the morphological characters given by Desikachary [19] and Rippka *et. al.*, [18].

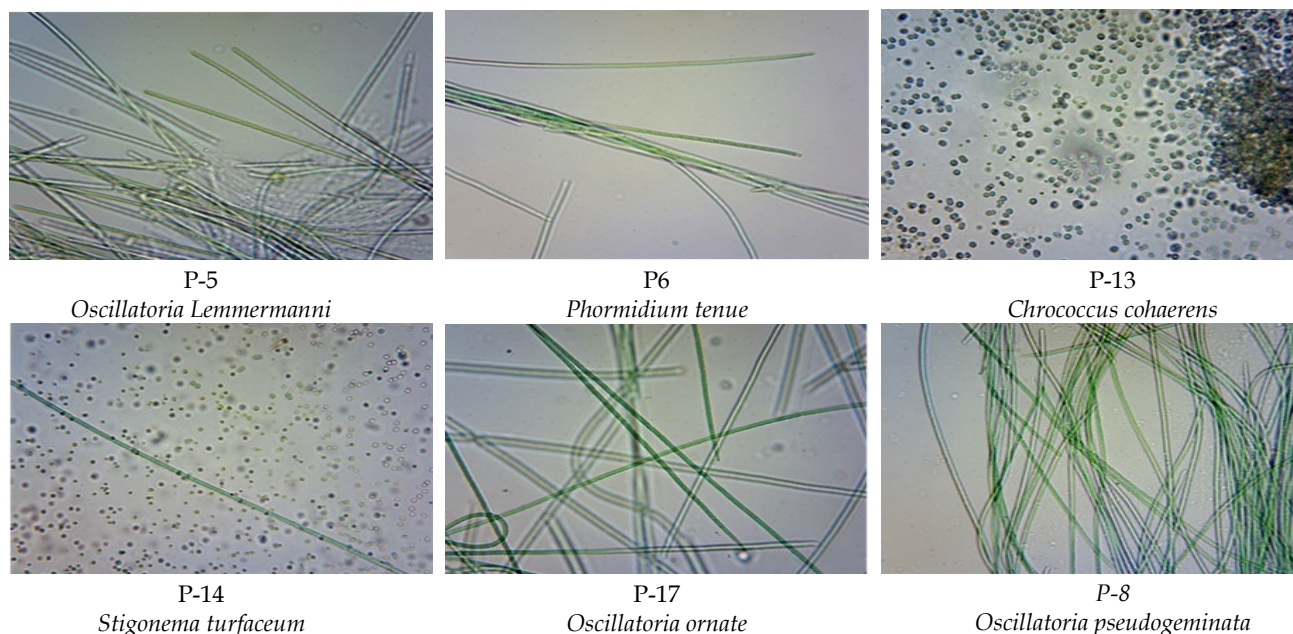


Figure 1 Microscopic observation of cyanobacterial cultures

This morphological form of cyanobacteria were observed under Lynx microscope. All cultures were maintained in BG-11 (pH 7.4) under 1800-2000 lux light intensity at temperature of $25 \pm 2^\circ\text{C}$.

3.2. Screening of cyanobacteria for synthesis of silver nanoparticles:

Cyanobacterial cultures were screened based on the preliminary visual color observation, which was changed from white to yellowish brown and based on UV spectra. From the twenty different isolated cultures, one culture was found to be capable of producing silver nanoparticles showing a peak at wavelength in the range between 420-450 nm. That culture was further used for large scale production.

3.3. Production and extraction of silver nanoparticles:

In the present study, extracellular biosynthesis of silver nanoparticles of isolates was studied. It shows color changes from colorless to dark brown due to reduction of silver (Ag^+) ions to silver nanoparticles (AgNPs) by the cyanobacterial reductase enzyme.

The exact mechanism leading to the extracellular formation of silver nanoparticles by the algal biomass is not fully understood; there are still several possible mechanisms involved in the process [11]. It is thought that the first step involves the trapping of metal ions on the surface of algal cells, possibly via electrostatic

interaction between the ions and negatively charged carboxylate groups present in the cell surface. Thereafter, the ions are reduced by the enzymes, leading to the formation of nuclei, which subsequently grow through the further reduction of metal ions and accumulation of these nuclei [22]. Most probably, the reduction of SNPs occurs due to the presence of cellular reductase released by *Spirulina platensis* into the solution. Also, in cyanobacteria, localized reducing conditions may be produced by a bacterial electron transport chain, via energy generating reactions within the cells [24]. In this respect, secreted cofactor NADH plays an important role [23].

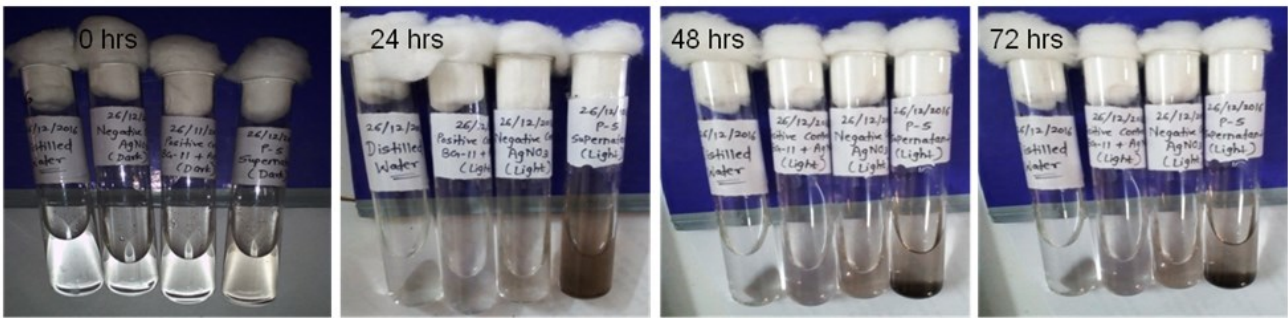
3.3. Characterization of silver nanoparticles

1. UV- Visible spectra analysis:

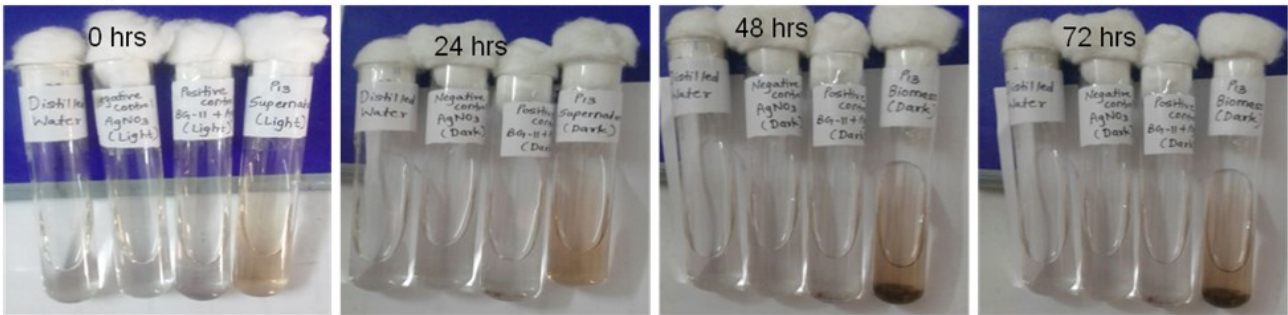
In this study, extracellular synthesis of SNPs has been shown from filamentous *Oscillatoria* spp. It is well known that SNPs exhibit a yellowish-brown color in aqueous solution, due to the excitation of Surface Plasmon Vibrations in SNPs [3]. Reduction of the silver ion to SNPs during exposure to the *Spirulina platensis* biomass could be followed by a color change, and thus, UV-Vis spectroscopy.

Figure 3 shows the UV-Vis spectrum of the nano silver formation and the change in the color of the reaction mixture to dark brown, indicating the biotransformation of ionic silver to reduced silver, and the subsequent formation of SNPs in an aqueous medium.

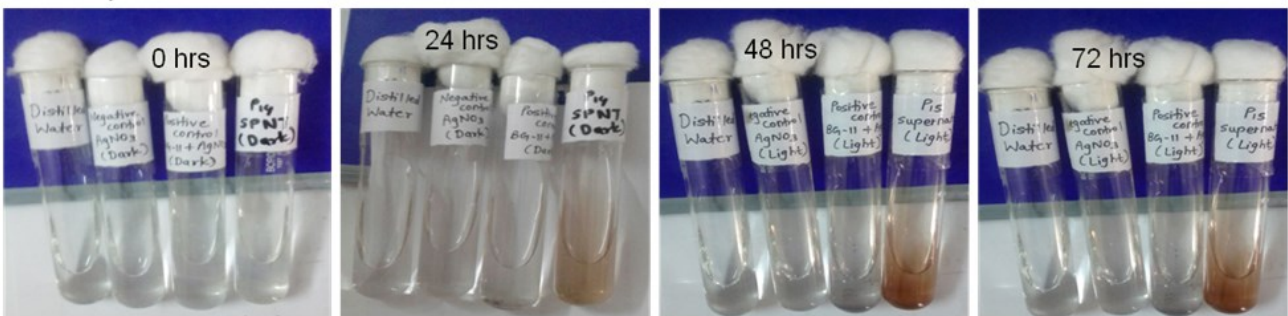
P-5- Cyanobacterial culture



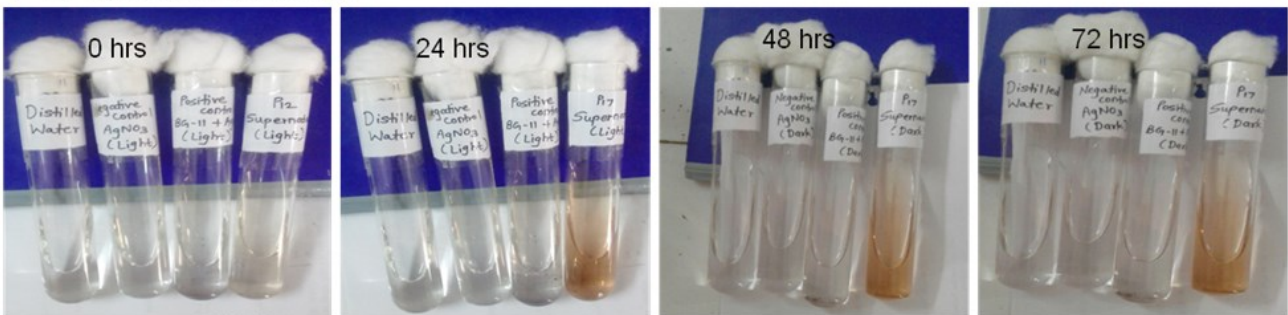
P-13- Cyanobacterial culture



P-14- Cyanobacterial culture



P-17- Cyanobacterial culture



P-18- Cyanobacterial culture

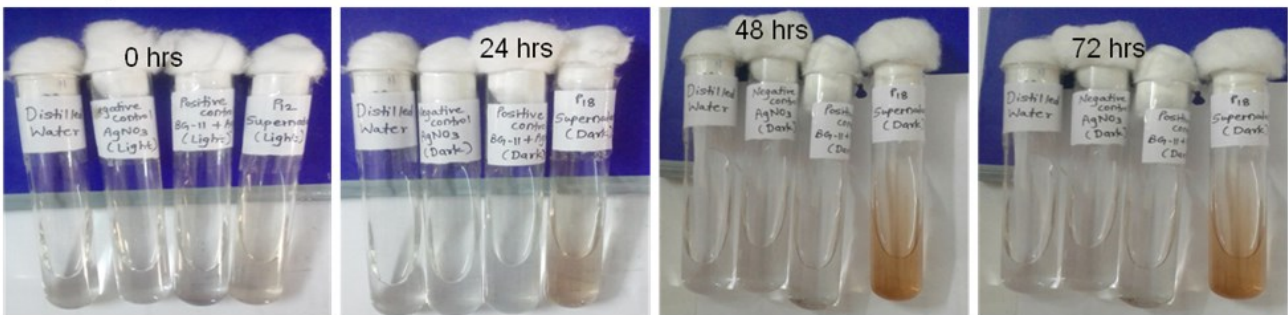


Figure: 2 Biosynthesized silver nanoparticles (formation of brown color) after 0, 24, 48 & 72 hrs incubation

It was observed that the maximum absorbance occurs at 430 nm (Figure 4 a & b). Mubarak *et al.* [15] reported that the extracellular biosynthesis of silver nanoparticles using marine cyanobacterium *Oscillatoria willei* NTDM01 which secreted protein. The silver nitrate solution incubated with washed marine cyanobacterium changed to yellow color indicating the formation of silver nanoparticles and the UV spectra was observed at 430 nm.



Figure: 3 Production and extraction of cyanobacterial silver nanoparticles

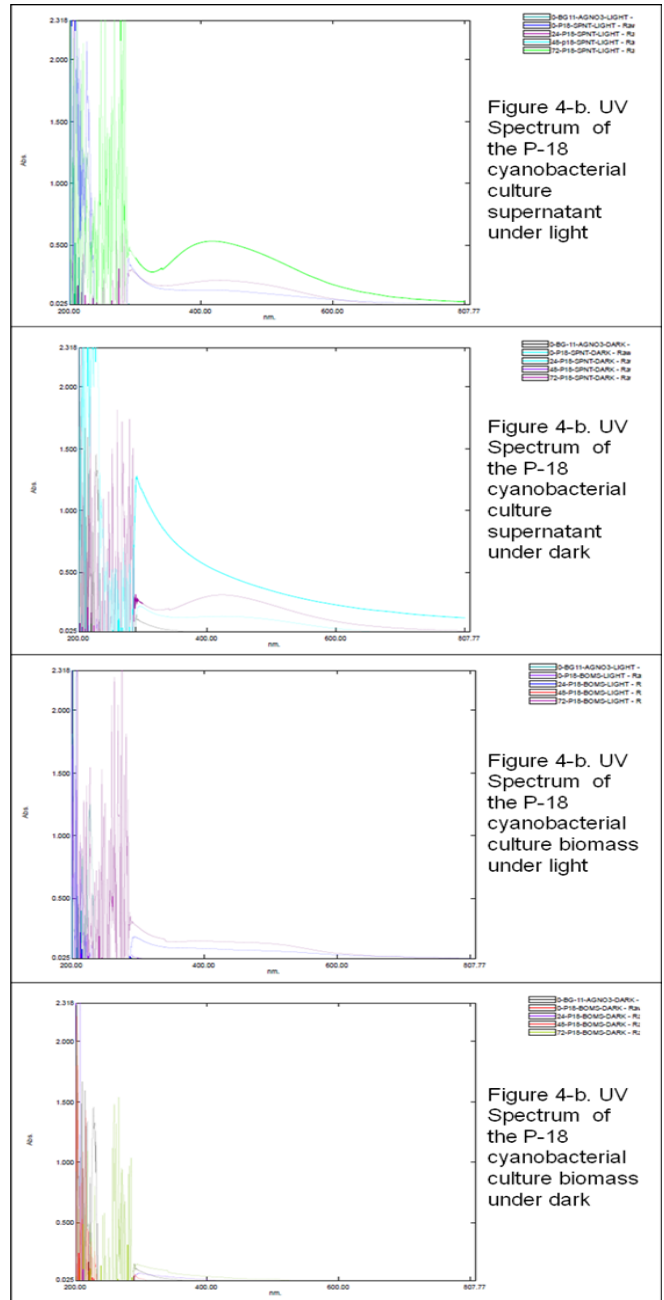
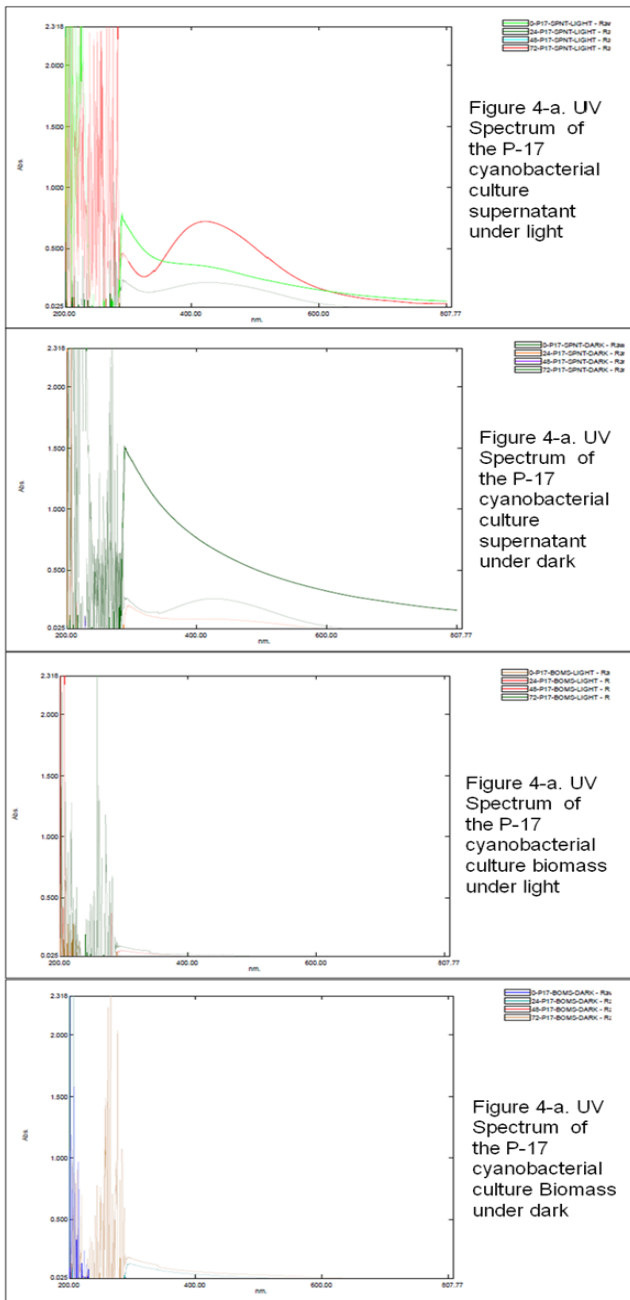


Figure 4 UV Spectrum of the P-17 & P-18 cyanobacterial culture

3.4.2. Fourier Transform Infrared (FTIR) Analysis:

FTIR was used to identify the biomolecules in *Oscillatoria* sp. responsible for the silver ions reduction and stabilization of reduced silver ions. The FTIR Spectrum of the cell free liquid media (Figure 5(A)) shows strong absorption peaks at 3246.34, 1791.29,

1649.21, 1219.06, 1086.93, 78.67 cm^{-1} which represents that the band at 324.34 were assigned to the stretching vibration of amides, 1791.29 represent acyl chlorides, 1649.21 represent alkenes, 1219.06 represent ethers group, 1086.93 represent ethers, 768.67 represent alky halides group.

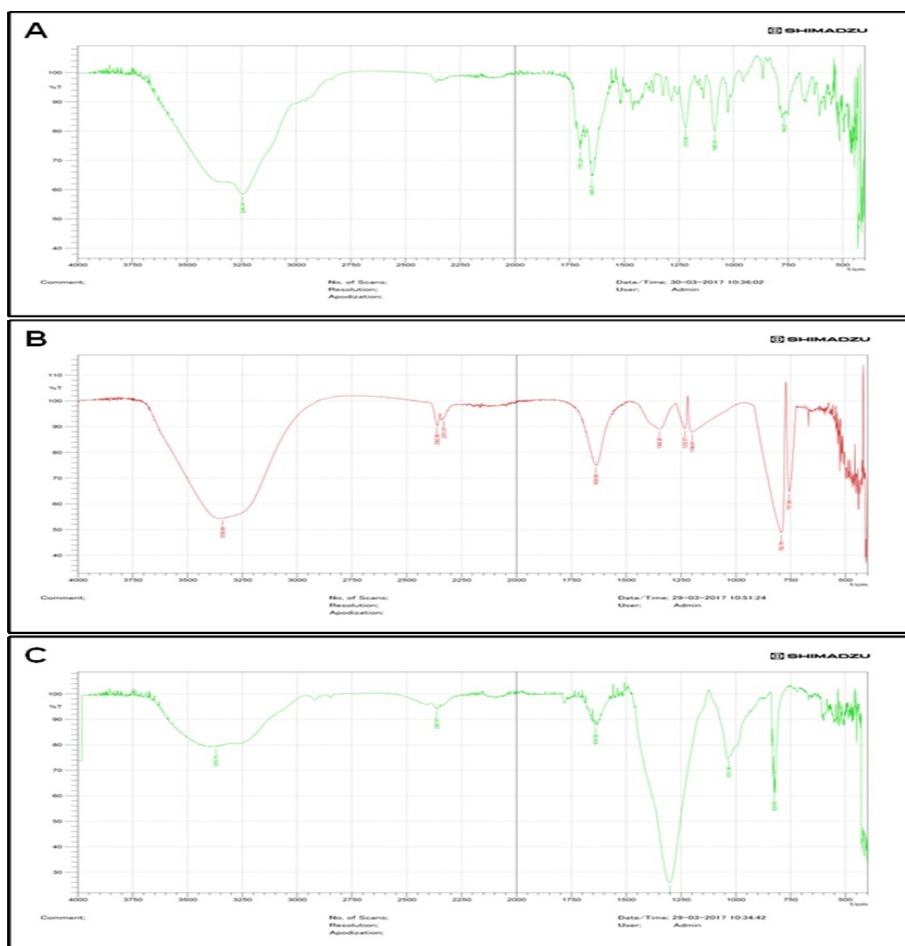


Figure 5 FTIR comparison of cell free liquid media(A), colloidal liquid AgNPs (B) and Powdered AgNPs (C).

Table 1. FTIR comparison of cell free liquid media, colloidal liquid AgNPs and Powdered AgNPs

Liquid media		Colloidal liquid AgNPs		Powdered AgNPs	
Vibration(cm^{-1}) Cell free liq. Media	Functional Group/Name of compound	Vibration(cm^{-1}) AgNPs (Liquid)	Functional Group/Name of compound	Vibration(cm^{-1}) AgNPs (Powder)	Functional Group/name of compound
768.67	R-Cl (Alkyl halides)	757.09	R-Cl (Alkyl halides)	624.60	C-Cl (Alkyl halides)
1086.93	R-O-R' (Ethers)	1198.81	RR'R''C-OH (3°) (Ter. alcohols)	1031.96	Ar-O-R (Ethers)
1219.06	C-O (Carboxylic acids)	1232.57 1349.26	C-O (Acids) N-O(Nitro)	1310	C-O (Acids)
1649.21	R-CH=CH ₂ (Alkenes)	1638.60	C=O (Carboxylic acids)	1639.56	R-C(O)-NR'R'' (Amide)
1791.29	Ar-C(O)-Cl (Acyl chlorides)	2331.07	R-C(O)-OH (Alcohols)	2363.87	R-C(O)-OH (Alcohols)
3246.34	R-C(O)-NH ₂ (Amides)	2362.90 3339.89	R-C≡N (Nitriles) O-H (Alcohols)	3770.75	O-H (Alcohols)

The FTIR spectrum was recorded from the colloidal silver nanoparticles (Figure 5(B), formed after 72 days of incubation with the cyanobacteria. The bands seen at 3339.89 cm^{-1} and 1198.81 cm^{-1} were assigned to the stretching vibrations of primary and tertiary alcohols. The corresponding bending vibrations were seen at 792.98 cm^{-1} respectively. The bands observed at 1349.26 cm^{-1} and 2362.90 and 1838.60 cm^{-1} can be assigned to the primary and secondary amides.

The FTIR spectrum was recorded from the freeze powder of colloidal silver nanoparticles (Figure 5(C), formed after 72 days of incubation with the cyanobacteria. The bands seen at 3770.75 cm^{-1} and 1639.56 cm^{-1} were assigned to the stretching vibrations of primary alcohols, and amides. Whereas frequencies 2363.87 and 1310 , shows $\text{C}=\text{O}$ and $\text{C}-\text{O}$ stretch vibration of carboxylic acid and ether. The overall observation confirms that the presence of protein used in the synthesis of silver nanoparticles, in the cell free liquid culture the protein present contains the free residual groups of alkene and acyl chloride groups' catalyses reduction of silver (Ag^+) ions to colloidal silver nanoparticles. Alkenes, Nitro and Nitrile groups were present in colloidal silver nanoparticles, which were

absent in powdered AgNPs, so it was found that Alkenes, Nitro and Nitriles may get evaporated during the process of evaporation.

3.4.3 Scanning Electron Microscopy

Light microscopy showed that clusters of nanoparticles were attached to the surface of the cyanobacterial filaments. This was confirmed by scanning electron microscopy (SEM) which showed that AgNPs were present and evenly distributed throughout the cell free liquid culture of the AgNO_3 -incubated culture (Figure 6). Elemental analysis by EDS identified those particles indeed as silver not being present in the control culture. At room temperature, the addition of AgNO_3 to the cyanobacteria caused the precipitation of silver nanoparticles at cell surfaces. Small spherical silver nanoparticles with size ranging from 100 nm to 200 nm (extracellular) were also precipitated in solution silver nanoparticles were deposited at cell surfaces. EDS showed the occurrence of silver particle in higher amount with trace of magnesium, calcium and chloride. In this analysis silver nanoparticles was confirmed the presence of elemental silver signal (Figure 7).

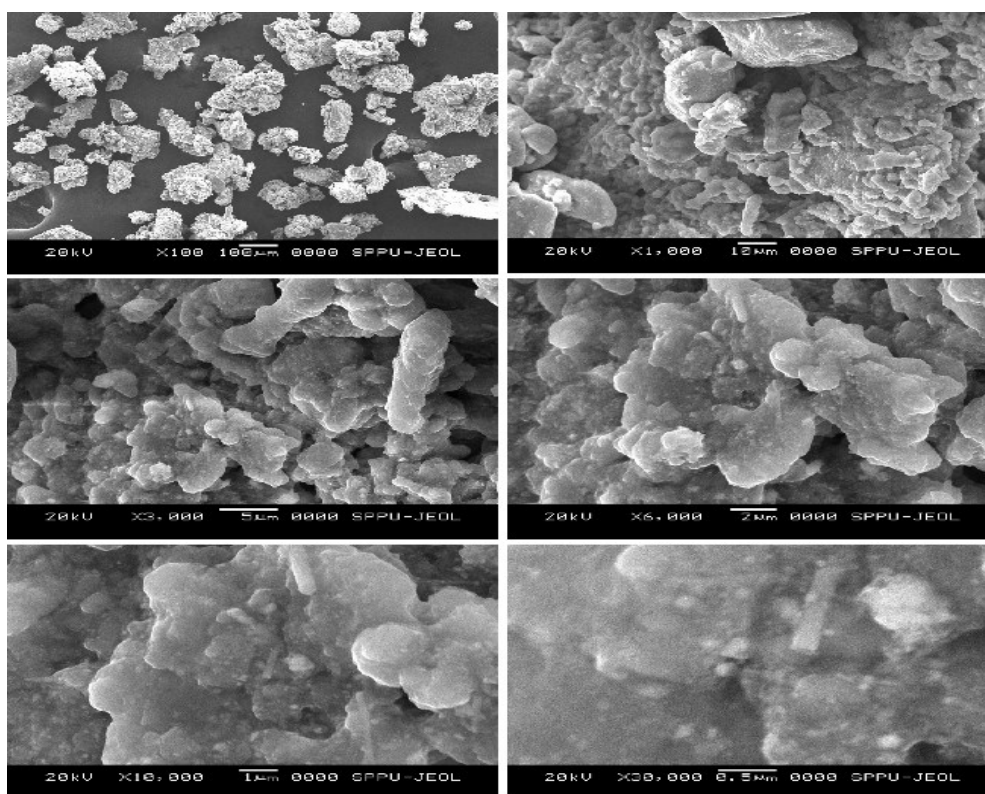


Figure 6 Scanning electron microscopic images of silver nanoparticles.

3.4.4. X-ray diffraction (XRD) analysis

X-ray diffraction (XRD) was carried out to confirm crystalline nature of the particles. X-RD pattern shown in Figure 7 and the XRD data analyzed using Expert Highscore plus software. From XRD data, it was concluded that the mix phase of AgNO₃ and silver nanoparticles is observed. Also it was found that the intense peak was observed for that of silver nitrate. The data is matched to the JCPDS Card No.01-073-1411 for untreated (Residual) silver nitrate.

For silver nanoparticles the peaks are matched to JCPDS Card No.00-004-0783. The "Five" peaks are observed for that of silver nanoparticles at 38.1044, 42.2917, 64.5068, 77.29, 80.75 and the remaining peaks

observed are of residual AgNO₂. It has been shown that biosynthesis of silver Nanoparticles process is not 100% completed due to incomplete oxidation of AgNO₃ and less incubation period. The silver ions were reduced in the presence of nitrate reductase, leading to the formation of a stable silver hydrosol 10-25 nm in diameter and stabilized by the capping peptide [11]. Most probably, the reduction of SNPs occurs due to the presence of cellular reductase released by *Spirulina platensis* into the solution [27]. Also, in cyanobacteria, localized reduce conditions may be produced by a bacterial electron transport chain, via energy generating reactions within the cells [29]. In this respect, secreted cofactor NADH plays an important role [23].

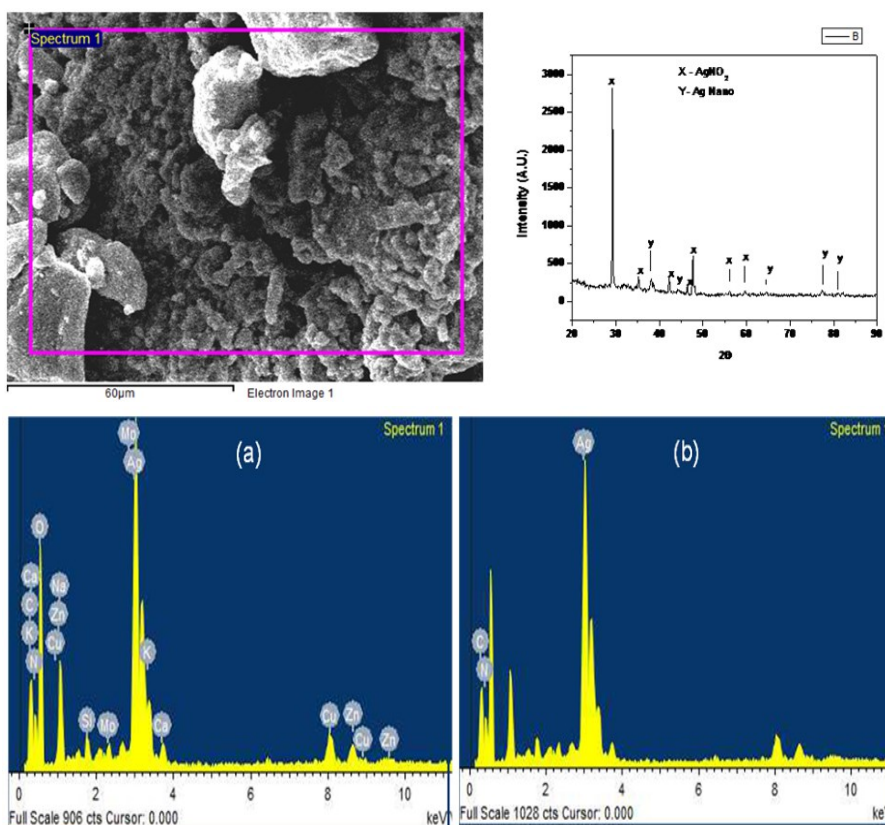


Figure 7 SEM image and EDS with of AgNPs with media (a) and only of AgNPs (b).

Table 2. XRD pattern of silver nanoparticles formed after reaction of culture supernatant with AgNO₃ solution

No.	Pos. [°2Th.]	d-spacing [Å°]	FWHM [°2Th.]
1	29.279	3.05036	0.2952
2	35.2155	2.54856	0.2952
3	38.1044	2.36172	0.3936
4	42.2917	2.13708	0.2952
5	46.4019	1.95691	0.3936
6	47.6759	1.90755	0.2952
7	59.6749	1.5495	0.5904
8	77.3901	1.23213	0.72

Table 3. Antimicrobial activity of silver nanoparticles against test bacteria

Pathogen	Zone of inhibition (mm)	
	Standard antibiotics	Biosynthesized AgNPs
<i>E. coli</i>	10 (Ciprofloxacin)	10
<i>Klebsiella sp</i>	17 (Azithromycin)	13
<i>Salmonella sp</i>	19 (Amphicilin)	14
<i>Pseudomonas sp</i>	18 (Gentamycin)	15



Figure 8 Antimicrobial activity of biosynthesized silver nanoparticles against pathogenic bacteria and zone of inhibition compared with standard antibiotics

Antimicrobial activity of silver nanoparticles:

The antibacterial activity of silver nanoparticles produced by *Oscillatoria sp.* was observed against pathogens, viz., *E. coli*, *Klebsiella sp*, *Salmonella sp*, *Pseudomonas sp.* using disc diffusion method (Figure 8). The antimicrobial activity of silver nanoparticles produced by *Oscillatoria spp.* (P-18) presented in Table 3. The result shows maximum antibacterial effects against *Pseudomonas sp.* (15 mm), *Salmonella sp.* (14 mm), *Klebsiella sp.* (13 mm) and minor antibacterial effect was recorded against *E. coli.* (10 mm) & *E. coli* showed resistance to AgNPs. Sondi and Salopek-Sondi, [17] reported that the silver nanoparticles are used as antimicrobial agents against the gram negative bacteria. Antibacterial activity of biosynthesized AgNPs was evaluated against the *Pseudomonas aeruginosa* and *S. auerus* [26,25].

CONCLUSION

It was concluded that among 20 cyanobacterial isolates *Oscillatoria sp.* was shown to be able to

synthesize Ag-NPs. The active factor involved in nanoparticles formation may be an extracellular molecule, activation of which requires light. In the analysis UV-visible spectrum and SEM the biosynthesis of silver nanoparticles was determined. XRD and FTIR analysis confirms the presence of functional groups of protein used in the synthesis of silver nanoparticles. The bioactivity of the synthesized silver nanoparticles had inhibitory effect on important human pathogens. More research is needed not only to identify the compounds responsible but also for better understanding the mechanism of nanoparticles formation by microalgae. It would be desirable to develop a technology in which the specific size and shape of the particles could be obtained by the use of a specific strain of cyanobacteria.

Acknowledgement:

Authors are thankful to the Principal, Tuljaram Chaturchand College and also to Dr. S. J. Sathe, Head, Department of Microbiology for providing necessary facilities and constant help during the research period.

REFERENCES

1. Pal S. A General Strategy for Nano crystal Synthesis. *Applied and Envi. Microbiology*, 2007;73(6): 1712-1720.
2. Chandrasekharan N and Kamat PV. Improving the photo-electrochemical performance of nanostructured TiO₂ films by adsorption of gold nanoparticles. *Journal of Physical Chemistry B*, 2000;104:10851-10857.
3. Ahmed A, Mukherjee P, Senapati S, Mandal D, Khan MI, Kumar R and Saty M. Extracellular biosynthesis of silver nanoparticles using the fungus *Fusarium oxysporum*. *Colloids Surface B*, 2003, 28, 313-318.
4. Edelstein AS and Cammarata RC. *Nanomaterials synthesis, properties and applications*. Institute of Physics Publications, Bristol and Philadelphia Publishers. 1996.
5. Duran N, Marcato PL and Alves OL. Mechanistic aspects of biosynthesis of silver nanoparticles by several *Fusarium oxysporum* strains. *J. Nanobiote*, 2005;3(8): 1-7.
6. Duran N, De Souza GIH, Alves OL, Esposito E and Marcato PD. Antimicrobial activity of silver nanoparticles synthesized by *Fusarium oxysporum* strain. *J Nanotechnol*, 2003;122-128.
7. Klaus T, Joerger R, Olsson E and Granqvist CG. Silver-based crystalline nanoparticles, microbial fabricated. *Proc. Natl. Acad. Sci. USA*. 1999; 96: 13611-13614.
8. Mahdieh M, Zolanvari A, Azimee AS and Mahdieh M. Green biosynthesis of silver nanoparticles by *Spirulina platensis*. *Scientia Iranica F*, 2012;3:926-929.
9. Sharma VK, Yngard RA and Lin Y. Silver nanoparticles: Green Synthesis and their antimicrobial activities. *Advances in Colloid and Interface Science*, 2009; 145: 83-96.
10. Nair B and Pradeep T. Coalescence of nanoclusters and formation of submicron crystallites assisted by *Lactobacillus* strains. *Cryst. Growth Des.* 2002; 2: 293-298.
11. Mukherjee P, Ahmed A, Mandal D, Senapati S, Sainkar SR, Khan MI, Ramani R, Parischa R, Ajayakumar PV, Alam M, Sastry M and Kumar R. Bioreduction of AuCl₄-ions by the fungus, *Verticillium* sp. And surface trapping of the gold nanoparticles formed. *Angew Chem. Int. Ed.*, 2001; 40: 3585-3588.
12. Mukherjee P, Senapati S, Mandal D, Ahmed A, Khan MI, Kumar R and Sastry M. Extracellular synthesis of gold nanoparticles by the fungus *Fusarium oxysporum*. 2002; 3(3), 461-463.
13. Kumar A, Joshi H, Pasricha R, Mandale AB and Sastry M. Phase transfer of silver nanoparticles from aqueous to organic solutions using fatty amine molecules. *Journal of Colloid and Interface Science*. 2003;264, 396.
14. Mehta SK and Gaur JP. Use of algae for removing heavy metal ions from wastewater: progress and prospects. *Crit Rev Biotechnol*, 2005; 25: 113-152.
15. Mubarak Ali D, Sasikala M, Gunashekharan M and Thajuddin N. Biosynthesis and characterization of silver nanoparticles using marine cyanobacterium, *Oscillatoria willei* NTDM 01. *Digest Journal of Nanomaterials and Biostructures*, 2011;6(2): 385-390.
16. Rai M, Yadav A and Gade A. Silver nanoparticles as a new generation of antimicrobials. *Bio.Ad.* 2009; 27:76-83.
17. Sondi I and Salopek-Sondi B. Silver nanoparticles as antimicrobial agent: A case study of *E. coli* as a model for Gram-negative bacteria. *J. Colloid Inferf. Sci.*, 2004; 2: 75-177.
18. Rippka R, Deruelles J, Waterbury JB, Herdman M and Stanier RY. Generic assignments, Strain histories and properties of pure culture of cyanobacteria. *J. Gen. Microbiol.*, 1979; 111: 1-61.
19. Desikachary TV. *Cyanophyta*, A Monograph. Indian Council of Agricultural Research, New Delhi. 1959
20. Jeevan P, Ramya K and Rena AE. Extracellular Biosynthesis of silver nanoparticles by culture supernatant of *Pseudomonas aeruginosa*. *Indian J. of Biote.*, 2012;11: 72-76.
21. Biradar D, Lingappa K and Dayanand K.. Antibacterial activity of nano gold particles synthesized by *Bacillus* sp. *Journal of Ecobiotechnology*, 2012; 4(1): 43-45.
22. Shankar SS, Rai A, Ahmad A and Sastry M. Rapid synthesis of Au, Ag, and bimetallic Au core Ag shell nanoparticles using Neem (*Azadirachta indica*) leaf broth. *J. Colloid. Interface Sci.*, 2004;275:496-502.
23. Senapati S, Ahmed A, Khan MI, Sastry M and Kumar R. Excellent biosynthesis of bimetallic Au-Ag alloy nanoparticles. *Small*, 2005;1, 517-520.
24. Lengke MF and Southam G. Bioaccumulation of gold by sulfatereducing bacteria cultured in the presence of gold (I)-thiosulfate complex. *Geochem. Cosmochim. Acta*, 2006;70: 3646-3661.
25. Deljou A and Goudarzi S. Green Extracellular Synthesis of the Silver Nanoparticles Using *Thermophilic Bacillus* Sp. AZ1 and its Antimicrobial Activity Against Several Human Pathogenetic Bacteria. *Iran J Biotech*, 2016;14(2), 25-32. DOI:10.15171/ijb.1259
26. Ottoni CA, Simoes MF, Fernandes S, dos Santos, JG, da Silva ES, de Souza RFB and Maiorao AE. Screening of filamentous fungi for antimicrobial silver nanoparticles synthesis. *AMB Express*, 2017;7(31), 1-10.
27. Sudha SS, Karthic R, Francis M, Soumya T and Renga Ramanujam. Isolation and preliminary characterization of associated microorganisms from *Spirulina* products and their silver mediated nanoparticles synthesis. *J. Algal Biomass Utln.*, 2011;2: 1-8.
28. Sudha SS., Rajamanickam K and Ringaramanujan J. Microalgae mediated synthesis of silver nanoparticles and their antibacterial activity against pathogenic bacteria. *Indian J. of Expe. Biology*, 2013;52: 393-399.

Synthesis of ZnO:TiO₂ Nanocomposite Thin Films by Spraypyrolysis

Waghmode JV, Bhosale SE, Shinde TB, Mohite VR and Sapkal RT*

Advanced Materials Laboratory, Department of Physics, T. C. College, Baramati-413102, Pune

E-mail: rt_sapkal.yahoo.co.in

Manuscript Details

Available online on <http://www.irjse.in>

ISSN: 2322-0015

Editor: Dr. Arvind Chavhan

Cite this article as:

Waghmode JV, Bhosale SE, Shinde TB, Mohite VR and Sapkal RT, Synthesis of ZnO:TiO₂ Nanocomposite Thin Films by Spraypyrolysis, *Int. Res. Journal of Science & Engineering*, December 2017; Special Issue A1 : 55-58.

© The Author(s). 2017 Open Access

This article is distributed under the terms of the Creative Commons Attribution 4.0 International License

(<http://creativecommons.org/licenses/by/4.0/>), which permits unrestricted use, distribution, and reproduction in any medium, provided you give appropriate credit to the original author(s) and the source, provide a link to the Creative Commons license, and indicate if changes were made.

ABSTRACT

In present study ZnO: TiO₂ composite thin film was successfully deposited on to glass substrate by using simple chemical spray pyrolysis technique. Effect of ZnO: TiO₂ composite on the prepared thin film has been studied. The structural properties of ZnO: TiO₂ composite thin film has been investigated by X-ray Diffraction (XRD). It is seen that films are polycrystalline and having dominant orientation (002) and (101) for pure ZnO (hexagonal) and TiO₂ (tetragonal) thin films respectively while for coupled films it shows mixture of both phases. It depicts that required phases of respective materials has been achieved. The absorption edge of TiO₂, ZnO and ZnO: TiO₂ films are at around 391, 398 and 414 nm, respectively. The optical energy gap energy is found to be, $E_g = 3.11$ eV, 3.27 eV, and 2.99 eV and which are deduced for ZnO, TiO₂ and ZnO: TiO₂ films respectively.

Keywords: ZnO: TiO₂ Composite; structural properties; films

INTRODUCTION

Nanocomposite films are thin films formed by mixing two or more dissimilar materials having nanodimensional phase(s) in order to control and develop new and improved structures and properties. The properties of nanocomposite films depend not only upon the individual components used but also on the morphology and the interfacial characteristics. unique physical, chemical, optical, mechanical, magnetic and electrical properties

unavailable from that of the component materials and have attracted much attention for a wide range of device applications such as gas sensors. Recently, various nanocomposite films consisting of either metal-metal oxide, mixed metal oxides, polymers mixed with metals or metal oxides, or carbon nanotubes mixed with polymers, metals or metal oxides have been synthesized and investigated for their application as active materials for gas sensors. Design of the nanocomposite films for gas sensor applications needs the considerations of many factors, for example, the surface area, interfacial characteristics, electrical conductivity, nanocrystallite size, surface and inter-facial energy, stress and strain, etc., all of which depend significantly on the material selection, deposition methods and deposition process parameters.

In recent years, the photocatalytic degradation of various kinds of organic and inorganic pollutants using semiconductors as photocatalysts has been widely studied [4-7]. Among these semiconductors, TiO_2 has been extensively investigated as the most promising photocatalyst due to its high photocatalytic activity, non-toxicity, high photochemical stability, and low-cost. However, it divulged some drawbacks. For example, TiO_2 (band gap 3.2 eV corresponds to 388 nm) can only absorb the UV region (only about 4%) of the solar radiation, whereas solar spectrum has about 40% visible region (400 to 700 nm), and it shows high recombination rate of photo-induced electron-hole pairs which may affect negatively the degradation ratio and rate [8]. In order to make TiO_2 suitable for receiving solar energy efficiently in a wide range from UV to visible, many methods such as dye sensitization, metal- or nonmetal-doped TiO_2 - based nanoparticles, and modification of TiO_2 by the addition of another metal oxide-based semiconductor have been used. It has been shown that coupled semiconductors seem to be simple and viable photocatalysts. Photocatalytic process is based on the generation of electron-hole pairs by means of band-gap radiation that can give rise to redox reactions with the species adsorbed on the surface of the photocatalysts. In principle, the coupling of different semiconductor oxides seems useful in order to absorb a wide range of solar radiation and to achieve a more efficient electron-hole pair separation, and consequently, a higher photocatalytic activity will be attained [9].

Various composites formed by TiO_2 and other inorganic oxides such as ZnO [10], SnO_2 [11], SiO_2 [12], In_2O_3 [13], Cu_2O [14], MgO [15], WO_3 [16], MoO_3 [17], and so on have been reported.

ZnO is a suitable alternative to TiO_2 because its photodegradation mechanism has been proven to be similar to that of TiO_2 . In fact, in comparison to TiO_2 , ZnO has been reported to have higher photocatalytic efficiency [18,19]. ZnO can absorb over a larger fraction of UV radiation, and the corresponding threshold of ZnO is 425 nm [20]. Therefore, nanocomposites of ZnO/TiO_2 thin films can be used as photocatalysts to degrade/ decolorize organic dyes under solar irradiation in aqueous system.

In present investigation composite thin film of $\text{ZnO}:\text{TiO}_2$ have been deposited using spray pyrolysis technique. The structural and optical properties of deposited thin films were studied

METHODOLOGY

Undoped ZnO , TiO_2 and $\text{ZnO}-\text{TiO}_2$ composite films will be deposited by spraying zinc acetate in alcoholic solution. The films will be prepared at different parameters like solvent for deposition, substrate temperature, concentrations of dopants in the spraying solution, total quantity of spraying solution, spray rate etc. To yield good quality films in terms of transparency and conductivity. $\text{ZnO}:\text{TiO}_2$ were deposited at different composition, viz 90ml:10ml, 80ml: 20ml, 70ml: 30ml, 50ml: 50ml. To obtain ZnO Zinc acetate (CH_3COO)₂ \cdot 2 H_2O (0.2M) dissolve in 35 ml of distilled water, 65ml of (CH_3OH) and 5ml (CH_3COOH) is used. Substrate was heated towards the temperature on which films was deposited at 400°C. The substrate to nozzle distance was maintained at 31cm. The time required to spray this solution is 11:45sec. To obtain TiO_2 (TAA) Titanium Acetyl Acetate (0.1M) dissolve in methanol. Substrate was heated towards the temperature on which films were deposited about 480°C. The time required to spray this solution is 13:21sec. The XRD study has been performed for identification of the crystal structure of $\text{ZnO}:\text{TiO}_2$. The Transmittance was measured by UV-Vis-NIR Spectrometer.

RESULT AND DISCUSSION

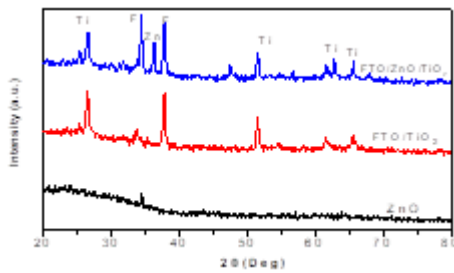


Fig.1. X-ray diffraction patterns of ZnO, TiO₂ and ZnO: TiO₂ thin films

Crystalline development of the thin films using X-ray diffraction analyzer ZnO normally forms the hexagonal (Wurtzite) structure with lattice constant ($a=b=0.32$ nm and $c=0.52$ nm). Each Zn atom is tetrahedrally co-ordinated to four O atoms. The structural characterization of the sample was carried out by powder X-ray diffraction method performed on X-ray diffractometer Fig.1 shows the XRD patterns of ZnO and ZnO/TiO₂ thin films. The entire ZnO thin films show only one diffraction peak which corresponds to the diffraction of (002) plane of ZnO with a hexagonal wurtzite structure. The diffraction peak can also be well indexed to the hexagonal phase ZnO reported in JCPDS card (No. 36-1451, $a = 0.3249$ nm, $c = 0.5206$ nm). The results indicate that the products consisted of a pure phase. This means all the ZnO thin films deposited on the glass or TiO₂ layered substrates are preferentially oriented along the c-axis perpendicular to the substrate surface. For the sample A and B their (002) peaks lie at 34.340. From the above data, it is clear that the (002) peak positions of ZnO/TiO₂ thin films are closer to the (101) peak position of ZnO powder. According to the order of sample A and B, the intensity of their (002) peaks gradually increases in sequence, but the full width at half maximum (FWHM) of the peaks gradually decreases [4,5]. It means the crystalline quality of ZnO thin films is improved after TiO₂ layers are used. The average crystallite sizes of the ZnO thin films can be calculated with Scherrer formula using parameters derived from XRD patterns. Scherrer formula is as follows:

$$D = 0.9\lambda / \beta \cos\theta$$

Where D is the crystallite size, λ is the X-ray wavelength, β is the FWHM and θ is the diffraction angle. As regards the sample B, there is not only the

(002) peaks of ZnO thin films but also two peaks of TiO₂ layers in the patterns. One of them corresponds to the (200) diffraction peak (48.30°) of anatase phase, another corresponds to the (211) peak (56.05°) of rutile phase. But the main components of TiO₂ layer are anatase structured crystals.

Optical properties:

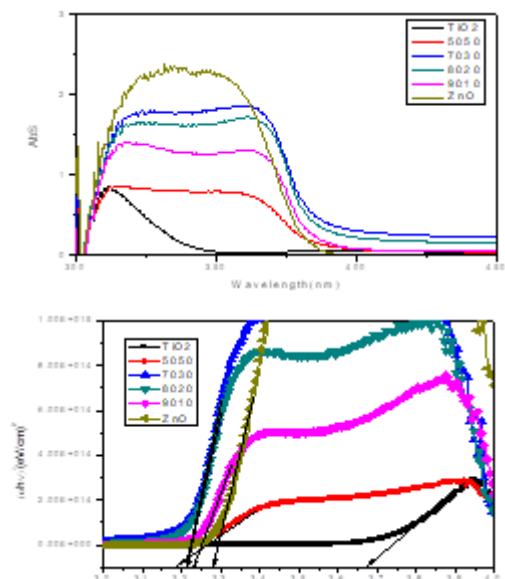
The absorption coefficient (α) has been determined as a function of wavelength from measured reflectance, R and transmittance, T , using following equation,

$$\alpha = 1/d \ln [(1-R)^2 / T]$$

Where d is the thickness of thin film, R and T the reflection and transmission, respectively. In high absorption region close to the beginning of band-to-band optical transmission, the absorption is characterized by the following relation,

$$\alpha = A (h\nu - E_{opt})^r$$

Where A is a constant, E_{opt} the optical band gap and r is the integer number which characterizes the transmission process.



The usual method for determining the values of E_{opt} involves plotting a graph of $(\alpha h\nu)^r$ vs $h\nu$. The optical energy gap, $E_g = 3.11$ eV, 3.27 eV, and 2.99 eV are deduced for ZnO, TiO₂ and ZnO: TiO₂ films respectively. The absorption edge of TiO₂, ZnO and ZnO: TiO₂ films are at around 391, 398 and 414 nm, respectively and similar results are reported by Zhang et al. The significant red-shift with lower band energy of ZnO: TiO₂ film comparing with the ZnO film and TiO₂ film may be owing to the differences in the surface state. The ZnO: TiO₂ film need lower energy to

be excited than the ZnO film and TiO₂ film. The reflectance of the films is shown in Fig. and inset shows transmittance. Transmittance is decreases from ZnO, TiO₂ to ZnO: TiO₂. The TiO₂, ZnO and ZnO: TiO₂ film shows about 30 %, 8 % and 2 % reflection respectively in visible region.

CONCLUSION

Composite of ZnO: TiO₂ thin film was deposited by a spray pyrolysis technique. The films were deposited onto glass as well as on FTO substrate at the selected temperature 450^o C, 480^o C respectively. The films has good optical quality properties and are well-suited for Solar Cell application. The optical energy gap, E_g = 3.26 eV, and 3.66 eV are deduced for ZnO, TiO₂ films respectively. The significant red-shift with lower band energy of ZnO: TiO₂ film comparing with the ZnO film and TiO₂ film may be owing to the differences in the surface state. The ZnO: TiO₂ film need lower energy to be excited than the ZnO film and TiO₂ film. It is seen that films are polycrystalline and having dominant orientation (002) and (101) for pure ZnO (hexagonal) and TiO₂ (tetragonal) thin films respectively while for coupled films it shows mixture of both phases. XRD depicts that required phases of respective materials has been achieved.

REFERENCES

- Galindo C, Jacques P, Kalt A: Photochemical and photocatalytic degradation of an indigoid dye: a case study of acid blue 74 (AB74). *J. Photochem. Photobiol. A: Chem.* 2001;141:47-56.
- Gong RM, Li M, Yang C, Sun YZ, Chen, J: Removal of cationic dyes from aqueous solution by adsorption on peanut hull. *J. Hazard. Mater. B* 2005;121: 247-250.
- Moza S, Tomaszewska M, Kosowska B, Grzmil B, Morawski AW, Kalucki K. : Decomposition of nonionic surfactant on a nitrogen-doped photocatalyst under visible-light irradiation. *Appl. Catal. B: Environ.* 2005; 55: 195-200.
- Hoffmann MR, Martin ST, Choi WY, Bahnemann DW: Environmental applications of semiconductor photocatalysis. *Chem Rev* 1995;95: 69-96.
- Mahmood AJ, Islam MS: ZnO mediated degradation of Brilliant Orange by visible light. *J. Bangladesh Chem. Soc.* 2003;16, 35-46.
- Mahmood AJ, Jabbar MA, Akhtar S: Influence of light on the degradation of a dye in homogeneous and heterogeneous media. *J. Bangladesh Chem. Soc.* 2003;16: 57-70.
- Habib MA, Ismail IMI, Mahmood AJ, Ullah, MR: Photocatalytic decolorization of Brilliant Golden Yellow in TiO₂ and ZnO suspensions. *J. Saudi Chem. Soc.* 2012;16:423-429.
- Aramendia MA, Borau V, Colmenares JC, Marinas A, Marinas JM, Navio JA, Urbano, FJ: Modification of the photocatalytic activity of Pd/TiO₂ and Zn/TiO₂ systems through different oxidative and reductive calcinations treatments. *Appl. Catal. B: Environ.* 2008;80, :88-97.
- Wang C, Xu, BQ, Wang, XM, Zhao, JC: Preparation and photocatalytic activity of ZnO/TiO₂/SnO₂ mixture. *J. Solid State Chem.* 2005;178: 3500-3506
- Marcí G, Augugliaro V, López-Munoz MJ, Martín C, Palmisano L, Rives V: Preparation, characterization and photocatalytic activity of polycrystalline ZnO/ TiO₂ systems. 2. Surface, bulk characterization, 4-nitrophenol photodegradation in liquid-solid regime. *J Phys Chem B* 2001;105: 1033-1040.
- Yang J, Li D, Wang X, Yang XJ, Lu LD: Rapid synthesis of nanocrystalline TiO₂/SnO₂ binary oxides and their photoinduced decomposition of Methyl Orange. *J. Solid State Chem.* 2002;165:193-198.
- Hu C, TangYC, Yu, JC, Wong PK: Photocatalytic degradation of Cationic Blue X-GRL adsorbed on TiO₂/SiO₂ photocatalyst. *Appl. Catal. B: Environ.* 2003;40:131-140.
- Shchukin D, Poznyak S, Kulak A, Pichat P: TiO₂-In₂O₃ photocatalysts: preparation, characterizations and activity for 2-chlorophenol degradation in water. *J. Photochem. Photobiol. A: Chem.* 2004;162:423-430.
- Li JL, Liu L, Yu Y, Tang YW, Li HL, Du FP: Preparation of highly photocatalytic active nano-size TiO₂-Cu₂O particle composites with a novel electrochemical method. *Electrochem Commun* 2004;6:940-943.
- Bandara J, Hadapangoda CC, Jayasekera WG: TiO₂/MgO composite photocatalyst: the role of MgO in photoinduced charge carrier separation. *Appl. Catal. B: Environ.* 2004;50: 83-88.
- Li XZ, Li FB, Yang CL, Ge WK: Photocatalytic activity of WO_x-TiO₂ under visible light irradiation. *J. Photochem. Photobiol. A Chem.* 2001;141: 209-217
- Takahashi YK, Ngaotranwiwat P, Tatsuma T: Energy storage TiO₂-MoO₃ photocatalysts. *Electrochim Acta.* 2005;49: 2025-2029.
- Gouvea K, Wypych F, Moraes SG, Duran N, Nagata N, Zamora PP: Semiconductor-assisted photocatalytic degradation of reactive dyes in aqueous solution. *Chemosphere* 2000;40: 433-440.
- Dindar S, Icli J: Unusual photoreactivity of zinc oxide irradiated by concentrated sunlight. *J. Photochem. Photobiol. A: Chem.* 2001; 140: 263-268.
- Behnajady MA, Modirshahla N, Hamzavi R: Kinetic study on photocatalytic degradation of C.I. Acid Yellow 23 by ZnO photocatalyst. *J. Hazard. Mater. B.* 2006;133: 226-232.

Nanomaterial applications as radiosensitizer in radiation therapy for cancer treatment

Singh Lalit Mohan¹, Singh KY¹ and Kumar Dinesh²

¹Department of Physics, B.S.A. College, Mathura -281004, ²Delhi State Cancer Institute, Dilshad Garden, New Delhi-110095

Email: drkysingh@gmail.com | Mob.+ 91-9412446831.

Manuscript Details

Available online on <http://www.irjse.in>
ISSN: 2322-0015

Editor: Dr. Arvind Chavhan

Cite this article as:

Singh Lalit Mohan, Singh KY and Kumar Dinesh. Nanomaterial applications as radiosensitizer in radiation therapy for cancer treatment, *Int. Res. Journal of Science & Engineering*, December 2017; Special Issue A1 : 59-63.

© The Author(s). 2017 Open Access

This article is distributed under the terms of the Creative Commons Attribution 4.0 International License

(<http://creativecommons.org/licenses/by/4.0/>), which permits unrestricted use, distribution, and reproduction in any medium, provided you give appropriate credit to the original author(s) and the source, provide a link to the Creative Commons license, and indicate if changes were made.

ABSTRACT

Treatment of cancer is done with three mode- Surgery, radiation therapy and chemotherapy. Preference of application depends on clinical indications. Among all three modalities, use of radiation therapy and combined with other modalities is popular due to its vast coverage area as well as effective marginal consideration for microscopic level. Nanomaterial's have unique properties such as enhanced permeability, superparamagnetism and retention effect which are well appropriate for application in radiation oncology. Radiosensitizer, a drug that makes tumor cells more sensitive to radiation with greater tumor inactivation. Nanoparticle enhances the effect of radiation by generating reactive oxygen species (ROS) or influence cell cycle. Nanomaterial's also have in diminishing the intercurrent damage caused by radiotherapy of malignant tumors. To make the tumors highly radiosensitive which are relatively resistive to radiation and to improve the therapeutic ratio of radiotherapy for better dose distribution for cancer treatment using nanomaterial, a review is carried out. A summary of application of nanomaterial's as radiosensitizers useful for radiation therapy modality for cancer treatment has been studies. Detail results and conclusion obtain from this study will discuss on during conference.

Key Words: Cancer, Radiosensitizers, Nanomaterial's, Radiotherapy.

INTRODUCTION

Radiation therapy as an important modality for treatment of cancer which uses high energy radiation to shrink tumors and kill cancer cells. Mainly X-rays, gamma rays, and charged particles are types of radiation which is used for cancer treatment. Application of physics using Biology gives the evaluation of a new field era known as Medical Physics. Therapeutic approach of Ionizing radiation generate various DNA damage and leads to radiation-induced cell death at target locations of lesions. Since cancer cells divide in an unregulated manner, they are more susceptible and prone to radiation-induced DNA damage (1-4). Cancer cells whose DNA is damaged beyond repair stop dividing or die. Today, more than 60% of cancer patients receive radiotherapy during their anti-cancer treatment (5), which is applied through various techniques, including external beam (electrons, protons, photons) and brachytherapy (internal therapy). Its mode of application depends on the clinical indications. Radioisotopes (radionuclide) emits energy from the nucleus and generates ionized atoms and free radicals to induce single strand cleavages in DNA. Radioisotopes applied in the clinical oncology include beta-emitters, like ^{186}Re , ^{188}Re , ^{166}Ho , ^{89}Sr , ^{32}P , and ^{90}Y , as well as alpha-emitters, like ^{225}Ac , ^{211}At , and ^{213}Bi (6). When used in vivo, beta-emitters have profound tissue penetration (20–130 mm) but low linear energy transfer, whereas alpha-emitters have limited penetration (50–80 μm) but a short half-life and the ability to inflict more damage to the cells. There are different type mechanisms which show the elimination of radioisotopes in human body.

Dependence of whose basis on half-life and properties of radioisotope. Many of the radioisotopes undergo rapid clearance by the kidney. In particular, renal clearance is size dependent, for which size smaller than 5 nm will be excreted rapidly. Radioisotopes having molecular size suffer short circulation time in blood and are unable to achieve therapeutic effect. Another possible elimination process of the radioisotopes is by opsonization, by which a pathogen is marked for ingestion and eliminated by a phagocyte. However, through loading or conjugating of the nanocarriers, radioisotopes are able to escape from these biological elimination mechanisms. For example, the

physical half-life of ^{89}Sr is 50.5 days, but it is cleared from plasma with an average half-life of 47 h. Nanoparticles such as liposomes, micelles, or polymeric complex are usually more than 10 nm, which greatly decreases the renal clearance and increases their half-life in blood due to the distinct pharmacokinetic properties and the increased size effect (7-9). Also, the nanocarriers can prevent opsonization through PEGylation. The presence of polyethylene glycol (PEG) on the surface of nanoparticles produces steric hindrance, which prevents the adsorption of opsonins. This particular characteristic of nanocarriers helps prolong the half-life of radiotherapeutic agents in blood. In a tumor-bearing mice model, the half-lives of ^{111}In - and ^{177}Lu - PEGylated liposomes in blood were 10.2 and 11.5 h, respectively; whereas the half-life of ^{111}In -DTPA in blood was extremely short as no longer than 2 hour (10).

In addition to the enhancement of circulatory half-life by the nanoparticles, the abnormal vasculatures in tumor may also help to extend the retention time of radiotherapeutics through the EPR effect. The abnormal tumor vasculatures possess aberrant branching components and leaky arterial walls, resulting from rapid proliferation of endothelial cells and a decrease in the number of pericytes. These abnormal vessels allow macromolecules, like nanoparticles, to easily penetrate the tumor via the circulatory system. Since the quick proliferation of tumor cells disrupts lymphatic vessels and makes them inefficient in drainage, the macromolecules that successfully perforate the tumor will be conserved inside the tumor with enhanced retention time. This is a perfect example of the EPR effect and also becoming a golden standard in drug delivery (11-12). For instance, Doxil, a PEGylated liposomal formulation of doxorubicin, is a nano-drug approved by Food and Drug Administration (FDA), showing a much slower clearance rate as 0.1 L/h compared with 45 L/h for free doxorubicin. Its AUC after a dose of 50 mg/m² is approximately 300-fold greater than that with free drug. Furthermore, considerable levels of doxorubicin are detected in both tumor cells and tumor interstitial fluids after Doxil administration. Moreover, the peak of drug concentration in tumors appears between 3 and 7 days post administration of Doxil, which reveals a much longer exposure time and a more enhanced concentration in

tumors than that after the administration of free doxorubicin (13).

Radioisotope-labeled nanoparticles have been developed to increase tumor accumulation and reduce undesired biodistribution. Li et al. applied the beta-emitter ^{64}Cu -labeled copper sulfide nanoparticles to suppress breast cancer. More than 90% of the nanoparticles were restricted in the tumor 24 h after the intratumoral injection. This radioisotope-labeled nanoparticle showed no obvious side effect, and once combined with photodynamic therapy, it helped to prolong the survival time of 4T1 bearing mice to 7.6 times longer than the control group and further reduced lung metastasis as well. Another example involved 50-nm lipid nanocapsules loaded with a lipophilic complex of ^{188}Re for internal radiotherapy of glioblastoma. The nanocapsules ensured maximum distribution of ^{188}Re within the brain 96 h after injection, compared with the solution of ^{188}Re -perrhenate. Therefore, it led to a noteworthy survival advantage in rat glioma models. Synthesized generation five dendrimers with NHAc-HPAO-PEG-FA and conjugated it with ^{131}I . Due to the modified folate ligand, the radioactive ^{131}I -labeled multifunctional dendrimers can be applied for single-photon emission computed tomography (SPECT) imaging and radiotherapy. The in vivo experiments demonstrated that the relative C6 xenografted tumor volume was only 8.78 times larger than the original one after 21 days, compared with 26.56 times for the control group (14).

Improving radiosensitizer delivery through nanomedicine

Nanoparticles application of known radiosensitizers can improve the delivery of these agents to tumor sites. For example, wortmannin is an inhibitor of phosphatidylinositol 3' kinases and phosphatidylinositol 3' kinase-related kinases such as DNA-dependent protein kinases. Preclinical results have shown that it is an effective radiosensitizer. However, its clinical application is limited due to less soluble ability, low stability, and high toxicity. The nanoradiosensitizer was demonstrated to be more effective than 5-FU on mice bearing KB cell xenografts and its MTD was three to five times greater than that of wortmannin (15). The same strategy was also used for DNA double-strand repair inhibitors, such as histone

deacetylase inhibitor, which is an effective radiosensitizer to a variety of solid malignancies such as colorectal cancer and prostate cancer. The inhibitor enhances the response of tumor cells to radiation through the prolongation of $\gamma\text{-H2AX}$ foci. However, it is inefficient at sustaining inhibition of DNA repair and highly toxic. Through encapsulation of nanoparticles, the inhibitors were released controllably for a durable effect. Conjointly, the radiosensitizers in the nano-formulation accumulated in tumors and had low distribution in normal tissue (16).

In addition to the use of drug-loaded polymeric nanoparticles as radiosensitizers, some nanomaterials with high atomic numbers (Z) also have the potential to become radiosensitizers because the dose absorbed by any tissue is related to the Z^2 of the material. For example, gold ($Z = 79$) nanoparticles are the most broadly used high Z nanomaterials for radiosensitizers. Xie et al. reported the application of ultrasmall glutathione-coated $\text{Au}_{29-43}(\text{SG})_{27-37}$ nanoclusters as radiosensitizers. The nanosensitizers had high tumor uptake of about 8.1% ID/g at 24-h post injection. The inhibition of tumor by irradiation was significantly improved when the gold nanoclusters were administered. Meanwhile, the damage to normal tissues was negligible. Gadolinium ($Z = 64$)-based nanoparticles are another type of commonly used radiosensitizers. In one study, Gd-based nanoparticles were used, with 250 kV photon irradiation, to kill SQ20B cells for increased DNA breaks and shortened G2/M phase blockage. In a SQ20B tumor-bearing mouse model, combining the Gd-based nanoparticles with 10 Gy irradiation led to significant delay of tumor growth. Shi et al. designed a rattle nanoparticle with an up conversion nanoparticle core and a hollow silica shell as radiation dose amplifiers. A hypoxia-activated prodrug, tirapazamine, was loaded to overcome the oxygen dependent radiotherapy. The rattle nanoparticles had low cytotoxicity and high in vivo histocompatibility. As radiosensitizers, the up conversion nanoparticles showed significant suppression of tumor growth. In junction with tirapazamine, they were capable of killing hypoxic tumor cells through synergetic effects. Other inorganic nanoparticles like Y_2O_3 or ZnFe_2O_3 are undergoing investigations for their potential in radiotherapy (17-18).

Reduction of side effects through nanomedicine:

Side effects of radiosensitizers can be reduced by decreasing distribution of radiosensitizers or radioisotopes in normal tissues and by controlling the release of these radiotherapeutic agents (19). The side effects of radiotherapy are often caused by unexpected damage to normal tissue. By using radiosensitizers, there are additive and synergistic advantages to the tumoricidal effect of radiation. Therefore, application of nanoparticle as radiosensitizer will allow less doses of radiation to achieve the same efficiency of killing cancer cells. However, the unspecific biologically distribution of radiosensitizers will lead to toxicity to normal tissues. Similarly, to radioisotopes, whose accumulation in normal tissues will cause direct injury. Nanoparticles were shown to have less penetration to normal vasculature and capillaries in various parts of the body, such as the skin, lung, and heart (20). Therefore, controlled and sustained release of nanoparticles into the tissue prolonged exposure to the agents, which is associated with a better effect and higher tolerance for normal tissues. This was demonstrated with the clinical use of Doxil, which dramatically reduced the cardiotoxicity of doxorubicin, without compromising its anti-tumor effect. Moreover, through chemical binding between nanoparticles and radiotherapeutic agents, the release can only occur under certain circumstances. It can either respond to the tumor microenvironment such as a low pH, redox or enzymes; or respond to an external stimuli's like temperature change or a magnetic field. Such strategies dramatically decrease the release of the agents in blood vessels or normal tissues, thereby potentially limiting the side effects (21).

Application of nanotechnology with combination of other therapies:

The combination of chemotherapy and radiotherapy is one of the most effective ways to improve clinical treatment of locally advanced cancers. The concept was proposed after the discovery of fluorouracil. The concurrent chemoradiotherapy outperforms sequential therapies because chemotherapy sensitizes the tumor cells to radiation-induced killing and treatment; meanwhile the concurrent therapy avoids the repopulation of cancer cells which will occur during the course of sequential treatment (22). However, the increased toxicity, which is the price to pay for the

synergism, becomes the main shortcoming of the strategy and is the limiting factor in its application in clinical trials.

Use of nanomedicine in radiation Oncology, radiation therapy uses radioactive substances, such as radioactive iodine, that travel in the blood to kill cancer cells.

Nanoparticles can increase radio sensitivity of tumor cells. This effect was shown in vivo and in vitro, at kilovoltage or megavoltage energies, in reviewed studies. Focus of studies was on gold nanoparticles. Radio sensitizing effects of nanoparticles depend on nanoparticles' size, type, concentration, intracellular localization, used irradiation energy and tested cell line (23)

CONCLUSION

This study shows that use of nanomaterials is increasing day by day in nanomedicine. In future, demand of nanoapplication as radiosensitizer will definitely increase in the field of radiation treatment for cancer.

Acknowledgements

Authors are thankful to Dr. Bindu Shekhar Sharma, Dr B.R.A. University, Agra for their valuable suggestions gratefully acknowledged.

REFERENCES

1. Rajamanickam B. Biological response of cancer cells to radiation treatment, 2014:1-24
2. Radiation Biology: A Handbook for Teachers and Students, Training Courses Series 42, 2010 p.29 & 33, IAEA-TCS-42
3. Yu Mi Application of nanotechnology to cancer radiotherapy *Cancer Nanotechnol.* 2016; 7(1): 11.
4. Baskar R, Lee KA, Yeo R, Yeoh KW. Cancer and radiation therapy: current advances and future directions. *Int J Med Sci.* ; 2012;9(3):193-199.
5. Schae D, McBride WH. Opportunities and challenges of radiotherapy for treating cancer. *Nat. Rev. Clin. Oncol.* ;2015;12(9):527-540.

6. Hamoudeh M, Kamleh MA, Diab R, Fessi H. Radionuclides delivery systems for nuclear imaging and radiotherapy of cancer. *Adv Drug Deliv* 2008;Rev 60(12):1329-1346.
7. Brigger I, Dubernet C, Couvreur P. Nanoparticles in cancer therapy and diagnosis. *Adv Drug Deliv* 2002;Rev;54(5):631-51.
8. Davis ME, Chen ZG, Shin DM. Nanoparticle therapeutics: an emerging treatment modality for cancer. *Nat Rev Drug Discov*. 2008;7(9):771-82.doi:10.1038/nrd2614.
9. Kim BY, Rutka JT, Chan WC. Nanomedicine. *N Engl J Med*. 2010;363(25):2434-43.
10. Wang HE, Yu HM, Lu YC, Heish NN, Tseng YL, Huang KL, Deng WP. Internal radiotherapy and dosimetric study for ¹¹¹In/¹⁷⁷Lu-pegylated liposomes conjugates in tumor-bearing mice. *NuclInstrum Methods Phys Res* 2006; Sect A; 569(2):533-7.
11. Fang J, Nakamura H, Maeda H, The EPR effect: unique features of tumor blood vessels for drug delivery, factors involved, and limitations and augmentation of the effect. *Adv Drug Deliv Rev*. 2011; 63(3):136-51.
12. Maeda H, Wu J, Sawa T, Matsumura Y, Hori K. Tumor vascular permeability and the EPR effect in macromolecular therapeutics: a review. *J Control Release*; 2000;65(1-2):271-84.
13. Barenholz Y, the first FDA-approved nano-drug: lessons learned. *J Control*. 2012;160(2):117-34.
14. Zhou M, Zhao J, Tian M, Song S, Zhang R, Gupta S, Li C Radio-photothermal therapy mediated by a single compartment nanoparticle depletes tumor initiating cells and reduces lung metastasis in the orthotopic 4T1 breast tumor model. *Nanoscale*. 2015;7(46):19438-47.
15. Karve S, Werner ME, Sukumar R, Cummings ND, Copp JA, Wang EC, Wang AZ. Revival of the abandoned therapeutic wortmannin by nanoparticle drug delivery. *PNAS USA*.2012; 109(21):8230-8235.
16. Tian X, Lara H, Wagner KT, Saripalli S, Hyder SN, Foote M, Wang AZ. Improving DNA double-strand repair inhibitor KU55933 therapeutic index in cancer radiotherapy using nanoparticle drug delivery. *Nanoscale*. 2015; 7(47):20211-20219.
17. Zhang XD, Luo Z, Chen J, Song S, Yuan X, Shen X, Xie J. Ultrasmall glutathione-protected gold nanoclusters as next generation radiotherapy sensitizers with high tumor uptake and high renal clearance. *Sci Rep*. 2015; 5:8669. doi: 10.1038/srep08669.
18. Miladi I, Aloy MT, Armandy E, Mowat P, Kryza D, Magne N, Rodriguez-Lafrasse C. Combining ultrasmall gadolinium-based nanoparticles with photon irradiation overcome radioresistance of head and neck squamous cell carcinoma. *Nanomedicine*. 2015;11(1):247- 257.
19. Torchilin VP. Structure and design of polymeric surfactant-based drug delivery systems. *J Control Release*. ;200173(2-3):137-172.
20. Sanhai WR, Sakamoto JH, Canady R, Ferrari M. Seven challenges for nanomedicine. *Nat Nanotechnol*. 2008 ;3(5):242-244.
21. Paul R. et al. Gold nanoparticles for applications in cancer radiotherapy: Mechanisms and recent advancements *Theranostics*, 2015;(109),84.101
22. Lawrence TS, Haffty BG, Harris JR. Milestones in the use of combined modality radiation therapy and chemotherapy. *J Clin Oncol*. ; (2014) ;32 (12) : 1173.
23. American Society for Radiation Oncology (ASTRO) Media / ASTRO news /Annual-Meeting-Guide-2013/The-future-of-nanotechnology-in-radiation-therapy.

Innovative applications of Nanophase alumina as dehydration catalyst and as humidity sensor

Sali Nitin¹, Gandhe Shrikant¹, Dighe Pradeep¹, Bhoraskar SV^{2*}

¹Department of Electronics Science P. V. P. College Pravaranagar, M.S. India,

²Department of Physics, Savitribai Phule Pune University, Pune-7, M.S. India.

*Corresponding author Email: snitind7@gmail.com

Manuscript Details

Available online on <http://www.irjse.in>

ISSN: 2322-0015

Editor: Dr. Arvind Chavhan

Cite this article as:

Sali Nitin, Gandhe Shrikant, Dighe Pradeep, Bhoraskar SV. Innovative applications of Nanophase alumina as dehydration catalyst and as humidity sensor, *Int. Res. Journal of Science & Engineering*, December 2017; Special Issue A1 : 64-68.

© The Author(s). 2017 Open Access

This article is distributed under the terms of the Creative Commons Attribution 4.0 International License

(<http://creativecommons.org/licenses/by/4.0/>), which permits unrestricted use, distribution, and reproduction in any medium, provided you give appropriate credit to the original author(s) and the source, provide a link to the Creative Commons license, and indicate if changes were made.

ABSTRACT

The nanophase alumina δ -Al₂O₃ powder was synthesized by using the novel DC thermal arc-plasma method. The as-synthesized powder was characterized by using physical techniques viz. X-ray diffraction (XRD), X-ray photoelectron spectroscopy (XPS), energy dispersive X-ray analysis (EDAX), and transmission electron microscopy (TEM). The catalytic behavior and humidity sensing characteristics of nanophase alumina δ -Al₂O₃ pellets were studied. The humidity sensing behaviour of compact nanophase δ -Al₂O₃ pellet was studied by using home-built static gas sensing characterization system. As-synthesized δ -Al₂O₃ particles were found to be spectroscopically phase-pure with δ symmetry, stoichiometric and spherical morphology with sizes in the range of 20-80 nm. Further, humidity sensing behaviour of compact nanophase δ -Al₂O₃ pellets showed the profound effect in capacitance rise with respect to % relative humidity (RH) as compared to the commercial compact and coarse fine grained α -Al₂O₃ pellets. Its catalytic activity was also studied with good results during ethanol dehydration.

Keywords: Catalyst, DC thermal arc plasma route, Nanomaterial, δ -Al₂O₃, Humidity sensor.

INTRODUCTION

There is increased growing interest in synthesis, characterization and applications of innovative nanophase materials [1] due to their vast technological importance.

The nanophase particles [2] which are ultrafine one with high surface energy provides a large surface to volume ratio and large fraction of atoms reside in the grain boundaries. Consequently the grain boundary structure of these materials play a significant role in the novel chemical, electro-mechanical, optical and magnetic properties which are different and improved from their conventional coarser grained counter parts [3] [4].

The humidity sensing is becoming ever more important for agricultural, industrial processes, human comfort and academic interest. We have explored presently the possibility of utilizing the larger surface area and grain boundary structure present in the nanophase powder of aluminum oxide (Al_2O_3 -alumina) for sensing different humidity levels.

Various varieties of ceramic, polymeric and composite sensors are being synthesized, processed and produced to serve these applications. Each of these types of sensors has limitations and new sensor concept continues to emerge. A better efficiency of sensing is expected from these materials compared to their counterpart consisting of coarser grained alumina. Ceramic capacitive air humidity sensors have emerged in increasing numbers [6] [7] [8].

However, a sensor with fine structure alumina has not been studied in detail. A Novel DC Arc plasma method was employed for synthesis of nanocrystalline alumina in the present paper.

METHODOLOGY

In this paper the laboratory made arc plasma reactor consisting of A1-C electrodes system were used in the present experimental setup. The arc was excited across A1-C electrodes by application of 70 V, 50 Amp D.C power supply at an electrode separation of 0.3-0.5 cm in a closed chamber. The fine powder which issued from the arc was deposited onto the inner walls of the reaction process chamber. The powder was gently scrapped after cooling of the interior surface from the roof of the chamber. This powder has shown a white colored appearance. The elemental analysis was carried out by 14 MeV Neutron Activation Analysis (N.A.A.) [5]. D-T reaction was used for

generating 14 MeV neutrons. Aluminum is irradiated with these neutrons to give radioactive Mg^{27} which has the life time of 10 min. and emits γ -rays of energy 0.84 MeV which is detected through detectors to give the amount of aluminum.

The TEM was used to study the topography of the particles using the bright field mode [9]. Through the XPS measurements the purity and stoichiometry were estimated properly.

Catalytic activity of alumina has been utilized in many chemical reactions since a pretty long time. However there are not many reports emphasizing the added advantages of its fine grained nature on the catalytic activity. Here an attempt is made in this direction and the ethanol dehydration reaction in presence of our as synthesized nanophase alumina and vis-a-vis coarse grained alumina was studied. The present work concerned with use of technique involving the capacitance measurement to study this activity with similar studies conducted with the coarse grained alumina catalyst. There are number of ways of making gaseous alkenes like ethane. If ethanol vapors are passed over surface of heated alumina pellet the ethanol is essentially cracked to give ethane and water vapor. This reaction is normally occurs at $\sim 250^\circ\text{C}$ in usual alumina [13]. Alumina enhances typically acid catalyzed reactions which its surface is saturated with water [14]. In another application the same powder was studied and tested for novel application as catalyst in alcohol dehydration process at different conditions. For this, the comparison between as synthesized and commercial grade alumina was carried out. It has been clear that the surfaces of most metal oxides have hydroxyl groups in the atmosphere which play important role in surface phenomenon such as catalytic action, selective adsorbability and hydrophilicity. IR spectroscopic studies have shown that water molecules are get adsorbed on the surface of oxides through hydrogen bonding with surface hydroxyl groups [15]. The oxidizing power and catalytic activities may be due to defects in the structure that is in coordination of metal ions in oxides [16]. The comparative studies for novel application of alumina as catalyst in the ethanol dehydration have shown challenging and remarkable results.

The humidity sensing was experienced and realized by measuring the change in the capacitance of a parallel plate capacitor made. Here the dielectric medium consisted of compacted powder of nanophase alumina pellets. The static controlled humidity chamber was used for obtaining different humidity levels. The capacitance was measured using a Systronics make digital capacitance meter. The steady state capacitance was measured for various solutions viz. distilled water, prepared solutions of CrO_3 , CuSO_4 , NH_4Cl , and LiCl .

RESULTS AND CONCLUSION

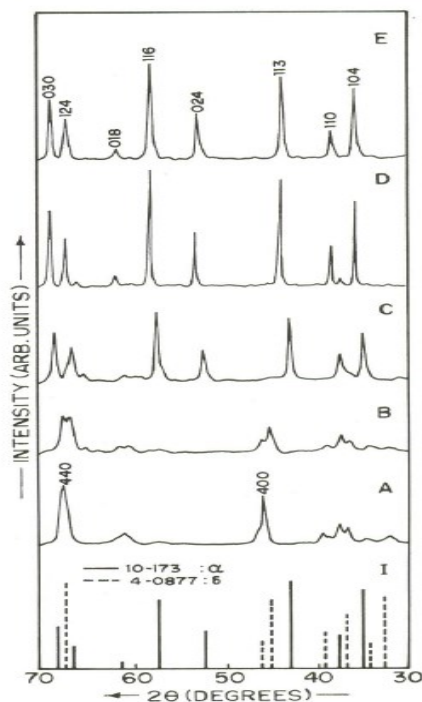


Fig. 2. XRD pattern of: (A) as-deposited; (B) calcined at 1200°C; (C) calcined at 1400°C; (D) calcined at 1600°C; (E) commercial alumina; and (I) pattern adapted from JCPDS 10-173 (α) and 16-394 (δ).

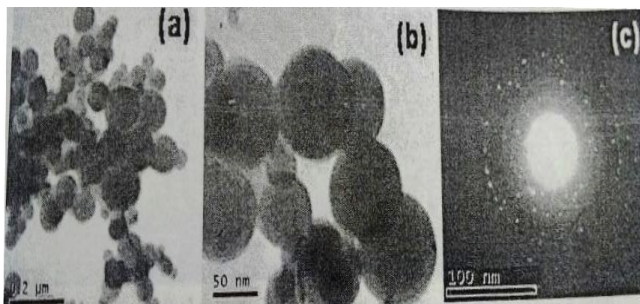
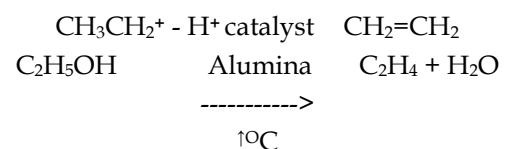


Figure 4: TEM images of nanophase alumina: Selected area diffraction pattern for nanophase δ - Al_2O_3

As revealed from XRD study shown in fig. 2 the as prepared powder of alumina exhibited δ -alumina phase. Using the Debye-Scherrer formula the particle size was estimated and was found to confirm the nanophase nature (20nm.). From the TEM analysis [10] the spherical size of particulate was confirmed as shown in fig.4. The special Neutron activation analysis (N.A.A.) was carried out on powders at 270°C, 300°C, 500°C, 700°C and 900°C. The results indicated that the concentration of aluminum and oxygen in 0.5 gm of Al_2O_3 varied with the calcinations temperature. The oxygen concentration increase indicating a peak for 500°C [5] for a nanophase powder wherein a similar peak was observed for the commercial microphase (Good Fellow UK, 45 mm size spherical particle) Al_2O_3 powder for a temperature of 700°C [5]. The increase in the oxygen concentration is explained on the basis of higher diffusion rates of oxygen into the pores. However, the grain growth prohibits the further diffusion of oxygen. The peak temperature might probable indicate the temperature at which the grain growth has occurred. Nanophase material seems to grow at lower temperature as compared to the micro phase powder. This experiment also clearly indicates that the oxygen adsorption capacity for nanophase powder is higher as compared to the coarser grained powder.

Among the vapors of different chemicals when vapors of ethanol were passed over the heated surface of nanophase alumina and the coarse grained alumina it exhibit dehydration reaction to give ethylene. In case of use of our as synthesized nanophase alumina the ethanol dehydration was observe to be occurred at the temperature $\sim 135^\circ\text{C}$. This reaction is normally occurs at $\sim 250^\circ\text{C}$ in usual alumina [13]. In this case the catalytic activity is not connected with the electron transfer mechanism. It is assumed that that the H^+ ions present in the alumina catalyst is responsible for this dehydration activity. A carbonium ion is formed in this step. It is destroyed on the surface of the catalyst to liberate the molecule of an unsaturated hydrocarbon and the proton is returned to the catalyst.



An H^+ ion in alumina obstructs the conductivity so the capacitance increases. Thus the mechanism of proton catalysis consists of continuous transition of proton from the catalyst to the reacting molecule. This mechanism was studied by the measurement of capacitance and graphically results are shown. When the protons are removed from the catalyst surface then there is change in the capacitance we observed and noted precisely.

The results show that the dehydration process occurs at quiet lower temperature using as synthesized alumina than commercial grade alumina as shown in fig.3. This has important and novel applications in industry. The reduction in temperature for certain chemical process has importance in view of cost also.

A comparative measure of the sensing capability of the fine grained Al_2O_3 as compared to the coarser grained powder is studied for various humidity levels fig.5

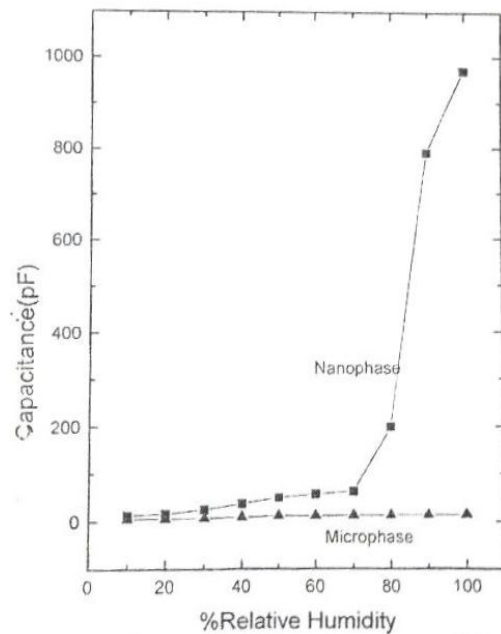


Fig: 5: Humidity sensing: Capacitance measurement

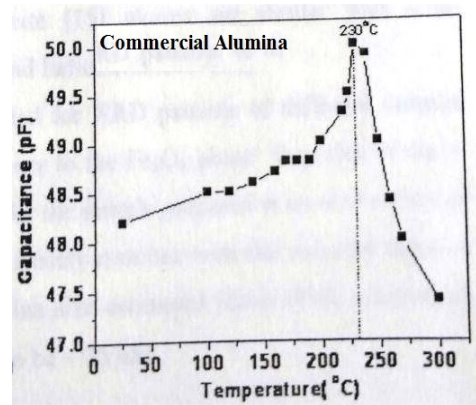
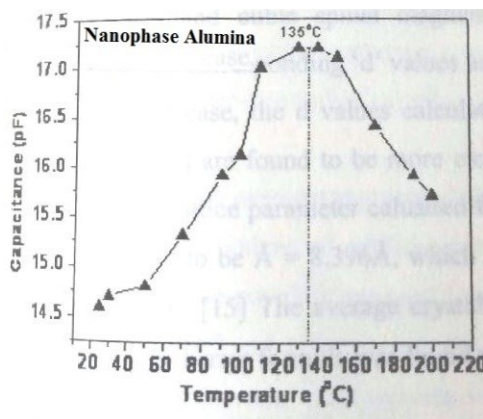


Figure 3: Catalytic activity: Role of Nanophase and Commercial alumina during dehydration

Acknowledgement:

The author would like to thank Department of Physics, Savitribai Phule Pune University Pune and National Chemical Laboratory Pune for the invaluable help and healthy cooperation throughout this work. Pravara Rural Education Society Pravaranagar, Loni, Department of Electronics Science and Physics, P.V.P. College Pravaranagar, is also honestly well acknowledged.

Conflicts of interest: The authors stated that no conflicts of interest.

REFERENCES

1. Gleiter H. Prog. Mater Sci,1989,33: 223.
2. Siegel RW. MRS Bulletin,1990.
3. Karch J, Birringer R and Gleiter H. Nature,1989, 330:556.
4. Granquist CG and Burhman RA. J. Appl.Phys.,1976, 47:2200.
5. Sali ND et. al. Mat. Sci. and Engg.,1997, B49:18-26.
6. Bernard M. Kulwicki. J.Am. Ceram.Soc,1991, 74[4]: 697.

7. Tsuneharu Nitta, *Ind Eng. Chem. Prod. Res. Dev.*,1981,20: 669.
8. Tsuneharu Nitta, Ziro Terada and Shigeru Hayakawa., *J. Am. Ceram. Soc.*,1980,63: 295.
9. Sali ND et. al. *Mat. Sci. and Engg.*,1999, B63:215-227.
10. P. Madhu Kumar et.al. *Mater. Chem. Phys*, 1994, 36: 354.
11. M. Phil Dissertation, Sali ND, Dept. of Physics, University of Pune, Nov.1995.
12. Ph.D. thesis, Sali ND, Dept. of Physics, University of Pune, August 2007.
13. Knozinger H, P. Ratnssamy *Catal. Rev.- Sci. Eng.*,1978,**17**: 31.
14. Mills GA et. Al. *J. Electrochem*,1956,60: 823
15. T. Morimoto et. Al. *J. Phy. Chem.*,1969, 73[7]:243-248.
16. Peri JB. *J phy. Chem*,1965,69:220

Structural and dielectric properties of Nd Substituted Ni-Co Nanoferrites by autocombustion route

Kokare MK^{1*} and Rathod SM²

¹Department of Physics, Tuljaram Chaturchand College, Baramati Pune, ²Department of Physics, A.G. College, Pune *Email: kokaremk@gmail.com

Manuscript Details

Available online on <http://www.irjse.in>
ISSN: 2322-0015

Editor: Dr. Arvind Chavhan

Cite this article as:

Kokare MK and Rathod SM. Structural and dielectric properties of Nd Substituted Ni-Co Nanoferrites by autocombustion route, *Int. Res. Journal of Science & Engineering*, December 2017; Special Issue A1 : 69-72.

© The Author(s). 2017 Open Access

This article is distributed under the terms of the Creative Commons Attribution 4.0 International License

(<http://creativecommons.org/licenses/by/4.0/>), which permits unrestricted use, distribution, and reproduction in any medium, provided you give appropriate credit to the original author(s) and the source, provide a link to the Creative Commons license, and indicate if changes were made.

ABSTRACT

Neodymium substituted nanocrystalline Ni-Co ferrites which are chemically represented as $\text{Ni}_x\text{Co}_{1-x}\text{Nd}_y\text{Fe}_{2-y}\text{O}_4$ were synthesized by sol-gel autocombustion route. The influence of Nd^{3+} on the structural and dielectric properties of prepared samples was studied in detail. X-ray analysis shows the single phase cubic spinel structure. The crystallite size was observed to be decreasing with increasing Nd content. However the lattice parameter initially decreases gradually and then increases with the substitution of Nd in Ni-Co ferrites. Dielectric parameters were studied for an applied AC field from 50 Hz to 5 MHz range. Dielectric constant and the dielectric tangent loss were observed to be decreasing with increase in frequency.

Keywords: $\text{Ni}_x\text{Co}_{1-x}\text{Fe}_2\text{O}_4$, Neodymium, Nanoferrites, Dielectric parameters.

INTRODUCTION

Cobalt spinel ferrite is most useful hard ferromagnetic material with high Curie temperature, high coercivity, high magneto-crystalline anisotropy, moderate saturation magnetization, good mechanical hardness and chemical stability [1]. Spinel ferrite is represented as MFe_2O_4 where M and Fe are divalent and trivalent cations respectively. CFO nanoferrites are useful for development of microwave and spintronic devices, solar cells, magnetostrictive sensors, drug delivery, transducers, actuators, lithium ion batteries, supercapacitors and memory devices for computers [2].

Due to higher values of magnetostriction CFO ferrites can be used for strain sensor and actuator applications [3]. Currently, nanoparticles and nano-architectures of CFO-based materials are gaining tremendous interest in view of their ability to exhibit tunable electrical and magnetic properties, which could be exploited in numerous technological applications [4-7]. Recently many researchers have concentrated on synthesis of spinel ferrites by substituting trivalent rare earth ions for Fe^{3+} . The doping of rare earth ions into the CFO spinel structure leads to structural distortion which can modulate structural, electrical, magnetic and dielectric properties of ferrites. Specifically, the degree of modification depends on the ionic radius, the electronic configuration of dopant and its site preference (A versus B site) and the extent of distribution at the specific sites within the spinel structure [8-10].

In present work we have synthesized Neodymium substituted Ni-Co nanoferrites by sol-gel autocombustion route. Impact of Nd ion doping on structural and dielectric properties of Ni-Co Nanoferrites have been studied.

METHODOLOGY

Nanoparticles of $\text{Ni}_{0.5}\text{Co}_{0.5}\text{Nd}_x\text{Fe}_{2-x}\text{O}_4$ with ($x = 0.025, 0.05, 0.075, 0.1, 0.125$) were synthesized by sol-gel autocombustion route. Stoichiometric amounts of Analytical Reagent (AR) grade $\text{Co}(\text{NO}_3)_2\text{H}_2\text{O}$, $\text{Ni}(\text{NO}_3)_2\text{H}_2\text{O}$, $\text{Fe}(\text{NO}_3)_3\text{H}_2\text{O}$, $\text{Nd}(\text{NO}_3)_3\text{H}_2\text{O}$ (99.99% pure) and citric acid were used as raw precursors. These chemicals were dissolved initially in 100 ml double distilled water. Citric acid was used as a complexing agent to get transparent solution with homogenous distribution of metal ions. The above mixture was stirred for 2 hrs to get homogenous clear solution and then heated with constant stirring upto 50°C using a magnetic stirrer with hot plate. Further the pH of solution was adjusted upto 7 by addition of ammonia solution. The resulting solution was evaporated by heating on a hot plate with continuous stirring to form a continuous network of gel. Further heating of the gel, results into fast flameless auto combustion reaction with the evolution of large amount of gases, it gives a burned powder of the

resultant product. The burned gel was ground to get a fine ferrite powder by using Agate Mortar and pestle. Finally the ground powders were sintered in air at 560°C for 4 hrs and then finally cooled to room temperature.

For structural determination, powder X-ray diffraction (XRD) patterns were recorded with Rigaku X-ray diffractometer using the $\text{Cu}(\text{K}\alpha)$ radiation ($\lambda = 1.5405 \text{ \AA}$). The dielectric parameters were measured by using precision LCR meter.

RESULT AND DISCUSSION

1. XRD analysis

The XRD pattern of $\text{Ni}_{0.5}\text{Co}_{0.5}\text{Nd}_x\text{Fe}_{2-x}\text{O}_4$ with $x = 0.025, 0.050, 0.075, 0.1, \text{ and } 0.125$ are shown in Fig.1. The obtained XRD data exactly matches with standard JCPDS data card Number 00-002-1045 and 01-074-2081. The diffraction peaks at (220), (311), (222), (400), (422), (333) and (440) confirms the single phase cubic spinel crystal structure. The lattice constant gradually decreases upto $x = 0.100$ and then increases with increase in Nd content.

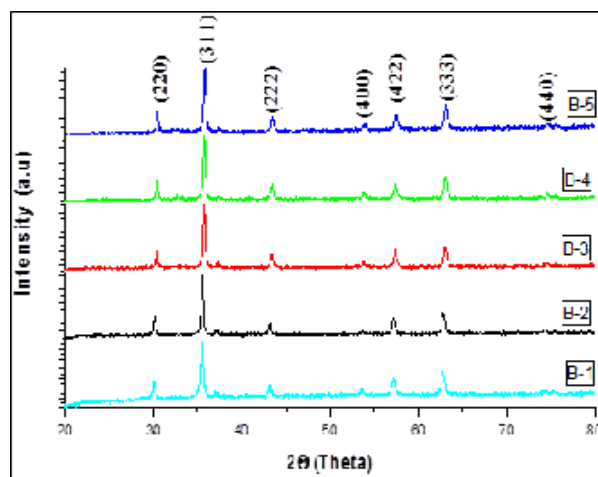


Fig.1. Shows XRD pattern for synthesized $\text{Ni}_{0.5}\text{Co}_{0.5}\text{Nd}_x\text{Fe}_{2-x}\text{O}_4$ samples with varying Nd concentration from B-1) 0.025, B-2) 0.05, B-3) 0.075, B-4) 0.1, and B-5) 0.125.

The calculated crystallite size decreases from 26 nm to 21 nm with increase in Nd content. It reveals that Nd substituted Ni-Co nanoferrites prevents the growth of particles and controls the crystallite size of the

prepared samples. This may attributed to the occupancy of Nd^{3+} ions at octahedral site. Incorporation of Nd^{3+} ions results into compressive stress which leads to decrease in crystallite size. The variation of lattice parameter and crystallite size with Nd concentration is shown in table 1.

Table 1: Variation in Lattice constant and Crystallite Size with increase in Nd concentration

% of Nd doping (x)	Lattice Constant ' a ' (Å)	Crystallite Size D (nm)
0.025	8.386	26.20
0.050	8.328	25.60
0.075	8.321	24.97
0.100	8.311	23.27
0.125	8.371	21.31

2. Micro-structural Analysis

The FE-SEM micrographs of various $\text{Ni}_{0.5}\text{Co}_{0.5}\text{Nd}_x\text{Fe}_2\text{O}_4$ samples are as shown in Fig.2. Microstructural analysis determines the average grain size of the prepared samples which influence the magnetic properties of the materials. It displays the surface morphology of the prepared samples. It is observed

that most of the NiCoNdFeO nanoparticles exhibit the hexagonal crystal structure. The average grain size of the samples decreases with Nd content. SEM image reveals that the grain size decreased with increasing Nd content, which is evident from the XRD analysis.

Fig.2 shows transmission electron micrographs (TEM) of $\text{Ni}_{0.5}\text{Co}_{0.5}\text{Nd}_x\text{Fe}_2\text{O}_4$ ferrite. TEM image reveals the uniform morphology of the ferrite powder with average particle size of 45 nm. These results are well supported by SEM image. The average crystallite size calculated from the XRD data is in the range of 21-26 nm.

3. Dielectric properties

The dielectric behavior of Nd doped ferrite material is due to the electric dipole moments developed by the charge transfer between the di and trivalent metal cations (ion exchange) within the spinel structure. The dielectric properties of ferrites also depend on the microstructure, method of sample preparation, sintering time, temperature, chemical composition and site occupancy of metal cations among the A and B site [11].

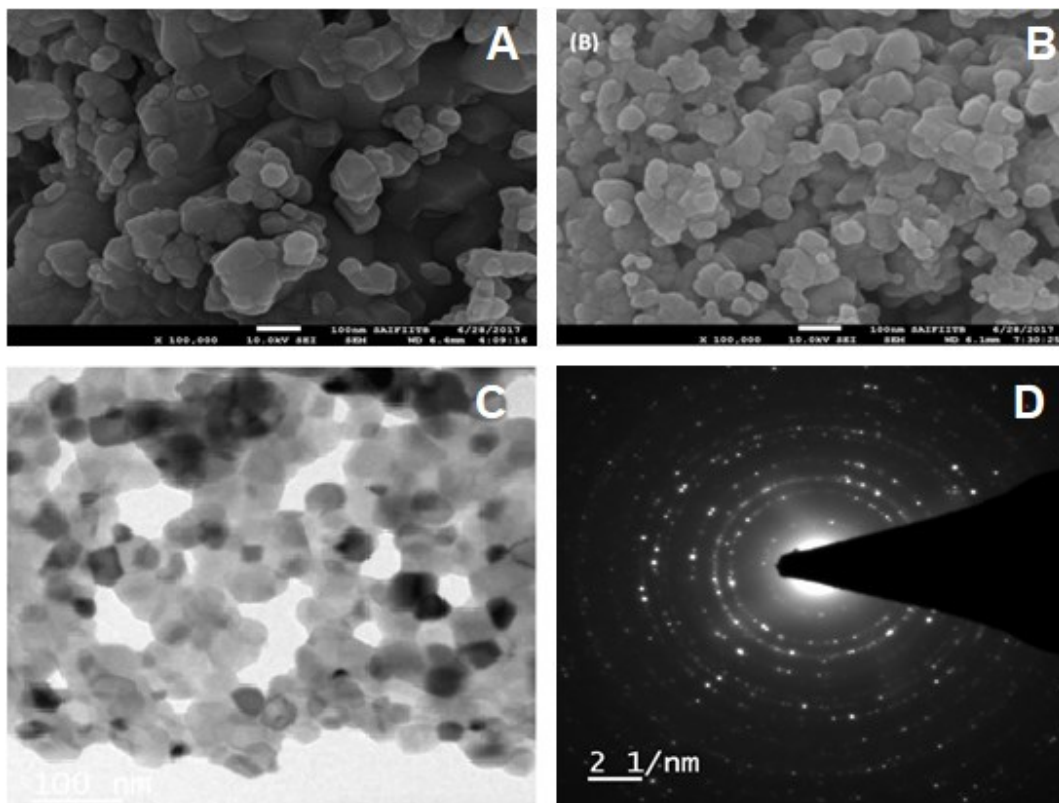


Fig.2. (A) & (B) SEM and (C) & (D) TEM images of sample

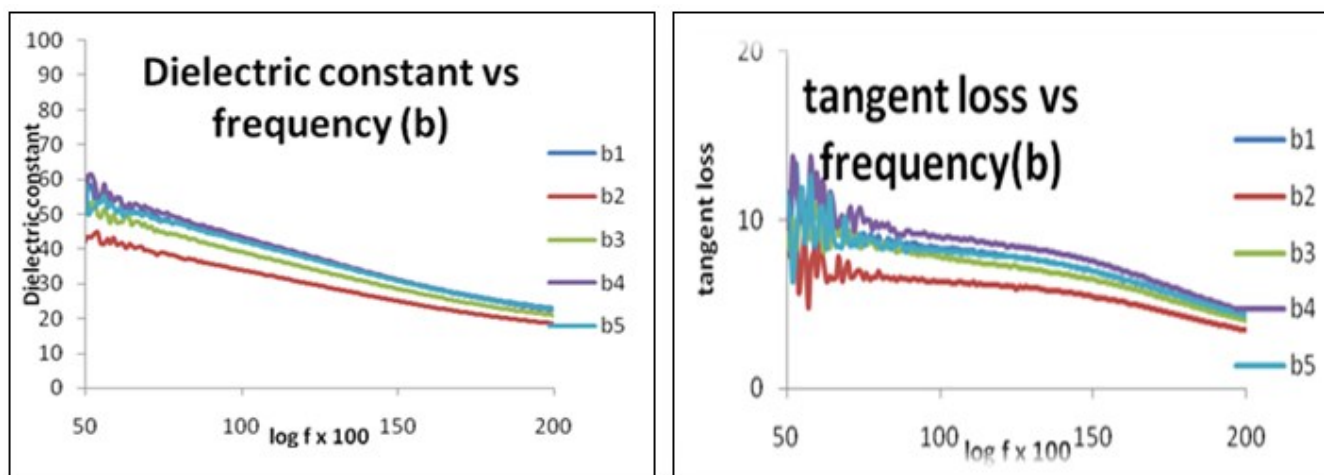


Figure 3A: Variation of dielectric constant with frequency. **Figure 3B:** Variation of tangent loss with frequency.

The dielectric behavior of ferrite material as a function of frequency provide valuable information about the localized electric charge carriers and better understanding of the mechanism of dielectric polarization in ferrites.

The variation of dielectric constant and dielectric tangent loss of Nd doped Ni-Co ferrite with frequency is shown in Fig.3A and 3B. The dielectric constant decreases slowly with increase in frequency. The variation of dielectric constant with frequency may be explained on the basis of space-charge polarization phenomena. Low dielectric loss of Nd doped Ni-Co nanoferrites are useful for high frequency applications like microwave devices, high density magnetic recording.

CONCLUSION

Neodymium substituted Ni-Co nanoferrites were successfully synthesized by sol gel auto combustion route. The prepared samples were investigated by XRD, SEM, TEM and dielectric measurements. XRD confirmed the single phase cubic spinel structure. The lattice constant initially decreased and then increased with the increase in Nd³⁺ content. The crystallite size decreased from 26 nm to 21 nm. Dielectric parameters were studied for an applied AC field from 50 HZ to 5 MHz frequency range. Both dielectric constant and the tangent loss were decreased with increases in frequency. Low tangent loss at high frequency

indicates the potential application of Nd doped Ni-Co nanoferrites in high frequency microwave devices.

REFERENCES

1. Kakade SG, Yuan-Ron Ma, Devan RS, Kolekar YD and Ramana CV, *J. Phys. Chem. C* 2016, 120:5682-5693.
2. Orozco C, Melendez A, Manadhar S, Singamaneni SR, Reddy KM, Gandha K, Niebedim I, Ramana CV, *J. Phys. Chem.* 2017; 121 (46): 25623-26140.
3. Chaa F, Liao C, Kuana J, Z. Xu, C. Yan, L. Chen, H. Zhed, Z.liu, *J. Appl. Phys.* 1999;85: 2782.
4. Kakade SG, Kamble RC, Kolekar YD, Ramana CV, *J. Phys. Chem. C* 2016; 113: 9070-9076.
5. Dmazario E, Menendez N, Herrasti P, Canete M, Connord V, *J. Phys.Chem. C* 2013;117: 11405-11411.
6. Mukherjee D, Hordagoda M, Hyde R, Bingham N, Hariharan S, Witanachchi S, *ACS Appl. Mater. Interfaces.* 2013; 5:7450-7457.
7. Mikalauskaite A, Kondrotas R, Niaura G, Jagminas A. *J. Phys. Chem. C.*2015;119:17398-17407.
8. Mahalakshimi S, Srinivasa MK, Nithiyanantham S. *J. Supercond. Nov. Magn.* 2014; 27: 2083- 2088.
9. Dascalu G, Popescu T, Feder M, Caltun OF, *J. Magn. Magn. Mater.* 2013; 333: 69-74.
10. Bharathi K, Ramanaa CV, *J. Mater. Res.* 2011; 26:584-591.
11. Ramana CV, Kolekar YD, Bharathi KK , Sinha B, Ghosh K. *J. Appl. Phys.* 2013; 114: 18s3907.

Synthesis and Characterization of Spray Deposited Lithium Ferrite Thin Film

Chilwar Rahul R¹, Somvanshi Sandeep B², Chavan Apparao R², Kharat Prashant B², Babrekar MK³ and Jadhav KM^{2*}

¹Yogeshwari college, Ambajogai, Beed, India, ²Dept. of Physics, Dr. Babasaheb Ambedkar Marathwada University, Aurangabad, ³Department of Physics, Indraraj College, Sillod, Aurangabad
E-mail : drjadhavkm@gmail.com

Manuscript Details

Available online on <http://www.irjse.in>
ISSN: 2322-0015

Editor: Dr. Arvind Chavhan

Cite this article as:

Chilwar Rahul R, Somvanshi Sandeep B, Chavan Apparao R, Kharat Prashant B, Babrekar MK and Jadhav KM. Synthesis and Characterization of Spray Deposited Lithium Ferrite Thin Film, *Int. Res. Journal of Science & Engineering*, December 2017; Special Issue A1 : 73-76.

© The Author(s). 2017 Open Access

This article is distributed under the terms of the Creative Commons Attribution 4.0 International License

(<http://creativecommons.org/licenses/by/4.0/>), which permits unrestricted use, distribution, and reproduction in any medium, provided you give appropriate credit to the original author(s) and the source, provide a link to the Creative Commons license, and indicate if changes were made.

ABSTRACT

Nanocrystalline, homogeneous spinel $\text{Li}_{0.5}\text{Fe}_{2.5}\text{O}_4$ thin film was deposited on glass substrate by using spray pyrolysis of metal nitrate aqueous solution. Respective metal nitrates (lithium nitrate) and iron nitrate were used as precursors. Phase composition, crystal structure and morphology of the obtained films were studied by X-ray diffraction (XRD), scanning electron microscopy (SEM) and energy dispersive X-ray microanalysis (EDAX). The analysis of XRD data confirms polycrystalline nature and single phase cubic spinel structure of the film. The surface morphology was studied using scanning electron microscopy (SEM) which reveals spherical morphology of the film. The thickness of deposited film was obtained using surface profiler which is found to be below 500 nm, but crystallite size was under 30 nm. The optical transmittance and reflectance measurements were recorded using UV-Vis spectrophotometer. The optical studies reveal that the transition is direct band gap energy.

Keywords: Lithium ferrite, Spray pyrolysis, XRD, SEM, UV-Vis.

INTRODUCTION

Spinel ferrite is an important class of magnetic material with large number of application in various fields [1, 2]. It can be represented by the formula MFe_2O_4 where M

stands for metal ions like cobalt, nickel, zinc, copper, manganese etc. Spinel ferrite possesses both electrical and magnetic properties. The high electrical resistivity, low eddy current and dielectric loss, high saturation magnetization, high permeability, high Curie temperature etc. are the remarkable properties of spinel ferrites [3]. These properties are sensitive to method of preparation, nature and type of dopant and distribution of cations at available interstitial sites. In spinel ferrites two interstitial sites are available namely tetrahedral A site and octahedral B site. Spinel ferrites can be studied in different forms viz. bulk, nano and thin film form. Recently, nanocrystalline thin films have become more important from the point of view of their applications.

In the family of spinel ferrite, lithium ferrite is a stable, insulating ferrimagnet that has applications in microwave electronics [4]. It is a close relative of magnetite, which can be represented as $[\text{Fe}^{3+} \{\text{Fe}^{3+}\text{Fe}^{2+}\} \text{O}_4$, where the square bracket represents the tetrahedral site and the curly bracket represents the octahedral site. Lithium is monovalent, so for $\text{Li}_{0.5}\text{Fe}_{2.5}\text{O}_4$, all the Fe must be in the 3^+ valence state, giving $[\text{Fe}^{3+} \{\text{Fe}^{3+1.5} \text{Li}^{+0.5}\} \text{O}_4$, assuming the inverse spinel structure. Lithium ferrites are superior to other spinel ferrites at the microwave frequencies due to their characteristic low insertion losses, high spin wave line widths and temperature stabilities of saturation magnetization [5]. Lithium ferrites in thin film configuration are of great interest for emerging microwave applications owing to their high resistivity, low eddy current losses, excellent thermal and chemical stability, and suitable dielectric properties [6, 7].

Nanocrystalline ferrite thin films have applications in high-density magneto-optic recording devices, colour imaging, bioprocessing, ferrofluids and magnetic refrigeration [4, 8, 9]. Apart from these applications, miniaturization in the field of microwave devices employing ferrite components compatible with monolithic microwave integrated circuits (MMICs) is one of the main area for the future growth of ferrite thin film technology.

There are various thin film deposition methods such as pulsed laser deposition [10], spin coating [11], RF

sputtering [12], spray pyrolysis [13], chemical bath deposition [14] etc have been employed to deposit nano structured spinel ferrite thin films. A spray pyrolysis deposition (SPD) with a simple apparatus is a versatile technique for producing various thin film materials of a wide range of the composition in air at a relatively low temperature and a high deposition rate. In the present work, lithium ferrite thin films have been prepared by using spray pyrolysis technique. The structural, morphological and optical properties of lithium ferrite thin films have been investigated using standard techniques and results are presented in this paper.

METHODOLOGY

The raw materials of AR grade as lithium nitrate and ferric nitrate $[\text{Fe}(\text{NO}_3)_3 \cdot 9\text{H}_2\text{O}]$ were used for deposition of lithium ferrite thin films without further purification. Lithium ferrite thin films were deposited on glass substrate by spray pyrolysis deposition technique. The stoichiometric amount of respective metal nitrates was dissolved in distilled and mixed together for spray. Lithium ferrite thin films were prepared by spraying the solution onto previously cleaned glass substrate. Glass substrates mounted on a holder were placed on the surface of a hot plate. A temperature controller was used to hold the preset temperature of 648 K with an accuracy of ± 50 C through a chromel-alumel thermocouple connected to the glass substrate. A prepared solution was atomized in air via pneumatic spray system under an air pressure of 2 kg/cm². The atomized droplets were transformed onto the heated glass substrate for 0.5 sec intermittently. The substrate temperature could be reduced under the effect of spray and requires several seconds to recover the preset temperature. The solution spray rate and the distance between nozzle and substrate were kept constant at 0.125 ml/s and 30 cm respectively. The films were annealed at a temperature of 550 °C for 4 hours. The deposited films were characterized by X-ray diffraction method (XRD), a scanning electron microscopy (SEM) and UV-Vis spectrometer to study the structural, morphological and optical aspects of lithium ferrite thin film under investigation.

RESULT AND DISCUSSION

Structural properties

Fig. 1 depicts the X-ray diffraction (XRD) pattern of lithium ferrite thin film. The XRD pattern revealed good crystallinity because of annealing of the film. The lithium ferrite film is oriented along (311) plane. The other planes viz. (210), (310), (311), (421), (422) (511) (440) and (441) also exist in the XRD film which is sharp and intense. The XRD patterns matches well with the characteristics reflections of cubic spinel structure. The analysis of XRD pattern revealed the formation of single phase cubic spinel structured lithium ferrite thin film. The interplanar spacing 'd' values of the film are in good agreement with the standard 'd' value of lithium ferrite. Using the 'd' values and corresponding Miller indices, the value of lattice constant of the lithium ferrite thin film was evaluated. The value of lattice constant 'a' is given in Table 1 which is in good agreement with the reported value. The value of 'a' was used to obtain the unit cell volume, X-ray density, bulk density, porosity and same are given in Table 1.

Table 1 Lattice parameter (a), Unit cell volume (V), Crystallite size (t), X-ray density (dx), Bulk density (dB), and Porosity (P) of lithium ferrite thin film

a (Å)	V (cm ³)	d _x (gm/cm ³)	d _B (gm/cm ³)	P (%)	t (nm)
8.3334	578.09	5.3802	3.638	32.3847	18.3

The crystallite size was determined from full width of half maximum (FWHM) of the most intense (310) peak, which was obtained by slow step scanning or on that peak at 0.20 per minutes based on Scherrer's formula Debye-Scherrer formula [15] for crystallite size determination is given by

$$D = \frac{0.9 \lambda}{\beta \cos \theta} \quad \dots 1$$

where, D is the crystallite size, λ is the wavelength of X-ray, β is the full width at half maximum (FWHM) after correcting the instrument peak broadening (β expressed in radians), θ is the Bragg's angle.

The crystallite size is of the order of 18 nano meter, which indicates the nano-crystalline nature of the film. The value of crystallite size is given in Table 1

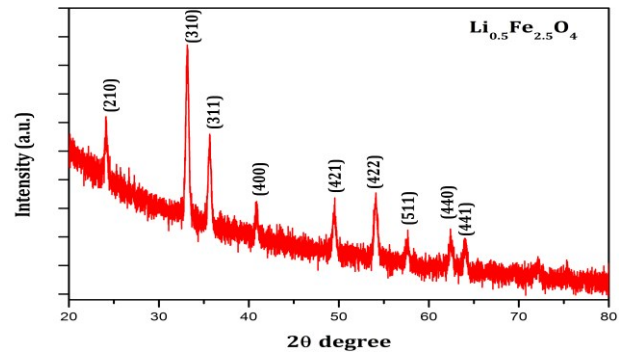


Figure 1: XRD pattern of lithium ferrite thin film

Morphological study

Scanning electron micrograph of lithium ferrite thin film on glass substrate is shown in Fig. 2. The micrograph shows agglomerated particles grown randomly on the substrate. The lithium ferrite thin film has covered the complete substrate surface with some random over growth of particles as evidenced by the micrographs. The grain size measured from SEM is found to be of the order of 14.58 nm, which is in good agreement with the particle size obtained from X-ray diffraction.

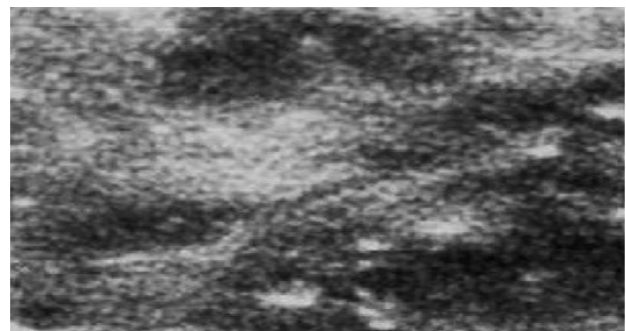


Figure 2: SEM image of lithium ferrite thin film

The chemical composition analysis was carried out on Li_{0.5}Fe_{2.5}O₄ thin film sample by energy dispersive X-ray (EDX) analysis. The EDX spectra, confirms the presence of elements as Li, Fe and O in stoichiometric proportion.

Optical study

Optical studies of lithium ferrite thin film were carried out to investigate the band gap energy of the film. The optical absorbance of annealed lithium ferrite thin film was studied in the range 400 - 1000 nm, using UV-Vis spectrophotometer, which has been further used for the energy band gap calculation. The optical characterization of the deposited thin films was used

to calculate the band gap by employing both indirect and direct band gap measurement methods. The optical band gap E_g for all the films were estimated from the absorption coefficient (α) using the Tauc relation [16] which is given by

$$\alpha h\nu = A (h\nu - E_g)^n$$

where, A is a constant depends on the transition probability, $h\nu$ is the energy of incident photon and n is an index that characterizes the optical absorption process. It is theoretically equal to 2, 1/2, 3 and 3/2 for allowed indirect, allowed direct, forbidden indirect and forbidden direct electronic transitions respectively depending on the nature of the electronic transition responsible for the reflection. The obtained band gap value for lithium ferrite thin film is 2.37 eV.

CONCLUSION

Nanocrystalline thin film of lithium ferrite has been successively deposited on glass substrate using spray pyrolysis technique. X-Ray diffraction analysis proves that, the film possess simple cubic spinel structure. The morphological studies carried out by SEM analysis shows agglomerated particles grown randomly on the substrate. The EDX analysis confirms the presence of all the elements (Li, Fe and O) in stoichiometric proportions. The optical studies confirmed the band gap value for lithium ferrite thin film is about 2.37 eV.

REFERENCES

1. Sugimoto M, The past, present, and future of ferrites, *Journal of the American Ceramic Society*, 1999; 82:269-280.
2. Pardavi-Horvath M, Microwave applications of soft ferrites, *Journal of Magnetism and Magnetic Materials*. 2000;215:171-183.
3. Suzuki Y, Van Dover R, Gyorgy E, Phillips JM, Korenivski V, Werder D, Chen C, Cava R, Krajewski J, Peck Jr W, Structure and magnetic properties of epitaxial spinel ferrite thin films, *Applied physics letters*. 1999;68:714-716.
4. Zaquine I, Benazizi H, Mage J, Ferrite thin films for microwave applications, *Journal of Applied Physics*, 1988;64 :5822-5824.
5. Dash J, Prasad S, Venkataramani N, Krishnan R, Kishan P, Kumar N, Kulkarni S, Date S, Study of magnetization and crystallization in sputter deposited LiZn ferrite thin films, *Journal of applied physics*. 1999;86:3303-3311.
6. Glass HL, Ferrite films for microwave and millimeter-wave devices, *Proceedings of the IEEE*. 1998;76:151-158.
7. Desai M, Dash J, Samajdar I, Venkataramani N, Prasad S, Kishan P, Kumar N, A TEM study on lithium zinc ferrite thin films and the microstructure correlation with the magnetic properties, *Journal of magnetism and magnetic materials*. 2001;231:108-112.
8. Lemaire HP, Croft WJ, Ferrite thin films, *Journal of Applied Physics*. 1961;32:S46-S47.
9. Sandu I, Presmanes L, Alphonse P, Tailhades P, Nanostructured cobalt manganese ferrite thin films for gas sensor application, *Thin Solid Films*. 2006; 495:130-133.
10. Sathaye S, Patil K, Kulkarni S, Bakre P, Pradhan S, Sarwade B, Shintre S, Modification of spin coating method and its application to grow thin films of cobalt ferrite, *Journal of Materials Science*. 2003;38:29-33.
11. Lai BK, Johnson AC, Xiong H, Ramanathan S, Ultra-thin nanocrystalline lanthanum strontium cobalt ferrite (La 0.6 Sr 0.4 Co 0.8 Fe 0.2 O 3- δ) films synthesis by RF-sputtering and temperature-dependent conductivity studies, *Journal of Power Sources*. 2009;186:115-122.
12. Wu Z, Okuya M, Kaneko S, Spray pyrolysis deposition of zinc ferrite films from metal nitrates solutions, *Thin Solid Films*. 2001;385:109-114.
13. Gunjekar J, More A, Gurav K, Lokhande C, Chemical synthesis of spinel nickel ferrite (NiFe 2 O 4) nano-sheets, *Applied Surface Science*. 2008;254: 5844-5848.
14. Alange R, Khirade PP, Birajdar SD, Humbe AV, Jadhav K, Structural, magnetic and dielectrical properties of Al-Cr Co-substituted M-type barium hexaferrite nanoparticles, *Journal of Molecular Structure* . 2016;1106:460-467.
15. Kumar V, Sharma SK, Sharma T, Singh V, Band gap determination in thick films from reflectance measurements, *Optical materials*, 1999;12:115-119
16. Chrisey DB, Hubler GK, Pulsed laser deposition of thin films. 1994.

Structural and Magnetization Behaviour in Magnetically Diluted Nickel Ferrite at Nanoscale

Deshmukh SS¹, Humbe Ashok², Keche Atul³, Patil Manisha¹, More SD¹, Shukla SJ¹ and Jadhav KM^{2*}

¹Department of Physics, Deogiri College, Aurangabad, India, ²Dept. of Physics, Dr. Babasaheb Ambedkar Marathwada University, Aurangabad, ³Department of Physics, Muktanand College, Aurangabad
E-mail : drjadhavkm@gmail.com

Manuscript Details

Available online on <http://www.irjse.in>
ISSN: 2322-0015

Editor: Dr. Arvind Chavhan

Cite this article as:

Deshmukh SS, Humbe Ashok, Keche Atul, Patil Manisha, More SD, Shukla SJ and Jadhav KM.
Structural and Magnetization Behaviour in Magnetically Diluted Nickel Ferrite at Nanoscale, *Int. Res. Journal of Science & Engineering*, December 2017; Special Issue A1 : 77-80.

© The Author(s). 2017 Open Access

This article is distributed under the terms of the Creative Commons Attribution 4.0 International License

(<http://creativecommons.org/licenses/by/4.0/>), which permits unrestricted use, distribution, and reproduction in any medium, provided you give appropriate credit to the original author(s) and the source, provide a link to the Creative Commons license, and indicate if changes were made.

Abstract

The present investigation deals with the sol-gel auto combustion synthesis of nanocrystalline Zn doped nickel ferrite with chemical formula $Ni_{1-x}Zn_xFe_2O_4$ ($x = 0.0$ and 0.4) using urea as a fuel and the effect of magnetic dilution by Zn on structural and magnetic properties. The single phase as well as nanocrystalline nature of the prepared $Ni_{1-x}Zn_xFe_2O_4$ sample has been confirmed through X-Ray diffraction (XRD) technique. The crystallite size obtained by using Scherrer's formula was found to be in the range of 12 nm to 19 nm. The doping of Zn^{2+} ion in place of Ni^{2+} ions causes the reduction in lattice parameter. The lattice parameter of the pure nickel ferrite calculated by XRD data is of the order of 8.334 Å which is in good agreement with the standard lattice parameter of nickel ferrite. The magnetic behaviour of pure and Zn doped nickel ferrite was studied through pulse field hysteresis loop technique. The hysteresis curve (M-H plot) was recorded at room temperature to know the magnetic behaviour. Using M-H plots, the magnetic parameters viz. saturation magnetization, remanence magnetization, coercivity and magneton number were deduced. It is observed that the doping of Zn dilutes the magnetic structure of Nickel ferrite. All the magnetic parameters were decreased after Zn doping. The magnetic behaviour of the present samples was discussed using Neel's theory. Using Neel's model the magneton number n_B was calculated. The observed and calculated magneton number nearly matches with each other indicating the magnetic structure is collinear.

Keywords: Nickel ferrite, Zn doping, XRD, M-H curve.

INTRODUCTION

The diverse and fascinating applications of nanosized spinel ferrites have opened new prospects in various fields viz. electronics, information technology, storage media, biomedical, transport, ferrofluids, etc [1-3]. The ferrites at nanoscale exhibit the novel properties like superparamagnetism, quantum confinement, single domain structure, high permeability, and chemical stability [4]. The large scale applications of fine particles of spinel ferrites exhibiting novel properties have been promoted development of various preparation techniques such as sol-gel auto combustion [5], co-precipitation [6], hydrothermal [7], micro-emulsion [8] etc which offer the right condition to tune the fine size, structure and morphology resulting an acute control over their properties. The physical properties of these nanomaterials are largely depends on the synthesis method and the optimized parameters. Selecting the appropriate parameters is crucial for the diverse applications. The sol-gel auto combustion synthesis route comprised of nitrates and fuel is commonly used method for ferrite nanoparticles preparation, since it is easy, cost effective, provides homogeneous size distribution and fine particle size. The most commonly used fuel is a citric acid, but now the approach of using new inorganic as a fuel has gained much importance. Glycine, tartaric acid, L-ascorbic acid, sucrose, dextrose, acetic acid, ethylene glycol and urea have been reported as a fuel. The most important factor which drastically influences the magnetic properties of the nanoferrites is the size and shape. Moreover, the magnetic and electrical properties of spinel ferrites primarily depend on the magnetic interactions between the cations, magnetic moments on tetrahedral (A) sites and octahedral [B] sites and hopping of electrons. In the family of spinel ferrite, Nickel ferrite is a unique and interesting ferrite exhibiting remarkable electrical and magnetic properties [9]. The crystal structure of nickel ferrite is an inverse in which Ni^{2+} ions occupy octahedral B site while Fe^{3+} ions occupy tetrahedral A and Octahedral B site. Many researchers have studied nickel ferrite in nanocrystalline form to study the structural, morphological and magnetic properties. These properties mostly depends on method of preparation, preparation condition and preparative parameters and therefore, nickel ferrite has been

studied widely. In the preparation of nickel ferrite using wet chemical method fuels like citric acid and glycine were commonly used. To our knowledge, few reports are available on the preparation of nickel ferrite taking urea as a fuel [10, 11]. To understand the structural and magnetic properties of $\text{Ni}_{1-x}\text{Zn}_x\text{Fe}_2\text{O}_4$ ($x = 0.0$ and 0.4) in detail, studies on synthesis, characterization and magnetic properties were carried out and the results obtained are presented in this work.

METHODOLOGY

The sol-gel auto combustion method which is most versatile, easy, low temperature, low cost and very much convenient to optimize the synthesis parameters was chosen to synthesize the pure nickel ferrite and zinc substituted nickel ferrite nanoparticles. The nitrates of nickel, zinc and ferric metal elements as oxidants and urea as a fuel were used as raw materials. The ratio of metal nitrates to fuel was selected as 1:2.5 (metal nitrates: urea) by balancing the metal nitrate to fuel valences adopting the propellant chemistry [22]. The calculated proportion of the urea was 1:4 but we have adopted the fuel deficient approach in the present synthesis. The weighed metal nitrates of respective elements were dissolved separately in 100ml distilled water and mixed together. The urea was also dissolved in 100ml distilled water and then added to mixed solution of metal nitrates. Then the solution was stirred at temperature of 90°C with 400 rpm for nearly 5h. Upon formation of very viscous gel the temperature was further raised to 120°C . The auto combustion of the gel carried out and the powder was formed which was ground using pestle and mortar. The as prepared fine powder was sintered at temperature 600°C for 6h to get better crystallization of the prepared spinel ferrite nanoparticles. The sample was coded as NF (NiFe_2O_4) and NZF ($\text{Ni}_{0.6}\text{Zn}_{0.4}\text{Fe}_2\text{O}_4$). The sintered powder of sample was used to characterize it by using Panalytical Xpert Pro X-ray powder diffractometer in the 2θ range of $15^\circ - 80^\circ$ degrees with $\text{Cu-K}\alpha$ radiation at room temperature. The magnetic measurements as M-H curve of all samples was studied with help of pulse field hysteresis loop tracer technique at room temperature with applied magnetic field of 5000 Oe.

RESULTS AND DISCUSSION

X-Ray diffraction studies

The phase identification and structural analysis of the NiFe_2O_4 and $\text{Ni}_{0.6}\text{Zn}_{0.4}\text{O}_4$ nanoparticles was done by XRD studies and the XRD patterns are shown in figure 1 which has the sharp and intense peaks. All the peaks were indexed by comparing them with the JCPD Card no. 019-0629 [12]. The presence of planes (220), (311), (222), (400), (422), (511), (440) and (533) in the XRD pattern reveals the cubic spinel structure of all the samples. The obtained XRD pattern exhibits the single phase cubic spinel structure since there is no other impurity peak and the only allowed peaks of cubic structure were observed. The structural parameters such as lattice parameter, crystallite size, unit cell volume and X-ray density were obtained using XRD data and their values are tabulated in table 1. It is observed from table 1 that, the lattice constant, X-ray density etc. are in the reported range. The crystallite size obtained through Scherrer's formula is found to be 20.87 nm which confirmed the

nanocrystalline nature of the sample. The structural parameters and crystallite size obtained in the present case are better than the reported values. The doping of nonmagnetic zinc ion in place of Ni ions in nickel ferrite leads to increase in lattice constant and hence increase in unit cell volume and X-ray density. The increase in lattice constant is attributed to lower ionic radii of Ni ions (0.78\AA) as compared to Zn ions (0.82\AA).

Magnetic studies

The M-H curve recorded at room temperature of NiFe_2O_4 and $\text{Ni}_{0.6}\text{Zn}_{0.4}\text{O}_4$ nanoparticles is depicted in figure 2 which represents the dependence of the magnetization (M) over the applied magnetic field (H) of nickel ferrite nanoparticles. These nanoparticles exhibit the ferrimagnetic nature which can be characterized by hysteresis loop with the magnetic parameters as saturation magnetization (M_s), remanence magnetization (M_r) and coercivity (H_c). The values of these magnetic parameters are tabulated in table 2.

Table 1 Lattice parameter (a), Unit cell volume (V), Crystallite size (t), X-ray density (d_x), Bulk density (d_B), and Porosity (P) of nickel ferrite nanoparticles

Sample	a (\AA)	V (cm^3)	t (nm)	d_x (gm/cm^3)	d_B (gm/cm^3)	P (%)
NF	8.334	578.9	20.875	5.379	3.638	32
NZF	8.376	587.6	18.028	5.359	3.587	33

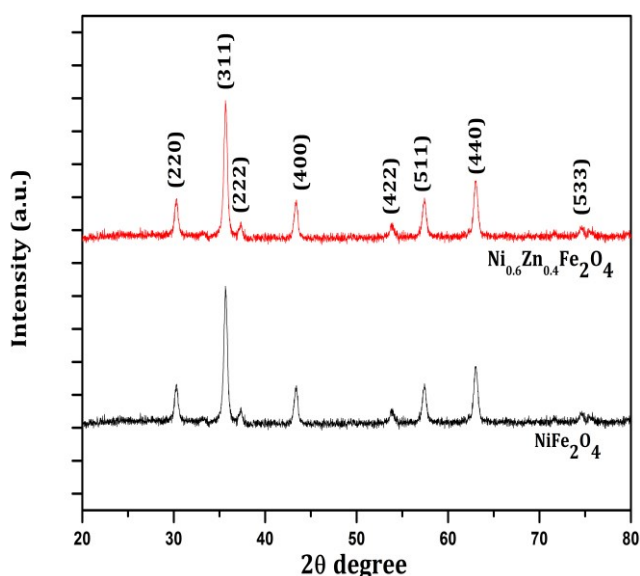


Figure 1: XRD patterns of NiFe_2O_4 and $\text{Ni}_{0.6}\text{Zn}_{0.4}\text{O}_4$ nanoparticles

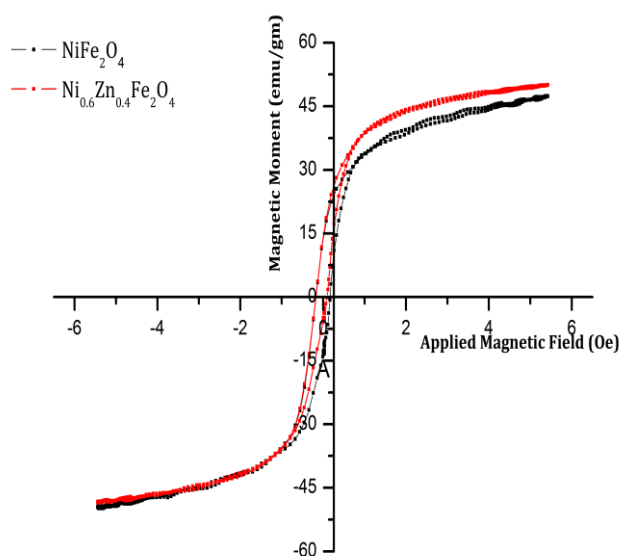


Figure 2: M-H curve of NiFe_2O_4 and $\text{Ni}_{0.6}\text{Zn}_{0.4}\text{O}_4$ nanoparticles

Table 2 Saturation magnetization (M_s), remanence magnetization (M_r), coercivity (H_c), remanence ratio (R) and magneton number (n_B) of nickel ferrite nanoparticle

Sample	M_s (emu/gm)	M_r (emu/gm)	H_c (Oe)	M_r/M_s	n_B (μ_B)
NF	47.44	13.64	170.07	0.287	1.9909
NZF	83.44	12.51	104.54	0.149	3.5417

It is observed from the table 2 that the values of saturation magnetization and other magnetic parameters are in close agreement with that reports in literature. However, we observed enhanced values of magnetic parameters. The doping of Zn ions leads to decrease in saturation magnetization and other magnetic parameters. This is because of the facts that, zinc ion are nonmagnetic in nature with zero magnetic moment which replaces magnetic Ni ions with two magnetic moment. Thus, the magnetic structure dilutes due to the doping of zinc ions. Further, the decrease in magnetization also may be due to the decrease in A-B interaction as zinc ions have a strong preference towards tetrahedral A site.

CONCLUSION

Urea assisted sol-gel synthesis of nickel ferrite produces high quality nanocrystalline particles with better structural and enhanced magnetic properties. The doping of Zn ions increases lattice constant and other structural parameters but decreases magnetic properties very significantly.

REFERENCES

- Harris VG, Geiler A, Chen Y, Yoon SD, Wu M, Yang A, Chen Z, He P, Parimi PV, Zuo X, Recent advances in processing and applications of microwave ferrites, *Journal of Magnetism and Magnetic Materials*, 2009; 321: 2035-2047.
- Sharifi I, Shokrollahi H, Amiri S, Ferrite-based magnetic nanofluids used in hyperthermia applications, *Journal of Magnetism and Magnetic Materials*, 2012; 324 :903-915.
- Reddy DHK, Yun YS, Spinel ferrite magnetic adsorbents: alternative future materials for water purification?, *Coordination Chemistry Reviews*, 2016;315 : 90-111.
- Liu C, Zou B, Rondinone AJ, Zhang ZJ, Chemical control of superparamagnetic properties of magnesium and cobalt spinel ferrite nanoparticles through atomic level magnetic couplings, *Journal of the American Chemical Society*, 2000;122:6263-6267.
- Sutka A, Mezinskis G, Sol-gel auto-combustion synthesis of spinel-type ferrite nanomaterials, *Frontiers of Materials Science*, 2012: 1-14.
- Kim YI, Kim D, Lee CS, Synthesis and characterization of $CoFe_2O_4$ magnetic nanoparticles prepared by temperature-controlled coprecipitation method, *Physica B: Condensed Matter*, 2003;337 42-51.
- Srivastava M, Chaubey S, Ojha AK, Investigation on size dependent structural and magnetic behavior of nickel ferrite nanoparticles prepared by sol-gel and hydrothermal methods, *Materials Chemistry and Physics*, 2009;118: 174-180.
- Mathew DS, Juang RS, An overview of the structure and magnetism of spinel ferrite nanoparticles and their synthesis in microemulsions, *Chemical Engineering Journal*, 2007;129:51-65.
- Kambale R, Shaikh P, Kamble S, Kolekar Y, Effect of cobalt substitution on structural, magnetic and electric properties of nickel ferrite, *Journal of Alloys and Compounds*, 2009;478:599-603.
- Sertkol M, Köseoğlu Y, Baykal A, Kavas H, Toprak MS, Synthesis and magnetic characterization of $Zn_{0.7}Ni_{0.3}Fe_2O_4$ nanoparticles via microwave-assisted combustion route, *Journal of Magnetism and Magnetic Materials*, 2010;322:866-871.
- Costa ACF, Morelli MR, Kiminami RH, Combustion synthesis: effect of urea on the reaction and characteristics of Ni-Zn ferrite powders, *Journal of Materials Synthesis and Processing*, 2001; 9: 347-352.
- Ren S, Prakash R, Wang D, Chakravadhanula VSK, Fichtner M, Fe_3O_4 Anchored onto Helical Carbon Nanofibers as High-Performance Anode in Lithium-Ion Batteries, *ChemSusChem*, 2012;5: 1397-1400.

Selective low-temperature chlorine gas sensing properties of bio-inspired nanocrystalline TiO₂

Ekar SU¹, Wani PN², Shaikh SF¹, Nakate UT³, Ghule BG¹, Shinde PV¹, Raut SD¹, Jadhav VV⁴, Jadhav SS⁵, Kholam YB^{6*} and Mane RS^{1*}

¹Centre for Nano-materials and Energy Devices, School of Physical Sciences, Swami Ramanand Teerth Marathwada University, Nanded 431606, M.S., India.,

²Department of Physics, Prof. Ramkrishna More College, Akurdi, Pune 411 044, M.S., India.,

³School of Semiconductor and Chemical Engineering, Semiconductor Physics Research Center (SPRC) Chonbuk National University, Jeonju 54899, Jeollabuk-do, Republic of Korea (South Korea),

⁴Department of Physics, Shivaji Mahavidyalaya, Udgir 413517, M.S., India.,

⁵D. S. M. Arts, Commerce and Science College, Jintur, Parbhani 431 509, M.S., India.,

⁶Department of Physics, Baburaoji Gholap College, Sangvi, Pune 411 027, M.S., India

*Corresponding author Email: rajarammane70@gmail.com ykhollam@yahoo.co.in

Manuscript Details

Available online on <http://www.irjse.in>
ISSN: 2322-0015

Editor: Dr. Arvind Chavhan

Cite this article as:

Ekar SU, Wani PN, Shaikh SF, Nakate UT, Ghule BG, Shinde PV, Raut SD, Jadhav VV, Jadhav SS, Kholam YB and Mane RS. Selective low-temperature chlorine gas sensing properties of bio-inspired nanocrystalline TiO₂. *Int. Res. Journal of Science & Engineering*, December 2017; Special Issue A1 : 81-86.

© The Author(s). 2017 Open Access

This article is distributed under the terms of the Creative Commons Attribution 4.0 International License

(<http://creativecommons.org/licenses/by/4.0/>),

which permits unrestricted use, distribution, and reproduction in any medium, provided you give appropriate credit to the original author(s) and the source, provide a link to the Creative Commons license, and indicate if changes were made.

ABSTRACT

TiO₂ nanoparticles (NPs) synthesized by using bio-inspired green method have shown selective low temperature gas sensing properties for Cl₂ gas. The TiO₂ NPs are characterized for their structures, morphologies, and optical studies by various means: X-ray diffraction, field emission scanning electron microscopy and UV-visible spectroscopy respectively. The average crystallite-size and band-gap of TiO₂ NPs are found to be respectively 7.2 nm and 3.3 eV. The TiO₂ NPs demonstrate good sensitivity towards chlorine (Cl₂) gas where TiO₂ NPs reveals Cl₂ gas response of 57 % at 250 °C operating temperature with response time of 97 s for 100 ppm concentration. The Cl₂ gas sensing properties are investigated for lower range 5 ppm to higher range 400 ppm. In further studies responses of TiO₂ as function of operating temperature and gas concentration are explored in addition to repeatability and stability measurements.

Keywords: Bio-synthesis, TiO₂, Cl₂ sensor, Low-temperature sensitivity, Selectivity.

INTRODUCTION

Over the decades, semiconducting wide band-gap metal oxides are being potential materials in various areas of applications such as biomedical, water purification, solar cells, chemical and biological sensors and so on [1-6]. The semiconducting metal oxides, such as ZnO [7], SnO₂ [8], WO₃ [9], NiO [10], TiO₂ [11] etc., have gained attention among the solid-state sensors due to their low-costs, eco-friendly nature, availability in different dimensions, compatibility, and low-power consumption methods. The major challenges in gas sensors include fast response, low working temperature and good selectivity etc. The rapid response of sensor gives early warning or message in order to monitor the environmental gas presence. The metal oxide-based gas sensors working at higher working temperature cause for ignition of fire related accidents and also consume more energy. They reveal sensing characteristic for multiple gases. Hence, it is necessary to fabricate sensors having high selectivity towards particular gas. The chlorine (Cl₂) is one of the poisonous gases that can cause health problems upon its inhalation. Moreover, also it is highly irritating, extremely reactive, destructive to living tissues and potentially lethal. Thereby, developing low-temperature Cl₂ gas sensors with good selectivity and fast response time is on priority. Till date, titanium dioxide (TiO₂) has not been much explored for gas sensors as there are a few reports available on TiO₂-based gas sensors even though it is non-toxic, abundantly available, cheap with excellent electrical and optical properties [12]. It is basically an *n*-type semiconducting wide-band gap material of promising applications not only in gas detection [13], solar cells, self-cleaning glasses, water purification, but also in food product industries as it shows potential biological activities like anti-fungal. This is because of the existence of three phases *viz.* rutile, anatase and brookite with different chemical, electrical, structural and optical properties. Further, the gas sensing properties can be improved in terms of fast response, low-operating temperature and good selectivity by decorating noble metal NPs on metal oxide sensor surface [14-22]. Several methods have been established for TiO₂ synthesis such as chemical bath deposition [12], sol-gel [23], hydrothermal [24] and so

on. Researchers also are attracting to develop biological methods [25-27], which are basically eco-friendly and have several advantages over chemical methods low synthesis temperature, cost-effective and free from chemical reactions that eventually produce hazardous waste as by-products.

Present work is novel in terms of both i.e. synthesis of TiO₂ NPs and Cl₂ gas sensor application. Efforts have been made to study the selectivity and gas sensing properties of TiO₂ NPs. For this purpose, in the present work, bio-synthesized TiO₂ NPs were envisaged for gas sensing application. The TiO₂ NPs were characterized by using standard material characterization tools. The gas sensing properties of TiO₂ NPs were investigated for various gases where Cl₂ has revealed an optimum performance thereby, the Cl₂ sensing properties were performed as function of operating temperature and gas concentration with error limit. The transient responses for both sensors were also studied for knowing respective response and recovery time values. The repeatability and stability tests of both sensor materials were recorded and reported.

METHODOLOGY

The biosynthesis method used for the synthesis TiO₂ nanoparticles (NPs) was adopted from our previous report Ekar et al. [27]. In a typical biosynthesis process, the extract of *Ganoderma* mushroom was prepared by boiling *Ganoderma* mushroom fine powder in 100 ml double distilled water at 85 °C for 15 min. The extract was filtered and stored as a stock solution at 4 °C. The 0.15 M titanium (Ti) precursor solution in ethyl alcohol was prepared by using titanium tetraisopropoxide. The 5 ml of extract was drop-wise added into 50 ml of 0.5 M Ti-precursor solution. The as-prepared precipitate was dried and annealed at 450 °C for 2 h to obtain TiO₂ powder. The glass pieces of 2 cm x 6 cm dimensions were used as substrates for preparation of sensor film of as-annealed TiO₂ powder by using doctor-blade method. The glass substrates were cleaned by using soap solution followed by ultrasonication in deionized water and ethanol. For making sensor film on pre-cleaned glass substrate, 0.1 gm/ml concentration of

TiO₂ powder in deionized water was used in the presence of polyvinyl alcohol binder. The resultant as-prepared film was air-annealed at 200 °C for 2 h in order to remove binder. The TiO₂ NPs film was employed for materials characterizations and gas sensing properties measurements by various means. The materials characterization of films was done by using X-ray diffraction, field emission scanning electron microscopy and UV-Visible spectroscopy. To study the gas sensing characteristics, two silver contacts at 10 mm apart from each other were given on the top surface of TiO₂ NPs sensor film by using commercial silver paste.

The sensor film was mounted onto a heating plate in a sealed chamber and measured stabilized resistances (R_a) in the air and (R_g) in the presence of target gas. The gas response was obtained by using the relation (1).

$$S (\%) = \frac{|R_a - R_g|}{R_a} * 100 \quad (1)$$

The gas sensing properties of TiO₂ NPs films were obtained by using a computer interfaced home-built static gas sensing system.

RESULTS AND DISCUSSION

The X-ray diffraction (XRD) pattern of pure TiO₂ NPs film is shown in figure -1. The presence of diffraction peaks in XRD pattern confirm the pyramidal crystal structure with anatase phase (JCPDS card no. 21-1272) [5, 24, 27] in resultant film. The occurrence of sharp

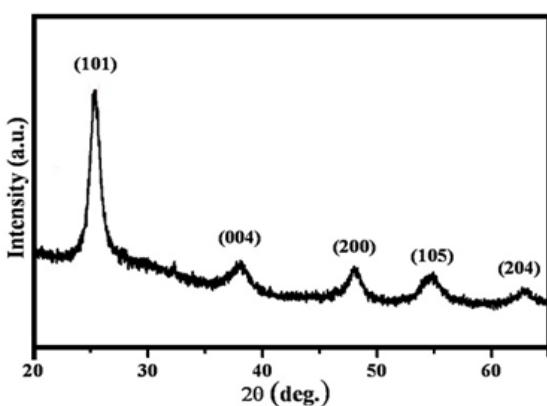


Figure 1. The X-ray diffraction (XRD) pattern of pure TiO₂ NPs film

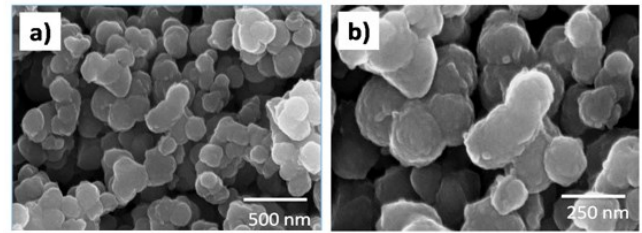


Figure2. Field emission scanning electron micrographs (FESEM) of TiO₂ NPs films at two different magnifications.

diffraction peaks indicates good crystallization and involvement of no impurity peaks. It reported that the gas sensing properties of sensors based on metal oxides are influenced by structural parameters such as crystallite-size, texture coefficient (TC), dislocation densities [28 - 31] etc. The average value of crystallite size obtained from all diffraction peaks by using Scherer's relation is found to be of 7.2 nm. The maximum TC value of 1.22 is associated with (101) plane, which indicates the preferred growth direction of as-prepared TiO₂.

The field emission scanning electron micrographs (FESEM) of TiO₂ NPs films at two different magnifications were carried out and are shown in figure - 2 (a-b). The nanoparticles (NPs)-like morphology of TiO₂ is confirmed from FESEM images. The energy dispersive spectrum (EDS) of TiO₂ NPs film surface showed the presence of peaks corresponding to only Ti and O. This confirms the purity of result films. The optical properties of TiO₂ NPs film was investigated by using UV-Visible spectroscopy. The UV-visible spectrum of TiO₂ NPs film is shown in figure -3. The UV absorbance peak was observed in ultra-violet region. The optical band gap value of TiO₂ NPs film was estimated from Tauc plot. The Tauc's relation of photon energy ($h\nu$) with absorption coefficient (α) is given as [3] in relation (2).

$$\alpha = \frac{\alpha_0 (h\nu - E_g)^n}{h\nu} \quad (2)$$

where, E_g = band gap energy, α = absorption coefficient, α_0 = constant.

The value of 'n' depends on the type of transition. The 'n' has values 1/2. The Tauc plot is shown as a inset of figure - 3. The optical energy band gap energy of TiO₂ NPs film is calculated to be 3.3 eV.

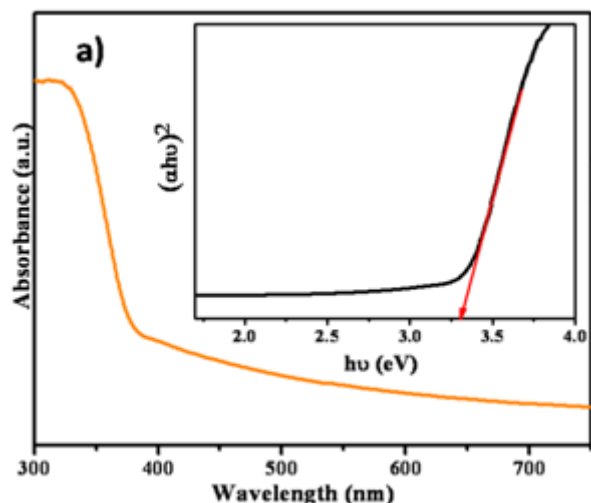


Figure 3. UV-visible spectrum of TiO₂ NPs film (inset: Tauc plot- variation of $(\alpha h\nu)^2$ versus photon energy, $h\nu$ (eV))

The TiO₂ NPs films were investigated for gas sensing properties. Generally, metal oxide gas sensors work at higher operating temperatures i.e. ≥ 150 °C. The adsorption/desorption of target gas molecules get affected due to increasing operating temperature. Optimization of operating temperature of present sensor is essential.

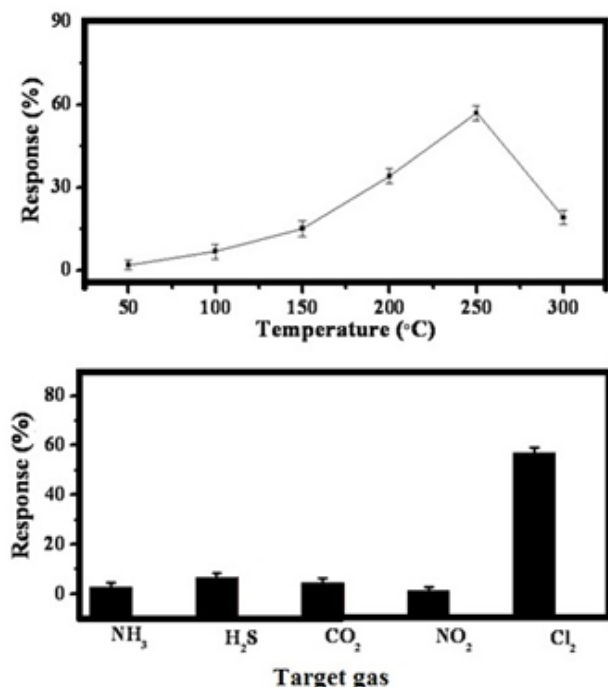


Figure 4. The variation of sensor response at different operating temperatures for TiO₂ NPs film at 100 ppm of Cl₂ target gas (Top) and sensor response for TiO₂ NPs film at 100 ppm for different test gases.

The sensors were studied for Cl₂ (keeping 100 ppm) at various operating temperatures (figure - 4 top). It was observed that the TiO₂ NPs film reveals highest Cl₂ response of 57 % at 250 °C operating temperature. Involvement of oxygen vacancies, which act as defects, is responsible for an *n*-type semiconducting behaviour of TiO₂. Hence, electrons are the majority charge carriers in conduction band. The basis for sensor working is the change of its resistance on the exposure of the target gas. The resistance of TiO₂ NPs sensor film is increased after Cl₂ gas exposure. A typical Cl₂ gas sensing mechanism has been explained for '*n*' type metal oxide semiconductor gas sensor by Navale et al. [32].

These sensors are further employed to check their responses for various gases besides Cl₂ such as NH₃, H₂S, CO₂, NO₂. The figure - 4 (bottom) gives the sensor response for TiO₂ NPs film at 100 ppm for different test gases: NH₃, H₂S, CO₂, NO₂ and Cl₂. It is observed that present sensors have good selectivity towards Cl₂ gas. The transient Cl₂ gas responses for TiO₂ NPs film sensors are also studied. As the Cl₂ gas injected in testing system, the target gas molecules diffuse through air and gets adsorbed onto the sensor surface for catalytic sensing reaction with time. As the time progresses, this sensor shows response in increasing order till saturation or equilibrium level for given concentration of target gas is achieved. At saturation level, sensor shows constant response. After gas testing system opened to an external atmosphere, the target gas molecules start desorbing and corresponding sensor response also decreases. The time taken by sensor to reach 90% of change in response or resistance value for given concentration of target gas is nothing but the response time. Similarly, recovery time can be also recorded. The response time value for TiO₂ NPs film sensor is recorded to be 97 s. The recovery time value for TiO₂ NPs film sensor is found to be 56 s.

The repeatability and transient gas response studies for TiO₂ NPs films are also studied. The good repeatabilities are observed for TiO₂ NPs film sensor at 100 ppm concentration of Cl₂ target gas.

The Cl₂ concentration effect on the gas response and stability for TiO₂ NPs film sensor was performed. The

figure – 5 (top) gives the variation of TiO₂ NPs film sensor response at different concentration (ppm) of Cl₂ target gas. The Cl₂ gas concentration was varied from 5 to 400 ppm for both the sensors. It is observed that both the sensors show lower gas response for less concentration of Cl₂ gas. As concentration of Cl₂ increases the corresponding responses are also increased.

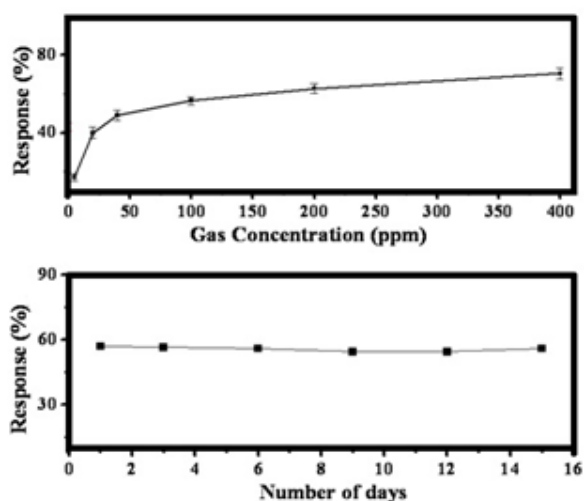


Figure 5. Variation of TiO₂ NPs film sensor response at different concentration (ppm) of Cl₂ target gas (top) and variation of TiO₂ NPs film sensor response at 100 ppm of Cl₂ target gas at different time intervals (bottom)

The response to maximum Cl₂ gas concentration is restricted by available area of sensor surface. As sensor surface area is limited, the sensor gets saturated meaning shows constant response for higher gas concentration. The stability of sensors was confirmed after periodic time interval. The figure – 5 (bottom) gives the variation TiO₂ NPs film sensor response for 100 ppm concentration of Cl₂ target gas at different time interval. It is observed that sensor shows good stability. All gas sensing studies were performed several times with good repeatability and stability with standard.

CONCLUSION

In summary, bio-synthesized TiO₂ NPs film sensors are characterized for their structures and morphologies and investigated for gas sensing

properties. The sensors show good selectivity towards Cl₂ gas sensing. The TiO₂ sensor shows highest Cl₂ gas response of 57 % for 100 ppm at 250 °C operating temperature. The response and recovery times for TiO₂ NPs film sensor are found to be 97 s and 56 s respectively. The lower Cl₂ detection is observed at 5 ppm concentration whereas, for higher concentration at 400 ppm. The present sensors highlight good repeatability and stability for Cl₂ sensing. Bio-synthesis of TiO₂ is economical method and is an easy way for developing commercial gas sensors.

Conflicts of interest: The authors stated that no conflicts of interest.

REFERENCES

1. Nakate UT, Patil P, Bulakhe RN, Lokhande CD, Kale SN, Naushad M, and Mane RS. Sprayed zinc oxide films: Ultra-violet light-induced reversible surface wettability and platinum-sensitization-assisted improved liquefied petroleum gas response, *J. Coll. Interfaces Sci.*, 2016; 480: 109-117.
2. Mirzaei H, and Darroudi M. Zinc oxide nanoparticles: Biological synthesis and biomedical applications, *Ceram. Inter.*, 2017; 43(1): 907-914.
3. Zhang J, Shao Y, Hsieh CT, Chen YF, Su TC, Hsu JP, and Juang RS. Synthesis of magnetic iron oxide nanoparticles onto fluorinated carbon fabrics for contaminant removal and oil-water separation, *Separ. Purif. Tech.*, 2017; 174: 312-319.
4. Dhamodharan P, Manoharan C, Bououdina M, Venkadachalopathy R, and Ramalingam S. Al-doped ZnO thin films grown onto ITO substrates as photoanode in dye sensitized solar cell, *Solar Ener.*, 2017; 141: 127-144.
5. Krško O, Plecenik T, Roch T, Grančič B, Satrapinsky L, Truchlý M, Ďurina P, Gregor M, Kúš P, and Plecenik A. Flexible highly sensitive hydrogen gas sensor based on a TiO₂ thin film on polyimide foil, *Sens. Actuators B: Chem.*, 2017; 240: 1058-1065.
6. Mishra RK, Upadhyay SB, Kushwaha A, Kim TH, Murali G, Verma R, Srivastava M, Singh J, Sahayb PP, and Lee SH. SnO₂ quantum dots decorated on RGO: a superior sensitive, selective and reproducible performance for a H₂ and LPG sensor, *Nanoscale*, 2015; 7(28): 11971-11979.
7. Zhang Y, Liu C, Gong F, Jiu B, and Li F. Large scale synthesis of hexagonal simonkolleite nanosheets for ZnO gas sensors with enhanced performances, *Mater. Lett.*, 2017; 186: 7-11.
8. Liu Y, Huang J, Yang J, and Wang S. Pt nanoparticles functionalized 3D SnO₂ nanoflowers for gas sensor

- application, *Solid-State Electronics*, 2017; 130: 20-27.
9. Shendage SS, Patil VL, Vanalakar SA, Patil SP, Harale NS, Bhosale JL, Kim JH, and Patil PS. Sensitive and selective NO₂ gas sensor based on WO₃ nanoplates, *Sens. Actuators B: Chem.*, 2017; 240: 426-433.
 10. Cindemir U, Trawka M, Smulko J, Granqvist CG, Österlund L, and Niklasson GA, Fluctuation-enhanced and conductometric gas sensing with nanocrystalline NiO thin films: A comparison, *Sens. Actuators B: Chem.*, 2017; 242: 132-139.
 11. Wang Y, Liu J, Wang M, Pei C, Liu B, Yuan Y, Liu S, and Yang H. Enhancing the sensing properties of TiO₂ nanosheets with exposed {001} facets by a hydrogenation and sensing mechanism, *Inorg. Chem.*, 2017; 56 (3): 1504-1510.
 12. Singh AK, Patil SB, Nakate UT, and Gurav KV. Effect of Pd and Au sensitization of bath deposited flowerlike TiO₂ thin films on CO sensing and photocatalytic properties, *J. Chem.*, 2013; Article ID 370578.
 13. Eranna G. Metal oxide nanostructures as gas sensing devices; CRC Press: Boca Raton, FL, U.S.A., 2012.
 14. Nakate UT, Bulakhe RN, Lokhande CD, and Kale SN. Au sensitized ZnO nanorods for enhanced liquefied petroleum gas sensing properties, *Appl. Surf. Sci.*, 2016; 371: 224-230.
 15. Zou AL, Qiu Y, Yu JJ, Yin B, Cao GY, Zhang HQ, and Hu LZ. Ethanol sensing with Au-modified ZnO microwires, *Sens. Actuators B: Chem.*, 2016; 227: 65-72.
 16. Kaneti YV, Yue J, Moriceau J, Chen C, Liu M, Yuan Y, Jiang X, and Yu A. Experimental and theoretical studies on noble metal decorated tin oxide flower-like nanorods with high ethanol sensing performance, *Sens. Actuators B: Chem.*, 2016; 219: 83-93.
 17. Samerjai T, Liewhiran C, Wisitsoraat A, Tuantranont A, Khanta C, and Phanichphant S. Highly selective hydrogen sensing of Pt-loaded WO₃ synthesized by hydrothermal/impregnation methods, *Int. J. Hydrogen Energy*, 2014; 39: 6120-6128.
 18. Tong PV, Hoa ND, Duy NV, Le DTT, and Hieu NV. Enhancement of gas-sensing characteristics of hydrothermally synthesized WO₃ nanorods by surface decoration with Pd nanoparticles, *Sens. Actuators B: Chem.*, 2016; 223: 453-460.
 19. Samerjai T, Tamaekong N, Liewhiran C, Wisitsoraat A, and Phanichphant S. NO₂ gas sensing of flame-made Pt-loaded WO₃ thick films, *J. Solid State Chem.*, 2014; 214: 47-52.
 20. Şennik E, Onur Alev, and Öztürk ZZ. The effect of Pd on the H₂ and CO sensing properties of TiO₂ nanorods, *Sens. Actuators B: Chem.*, 2016; 229: 692-700.
 21. Trunga DD, Hoaa ND, Tonga PV, Duya NV, Daob TD, Chungb HV, Nagaob T, and Nguyen Van Hieu. Effective decoration of Pd nanoparticles on the surface of SnO₂ nanowires for enhancement of CO gas-sensing performance, *J. Hazard. Mater.*, 2014; 265: 124-132.
 22. Salunkhe RR, Dhawale DS, Patil UM, and Lokhande CD. Improved response of CdO nanorods towards liquefied petroleum gas (LPG): effect of Pd sensitization, *Sens. Actuators B: Chem.*, 2009; 136: 39-44.
 23. Yin Q, Wang X, Zhang K, Guo X, and Shen G. Fabrication of mesoporous TiO₂ with high crystallinity by a fast sol-gel method, *J. Porous Mater.*, 2017; 24(1): 157-163.
 24. Huang X, Meng L, Du M, and Li Y. TiO₂ nanorods: hydrothermal fabrication and photocatalytic activities, *J. Mater. Sci. Mater. Elect.*, 2016; 27(7): 7222 - 7226.
 25. Jayaseelan C, Rahuman AA, Roopan SM, Kirthi AV, Venkatesan J, Kim SK, Iyappan M, and Siva C. Biological approach to synthesize TiO₂ nanoparticles using *Aeromonas hydrophila* and its antibacterial activity, *Spectrochimica Acta Part A: Molecular and Biomolecular Spectroscopy*, 2013; 107: 82-89.
 26. Tarafdar A, Raliya R, Wang WN, Biswas P, and Tarafdar JC. Green synthesis of TiO₂ nanoparticle using *Aspergillus tubingensis*, *Adv. Sci., Engg. & Medicine*, 2013; 5 (9): 943-949.
 27. Ekar SU, Shekhar G, Kholam YB, Wani PN, Jadhav SR, Naushad M, Chaskar MG, Jadhav SS, Fadel A, Jadhav VV, Shendkar JH, and Mane RS. Green synthesis and dye-sensitized solar cell application of rutile and anatase TiO₂ nanorods, *J. Solid State Electrochem.* DOI 10.1007/s10008-016-3376-3.
 28. Xu C, Tamaki J, Miura N, and Yamazoe N. Grain size effects on gas sensitivity of porous SnO₂-based elements, *Sens. Actuators B: Chem.*, 1991; 3(2): 147-155.
 29. Kumar M, Kumar A, and Abhyankar AC. Influence of texture coefficient on surface morphology and sensing properties of W-doped nanocrystalline tin oxide thin films, *Appl. Mater. Interfaces*, 2015; 7(6): 3571-3580.
 30. Singh I, and Bedi RK. Studies and correlation among the structural, electrical and gas response properties of aerosol spray deposited self assembled nanocrystalline CuO, *Appl. Sur. Sci.*, 2011; 257: 7592-7599.
 31. Jimenez I, Arbiol J, Dezaneeau G, Cornet A, and Morante JR. Crystalline structure, defects and gas sensor response to NO₂ and H₂S of tungsten trioxide nanopowders, *Sens. Actuators B: Chem.*, 2003; 93: 475-485.
 32. Navale ST, Jadhav VV, Tehare KK, Sagara RUR, Biswasa CS, Galluzzi M, Liang W, Patil VB, Mane RS, and Stadler FJ. Solid-state synthesis strategy of ZnO nanoparticles for the rapid detection of hazardous Cl₂, *Sens. Actuators B: Chem.*, 2017; 238: 1102-1110.

Synthesis and Characterization of Gd doped Y_2O_3 Phosphor Material

Kale Sanjay R¹ and Thube Dilip R²

¹Post-Graduate Department of Chemistry, Tuljaram Chaturchand College of Arts, Science and Commerce, Baramati, 413 102, Dist. Pune. Maharashtra (INDIA),²Post-Graduate Department of Chemistry and Research Center, New Arts Commerce and Science College, Parner, 414 302 Dist-Ahmednagar. Maharashtra (INDIA)
E-mail: kalesanjay29@gmail.com (* Corresponding Author)

Manuscript Details

Available online on <http://www.irjse.in>
ISSN: 2322-0015

Editor: Dr. Arvind Chavhan

Cite this article as:

Kale Sanjay R and Thube Dilip R. Synthesis and Characterization of Gd doped Y_2O_3 Phosphor Material, *Int. Res. Journal of Science & Engineering*, December 2017; Special Issue A1 : 87-90.

© The Author(s). 2017 Open Access

This article is distributed under the terms of the Creative Commons Attribution 4.0 International License

(<http://creativecommons.org/licenses/by/4.0/>), which permits unrestricted use, distribution, and reproduction in any medium, provided you give appropriate credit to the original author(s) and the source, provide a link to the Creative Commons license, and indicate if changes were made.

ABSTRACT

In particular, the nanostructures phosphor materials are of great interest as they offer brighter cathodoluminescence and much improved screen packing. Inorganic nanoparticles manifest unique size and shape (surface to volume ratio) dependent properties, which in some extent depend on their crystallinity, defect contents, and preparation techniques. In the present work we have synthesized phosphor material by homogenous coprecipitation method (HCP) using Y_2O_3 as host material and inner transition metal, Gd as dopant. The synthesized phosphor material has been analyzed by XRD, SEM, and FTIR for their morphology and by PL spectrophotometer for their luminescence property. Using obtained data the effect of concentration of dopant on morphology and luminescence property of phosphor material have been studied.

Keywords: phosphor, homogeneous coprecipitation method, $Y_2O_3:Gd^{3+}$, photoluminescence.

INTRODUCTION

In literature large numbers of reports are found on inner transition metal doped Y_2O_3 nanostructures with different morphologies. These materials have been synthesized by different methods such as gas phase condensation technique, sol-gel route, homogeneous coprecipitation, spray pyrolysis, and hydrothermal method by various research groups.

Y_2O_3 phosphors doped with rare earth (RE) ions are considered as promising candidate in the field of cathodoluminescent display, catalysis and lumino-phors due to their high chemical durability and thermal stability [1,2]. In some reports HCP method was described to synthesize Y_2O_3 : Eu red phosphors [3]. We observed few reports which describes synthesis of Y_2O_3 phosphors codoped with rare earth ions like Eu^{+3} , Gd^{+3} and Tb^{+3} for their color tunable properties [4,5]. Over last few years, $Y_2O_3:Ln^{3+}$ has been recognized as one of the best commercial color phosphors for plasma display panels (PDP) and Hg free fluorescent lamps. Synthesis of Eu^{3+} doped Y_2O_3 and effect of different surfactant on morphology of phosphors was reported [6]. Study on novel preparation method and luminescent properties of Eu^{3+} doped YBO_3 phosphors was reported [7]. Synthesis and characterization of Eu^{3+} doped Y_2O_3 (red phosphor) and Tb^{3+} doped Y_2O_3 (green phosphor) by hydrothermal method was reported [8]. Sensitization effect of Yb^{3+} in upconversion luminescence of Eu^{3+} codoped Y_2O_3 phosphor was reported [9]. Photoluminescence studies of Eu^{3+} doped Y_2O_3 phosphor was reported [10].

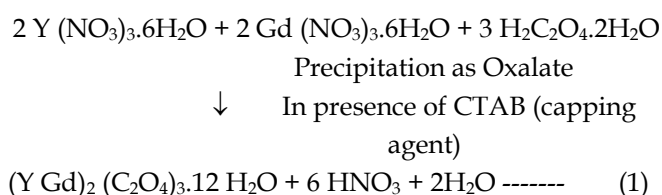
The present work describes the homogenous co precipitation method (HCP) for synthesis of inner transition metal ion, Gd^{3+} doped Y_2O_3 phosphor material in aqueous medium. The formed precipitate after sintering and calcinations gives nanostructure phosphor material in powder form. The nanostructure, $Y_2O_3: Gd^{3+}$ is obtained by changing, the concentration of dopant ion, time for precipitation and calcinations, with suitable capping agent. Thus, formed phosphors can be tested towards their homogenous crystallinity, high distribution and good luminescence intensity with required color- tunable properties.

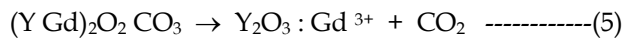
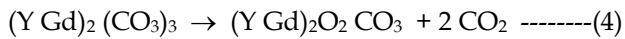
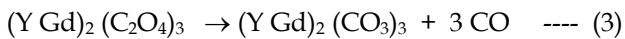
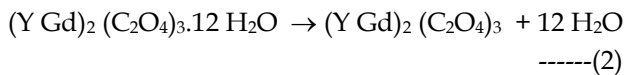
The characterization of phosphor material towards its crystalline phase can be done by X-ray analysis. The morphology and crystal size of samples can be determined by SEM, technique. The presence of desired constituents/ groups in as-synthesized product is determined by FTIR spectra. The photoluminescence characterization will be done by PL spectra at room temperature. Thus, formed phosphors shows wide ranged applications in various fields.

METHODOLOGY

The phosphor $Y_2O_3:Gd^{3+}$ are prepared by homogenous coprecipitation method (HCP) in aqueous medium offers comparatively low temperature route, higher crystal controllability. The starting materials, Yttrium Nitrate hexahydrate [$Y(NO_3)_3 \cdot 6H_2O$], Sigma-Aldrich (99.9%) and Gadolinium Nitrate hexahydrate [$Gd(NO_3)_3 \cdot 6H_2O$] Alfa-Aesar (99.9%) were purchased. Other chemicals, oxalic acid (AR grade) used, as precipitant and CTAB (Cetyl Trimethyl Ammonium Bromide) as a capping agent/surfactant were purchased from Loba Chemie Co. Ltd. The aqueous solution of mixed metal nitrate precursor was prepared in 25 ml DI water by taking [$Y(NO_3)_3 \cdot 6H_2O$] and [$Gd(NO_3)_3 \cdot 6H_2O$] in specific mole ratio represented as $[1-x \cdot Y(NO_3)_3 \cdot 6H_2O + x \cdot Gd(NO_3)_3 \cdot 6H_2O]$. Thus, prepared solution was kept on magnetic stirrer for one hour at $40^\circ C$. Afterwards, the aqueous solution of oxalic acid (precipitant) was added drop wise (4 drops per min.) in above prepared aqueous solution of mixed metal nitrate precursor in presence of 1-2 ml CTAB (capping agent) for 2 hours, with constant stirring on magnetic stirrer keeping temperature at about $40^\circ C$ and pH about 6.5 to 7.0. After complete addition of oxalic acid, thus formed precipitate was removed by filtration, dried under IR lamp. After step wise sintering and calcinations at about $800^\circ C$, for 4 hour we get stoichiometric white powdered phosphor material. For synthesis of $Y_2O_3 : Gd^{3+}$ phosphor material CTAB is used as capping agent/surfactant which control the particle size, avoids agglomeration effectively by forming reverse micelle. It reduces the oxygen bridge bonds between the particles.

The characterization of phosphor material was done by X-ray analysis, SEM, FTIR techniques. The photoluminescence characterization was done by PL spectra at room temperature. The step wise chemical reactions are represented in stepwise manner as follows:





RESULTS AND DISCUSSION

XRD analysis:

The crystalline phase formation in products, $(Y_{1-x} Gd_x)_2O_3$ prepared by HCP method was confirmed by X-ray diffraction pattern shown in Fig.1. It agrees with the standard JCPD data. The peaks at 20.16, 29.42, 33.14, 36.24, 40.17, 43.23, 48.34 and 57.47 corresponding to (211), (222), (400), (411), (332), (134), (440) and (622) respectively, show exact matching with JCPD data. The space group of Y_2O_3 is ($I \bar{a} 3$). Also the XRD pattern confirms single crystalline phase of product having cubic structure with comparable cell parameters (a/nm) as that of Y_2O_3 .¹¹ It indicates the substitution of Gd^{3+} in cation sites in host matrix of Y_2O_3 internally.

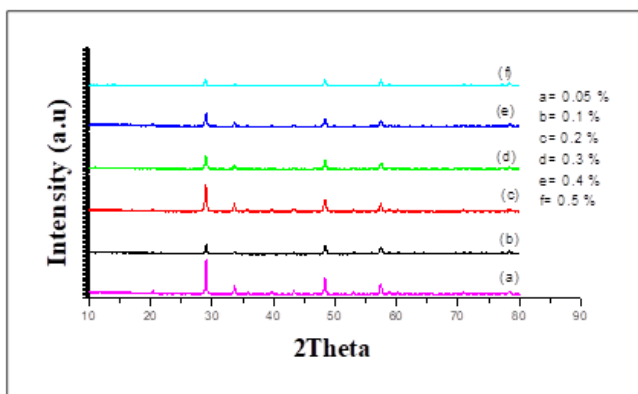


Fig.1: XRD patterns of $(Y_{1-x} Gd_x)_2O_3$ prepared by HCP method with variable concentration of dopant ($x= 0.05$ to 0.5 %)

SEM analysis:

The SEM image of $Y_2O_3 : Gd^{3+}$ ($x= 0.2$ %) crystal is shown in Fig.2. As can be seen, $Y_2O_3 : Gd^{3+}$ particles synthesized shows uniform shape and agglomerates of little spheres.

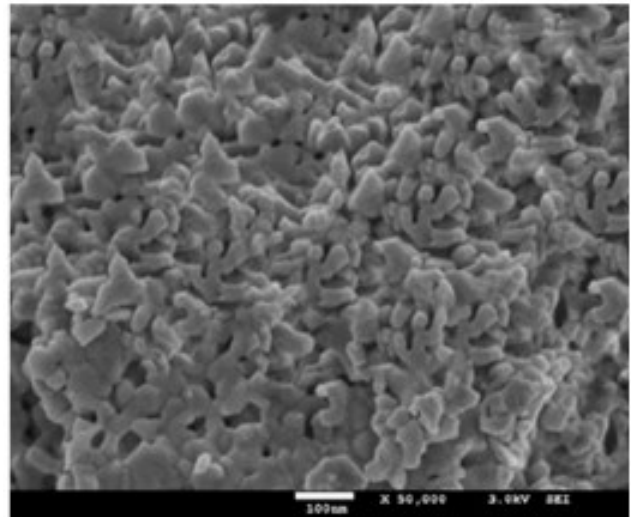


Fig.2: SEM image of $Y_2O_3 : Gd^{3+}$ ($x= 0.2$ %) phosphor prepared by HCP method.

FTIR spectra analysis:

The FTIR spectra of $Y_2O_3 : Gd^{3+}$ ($x= 0.2$ %) crystal is shown in Fig.3. It shows different peaks from $4000 - 600$ cm^{-1} confirms presence of all constituents in prepared phosphor.

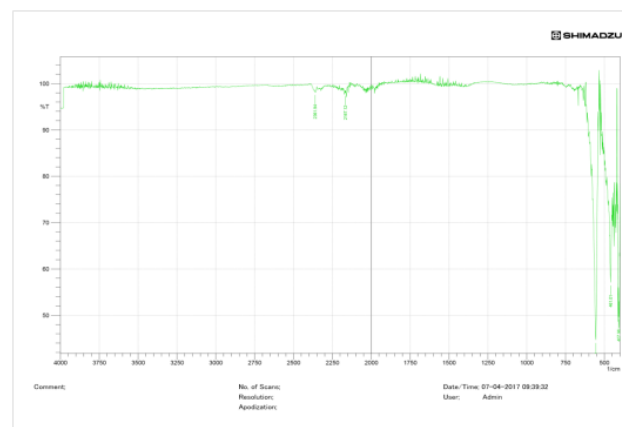


Fig.3: FTIR spectra of $Y_2O_3 : Gd^{3+}$ ($x= 0.2$ %) phosphor prepared by HCP method.

Luminescence properties:

The emission spectra of $Y_2O_3 : Gd^{3+}$ ($x= 0.2$ %) phosphor prepared by HCP method is shown in Fig.4. This spectrum is taken at room temperature using 220 nm Xenon lamps. It shows sharp emission line corresponding to $^5D_0 \rightarrow ^7F_2$ at 610 nm for Gd^{3+} dopant ion. The other emission lines corresponding to $^5D_0 \rightarrow ^7F_1$ ($J= 0, 1, 3, 4$) are also observed at 580, 590, 630, 660 nm are also observed. This observation confirms greater luminescence property of phosphor due to doping of Gd^{3+} of said concentration.

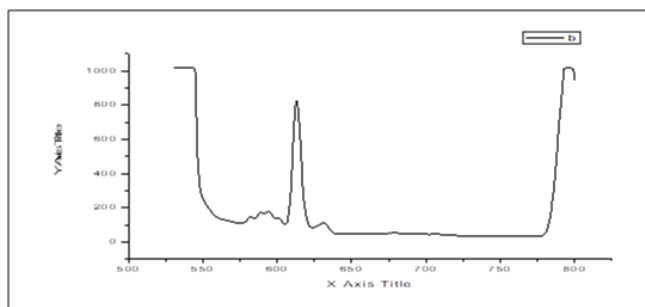


Fig. 4 : Photoluminescence emission spectra of $Y_2O_3 : Gd^{3+}$ ($x=0.2\%$) phosphor prepared by HCP method

CONCLUSION

The cubic crystalline phosphor $Y_2O_3 : Gd^{3+}$ was successfully prepared by HCP method. The results of XRD, SEM and FTIR investigation shows doping of Gd^{3+} in host matrix of Y_2O_3 . As compared with other methods phosphor prepared by HCP method shows comparable luminescent properties with less concentration of dopant ion. It is an efficient way to save the cost of the phosphor while luminescent properties are retained. Thus prepared $Y_2O_3 : Gd^{3+}$ color emitting phosphor used for display devices and lamp manufacturing.

Conflicts of interest: The authors stated that no conflicts of interest.

REFERENCES

1. Yen WM et.al. Phosphor Handbook, CRC Press, 2006.
2. Matuura D. *Appl. Phys. Lett.*, 2002, 81, (24).
3. Chi LS et.al. *J. Electrochem. Soc.* 152, 2005
4. Tu D. *J. Lumin.* 131, 2011
5. Atabaev et.al. *Nano. Res. Lett.* 7 (556), 2012
6. Jadhav et.al. *J. Phys. Chem. C* 2009, 113
7. Wankhede R. N. et.al. *Int. J. Sc. & Env.* (4) 2015
8. Singh R.P. et.al *WJNSE*, (2) 2012
9. Panday et.al. *J. Phys. Chem. Biophys.* (3.5) 2013
10. Srinivas M, *Ind. J. Sci. & Tech.* (10-18) 2017
11. Zhang Ming, et al *Trans. Nonferrous Met. Soc. China* 20 9115-118) 2010.

Preparation of MnS thin films by chemical bath deposition and effect of bath temperature on their optical properties

Sonavane DK^{*1}, Jare SK¹, Suryawanshi RV², Kathare RV³, Bulakhe RN⁴

¹P.G. Department of Electronic Science, New Arts, Commerce and Science College, Ahmednagar - 414001, India,

²Department of Electronic Science, Azad mahavidyalaya, AUSA, Latur-413520, India.

³Karmaveer Mamasahab Jagdale Mahavidyalaya, Washi, Osmanabad, 413503, India.

⁴School of Chemical Engineering, Yeungnam University, Gyeongsan, Gyeongbuk, 712-749, Republic of Korea

Manuscript Details

Available online on <http://www.irjse.in>
ISSN: 2322-0015

Editor: Dr. Arvind Chavhan

Cite this article as:

Sonavane DK, Jare SK, Suryawanshi RV, Kathare RV, Bulakhe RN. Preparation of MnS thin films by chemical bath deposition and effect of bath temperature on their optical properties, *Int. Res. Journal of Science & Engineering*, December 2017; Special Issue A1 : 91-94.

© The Author(s). 2017 Open Access

This article is distributed under the terms of the Creative Commons Attribution 4.0 International License

(<http://creativecommons.org/licenses/by/4.0/>), which permits unrestricted use, distribution, and reproduction in any medium, provided you give appropriate credit to the original author(s) and the source, provide a link to the Creative Commons license, and indicate if changes were made.

ABSTRACT

MnS thin films were deposited onto glass substrates by chemical bath deposition at different temperatures (40°C and 70°C). The deposition parameters such as deposition time, pH and concentrations of solution were optimized. The films were prepared from the mixture as the solution of manganous acetate tetrahydrate as a manganese ion source, thiourea as a sulphur ion source and triethanolamine (TEA) as a complexing agent. The MnS thin films were characterized by optical absorption spectroscopy and band gap energy were determined. The band gap energy is found to be in the range of 2.81-3.1eV.

Keywords: Optical properties, CBD method, Band gap, Thin films, Chemical synthesis.

INTRODUCTION

During the past few decades manganese chalcogenides (MnS, MnSe, MnTe etc.) have given much interest concerning their structural, chemical and physical properties [1-3]. Depending upon the deposition conditions, the structural, electrical and optical properties of these materials can be controlled in many ways [4]. The deposition of DMS materials in the thin films form has been the subject of intense research over the past few decades due to application in a variety of fields such as photoconductors, solar selective coatings, solar cells, antireflection coatings and optical mass

memories [5-6]. MnS thin films or powder can be found in several polymorphic forms: the rock salt type structure (α -MnS). Which is the most common form, by low temperature growing techniques it crystallizes into the Zincblend (β -MnS) or Wurtzite (γ -MnS) structure [7]. Many research groups have shown a great interest in the development of this material in the various deposition chemical and physical processes such as hydrothermal [8-10], radio-frequency sputtering [11-12], molecular beams epitaxy [13] and chemical bath deposition (CBD) [7, 14]. We have selected chemical bath deposition method because of its simple, inexpensive and convenient technique for large area deposition.

METHODOLOGY

2.1 Materials

All the chemicals used for the deposition were analytical grade. It includes manganous acetate tetrahydrate [$C_4H_6MnO_4 \cdot 4H_2O$], thiourea [$(H_2N)_2CS$], ammonia (NH_3), triethanolamine (TEA) [$(HOC_2H_4)_3N$]. All the solutions were prepared in distilled water. During the deposition, the triethanolamine was used as a complexing agent while manganous acetate tetrahydrate acted as a source of manganese ions and thiourea acted as a source of sulphide ions, respectively.

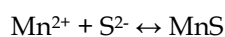
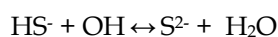
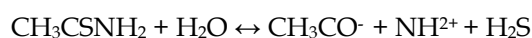
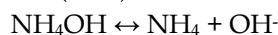
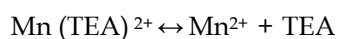
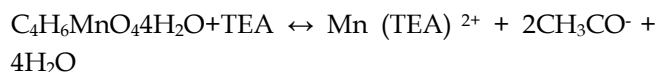
2.2 Cleaning procedure of glass substrate

The deposition was carried out using commercial glass slides of dimensions 25 mm X 30 mm X 1.2 mm. To maintain homogeneity and better quality of films the substrate surface must be cleaned scrupulously. The slides were washed with detergent and then boiled in concentrated chromic acid (0.5 M) for 1 hour. The substrates were then washed with distilled water. The substrates were then taken out and immersed in distilled water prior to the deposition.

2.3 Synthesis of MnS thin films

The deposition was carried out in a reactive solution prepared in a 250 ml beaker containing equimolar solutions of manganous acetate tetrahydrate, and thiourea. TEA was used as a complexing agent and a pH of the reaction mixture was adjusted to ~ 10 , with the help of ammonia solution. The resulting solution

was thoroughly mixed and stirred. Finally distilled water was added to make up the bath solution 200 ml, while stirring continued. The bath temperature was fixed at temperature ($40^\circ C$ and $70^\circ C$). Pre-treated substrates were inserted vertically into the beaker. After deposition for 7 hours, the substrates were taken out, washed with distilled water and dried in air. The probable reaction mechanism was carried out for the formation of MnS.



RESULTS AND DISCUSSION

The optical absorbance of the MnS thin films were measured by using Systronics, AU-2701, UV-VIS, Double beam spectrophotometer in the wavelength range 300 to 1100 nm. The film indicates a gradually increasing absorbance throughout the visible region, which makes it possible for this material to be used in the photo electrochemical cell. The absorption of these films was studied to evaluate the band gap (E_g). The fundamental absorption, which corresponds to electron excitation from the valence band to the conduction band [17] was used to determine the nature and the optical energy band gap. The optical absorption is characterizes the relation between the absorption coefficient (α) and photon energy ($h\nu$) for different allowed transition as

$$\alpha h\nu = A (h\nu - E_g)^n \quad (1)$$

Where α is the absorption coefficient, $h\nu$ is the photon energy, E_g is the optical band gap and A is the constant which is related to the efficient masses associated with the valence band and conduction band. To determine the possible transitions $(\alpha h\nu)^2$ versus $h\nu$ was plotted. The corresponding band gap energies were obtained from extrapolating the straight portion of the graph on the $h\nu$ axis at $(\alpha h\nu)^2 = 0$. Fig.2

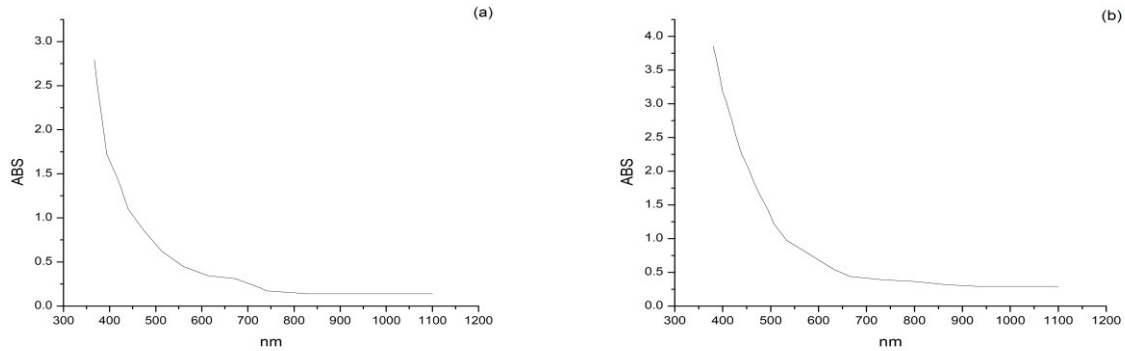


Fig.1: Optical absorbance spectra of the MnS thin film (a) 40°C (b) 70°C.

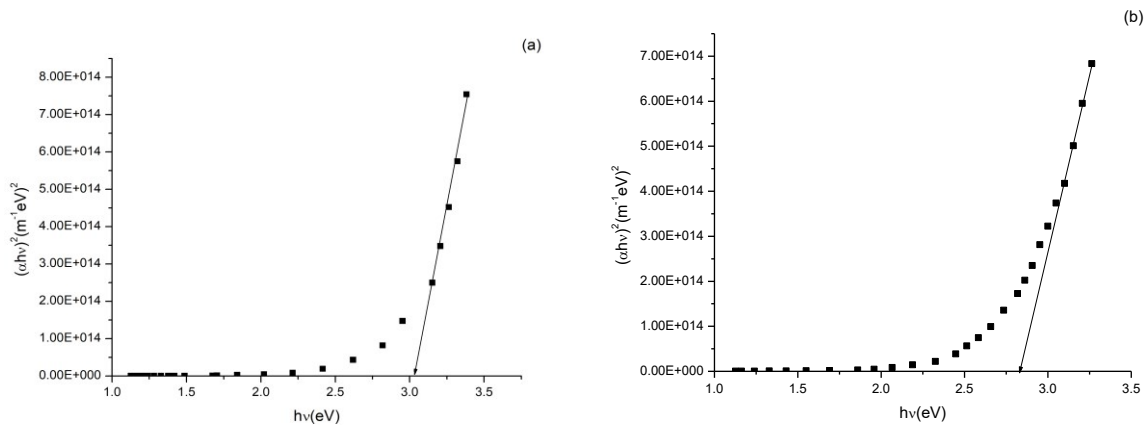


Fig.2: Plot of $(\alpha hv)^2$ versus $h\nu$ showing the estimation of direct band gap energy (a) 40°C (b) 70°C.

plot of $(\alpha hv)^2$ versus $h\nu$ shows band gap for MnS thin films deposited at different bath temperatures (40°C and 70°C). It is seen that the band gap values are decreases (3.1 to 2.81 eV) when the bath temperature is increased from 40°C to 70°C. The decrease in the band gap as a consequence of the increase in particle size is in conformation with the earlier studies. The obtained band gap width is consistent with the reported values [18].

CONCLUSION

MnS thin films have been prepared successfully using a chemical bath deposition technique onto glass substrates. The optical absorbance spectra of the MnS thin film indicates a gradually increasing absorbance throughout the visible region, which makes it possible for this material to be used in the photo electrochemical cell. It is seen that the band gap values are decreases (3.1 to 2.81 eV) when the bath

temperature is increased from 40°C to 70°C. The decrease in the band gap as a consequence of the increase in particle size.

Conflicts of interest: The authors stated that no conflicts of interest.

REFERENCES

1. Wei SH and Zunger A. Phys. Rev.1993; B48: 6111.
2. Tappero R, Wolfers P, Lichanot A. Chem. Phys. 2001; Let. 355: 449.
3. Wu GR, Nagatomo K, Sasaki M, Nagasaki F, Sato H, Taniguchi M, Gav WX. *Solid State Comm.*2001; 118: 425.
4. Gumus C, Ulutas C et al. *Thin Solid Films.*2005; 492:1-5.
5. Pawar SM, Pawar BS, Kim JH, Joo OS, Lokhande CD. Recent Status of chemical bath deposited metal chalcogenides and metal oxide thin films,

- Curr. Apl. Phys.* 2011; 11(2): 117-61.
6. Mane RS, Lokhande CD. Chemical deposition method for metal Chalcogenide thin films. *Mater Chem. Phys.* 2000; 65(1):1-3.
 7. Adel S, Sharma R. *International Journal of Pure and Applied Physics.* 2017; 13: 241-248.
 8. Zhang Y, Wang H, Wang B, Yan H, Yoshimura M. *J. Cryst Growth.* 2002; 243:214.
 9. An C, Tang K, Liu X, Li F, Zhou G, Qian YJ. *Cryst Growth.* 2002; 252:575.
 10. Zhang Y, Wang H, Wang B, Xu H, Yan H, Yoshimura M, *Opt. Mater.* 2003; 23:433.
 11. Kobayashi M, Nakai T, Mochizuki S, Takayama N, *J. Phys. Chem. Solids.* 1995; 56:341.
 12. Mayen- Hernandez SA, Sandoval SJ, Perez RC, Delgado GT, Chao BS, Sandoval OT. *J. Cryst. Growth.* 2003; 256:12.
 13. David L, Bradford C, Tang X, Graham TC, Prior KA, Cavenett BC. *J. Cryst. Growth.* 2003; 251:591.
 14. Fan D, Wang W, Zhang YC, Cheng J, Wang B, Yan H. *Mater. Chem. Phys.* 2003; 80:44.
 15. Lokhande CD, Gadave KM. *J. Phys.* 1194; 18:83.
 16. Mane RS, Lokhande CD. *Mater. Chem. Phys.* 2000; 65:1.
 17. Gosh PK, Chattopahyay KK. *Nanotechnology.* 2005; 16:107.
 18. Ulutas C, Guneri E, Kirmizigul F, Altindemir G, Gode F, Gumus C. *Materials Chemistry and Physics.* 2013; 138:817-822.

Study of electrical properties of semiconducting nanocomposites

Tiwari KP and Pandey Anand

Department of Physics, Agra College, Agra- 282002 (Affl. to: Dr.B.R.Ambedkar University, Agra- 282002, India)
E-mail: drkptiwari@rediffmail.com

Manuscript Details

Available online on <http://www.irjse.in>
ISSN: 2322-0015

Editor: Dr. Arvind Chavhan

Cite this article as:

Tiwari KP and Pandey Anand. Study of electrical properties of semiconducting nanocomposites, *Int. Res. Journal of Science & Engineering*, December 2017; Special Issue A1 : 95-98.

© The Author(s). 2017 Open Access

This article is distributed under the terms of the Creative Commons Attribution 4.0 International License

(<http://creativecommons.org/licenses/by/4.0/>), which permits unrestricted use, distribution, and reproduction in any medium, provided you give appropriate credit to the original author(s) and the source, provide a link to the Creative Commons license, and indicate if changes were made.

ABSTRACT

Semiconducting nano-composites are the hybrid materials which are the combination of one or more semiconducting nano-particles with a conducting polymer. These materials have unique properties which can be used for wider applications. We have prepared a nano-composite of II-IV semiconducting nano-material and a conducting polymer by precipitation method at room temperature. The synthesized nano-composites with different weight percentage (5%, 10%) of semiconducting nano-particles were characterized by FTIR and UV-Vis spectroscopy. The measured electrical parameters of these composites are compared with certain values available with other studies. The activation energy and electrical parameters of these nano-composites have been calculated from the plots between conductivity and temperature. It is concluded that the measured values are in better agreement with the available experimental values. This study also reveals that the electrical conduction behaviour of these composites is the intermediate behaviour of conducting polymer and pure semiconducting nano-crystals. Thus, we can conclude that nano-composites can be more useful with designed optical band gap energy which can be obtained by controlling size and shape of the semiconducting materials. Certain technological applications in nano-electronic devices, gas sensors, solar cells etc. have been suggested.

Keywords: Semi-conducting crystals, nano-particles, FTIR, UV Vis-spectroscopy, composites etc.

INTRODUCTION

During last few years, a lot of emphasis is on production of semi conducting materials at nanoscale. We know that producing automatically flat surfaces in single crystalline materials is possible by manipulating atoms, whereas, this is meaningless, in case of glassy systems. The structure of amorphous materials is disordered at the atomic level. Therefore, these nano materials can easily be tailored and may yield a great variety than that of crystalline nanostructures. It is well known that the selenium and tellurium rich semi conducting materials exhibit the phenomena of electrical switching. Two types of electrical switching namely, reversible (threshold) and irreversible (memory) switching are observed in semi conducting materials glasses. Studies on semi conducting materials glasses are of great interest due to their application in electronic switches and memories. Recently there are many reports on semi conducting materials available in the literature. Since, semi conducting materials are much cheaper and exhibit more than one type of memory switching; the switching and memory devices based on semi conducting materials are expected to provide more efficient and costeffective devices. Conducting polymers provide tremendous scope for turning of their electrical conductivity from semiconducting materials to metallic regime [1,2]. The conductivity of the conducting polymer as can be tuned by polymers and by the nature of dopant, by the degree of doping, and by making composites with inorganic materials. When conducting polymers are taken in the composite from their electrical properties are altered from those of basic materials. It has been shown that the conductivity of these heterogeneous systems depends upon number of factors such as the concentrations of the conducting fillers, their shape, orientation and inter-action between filler molecules [3]. Polymer Nano-composites are polymer matrix composites in which the filler is less than 100 nm in at least in one dimension [4]. These composites exhibit extraordinary interesting properties. A feature of polymer Nano-composites is that the small size of the filler leads to a dramatic increase in the interfacial area creates a significant volume fraction of interfacial polymer with properties different from the bulk polymer even at low loadings. Experimental work has generally shown that all types and classes of nano

composite materials lead to new and improved properties when compared to their nano composites counterparts. Therefore nano-composites promise new applications in many fields such as mechanically reinforced lightweight components, non-linear optics, nano wires, sensors and other systems. Now days fillers have emerged, providing an opportunity for the development of high performance multifunctional nano-composites. The recent resurgence of interest in conducting polymer nano-composites has emerged for several reasons. For example, as the size of silicon nano-particles decrease, the band gap changes and the colour of particles changes [5,6]. Number of II-VI semiconducting materials have been investigated in which ZnS have considerable interest due to its vast applications like solar cell, fluorescent material and photonic receiver etc. [7] Therefore, a synthesis of ZnS nanoparticles with polymer to form composites with conducting polyaniline is proposed. Zinc sulphide (ZnS) has unique physical properties, such as high refractive index, low optical absorption in the visible and infrared light range and wide optical gap, such film is widely used in many optical and electronic areas. In the area of optics, ZnS can be used as reflectors and dielectric filters because of its high refractive index and high transmittance in visible range. ZnS can be used for fabrication of optoelectronic devices such as blue emitting diodes, electroluminescent devices, electro optic modulator, optical coating, heterojunction solar cells and photoconductor.

METHODOLOGY

Numbers of methods have been reported for the preparation of nanoparticles. ZnS has unique physical properties such high refractive index, low optical absorption in visible and infra red light range and wide optical gap. This film is widely used in many optical and electronic areas. ZnS can also be used for fabrication of optoelectronic devices such as LED, Solar cells etc. Synthesis of ZnS nano-particles is one of the II-VI semiconductor compounds which have wide ranging applications in solar cells, infrared window materials, photo-diode and cathode ray tube, electroluminescent devices and multilayer dielectric filters. Keeping in mind, we have prepared nano

composites of ZnS with conducting polymer at room temperature using precipitation method.

Synthesis of zinc sulphide (ZnS) nanoparticles

0.1M Zinc salt solution was made by dissolving Zinc Acetate in double distilled water and 0.1 M Na₂S solution was also made in double distilled water. From these stock solutions, 100ml of solution of Zinc acetate solution was mixed with 100 ml of DMF and stirred for 10 minutes. Then to above mixture 100 ml Na₂S solution was added drop wise with constant stirring. The stirring was continued for 1 hour. This results in milky white solution. The solution was kept overnight. The same procedure was repeated for the washing of resultant solution. Dry white powder of ZnS so obtained by this process and by precipitation method a composite of ZnS-PANI is prepared for experimental purpose [8].

RESULTS AND DISCUSSION

The nano composites of PANI-ZNS are characterized by using FTIR and UV VIS spectrography and measured the parameters at room temperature. On the basis of above measurements, it is concluded that inorganic semiconducting nanoparticles of ZnS have been synthesized successfully by chemical precipitation method. Polyaniline and its nano-composites with ZnS under investigation have been synthesized by chemical oxidation polymerization method. The powdered form of the synthesized material was used for the further study. The synthesized materials were characterized by UV -Vis, fluorescence spectroscopy at other weight percentage of ZnS. Thus, we successfully synthesized the nanomaterials by simple precipitation method and conducting polymer and compo-

sites by chemical oxidation polymerization at room temperature. A comparison of these data infers that the measured values of electrical parameters are in better agreement with other available results [8,9,10].

Characterization

The synthesized PANI-ZnS is characterized by using UV-Vis and FTIR spectroscopy.

UV-Vis spectroscopy:

A study of UV-Vis spectra of PANI and PANI - ZnS is given in fig.-1. It is observed that there is a shift in the absorption maxima. The shift in the absorption bands due to addition of ZnS which changes the delocalisation in the polymer chain. The increase in intensities of the excitonic and polaronic bands is observed in the nanocomposites indicating the interaction of ZnS with PANI chain. By increasing the weight percentage of ZnS nanofiller the peak centred at in PANI becomes substantially broadened and shifts towards higher wavelength.

FTIR spectroscopy:

Fig.-2 representing the absorption of radiation by high frequency phonon vibrations. The IR-spectra of PANI are shown in adjacent fig. These spectra shows the characteristic vibration bands. All these bands are well matches with the earlier reported values polyanniline. The IR spectra of pure PANI - ZnS shows that the composites of PANI-ZnS are built up of repeating units as that of pure PANI indicating the formation of conducting polymer nanocomposites. IR study also reveals that peak intensities and conductivity variation in the polymer sample are in tight interaction with each other. It is also observed that of PANI -ZnS enhanced polaronic and bipolaronic bands for the 5%, 10% composites.

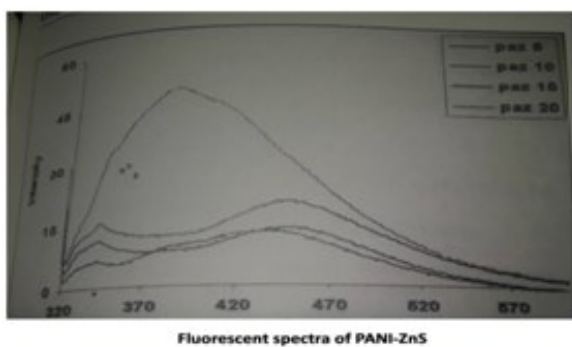


Fig.1

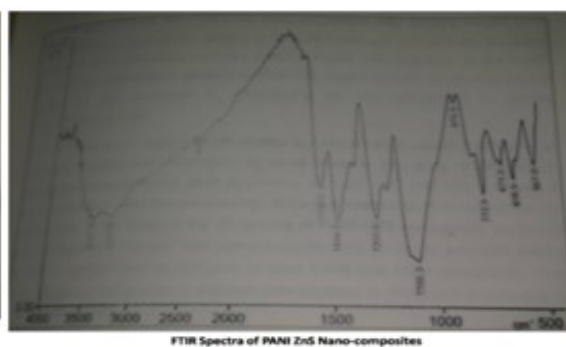


Fig.2

The blue shift in absorption maxima and increased band gap of the synthesized ZnS confirms the formation of nanosized inorganic semiconductor ZnS.

CONCLUSION

The conductivity increases only for the composites containing 5% and 10% ZnS. For higher concentrations the conductivity decreases. From the above discussion we conclude that there is a change in the corresponding frequencies of pure PANI and its composites as well as the new polymer nanocomposites can be synthesized with desired thermal stability, optical band gap energy and tunable electrical conductivity. It is also observed that peak intensities in IR spectra and conductivity variation in the polymers are in better interaction with each other. The desired electrical band gap could be synthesized by controlling the size, shape and amount of nanofiller in the polymer matrix. Such nanocomposites can be used in the tuned circuits, optical devices, gas sensors and nanoelectronic devices. Transparent conducting polymer/solar cell electrode, transparent coating in cell phone and compact disc technology. Also nanoparticles are being considered for enhancing matrix properties of traditional composites to increase out of plane properties and add conductivity and sensing capabilities.

Conflicts of interest: The authors stated that no conflicts of interest.

REFERENCES

1. Scotheim TA, Elsenbaumer RL and Reynolds JR (Marcel Dekker, Handbook of conducting polymers; Vol.1,2, edited by Inc., New York, 1998).
2. Hadziioannou G and Hutten PFV. Semiconducting polymers; Vol., edited by (Wiley -VCH, Weinheim, 2007).
3. Tiwari KP, Sarkar KK. Correlation between electronic dielectric and refracting properties of binary solids, Ind. Journ. Pure and appl. Physics, (2007), 73, 169.
4. Burroughes JH, Bradley DDC, Marks AR, MacKay RN, Friend K, Burns RH, Homes PL. AB.Light emitting diodes based on the conjugated polymers, 1990,*Nature* 347:539. doi: 10.1038/3475.
5. Sariciftci NS, Smilowitz Heeger, AJ Wudl F. Photo induced electron transfer from a conducting polymer to buckminsterfullerenes.1992. *Science* 258 (5087): 1474. doi: 0.1126/science.258.5087.1474. PMID 17755110.
6. Siringhaus H. Device Physics of solution-processed Organic Field Effect Transistors." (2005). *Advanced materials* 17:2411. doi: 10.1002/adma.200501152.
7. Yannoni, CS, Clarke TC. Molecular Geometry of cis- and trans- polyacetylene by nutation MR Spectroscopy." (1983). *Physical Review Letters* 51: 1191.doi; 10.1103/Phys Rev Lett. 51.1191.
8. Sarkar KK, Goyal SC. Quantum-dielectric behavior of ANB8-N binary. *Solids, Phys. Rev*,1980, 21, 879.
9. Sarkar KK,. Goyal SC. Quantum-dielectric behavior of ANB8-N binary-Solids, *Phys. Rev*, (1980), 21, 879.
10. Meena D. Vidhale, Saroj S. Hole, D.S. Dhote. Analysis of transport properties of PANI-ZnS with different weight percentage of nanofiller. ISBN 978-81-922256-9 (2013).
11. Ovshinky SR, Strand D, J. optoelectronics Adv. Mater., 7 (2005) 1679.
12. Zishan H. Khan, A.A. Al-Ghamdi, Shashmad A Khan, Sami Habib & Numan Salah, *Nanoscience & Nanotechnology Letters (USA)*3 (2011)1-5.

Study of temperature change on ultrasonic velocity and some acoustic parameters of binary liquid mixture of DMSO+ Chlorobenzene

Kolhe RK¹ and Bhosale BB²

Research Scholar, JJT University, Jhunjhunu, Rajasthan, (India). Department of Physics, K.J. Somaiya College, Kopergaon (Maharashtra) India. | E-Mail- rangnath_kolhe@rediffmail.com

Manuscript Details

Available online on <http://www.irjse.in>

ISSN: 2322-0015

Editor: Dr. Arvind Chavhan

Cite this article as:

Kolhe RK and Bhosale BB. Study of Temperature Change on Ultrasonic Velocity and Some Acoustic Parameters of Binary Liquid Mixture of DMSO+ Chlorobenzene, *Int. Res. Journal of Science & Engineering*, December 2017; Special Issue A1 : 99-102.

© The Author(s). 2017 Open Access

This article is distributed under the terms of the Creative Commons Attribution

4.0 International License

(<http://creativecommons.org/licenses/by/4.0/>),

which permits unrestricted use, distribution, and reproduction in any medium, provided you give appropriate credit to the original author(s) and the source, provide a link to the Creative Commons license, and indicate if changes were made.

ABSTRACT

The Ultrasonic velocity, density and viscosity have been measured for binary liquid mixture of DMSO + Chlorobenzene of fixed equal volumes of the mixtures at temperatures of 298K, 303K, 308K, 313K and 318K. The experimental measured values of ultrasonic velocity, density and viscosity are used to calculate some acoustic and thermodynamic parameters such as adiabatic compressibility, acoustic impedance, free length, relaxation time, free volume and internal pressure. It was observed that ultrasonic velocity (U), density (ρ) and viscosity (η) decreased with increase in temperature. The adiabatic compressibility (β), free length (L_f) and free volume (V_f) increases with increase in temperature, whereas acoustic impedance (Z), relaxation time (τ) and internal pressure (π_i) decreased with increase in temperature. Some probable reasons on the increase or decrease of acoustic and thermodynamic parameters with temperature change are presented.

Keywords: Binary mixtures, Density, Relaxation time, quartz crystal.

INTRODUCTION

The ultrasonic study of liquids is of most important in understanding the nature and strength of molecular interactions. The biological activity of drug molecules and the activation energy of the metabolic process basically depend on the type and strength of the intermolecular interactions.

Thermodynamic and transport properties of liquids mixtures have been used to study the departure of a real liquid mixture behavior from ideality. From the literature, the nature and degree of molecular interactions in different solutions depend upon the nature of solvent, the structure of solute molecule and extent of solutes taking place in the solution [1]. In recent years ultrasonic investigations find large number of applications in characterizing of thermodynamic and physicochemical aspect of binary liquid mixtures. The thermodynamic and acoustical parameter have been used to study different kinds of associations, molecular motion and various types of interaction and their strengths influenced by the size of pure component and the mixtures [2].

Ultrasonic investigation of liquid mixture with components is of considerable importance in understanding intermolecular interaction between the component molecules which finds application in several industrial and technological processes. Ultrasonic velocity, density, viscosity and the derived acoustical parameters like adiabatic compressibility, free length, free volume, acoustic impedance, relaxation time, internal pressure, etc., provide valuable information about the molecular environments. This has been studied for various binary and ternary mixtures with respect to variation in concentration of the liquids and temperatures [3].

In this paper, variation of some acoustic and thermodynamic parameters of binary liquid mixture of Dimethylsulphoxide and Chlorobenzene with temperature has been studied for a fixed concentration of equal volumes of the individual liquids making up the mixture.

METHODOLOGY

A concentration in volume fraction of mixture was prepared by taking liquids of DMSO and Chlorobenzene (Merck, AR grade Germany, 99.5%). The volume fractions of the component liquids making the mixture were kept constant in the ratio of 1:1 through-out the variation of temperature. The ultrasonic velocity, density and viscosity were measured as a function of temperature of the binary liquid mixture at 2MHz and at temperatures of 298K, 303K, 308K, 313K and 318K.

The density of the mixture at different temperatures were measured by using a specific gravity bottle with an accuracy of $\pm 0.5\%$ and viscosity of the system at different temperatures were measured using an Ostwald's viscometer. The flow time was determined using a digital stopwatch with an accuracy of $\pm 0.01\text{sec}$. The ultrasonic velocity of the liquid mixture was measured using ultrasonic interferometer at 2MHz. The required temperature of the liquid mixture was maintained constant by circulating water from a thermostatically controlled water bath with an accuracy of $\pm 0.1\text{K}$. Some acoustic and thermodynamic parameters were calculated [4]

- 1) Adiabatic compressibility (β)

$$\beta_{ad} = \frac{1}{v^2 \rho} \quad (1)$$

- 2) Acoustic impedance (Z)

$$Z = \rho U \quad (2)$$

- 3) Free length (L_f)

$$L_f = K T \beta^{1/2} \quad (3)$$

- 4) Relaxation time (τ)

$$\tau = \frac{3}{4} \eta \beta_{ad} \quad (4)$$

- 5) Free volume (V_f)

$$V_f = [M_{eff} U / K \eta]^{3/2} \quad (5)$$

- 6) Internal pressure (π_i)

$$\pi_i = bRT[(K\eta/U)^{1/2}(\rho^{2/3} M^{7/6})] \quad (6)$$

Where U is ultrasonic velocity, ρ is density of the mixture, f is the frequency of ultrasonic wave, K_T is temperature dependent constant known as Jacobson's constant ($K_T = 2.131 \times 10^{-6}$ at 318K), M_{eff} is the effective molecular weight of the mixture, k is a temperature independent constant which is equal to 4.281×10^9 for all liquids, η is the viscosity of the mixture, b stand for cubic packing, which is 2 for all liquids, T is the absolute temperature in Kelvin, R is the universal gas constant, k_B is Boltzmann's constant, h is Planck's constant.

RESULT AND DISCUSSION

The experimental data related to ultrasonic velocity, density and viscosity at indicated temperatures for frequency 2MHz, for the given liquid mixture have been presented in Table 1. The calculated values of adiabatic compressibility, acoustic impedance, intermolecular free length, relaxation time, free volume and internal pressure are presented in Table 2.

Table 1: The values of Ultrasonic Velocity (U), Density (ρ) and Viscosity (η) of DMSO + Chlorobenzene at 298^oK, 303^oK, 308^oK, 313^oK and 318^oK.

T(K)	Ultrasonic Velocity U(ms ⁻¹)	Density (kg m ⁻³)	Viscosity 10 ³ (Nm ⁻² s)
298 ^o K	1372.00	1094.70	0.1361
303 ^o K	1355.36	1089.43	0.1164
308 ^o K	1337.05	1086.30	0.0981
313 ^o K	1321.05	1081.58	0.0818
318 ^o K	1302.10	1076.42	0.0622

Table -2 The values of adiabatic compressibility (β), acoustic impedance (Z), free length (L_f), relaxation time (τ), free volume (V_f), internal pressure (π_i) of DMSO + chlorobenzene at 298^oK, 303^oK, 308^oK, 313^oK and 318^oK.

T(K)	$\beta \times 10^{-10} \text{ ms}^2 \text{ kg}^{-1}$	$Z \times 10^6 \text{ kg m}^{-2} \text{ s}^{-1}$	$L_f \times 10^{-9} \text{ m}$	$\tau \times 10^{-12} \text{ sec}$	$V_f \times 10^{-6} \text{ (ml)}$	$\pi_i (\times 10^3 \text{ Nm}^{-2})$
298	4.853	1.502	0.453	88.06	10.9275	3.535
303	4.997	1.477	0.464	77.55	13.5413	3.338
308	5.149	1.452	0.475	67.35	17.1224	3.133
313	5.298	1.429	0.486	57.78	22.0338	2.921
318	5.479	1.402	0.499	45.44	32.4442	2.602

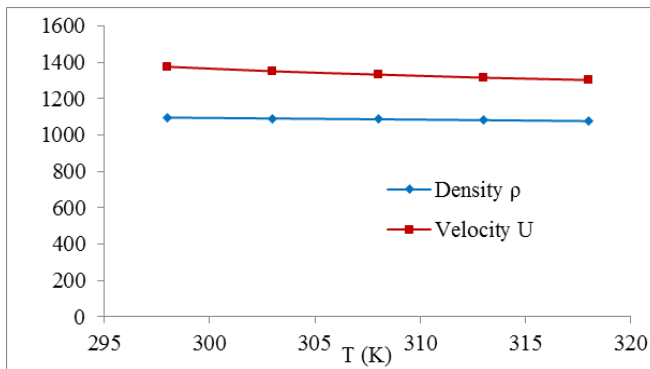


Fig.1

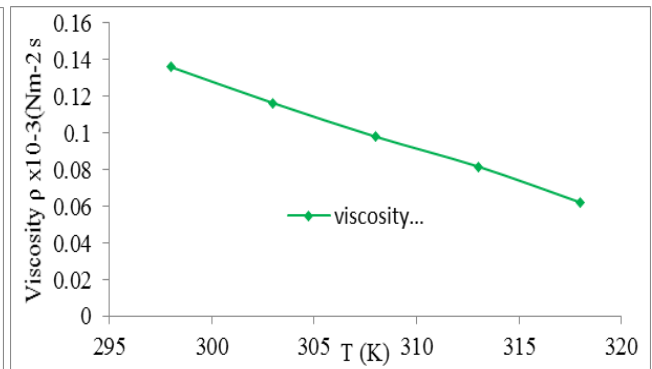


Fig. 2

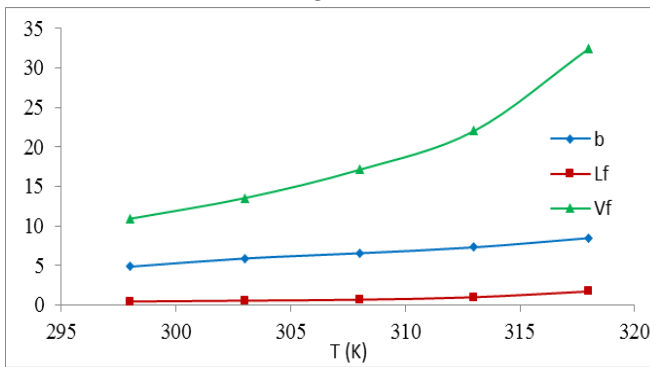


Fig.3

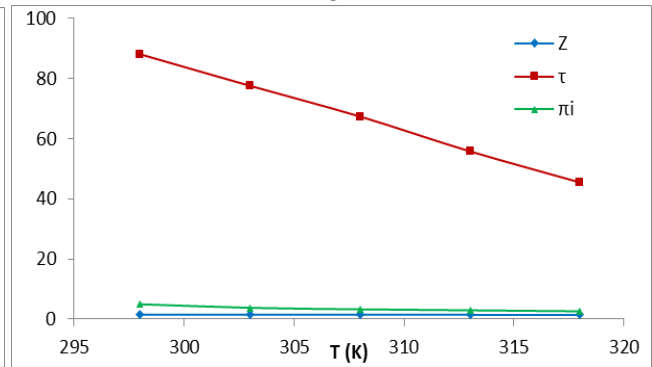


Fig. 4

Fig 1: Variation of Ultrasonic velocity U (m/sec) and density ρ (Kg/m³) with temperature T (K) **Fig 2:** variation of viscosity η with temperature T(K) **Fig 3:** Variation of adiabatic compressibility β , free length L_f and free volume V_f of mixture with temperature **Fig 4:** Variation of acoustic impedance Z, relaxation time τ and internal pressure π_i of mixture with temperature

From table-1 and figure-1 and 2 it is seen that the ultrasonic velocity, density and viscosity decreases with increase in temperature. The decrease of values with temperature shows decrease in intermolecular forces due to the increase in the thermal energy of the system. The velocity decreases with increase in

temperature because as the free length increases with the increase of temperature (Table-2). Thus the association of the interacting molecules varies with the temperature of the ultrasonic wave, cohesive force as well as internal pressure decreases with the increase of temperature[5,6].

From Table 2 and figure 3 it is seen that adiabatic compressibility (β), free length (Lf) and free volume (Vf) increases with increase in temperature. The free length depends on the adiabatic compressibility and shows a similar behavior to that of compressibility and inverse to that of velocity. It increased with increase in temperature of mixture, indicating that there is a less interaction between solute molecules. Free volume of the mixture increased as the internal pressure decreased (Figure-4) with increase in temperature of the mixture. This is due to the loose packing of the molecules inside the shield, that results in decreasing magnitude of interactions [7]. It is seen from table-2 and figure-4 that acoustic impedance (Z), relaxation time (τ) and internal pressure (π) decreases with increase in temperature. This is similar to the change found in viscosity, showing that viscous forces play a dominant role in the relaxation process. It is observed that acoustic impedance decreases with increase in temperature, this is in agreement with ultrasonic velocity and density [8].

From figure- 3 and 4, it is observed that adiabatic compressibility (β), free length (Lf) and free volume increases almost linearly with increase in temperature, while acoustic impedance (Z), relaxation time (τ) and internal pressure (π) decreased almost linearly with increase in temperature. Figure-1 and 2 shows that ultrasonic velocity (U), density (ρ) and viscosity (η) of the system decreases with increase in temperature. The molecules in a liquid are held together much more strongly than in a gas. A force is needed to overcome the mutual attraction of the molecules so that they can be displaced relative to each other. The more strongly the molecules are held together, smaller the flow for a given shearing stress. With increasing temperature, the random kinetic energy of the molecules helps to overcome the molecular forces and reduces the viscosity [9].

CONCLUSION

The adiabatic compressibility, free length and free volume of DMSO+Chlorobenzene mixture increases almost linearly with increase in temperature, while acoustic impedance, relaxation time and internal pressure decreases almost linearly with increase in

temperature. As usual, the ultrasonic velocity, density and viscosity decreases with increase in temperature. This is due to the energy obtained to overcome the resistance to flow. The almost linear variation of acoustical parameters with temperature shows that there exist less intermolecular forces between the components of the binary liquid mixture.

REFERENCES

1. Bedare GR, Suryawanshi BM, Vandakkar VD Acoustical Studies on Binary Liquid Mixture of Methylmethacrylate in 1, 4-Dioxane at 303K, *International Journal of Advanced Research in Physical Sciences, (IJARPS)*, 2014; Vol.1(5): 1-5.
2. Dange SP, Chimankar OP Acoustic Properties of Ternary Liquid Mixture Using Ultrasonic Interferometer Technique, *Global Research Analysis*, 2013; 2(7):167-168
3. Vasantharani P, Kalaimagal P, Kannappan A.N. Molecular Interaction Studies on Some Organic Liquid Mixtures at Different Temperatures using Ultrasonic Technique. *Asian J Applied Sciences*, 2009; Vol. 2:96-100.
4. Kaur K. and Juglan K. Studies of Molecular Interaction in the Binary Mixture of Chloroform and Methanol by Using Ultrasonic Technique, *Der Pharma Chemica*, 2015; 7(2): 160-167.
5. Praharaj M. et al., Ultrasonic Studies of Ternary Liquid Mixtures of N-N-Dimethylformamide, Nitrobenzene, and Cyclohexane at Different Frequencies at 318K, *Journal of Theoretical and Applied Physics*. 2013:7-23.
6. Furniss BS et al Vogel's Textbook of Practical Organic Chemistry, 5th Edn, Harlow, Longman, 1989; ISBN: 0-582-46236-3.
7. Mecke R. Infrared Spectra Hydrocyclic Compounds, *Discuss Faraday Soc* 1950; 9:161-177.
8. Rajavelu S, Ultrasonic Study of Molecular Interaction in Binary Liquid Mixtures at 303K, 308K and 313K, *International Journal of Science and Research (IJSR)*, 2014; 3(4):845-848.
9. Dikko AB, Ahmed AD, Oriolowo NZ, Effect of Temperature Change on Ultrasonic Velocity and some Acoustic Parameters of Ternary Liquid Mixture of Methanol+Ethanol+1-Propanol, *International Journal of Applied Research*, 2015; 1(3):75-77.

Novel synthesis of $\text{Cu}_2\text{CoSnS}_4$ thin films for photovoltaic application

Maldar PS¹, Mane AA¹, Nikam¹ SS, Mohite² VS, Giri SD³, Sarkar A³, Moholkar AV^{1*}

¹Thin Film Nanomaterials Laboratory, Department of Physics, Shivaji University, Kolhapur 416-004, M. S., India.,

²Tuljaram Chaturchand college of Arts, Science & Commerce, Baramati 413102

³Department of Chemical Engineering, Indian Institute of Technology Bombay, Powai, Mumbai 40 M. S., India,

*Corresponding author: Email: avmoholkar@gmail.com

Manuscript Details

Available online on <http://www.irjse.in>
ISSN: 2322-0015

Editor: Dr. Arvind Chavhan

Cite this article as:

Maldar PS, Mane AA, Nikam SS, Mohite VS, Giri SD, Sarkar A, Moholkar AV. Novel synthesis of $\text{Cu}_2\text{CoSnS}_4$ thin films for photovoltaic application, *Int. Res. Journal of Science & Engineering*, December 2017; Special Issue A1 : 103-108.

© The Author(s). 2017 Open Access

This article is distributed under the terms
of the Creative Commons Attribution

4.0 International License

(<http://creativecommons.org/licenses/by/4.0/>),
which permits unrestricted use, distribution, and
reproduction in any medium, provided you give
appropriate credit to the original author(s) and the
source, provide a link to the Creative Commons
license, and indicate if changes were made.

ABSTRACT

Chemical spray pyrolysis technique (CSPT) can be used for preparation of thin films that can be utilized in different fields such as solar cells, sensors, and solid oxide fuel cells. In spray pyrolysis the deposition rate, area and thickness of the thin films can be controlled at a wide working temperature range such as, from 100 °C to 500 °C for soda lime glass (SLG) substrates. The present paper reports synthesis and characterizations of the spray deposited CCTS films at substrate temperature of 350 °C. A power conversion efficiency of 1.78 % is observed for the photoelectrochemical solar cell fabricated with CCTS film on FTO substrate as working electrode, Sodium sulphate as electrolyte and platinum based counter electrode.

Keywords: $\text{Cu}_2\text{CoSnS}_4$ thin films; spray pyrolysis; Photoelectrochemical

INTRODUCTION

Thin films are useful in variety of applications such as solar cells, sensors, and solid oxide fuel cells [1]. Most of the chemical synthesis processes for preparation of thin films like; hydrothermal, sol-gel, solid state reaction and liquid phase synthesis require a long heat treatment processes. Additionally, these methods need precise control over preparative parameters like pH, temperature, controlled supply of reacting species, and use of stabilizing agent to preserve monodispersity, followed by

post processing steps like washing, drying, and calcination [2-5]. These post deposition processes are time consuming that increase production cost. To reduce high mfg cost of large scale production of thin films which are used in various applications it is essential to implement single step process which is more suitable and economic. Among the diverse methods accessible for deposition of thin films, the chemical spray pyrolysis technique (CSPT) is widely used and has many advantages such as non-vacuum, easy handling and large deposition area [6]. CSPT can facilitate working temperature range from 100 °C to at least 500 °C which is quite useful for SLG substrates, those can be preheated using temperature control arrangement.

The present paper reports synthesis and characterization of $\text{Cu}_2\text{CoSnS}_4$ (CCTS) thin films prepared by CSPT for photovoltaic application. CCTS is a compound semiconductor, which has stannite structure and crystallizes in tetragonal unit cell, inside which all three metals are tetrahedrally surrounded by sulfur atom, and each sulfur atom is surrounded by one Co, one Sn, and two Cu atoms [7]. The p type conductivity and direct band gap values in the range of 1.46 eV to 1.61 eV of CCTS are of significant importance as an absorber layer in development of efficient thin films solar cells (TFSC). Due to its direct band gap CCTS reduces the material need in comparison with other indirect band gap materials like silicon [8]. The availability of copper, cobalt, tin, and sulfur in earth's crust is found to be 50 ppm, 20 ppm, 2.2 ppm, and 260 ppm respectively. To reduce the pressure on current photovoltaic (PV) technology much attention is required on the development of PV technology rooted in abundant and nontoxic elements like CCTS [9].

To carry out deposition of thin films by CSPT, here electronic control system is designed with the help of single push button switch and potentiometer. Control system also handles automatic movement of nozzle through a slider crank arrangement driven by dc geared motor. Solid state relay is used to make ON/OFF arrangement of heater to keep the temperature in the desired range. The system is designed around open source Arduino microcontroller platform with 0 °C to 1000 °C range k-

type thermocouple, and MAX6675 to sense temperature of heater plate in closed loop arrangement. The working temperature range is selected in the range of (± 2) °C with respect to threshold set point entered by user through PID temperature controller.

METHODOLOGY

The reaction chamber of spray pyrolysis unit used for preparation of thin films has dimensions of $90\text{ cm (length)} \times 60\text{ cm (breadth)} \times 90\text{ cm (height)}$ is a metallic chamber. The inner sides of a metallic chamber are covered by fire proof cement board to sustain the temperature of reaction chamber due to heat loss. The different by-products evolved during the pyrolysis are removed by exhaust fan fitted to reaction chamber. The electric plate heater was made from 1500 W nichrome coil, which is wound parallel with a spacing of 1 cm on a ceramic base having thickness of 2.5 cm and diameter of 19 cm. The free ends of coil are connected to 230V/16A power supply through solid state relay. The Arduino platform activates and deactivates the relay as per requirement of temperature to accomplish the deposition of thin films. The preheated SLG substrates with dimensions $7.5\text{ cm (length)} \times 2.5\text{ cm (breadth)} \times 1.4\text{ cm (thickness)}$ are used for deposition of $\text{Cu}_2\text{CoSnS}_4$ thin films. These substrates are kept on circular stainless steel plate which has a diameter of 20 cm and thickness of 0.5 cm. The atomization of the precursor solution is achieved by filtered compressed air. Pressure of the compressed air is kept at ≈ 1 bar. Single phase, 1 HP compressor provides compressed air which is used as a carrier gas.

A specially designed borosilicate glass nozzle is used for atomization of precursor solution by carrier gas. Pressure of the carrier gas creates a vacuum at the tip of nozzle, due to which precursor solution is sucked at a liquid opening. It initiates the spraying of precursor solution [10]. To achieve the regular deposition of the thin films, mechanized to and fro movement with frequency of 0.16 Hz has been employed to spray nozzle. For deposition of CCTS thin film, the precursors used were $\text{CuCl}_2 \cdot 2\text{H}_2\text{O}$ (Cupric Chloride)

for copper, $\text{CoCl}_2 \cdot 6\text{H}_2\text{O}$ (Cobalt Chloride hexahydrate) for cobalt, $\text{SnCl}_4 \cdot 5\text{H}_2\text{O}$ (Stannic Chloride) for tin and $\text{CH}_4\text{N}_2\text{S}$ (thiourea) for sulfur. The 0.05M $\text{CuCl}_2 \cdot 2\text{H}_2\text{O}$, 0.025M $\text{CoCl}_2 \cdot 6\text{H}_2\text{O}$, 0.025M $\text{SnCl}_4 \cdot 5\text{H}_2\text{O}$ solutions were prepared separately in methanol as a solvent. The appropriate amount of thiourea powder was dissolved in methanol so that the ratio of cations to anions should be more than stoichiometry in the final precursor solution. The molarity of thiourea was chosen in excess than the stoichiometry to avoid the loss of sulfur at elevated temperature [11]. All the cationic solutions were mixed together in a proper order, which resulted into brown colored solution with $\text{pH} \approx 1$. Thiourea was added drop wise to this cationic solution under vigorous stirring. The addition of complete thiourea to this cationic solution resulted into change in the pH value of the final precursor solution to ≈ 3 , and has dark blue color. With a flow rate of 5 mL/min, the 80 mL of the precursor solution was sprayed onto SLG and FTO substrates which were preheated using temperature control arrangement. Fig.1 shows the schematic of spray pyrolysis unit used for deposition of CCTS thin films.

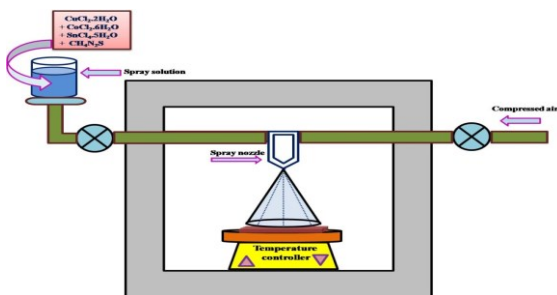


Fig.1-Schematic of spray pyrolysis unit used for deposition of CCTS thin films

The structural properties of spray deposited CCTS thin films were studied by using X-ray diffractometer (XRD) operated at 40 kV, 30 mA with $\text{Cu K}\alpha$ radiation ($\lambda = 1.5406 \text{ \AA}$). Surface profiler (Ambios, XP-I stylus profiler, USA) was used to carry out the thickness measurement of the CCTS thin films. The surface morphology of the CCTS films was studied with a MIRA 3 FE-SEM microscope (TESCAN) attached with EDX detector (Oxford Instruments, UK). UV-Visible spectrophotometer (UV 1800, Shimadzu, Japan) was used to record UV-visible absorbance spectra of the CCTS thin films.

RESULTS AND DISCUSSION

The reflections corresponding to (112), (204) and (312) planes are observed at diffraction angles 28.64° , 47.36° and 56.38° respectively. The spray deposited CCTS thin film is polycrystalline in nature and show a preferred orientation along (112) plane. From XRD spectrum it is confirmed that the spray deposited CCTS thin film exhibit stannite structure compared to standard JCPDS card no. 00-026-0513. The average crystallite size (D) is calculated by Scherrer's equation [12].

3.1 Structural analysis:

Fig.2 shows XRD pattern of CCTS thin film deposited at a substrate temperature of 350°C .

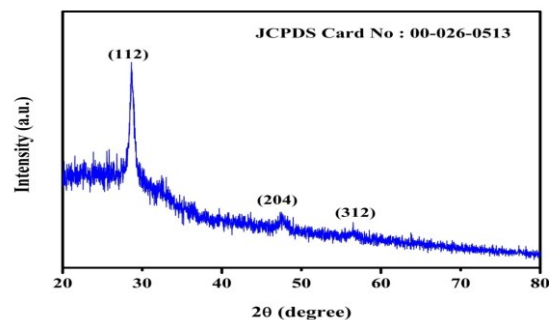


Fig.2 -XRD pattern of CCTS thin film deposited at a substrate temperature of 350°C

$$D = \frac{k\lambda}{\beta \cos(\theta)} \quad (2)$$

Where k is the shape factor, usually taken as 0.9 for spherical crystallites, λ is the wavelength of X-ray used, β is the FWHM and θ is the Bragg's angle. The average crystallite size calculated for the CCTS films deposited at 350°C is equal to 11.78 nm. Table 1 shows the structural parameters obtained for CCTS thin films.

3.2 Morphology of the films:

Fig.3 shows the FE-SEM image of the CCTS film deposited at a substrate temperature of 350°C . Flake like morphology is observed for the CCTS thin film deposited at substrate temperature of 350°C . Surface of the film shows the chain of flakes at some region with nonuniform distribution of flakes. The density of the flakes is not the same all over surface. The surface morphology of the films seems to be compact with existence of few of voids over the film surface.

3.3 Thickness measurement:

The thickness of the CCTS film deposited at a substrate temperature of 350 °C is found to be 325 nm.

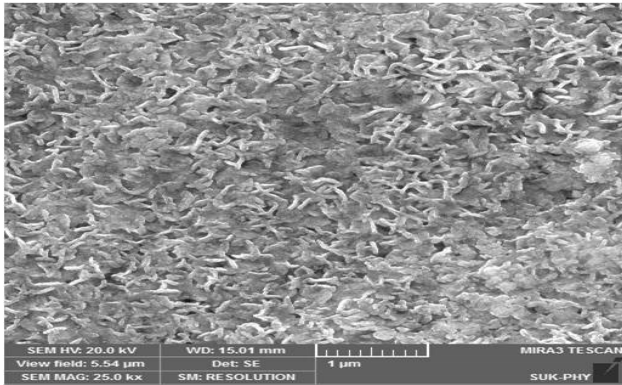


Fig.3-FE-SEM image of CCTS film deposited at 350 °C with 25k × magnification.

3.4 Compositional analysis:

The elemental composition of different constituent elements in the CCTS film is analysed using EDAX. The EDAX spectra of the films deposited at a substrate temperature 350 °C is shown in Fig.4.

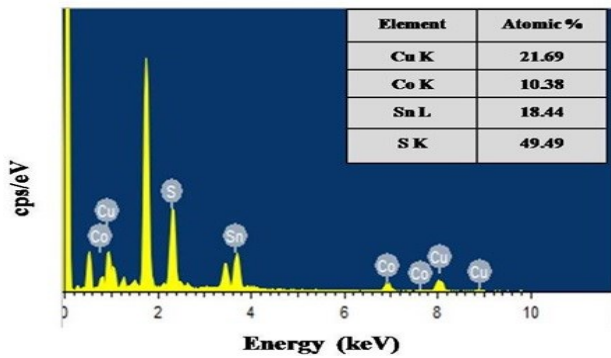
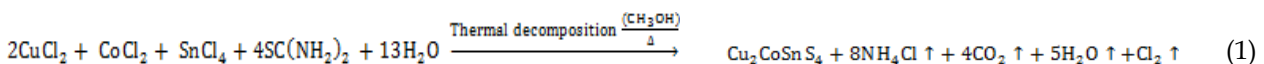


Fig.4- EDAX spectrum of CCTS film deposited at 350 °C

3.5 CCTS formation mechanism

Thin film Material	Substrate temperature (°C)	Miller indices (hkl)	Standard diffraction angle (2θ)°	Observed diffraction angle (2θ)°	Calculated d(Å)	FWHM (rad)	Crystallite size D (nm)	Average Crystallite size (nm)
CCTS	350°C	(112)	28.59	28.64	3.11	0.010	13.84	11.78
		(204)	47.56	47.36	1.91	0.013	11.31	
		(312)	56.47	56.38	1.63	0.015	10.21	

The chemical reaction for CCTS formation on SLG substrates is given by



The peaks corresponding to different constituent elements like Cu, Co, Sn, and S are clearly seen in the EDAX spectrum of the films. For the films deposited at 350 °C the composition ratio of Cu: Co: Sn: S is found to be 2.08:1:1.77:4.76 the composition of the films appears slightly Sn, and S rich. The S as to mental ratio is found to be 0.97.

3.6 Optical properties of CCTS thin film:

The relation between absorption coefficient α and incident photon energy hv is given by equation [13].

$$(\alpha h\nu) = A(h\nu - E_g)^n \quad (3)$$

where A is proportionality constant, E_g is optical band gap energy, n is an index representing the optical absorption process and it takes values equal to 1/2 or 2 for the direct and indirect allowed transitions respectively. The optical band gap of CCTS thin film can be obtained by extrapolating the linear portion of the plots (αhv)² against hv at α = 0 as shown in Fig.5

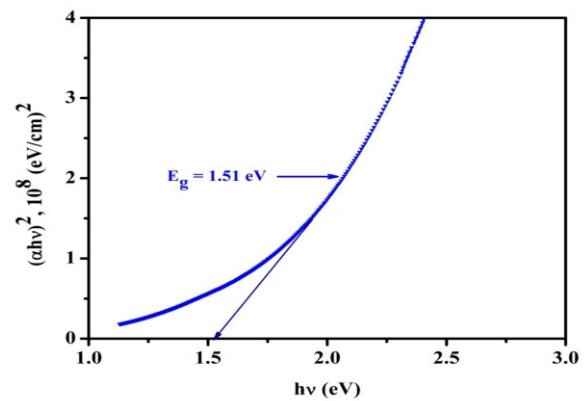


Fig.5- Plot of (αhv)² versus hv of CCTS film deposited at substrate temperature 350 °C

Table 2-Parameters of PEC solar cell based on CCTS thin film as working electrode deposited at substrate temperature of 350 °C

Substrate Temperature (°C)	J_{sc} ($\mu\text{A}/\text{cm}^2$)	V_{oc} (mV)	J_{max} ($\mu\text{A}/\text{cm}^2$)	V_{max} (mV)	FF	Efficiency (η)%
350 °C	12.73	350	8.07	134	0.24	1.78

The straight line nature of graph indicates the direct allowed transitions. Thus the index n takes value equal to $\frac{1}{2}$. The energy band gap value of the CCTS films deposited at substrate temperature 350 °C is found to be 1.51eV. The obtained band gap value for CCTS films is quite close to the most promising band gap value of the materials used for a solar cell application [14].

3.7 Photoelectrochemical cell performance (PEC)

study:

The PEC solar cell is fabricated with two electrode configuration in which CCTS thin film deposited on FTO substrate was used as working electrode, and platinum based counter electrode with spacing of 1 cm between working electrode and counter electrode. The electrolyte used was 0.5 M Na_2SO_4 , pH of which was adjusted to ≈ 10 by adding few drops of 0.5 M NaOH. A 500 W tungsten lamp with intensity of 60 mW/cm^2 is utilized as light source of illumination for PEC measurement. The light is exposed on active area of 0.25 cm^2 of working electrode, by masking rest of its area with insulating tape. Fig.6 shows the current density-voltage (J-V) characteristics of the CCTS based photoelectrochemical solar cell, under illumination.

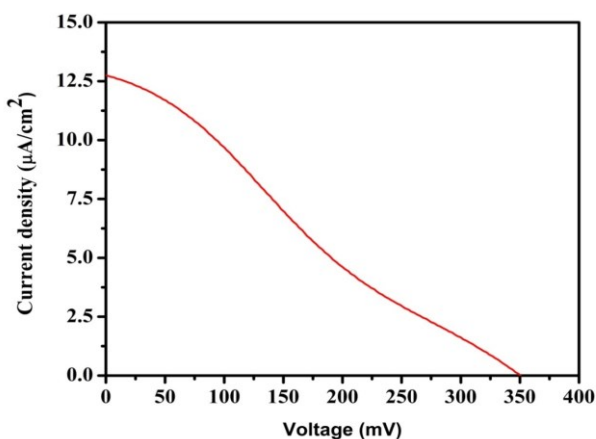


Fig.6- Current density-voltage (J-V) characteristics of the CCTS based photoelectrochemical solar cell

The fill factor (FF) and power conversion efficiency (η) of the PEC solar cells is calculated by using equations

$$FF = \frac{J_{max} \times V_{max}}{J_{sc} \times V_{oc}} \quad (4)$$

$$\eta = \frac{J_{sc} \times V_{oc}}{P_{in}} \times FF \times 100 \quad (5)$$

Where V_{oc} is the open circuit voltage, J_{sc} is the short circuit current density, V_{max} is maximum voltage, J_{max} is maximum current density, FF is fill factor, and P_{in} is input power density of illuminated light. Table 2 summarizes the results for PEC performance of CCTS thin film deposited at substrate temperature of 350 °C. The power conversion efficiency of 1.78 % is obtained for the PEC cell fabricated with CCTS film as working electrode that may be ascribed to optimal band gap value of the CCTS film, which helps to enhance effective absorption of incident light, while compact morphology of the film promotes fast electron transfer in the PEC cell fabricated with CCTS as working electrode [15].

CONCLUSION

The stannite structure of CCTS thin films with preferential orientation along (112) plane was confirmed by XRD study. The presence of constituent elements like Cu, Co, Sn and S is confirmed from EDAX spectrum of CCTS thin films. Photoelectrochemical solar cell based on CCTS thin film as a working electrode provided a conversion efficiency of 1.78 %. This novel synthesis of CCTS thin films for photovoltaic application will open a new avenue for development cost effective thin film solar cells rooted in earth abundant and nontoxic elements.

REFERENCES

1. Perednis D and Gauckler LJ, "Thin Film Deposition Using Spray Pyrolysis," 2005: 103-111.
2. Jung DS, Bin Park S, and Kang YC, "Design of particles by spray pyrolysis and recent progress in its application," 2010;27:1621-1645.
3. Capek I, "Preparation of metal nanoparticles in water-in-oil (w/o) microemulsions," 2004;110:49-74.
4. Tavakoli AKA, Sohrabi M, "A Review of Methods for Synthesis of Nanostructured Metals with Emphasis on Iron compounds," *chem.pap.*, 2007:151-170
5. Klabunde KJ, Ed, NANOSCALE MATERIALS IN CHEMISTRY. A John Wiley & Sons, Inc., Publication, 2001.
6. Desai SP, Suryawanshi MP, Bhosale SM, Kim JH, and Moholkar AV, "Influence of growth temperature on the physico-chemical properties of sprayed cadmium oxide thin films," *Ceram. Int.* 2015;41:4867-4873.
7. Schfifer W and Nitsche R, "Tetrahedral quaternary chalcogenides of the the type $Cu_2-II-IV-S_4(Se)_4$ " *Mat.Res.Bull.* 1974; 9:645-654.
8. Xie Y, Zhang C, Yang G, Yang J, Zhou X, and Ma J, "Highly crystalline stannite-phase $Cu_2XS_nS_4$ (X = Mn, Fe, Co, Ni, Zn and Cd) nanoflower counter electrodes for ZnO-based dye-sensitised solar cells," *J. Alloys Compd.* 2017;696:938-946
9. Wang H, "Progress in thin film solar cells based on $Cu_2 ZnSnS_4$," *Int. J. Photoenergy*, 2011 (2011).
10. Godbole B, Badera N, Shrivastav SB, and Ganesan V, "A simple chemical spray pyrolysis apparatus for thin film preparation," *Jl. instrument. Soc. India.* 2009;39:42-45.
11. Ghosh G, Biswas A, Thangavel R, and Udayabhanu. "Photo-electrochemical properties and electronic band structure of kesterite copper chalcogenide $Cu_2 -II-Sn-S_4$ (II = Fe, Co, Ni) thin films," *RSC Adv.* 2016;6: 96025-96034,.
12. Shi L, Li Y, Zhu H, and Li Q, "Well-aligned quaternary Cu_2CoSnS_4 single-crystalline nanowires as a potential low-cost solar cell material," *Chempluschem.* 2014;79:1638-1642.
13. Murali B and Krupanidhi SB, "Facile synthesis of Cu_2CoSnS_4 nanoparticles exhibiting red-edge-effect: Application in hybrid photonic devices," *J. Appl. Phys.* 2013;114.
14. Ghosh A, Chaudhary DK, Biswas A, Rajalingam T, and Udayabhanu G, "Solution processed $Cu_2XS_nS_4$ (X= Fe, Co, Ni) photo-electrochemical and thin film solar cells on vertically grown ZnO nanorod arrays," *RSC Adv.*, 2016.
15. Suryawanshi MP *et al.*, "Improved solar cell performance of Cu_2ZnSnS_4 (CZTS) thin films prepared by sulfurizing stacked precursor thin films via SILAR method," *J. Alloys Compd.*, 2016; 4.

Study of chromium atom adsorption on single wall carbon nanotube using first-principles density functional theory

Nirmal Sangeeta A¹, Sonawane MR² and Atram RG²

¹Institute of Science, Mumbai | ²Institute of Science, Nagpur

E-mail: sangeetakanojia@gmail.com, smahadev123@gmail.com, ramdasatram@yahoo.co.in

Manuscript Details

Available online on <http://www.irjse.in>
 ISSN: 2322-0015

Editor: Dr. Arvind Chavhan

Cite this article as:

Nirmal Sangeeta A, Sonawane MR and Atram RG. Study of chromium atom adsorption on single wall carbon nanotube using first-principles density functional theory, *Int. Res. Journal of Science & Engineering*, December 2017; Special Issue A1 : 109-116.

© The Author(s). 2017 Open Access

This article is distributed under the terms of the Creative Commons Attribution 4.0 International License

(<http://creativecommons.org/licenses/by/4.0/>), which permits unrestricted use, distribution, and reproduction in any medium, provided you give appropriate credit to the original author(s) and the source, provide a link to the Creative Commons license, and indicate if changes were made.

ABSTRACT

The effect of adsorption of Chromium (Cr) atoms on single-wall carbon nanotube (SWCNT) is studied using first-principles density-functional theory with the generalized gradient approximation. The adsorption energy, geometry, band Structure, density of states (DOS), Band gap, Charge transfer and spin of Cr atom-SWCNT system are calculated. The electronic properties like DOS, Band structure and HOMO-LUMO shows reduction in band gap of pure carbon nanotube from 0.7eV to 0.33eV due to interaction of Cr, which leads to transfer of semiconducting characteristics of SWCNT to semi metallic. The results are consistent with ionic bonding, and the adsorption is characterized by change in the electronic states and large charge transfer from Cr atom to the SWCNT. The Binding Energy and charge density analysis shows the formation of sigma bond between Carbon and chromium atom. The formation of such covalent bonding and the adsorption is characterized by strong hybridization between Cr atom-SWCNT. The molecular orbital and iso-surface charge distribution shows Cr atom is chemisorbed on carbon nanotube.

Key Words: DFT, Cr Atom, adsorption, CNT

INTRODUCTION

The design and engineering of new materials with tailor-made functionality plays an important role in materials science, and new classes of designer nanoscale materials will likely play a decisive role in the development of future technologies.

Single wall carbon nanotubes (SWCNTs) have received great interest following their discovery by Iijima in 1991 [1], owing to their excellent mechanical, thermal, and electrical properties [2-6]. In order to harness the exceptional properties of SWCNTs, one strategy is to functionalizing CNT by transition metal. Transition metal as promising functional materials have been widely used along with CNTs for catalysis applications, gas sensors, energy conversion and storage devices due to their abundance, environmental friendliness for specific physical and chemical properties [7-11]. Also carbon nanotubes can enhance the electron transport from within while the outside layer can facilitate ion transport which could bring benefits to applications in various electrochemical technologies. Therefore, SWCNTs are considered to be promising materials and building blocks for applications of future electronic devices [12, 13]. Some experimental and theoretical study of the interaction between metal and carbon nanotubes, including metal-doped, metal-cluster, and transition metal, has therefore drawn attention in the last decade. For example, the adsorption of Pt atoms on SWCNTs depends heavily on the curvature and the chirality of tube, and the diffusion barriers of the Pt atom are rather small and depend on the radii and the chirality of the supporting SWNTs [14]. Upon Pd doping, Pd4-cluster-functionalized (5, 5) and (8, 0) CNT model systems shows that the conductance of the semiconducting CNTs increases due to the narrowing band gap [15]. Study of isolated and bundled CNTs with transition-metal atom doping shows the richness of the electronic and magnetic properties [16]. However, there is little attention paid to the physical behaviour between element and CNT. In this paper, we study the interaction between the (8, 0) CNT nuclei such as Chromium. We compare their electronic characteristics by computing the band structure, density of state (DOS), Binding energy, Band Gap, HOMO-LUMO, Charge transfer and spin. With these electronic characteristic of CNT we predict the change in its semiconducting nature. As well as we found behaviour of adsorption of Chromium on CNT with the help of Binding energy, iso-surface Charge density distribution and molecular orbital. We also found the amount of charge transfer between SWCNT and Cr atom to predict type of semi-conductivity of SWCNT.

METHODOLOGY

All the calculations were carried out using first principle density functional theory (DFT), Doml³ code. The Geometry optimizations of SWCNT with Transition metal were performed using GGA and PBE functional [17-20]. For Supercell geometries, spin unrestricted calculations were carried out with a double numeric polarised (DNP) basis set available and orbital cut-off set to 4.4 Å. Scalar relativistic effects were included via a pseudo potential for all-electron calculations. $1 \times 1 \times 2$ k-points were used for the Brillouin zone. All the calculations were performed using boundary conditions with 64 atoms within the Supercell. The tetragonal unit cell of $20 \times 20 \times 8.4$ Å dimensions and sufficient separation between tubes is used to avoid interaction between the atoms. The chosen cut off value leads to atomic energies with an accuracy of 0.1eV/atom, allowing calculations without sufficient loss of accuracy. The calculations were performed to find the structural and electronic properties of optimized structures. Milliken population analysis was carried out to predict the charge transfer and spin between Cr-Atom and nanotubes.

We have selected (8, 0) zigzag CNT of diameter 6.26 Å and the length of tube is 8.52 Å as a model to study the adsorption of Chromium atom. We have examined different site for adsorption of Chromium atom as shown in figure (1). 1) Carbon Atom (Site A), 2) Carbon-Carbon Axial Bond (site B), 3) Carbon-Carbon Chiral bond (site C) and 4) Hexagon (site D). In all calculations, the carbon nanotubes along with Chromium atom were first optimized to occupy their minimize energy state. For each site Cr has kept at a finite distance of 3.0 Å to optimize the system to get stable structure. The binding energy (E_b) of adsorption of Cr atom on nanotube for all ground state structures were calculated by

$$E_b = - [E_T(\text{adsorbent} + \text{adsorbate}) - E_T(\text{adsorbent}) - E_T(\text{adsorbate})].$$

Where $E_T(\text{adsorbent} + \text{adsorbate})$ is the total energy of atom and CNT system, $E_T(\text{adsorbent})$ is total energy of CNT and $E_T(\text{adsorbate})$ is the total energy of atom. To verify the computational accuracy of the structure we have calculated the binding energy of CNTs, density of state, band gap Charge Density, HOMO-LUMO, Milliken Charge and spin [21].

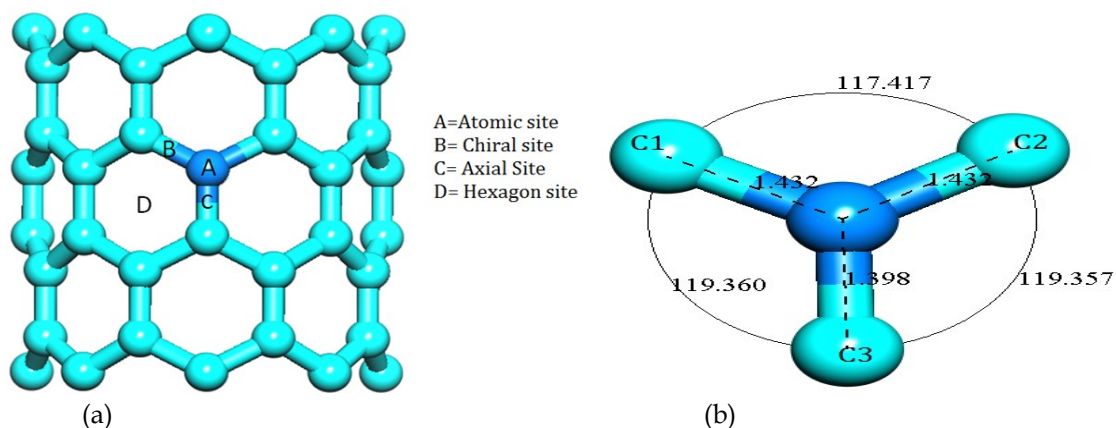


Figure1: (a) Structural model of CNT (8, 0) (b) structural parameter at target atom

RESULTS AND DISCUSSION

The Chromium atom is steely-grey, lustrous, hard and brittle metal in nature which takes a high polish, resists tarnishing, and has a high melting point. The radius of a Cr atom is 206 pm (0.206 nm) which is much greater than of a carbon atom 70 pm (0.070nm). So we studied the effect of adsorption of Cr atom on SWCNT. We are reporting here change in geometrical and electronic properties SWCNT, also adsorption nature of Cr atom.

Geometrical and Electronic properties

We have first performed geometry optimization for Cr adatom - SWCNT system and then found most stable configuration to get geometrical properties of the system. We performed first principal calculated for total energy to investigate electronic property and to observe the nature of adsorption of Cr atom on nanotube. The four different interactive sites were tested as mentioned above for the absorption of adatom. For all sites it is observed that Cr adatom get Chemisorbed with slight change bond length as in figure 2(a-d).

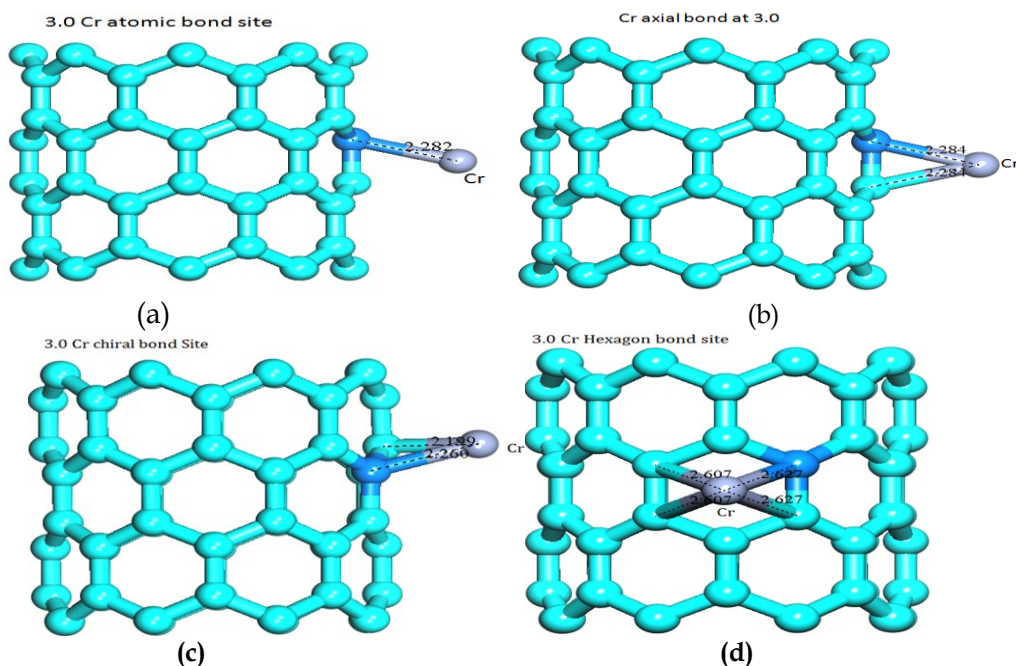


Figure (2): (a) Optimized structure of Cr-CNT at atomic bond position with bond length (b) Optimized structure of Cr-CNT at axial bond position with bond length (c) Optimized structure of Cr-CNT at Chiral bond position with bond length and (d) Optimized structure of Cr-CNT at Hexagon bond position with bond length.

Before optimization, in the prepared model the distance of adsorption of Cr adatom is about 3.0 Å from carbon atom or carbon-carbon bond. After performing optimization Cr adatom get attached to carbon atom of nanotube by covalent bond of bond length 2.28 Å. There is minute difference in bond length of carbon - Cr atom at different sites as shown in Figure 2(a-d). Due to adsorption of Cr atom the bond lengths between C - C atom of both chiral bond at absorption site-B is changed from 1.432 Å to 1.449 Å

and 1.452 Å. For axial site - C the bond length of C - C atom is changed from 1.398 Å to 1.421 Å.

So slight variation in bond lengths at absorption sites were observed for chiral and axial bonds. This shows the carbon atom at adsorption sites are slightly bumped out of the cylindrical structure of nanotube and the bond angles between C - C - C bonds were ranging from 115° to 119° which is less than 120° indicates trigonal structure of bonding and prefers SP² hybridization as shown in Table 1.

Table 1: The Table shows Structural properties of adsorption of Cr atom on CNT: Bond lengths, bond angles.

Site	Distances in Å for CNT	Binding distance in Å	Angle of CNT in degree	Angle of CNT with Cr in degree
Pure (8,0) CNT	d(C-C) CH L=1.432 Å		(C-C-C)CH-CH =117.41	
	d(C-C) CH R= 1.432 Å		(C-C-C)CHAx1=119.36	
	d(C-C) Axial = 1.398 Å		(C-C-C)CHAx2=119.36	
3.0 Cr Atomic	d(C-C) CH L=1.45 Å	<i>l(C-Cr)</i>	(C-C-C)CH-CH =115.86	
	d(C-C) CH R= 1.451 Å	2.282 Å	(C-C-C)CH-Ax1=118.8	
	d(C-C) Axial = 1.421 Å		(C-C-C)CH-Ax2=118.7	
		<i>l(C-Cr)</i>	(C-C-C)CH-CH =115.86	<(C-Cr-C)=36.245
3.0 Cr Axial Bond	d(C-C) CH L=1.449 Å	2.283 Å	(C-C-C)CHAx1=118.78	
	d(C-C) CH R= 1.452 Å		(C-C-C)CHAx2=118.702	
	d(C-C) Axial = 1.421 Å		(C-C-C)CHAx2=118.702	
3.0 Cr Chiral Bond	d(C-C) CH L=1.454 Å	<i>l(C-Cr)</i>	(C-C-C)CH-CH =116.012	<(C-Cr-C)=39.047
	d(C-C) CH R= 1.485 Å	2.248-2.201	(C-C-C)CH-Ax1=118.46	
	d(C-C) Axial = 1.408 Å		(C-C-C)CH-Ax2=116.926	
3.0 Cr Hexagon	d(C-C) CH L =1.467 Å	<i>l(C-Cr)</i>		<(C-Cr)CH-CH=56.252
	d(C-C) CH R =1.466 Å	2.627-2.608		<(C-Cr-C)Axial L=30.944
	d(C-C) Axial L = 1.39 Å			<(C-Cr-C) Axial R=30.694
	d(C-C) Axial R = 1.39 Å			
	d(C-C) CH L below=1.467 Å			
	d(C-C) CH R below=1.466 Å			

Table 2: The Table shows Electronic Properties of adsorption of Cr atom on SWCNT: Binding Energy, Band gap, Charge, Spin, HOMO and LUMO energy

	B.E (eV)	Band gap (eV)	Charge (Qt)	Spin	HOMO energy (eV)	LUMO energy (eV)
CNT (8,0)		0.701				
CNT - 3.0 Cr Atomic	-0.5822	0.3278	0.407	5.256	-3.698	-3.459
CNT - 3.0 Cr Axial Bond	-0.5822	0.3277	0.406	5.257	-3.695	-3.459
CNT - 3.0Cr Chiral Bond	-0.5632	0.3824	0.453	5.072	-3.484	-3.420
CNT - 3.0 Cr Hexagon	- 1.2545	0.3935	0.501	0	-3.363	-3.282

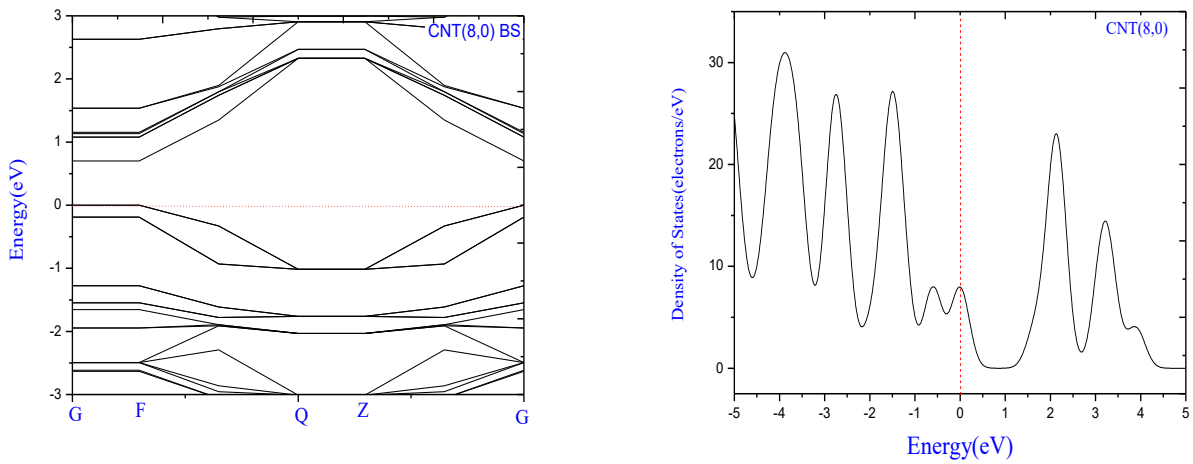


Figure 3: (a) Band structure and DOS of Pure CNT (8,0)

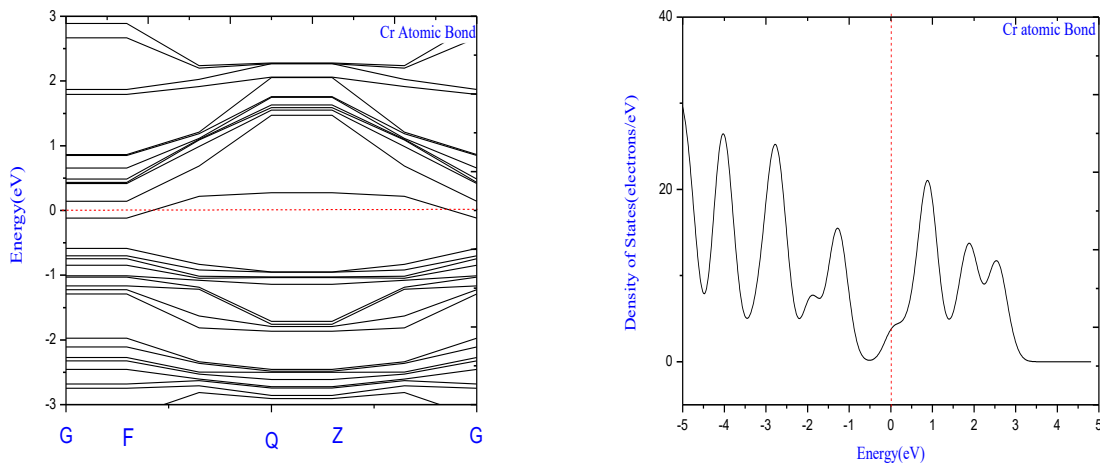


Figure 3: (b) Band structure and DOS of CNT with adatom Cr for Atomic site - A

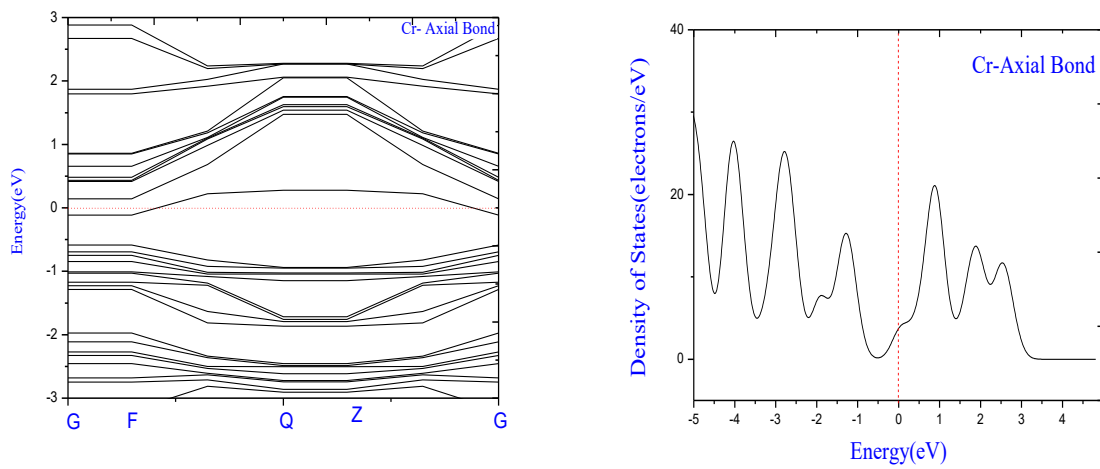


Figure 3: (c) Band structure and DOS of Cr-CNT at axial bond site - C

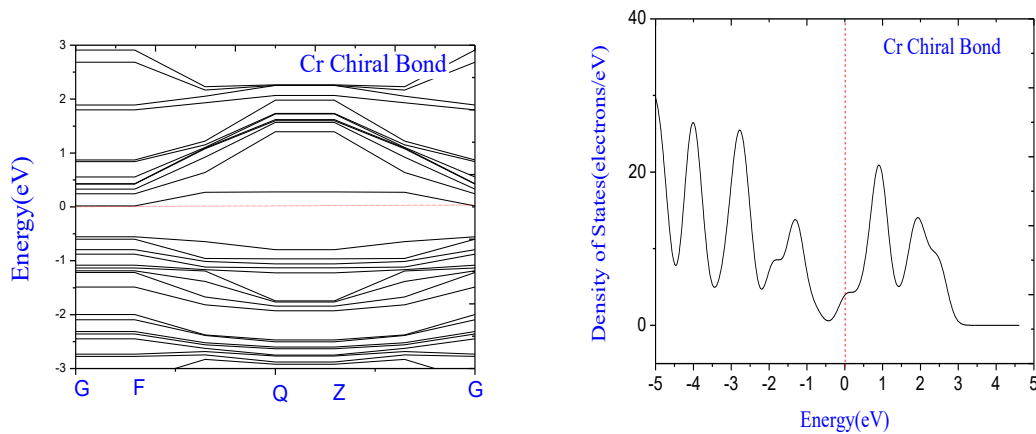


Figure 3: (d) Band structure and DOS of Cr-CNT at Chiral bond site - B

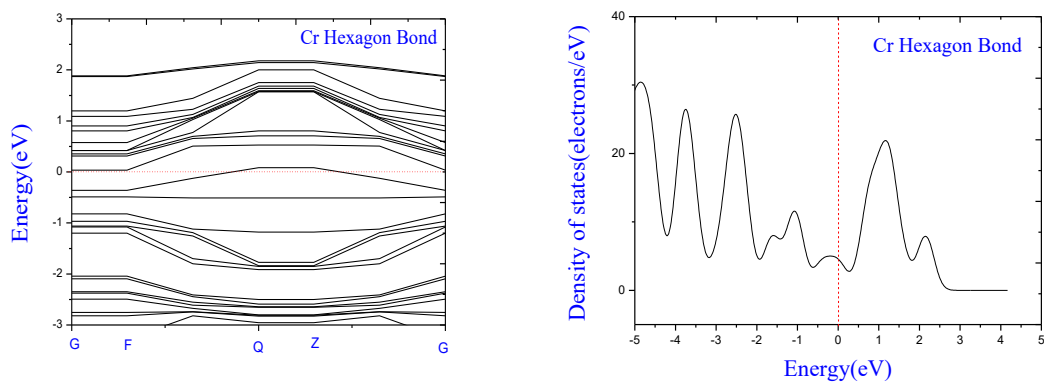
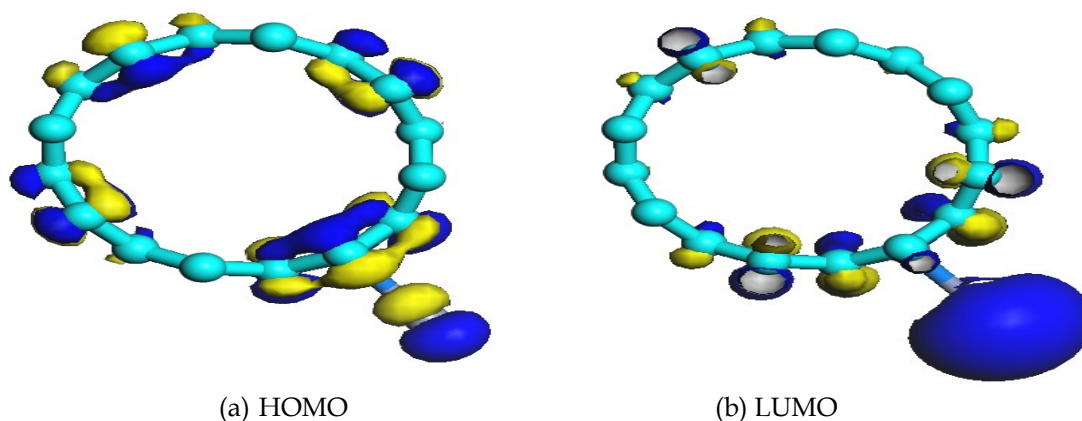


Figure 3: (e) Band structure and DOS of Cr-CNT Hexagon site - D

The binding energy of Cr adatom on SWCNT for Atomic site - A and Axial bond site - C is -0.585eV , whereas for Chiral bond site - B is -0.56eV and for Hexagon site - D is -1.25eV . The binding energy for Hexagon is more. The binding energy values clearly indicate the Cr atom is chemisorbed on CNT for all four sites.

The Band Structure (BS) and Density of State (DOS) of pure SWCNT is Shown in figure 3(a). The energy band gap found from BS and DOS for pure CNT is 0.701eV , which is competent to theoretically and experimentally reported result. Figure 3(b-e) shows BS and DOS for interaction Cr atom with CNT at four different sites. BS and DOS for atomic site - A, axial bond site - C and chiral bond site - B shows there is an extra occupied states near Fermi energy in valance band. For hexagon site - D there is heavily occupied state near Fermi energy in valance band. The energy levels in valance band are at -1.7068eV and -0.479eV as compared to CNT. The newly formed extra state at

0.244eV in conduction band for interaction of Cr atom with CNT is almost reduced and shifted near to Fermi level as compared to CNT. This results in reduction of band gap of CNT from 0.7eV (of pure CNT) to 0.327eV for atomic and axial bond site. For chiral bond and Hexagon position band gap reduced to 0.382eV and 0.393 respectively as shown in Table 2. The Charge transfer between Cr atom and nanotube has been calculated by using Mulliken population analysis. The charge transferred from Cr atom to CNT therefore Cr atom occupies positive charge. The magnitude of charge donated by Cr atom to CNT at site - A is 0.407e and at site - C is 0.406e . The quantity of charge transfer from Cr to CNT for sit - B is 0.453e and that of sit - D is 0.501e . The higher values shoes sharing of charge with more carbon atom in CNT leads to form multiple covalent bonds. We have also calculated spin of electron in Cr atom which has more values for site - A, site - C and less for site - B where for site - D is almost zero because of pairing electron in four covalent bonds.



(a) HOMO
(b) LUMO
Figure 4: (a) HOMO for Cr-CNT (b) LUMO for Cr-CNT

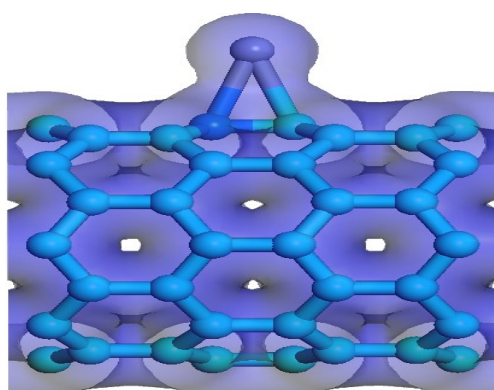


Figure 5(a) shows the iso-surface of charge density. It shows formation of sigma bond between Cr atom and carbon atoms

The Frontier molecular orbitals are important in interpreting chemical reactivity. We thus exhibit the highest occupied molecular orbitals (HOMO) and Lowest Unoccupied Molecular orbitals (LUMO) as shown in figure 4(a-b). The HOMO energy is -3.695 eV and LUMO energy is -3.458 eV for atomic bond and axial bond.

CONCLUSION

The density functional theory based on linear combination of atomic orbital is used to study the adsorption of chromium atom on CNT at various four sites. In all four adsorption sites chromium atom is chemisorbed onto CNT by forming covalent bonds with carbon atoms. Chromium atom creates extra states near the Fermi energy level in each case of adsorption, producing fictionalization in carbon nanotube. We also found that there is net charge

transfer from chromium to CNT which converts semiconducting carbon nanotube into semimetal. The change in electronic properties of carbon nanotube leads to its use as a basic building block in nano-electronic devices and sensors. The charge density and molecular orbital clearly show the formation of a sigma bond between chromium and carbon atoms.

Acknowledgements

We would like to acknowledge Ismail Yusuf College, Jogeshwari (E), Mumbai for providing us facility of computing system and software material studio.

REFERENCES

1. Martel R, Schmidt T, Shea HR, Hertel T, and Ph. Avouris, "Many Single- and multi-wall carbon nanotube field-effect transistors" 1998, *Appl. Phys., Lett.* 73: 2447.
2. Baughman Ray H, Anvar A. Zakhidov, Walt A. de Heer, "Many Carbon Nanotubes—the Route Toward Applications" 2002, VOL 297.
3. Iijima S, "Helical microtubules of graphitic carbon", 1991:56-58.
4. Chen XQ and Saito T. "Aligning single-wall carbon nanotubes with an alternating-current electric field", 2001, *Appl. Phys. Lett.* 78: 3714.
5. Gao, B., Kleinhammes, A., Tang, X. P., Bower, C., Fleming, L., Wu, Y., & Zhou, O., "Electrochemical intercalation of single-walled carbon nanotubes with lithium" 1999: 153-157
6. Yahachi Saito, Sashiro Uemura "Field emission from carbon nanotubes and its application to electron sources" 2000: 169-182.
7. Spataru CD, Ismail-Beigi S, Benedict LX, and Louie SG. "Excitonic Effects and Optical Spectra of

- Single-Walled Carbon Nanotubes", 2004 Physical Reviews Letters 92:077402
8. Odom TW, Huang JL, Kim P and Lieber CM. Atomic structure and electronic properties of single-walled carbon nanotubes" 1998: 62-64.
 9. McEuen PL, Fuhrer MS, Hongkun Park. Single-walled carbon nanotube electronics", 2002 :78 – 85.
 10. Kazuyuki Uchida and Susumu Okada, "Electronic properties of a carbon nanotube in a field-effect transistor structure: A first-principles study" 2009:085402.
 11. Sander J. Tans, Michel H. Devoret, Hongjie Dai, Andreas Thess, Richard E. Smalley, L. J. Geerligs, Cees Dekker, "Individual single-wall carbon nanotubes as quantum wires" 1997:474–477.
 12. Martin Pumera, Miloš Cabala, Kateřina Veltruská, Izumi Ichinose and Jie Tang "Nanoprecise Spontaneous Coating of Carbon Nanotubes with a Europium Hydroxide Layer", 2007: 6513–6517.
 13. Ting Liang a , Wei-Xue Li b , Hong Zhang a "A first-principles study on the behavior of HCl inside SWCNT ", 2009:44–47.
 14. Ji-Chun Xie, Yong-Jian-Tang, Hong Zhang, "A DFT study on the interaction between europium, uranium and SWCNT" 2011: 716–721.
 15. Ya Kun Chen, Lei Vincent Liu, Wei Quan Tian and Yan Alexander Wang "Theoretical Studies of Transition-Metal-Doped Single-Walled Carbon Nanotubes", 2011:9306–9311.
 16. Chang lun Chen, Jun Hu, Di Xu, Xiaoli Tan, Yuedong Meng, Xiangke Wang , "Surface complexation modeling of Sr(II) and Eu(III) adsorption onto oxidized multiwall carbon nanotubes", 2008:33–41.
 17. Hyun-Hee Cho, Billy A. Smith, Joshua D. Wnuk, D. Howard Fairbrother and William P. Ball, "Influence of Surface Oxides on the Adsorption of Naphthalene onto Multiwalled Carbon Nanotubes", 2008:2899–2905.
 18. Xiangke Wang, Changlun Chen, Jinzhou Du, Xiaoli Tan, Di Xu, and Shaoming Yu, "Effect of pH and Aging Time on the Kinetic Dissociation of 243Am(III) from Humic Acid-Coated γ -Al₂O₃: A Chelating Resin Exchange Study", 2005:7084–7088.
 19. Segall, M D; Lindan, P J D; Probert, M J; Pickard, Christopher James; Hasnip, P J; Clark, S J; Payne, M C. "First-principles simulation: ideas, illustrations and the CASTEP code", 2002:2717–2744.
 20. Stewart J. Clark, Matthew D. Segall, Chris J. Pickard, Phil J. Hasnip, Matt I. J. Probert, Keith Refson and Mike C. Payne, "First principles methods using CASTEP", 2005: 567–570:
 21. Engel E, Keller S, and Dreizler RM, "Generalized gradient approximation for the relativistic exchange-only energy functional", 1996:1367.
 22. John P. Perdew, Kieron Burke, and Matthias Ernzerhof, "Generalized Gradient Approximation Made Simple", 1996: 3865.

Synthesis and Characterization of Polyaniline-SnO₂ Composite for Volatile Organic Compounds (VOCs) Detection

Varade PS, Gangal SA, Shaligram AD

Department of Electronic Science, Savitribai Phule Pune University, Pune (Maharashtra), India.

Manuscript Details

Available online on <http://www.irjse.in>
ISSN: 2322-0015

Editor: Dr. Arvind Chavhan

Cite this article as:

Varade PS, Gangal SA, Shaligram AD. Synthesis and Characterization of Polyaniline-SnO₂ Composite for Volatile Organic Compounds (VOCs) Detection, *Int. Res. Journal of Science & Engineering*, December 2017; Special Issue A1 : 117-122.

© The Author(s). 2017 Open Access

This article is distributed under the terms of the Creative Commons Attribution 4.0 International License

(<http://creativecommons.org/licenses/by/4.0/>), which permits unrestricted use, distribution, and reproduction in any medium, provided you give appropriate credit to the original author(s) and the source, provide a link to the Creative Commons license, and indicate if changes were made.

ABSTRACT

Polyaniline- SnO₂ nanocomposite was synthesized using an in-situ polymerization of aniline in presence of synthesized SnO₂ nanoparticles. Structural and elemental characterization was done using FT-IR, XRD and FE-SEM techniques. The gas sensitivity of Polyaniline- SnO₂ nanocomposite material to volatile organic compounds (VOCs - ethanol, methanol, acetone and toluene) was studied. Thin films of polyaniline - SnO₂ nanocomposite material were deposited by drop cast method on interdigitated structure (IDT). DC resistance of the films was measured using electrometer. The resistance of the films in normal air is in the range of 0.2 to 0,8 GΩ. It is observed that polyaniline-SnO₂ composite material is sensitive to VOCs at room temperature. The sensitivity of the material for VOCs is studied in ppm range of 200 -1000. The polyaniline-SnO₂ composite material shows the linear increase in sensitivity with the increase of ethanol concentration. It is observed that polyaniline - SnO₂ thin film is more sensitive to ethanol (50.68%) as compared to methanol (9.74%), acetone(7.22%) and toluene (4.99%). The response mechanism of polyaniline-SnO₂ material to VOCs is also discussed.

Keywords Polyaniline- SnO₂ composite, Volatile organic compounds, sensitivity.

INTRODUCTION

Volatile organic compounds (VOCs) are organic chemicals which have a high vapor pressure at room temperature. Their high vapor pressure results in low boiling point, which causes large numbers of molecules to evaporate or sublime from the liquid or solid form of the compound and enter the surrounding air. These kinds of chemicals can enter the human body through many ways such as breathing, touching or swallowing. These VOCs causes an adverse effect on human health, so detection of VOCs has become important. Different types of sensors are available for detection of the VOCs. Sensors TGS 812(Figaro) for propane, butane detection and STEINEL SGAS 2000 for ethanol detection [1] are commercially available. These sensors basically operate above room temperatures. Many studies showed that the inorganic semiconductors such as TiO₂, ZnO, SnO₂, and Fe₂O₃ are used for making sensors, but they need to be operated at temperature above 300°C which increases the power consumption and reduce operating life of the sensor. In commercial devices organic semiconductors are used because they operates at low temperatures. But the main limitation is their slow response time [1-2].

To manifest the characteristics of pure inorganic and organic materials and explore the sensing materials with low operating temperature and good selectivity, organic-inorganic sensing composites have been developed. GENG Li-na [3] reported that polyaniline-SnO₂ composite material has good sensitivity to VOCs at 90°C and can respond at a wide concentration range with fast response (10-32, 54-148, 79-49 seconds) and recovery times (47-109, 79-118, 65-160 seconds) for ethanol, methanol and acetone respectively. H. Gong et. al. [4] reported that thin films of tin oxide show maximum sensitivity to VOCs at 450°C. Min-Hyun Seo et. al. [5] reported that the TiO₂ nanotubes can detect toluene upto 50 ppm at an elevated temperature of 500°C in dry air. Anjali A. Athawale et. al. [6] synthesized Pd-polyaniline nanocomposite by oxidative polymerization and tested the response for methanol, ethanol and isopropanol for the concentrations of 1, 5, 10, 100 and 2000 ppm. It is reported that Pd-polyaniline nanocomposite is highly sensitive ($8.9 \times 10^5 \Omega \text{ ppm}^{-1}$) and selective in presence

of Pd nanoparticles to methanol vapors with stable response for a sufficiently long time at room temperature. Recently K. Inyawilert et. al. [7] reported that sparked-In₂O₃ sensing films with different thicknesses can be used for ethanol and acetone sensing applications. The sensor with optimal thickness of $\sim 3 \mu\text{m}$ (100 sparking cycles) exhibited the highest ethanol/acetone response of ~ 19 . Shortest response times within seconds and lowest detection limit 100 ppm at 350 °C. Very few researchers [1, 6] worked on VOCs detection using polyaniline-SnO₂ nanocomposite at room temperature. So we focused on the study of polyaniline-SnO₂ nanocomposite material synthesis to improve its sensitivity. In present work, polyaniline-SnO₂ nanocomposite is prepared by in situ polymerization of aniline in presence of synthesized SnO₂ nanoparticles using ammonium persulphate (APS) as an oxidant in acidic medium. The composite is characterized by FTIR, XRD and FE-SEM with EDS. The prepared material is tested for four different volatile organic compounds (ethanol, methanol, acetone and toluene) with their exposure range of 200-1000 ppm. The results related to sensitivity of the sensing material to VOCs have been discussed.

METHODOLOGY

Aniline (99.5%) monomer was distilled using condenser method to remove the additives and to get pure aniline monomers before its use. Tin chloride (SnCl₄ : 5H₂O) (99%), hydrogen peroxide (H₂O₂) (99.5%) Ammonium per sulphate (98%), starch (98.5%) and ammonia (99%) were purchased from High Purity Laboratory Chemicals PVT. LTD. All chemicals were of analytical grade and used as they are. The solutions were prepared with distilled water.

Synthesis of SnO₂ nanoparticles

Sol-gel method was used for the synthesis of SnO₂ nanoparticles. In a typical method, 0.1M SnCl₄:H₂O was added in 1M starch solution and the mixture was stirred for half an hour. Then 0.2M ammonia was added drop wise in the solution under constant stirring. The stirring was continued for further 3 hours and then the solution was allowed to settle overnight. Supernatant liquid was then discarded carefully and

the remaining solution was centrifuged for 15 minutes and then filtered. The precipitate of SnO₂ was washed completely using distilled water to remove by-product and the excessive starch those were bound with the nanoparticles. The product was dried in hot air oven at 80°C for overnight. Then powder was sintered at 600°C using oven for 6 hours and nanocrystalline SnO₂ was obtained [8].

Synthesis of polyaniline-SnO₂ nanocomposite

Polyaniline - SnO₂ nanocomposite was synthesized by an in-situ polymerization of aniline in presence of synthesized SnO₂ nanoparticles using ammonium persulphate (APS) as an oxidant in acidic medium. Aniline (0.1M) and APS (0.1M) were dissolved separately in 1M HCl solution and stirred for 80 minutes. As-synthesized SnO₂ nanoparticles were suspended separately in 1 M HCl (100 ml) solution and sonicated for 90 minutes to reduce aggregation of SnO₂ nanoparticles. 100 ml aniline solution and 10 ml SnO₂ nanoparticles suspension were mixed and further sonicated for 90 minutes. 100 ml APS solution was then slowly added drop wise to well disperse suspension mixture with continuous stirring. After 2 hours, a good degree of polymerization was achieved. The green color precipitate was obtained. The precipitate produced in the reaction was removed by filtration, washed repeatedly with 1 M HCl and dried at room temperature in dust free environment. The composite powder was in conductive emeraldine salt (ES) form of polyaniline -SnO₂ nanocomposite [8].

Structural and morphological Characterization of polyaniline-SnO₂ nanocomposite

The FTIR spectra of synthesized product were recorded by using Bruker spectrophotometer in the wavenumber range of 400-4000 cm⁻¹. Phase identification of the composite was done by X-ray diffraction using Bruker AXSD8 diffractometer with Cu-K α radiation source. The morphological study of the composite was carried out by field emission scanning electron microscope (FESEM- Nova NanoSEM NPEP303), and SEM JEOL, OXFORD instruments).

VOC Sensing characteristics of Polyaniline - SnO₂ nanocomposite

The film of synthesized Polyaniline-SnO₂ nanocomposite was formed by drop casting method on the interdigitated structure (IDT) made in copper film on glass

epoxy. IDT structure has five finger pairs having finger width and gap of 2mm each. 20 micro-liter solution was dropped from micropipette on the IDT structure. The film is dried at room temperature before use for VOC detection. The experimental set-up used for VOCs detection is shown in figure1. The gas sensing characteristics were studied in a custom-made testing chamber. The testing chamber is made of glass having air tight plastic cap on which the gas inlet rubber and electrical contacts for sensor are fitted. The volume of the chamber is 500cc. The vapors of VOCs in liquid form are added in the chamber by using the plastic syringe. The sensor was tested for 200- 1000 ppm (VOCs concentration). The sensitivity of the sensor was determined by measuring the resistance of the sensor at room temperature with and without presence of the VOCs using Keithley's Electrometer (Model -2000).



Figure 1: Experimental set-up for VOC study

RESULTS AND DISCUSSION

Figure 2 shows the XRD pattern of the obtained Polyaniline- SnO₂ composite. It can be seen that the nanocrystalline SnO₂ peaks are observed at 2 θ values of 26.580, 34.900, 38.140, 52.130, 66.120 and matched with those peaks along planes (1 1 0), (1 0 1), (2 0 0), (2 1 1), and (3 0 1) having primitive tetragonal structure (JCPDS DATA CARD 41-1445). The XRD spectrum peaks are close to the standard XRD of SnO₂]. However, these peaks show a small shift (0.20 to 0.50) from their respective standard positions which may be due to polyaniline matrix. In addition, we observed relatively larger peak broadening, compared with XRD of pure SnO₂ [9] This suggests that tin oxide is present in the polyaniline matrix, and presence of

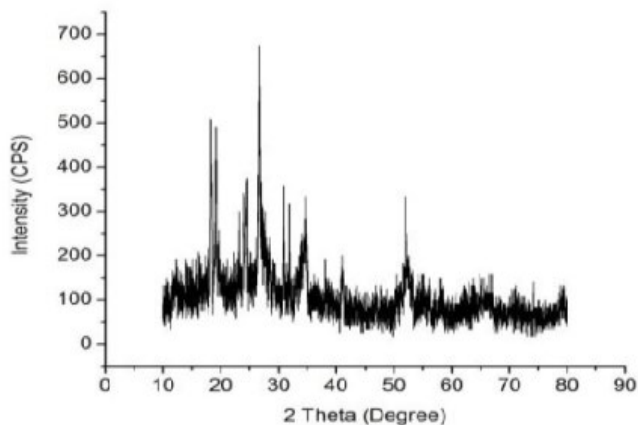


Figure 2: XRD of polyaniline -SnO₂ Composite

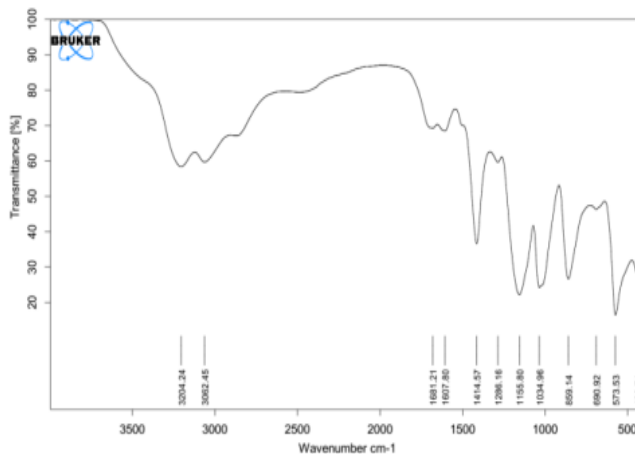


Figure 3: FTIR spectra of polyaniline-SnO₂ Composite

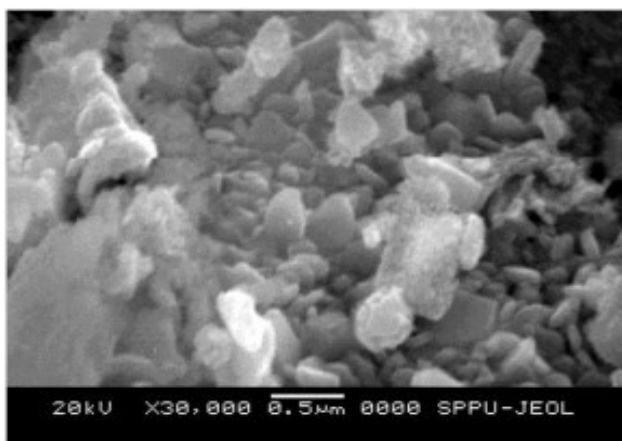


Figure 4: SEM of SnO₂ nano particles

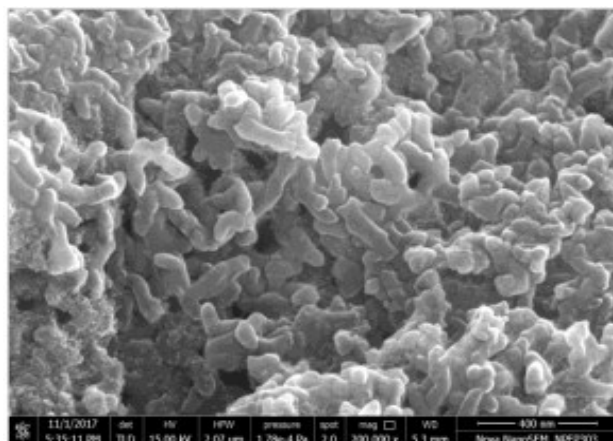


Figure 5: FE- SEM of polyaniline-SnO₂ nanocomposite

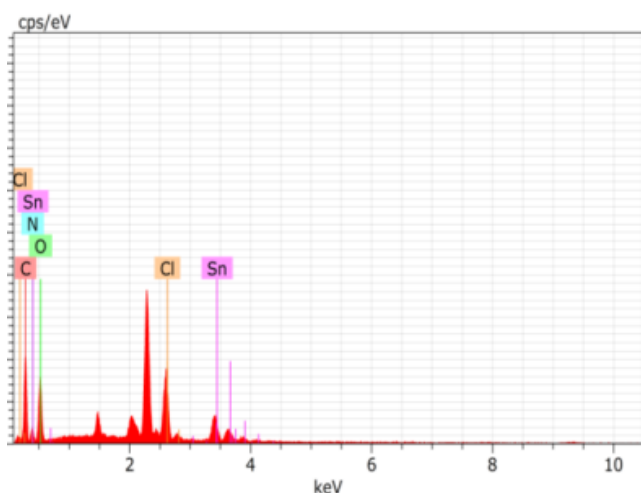


Figure 6: EDS of PANI-SnO₂ Composite

polyaniline has influenced the preferred orientation of tin oxide grains in the composite to some extent. The lattice constant was found to be $a = b = 4.741 \text{ \AA}$, $c = 3.31$. Peaks in Figure 2 are similar to those observed by other researchers [8,10]. The chemical structure of the

composite was characterized by Fourier Transform Infrared (FTIR) spectroscopy.

In the FTIR spectrum of a composite (figure 3), the characteristic peaks at 3062.45 & 3204.24 cm⁻¹ & 1681.21cm⁻¹ correspond to C-H stretching vibrations, and C=C stretching vibrations respectively. Peaks at 1607.80 and 1414.57 cm⁻¹ correspond to quinoid and benzene rings of polyaniline, while the peak at 690.92 cm⁻¹ corresponds to the anti-symmetric Sn-O-Sn mode [8,10]. Thus it shows the characteristics of polyaniline as well as the tin oxide. Figure 4 shows the SEM image synthesized SnO₂ nanoparticles. Which shows that the particle size is not uniform. Figure 5 shows the field emission scanning electron microscopic image of polyaniline-SnO₂ image. We took the images at different points on the material. At few places it is observed the particle structure like nano rods with their length varying from ~450-700nm.

Table 1. Concentrations of chemical elements composing the sample

Elements	C	O	N	Sn	Cl
EDX at %	48.86	30.33	16.39	1.42	3.00
EDX Weight %	37.22	30.78	14.56	10.72	6.74
Chemical Analysis, Weight %	25.26	20.89	9.88	7.27	4.57

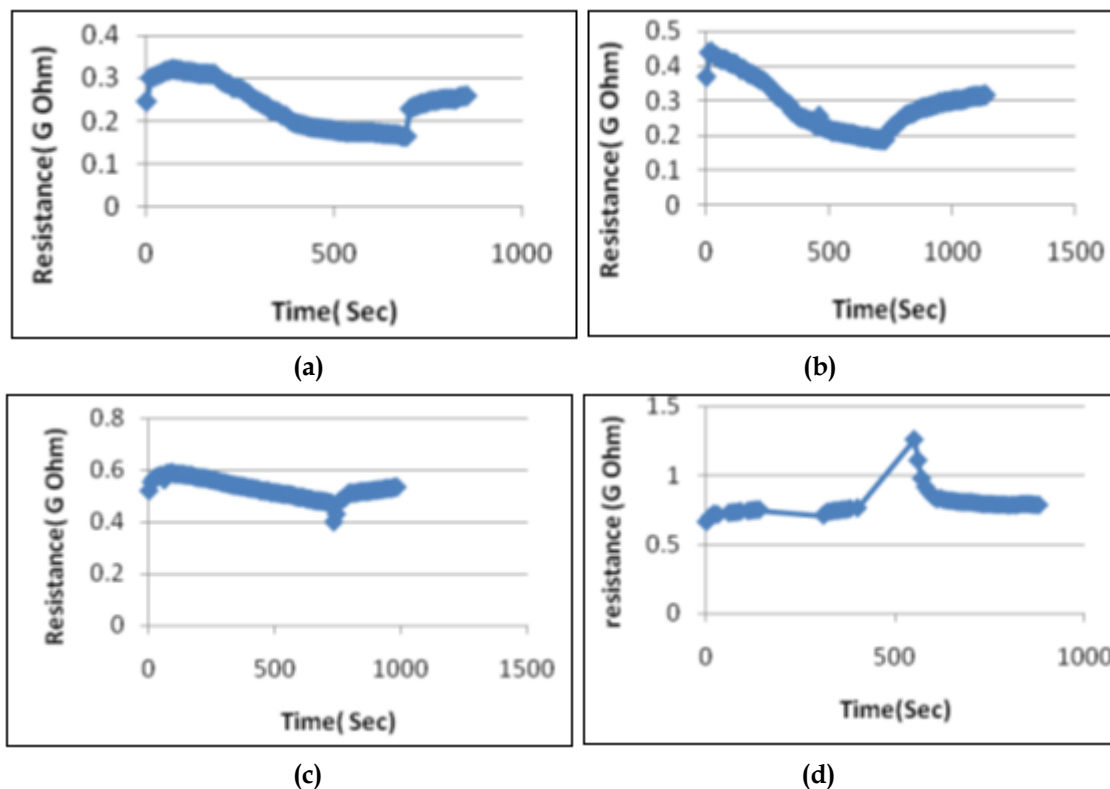


Figure 7: VOCs (a) ethanol, b) methanol, c) acetone d) , toluene) response to PANI- SnO2 nanocomposite

Study of the composition of samples by the technique of EDX microanalysis has shown (Figure 6.) that in the spectrum of characteristic X-ray radiation appearing at interaction of the electron probe with the sample surface, there are peaks of chemical elements entering the experimental set-up for VOC study composition of polyaniline (only C and N, because this technique does not detect H) and tin dioxide (Sn and O), as well as the peaks of sulfur and chlorine. Measurements were performed in different regions of the sample surface [10].

Table 1 lists average values of concentrations of chemical elements in the sample. sensitivity of the sensor is defined as the ratio of the change in resistance of the sensor on exposure to the target gas to the original resistance in air. The relation for sensitivity S is as:

$$S = (R_g - R_a) / R_a,$$

where R_a and R_g are the resistance of sensing materials in air and in a target gas medium respectively.

Figure 7 shows the responses of polyaniline-SnO₂ film to the ethanol methanol, acetone and toluene respectively at room temperature. These responses are recorded for 200-1000 ppm of these VOCs. The response shown in figure 7 is for 200 ppm exposure of each VOC to the sensor. For exposure of these VOCs it is observed that the resistance initially increases for short time and then it decreases. Initially the adsorption of oxygen from VOCs on the surface of sensing material increases the resistance of the sensor material due to transport of electrons from conduction band to adsorbed oxygen [1, 2], this indicates that our material is p type. After short time the resistance of polyaniline-SnO₂ materials decreases because of water content in VOCs is get adsorbed on the

material, which increases the surface conductivity of the material. The decrease in resistance is below the base line resistance of the composite material. This is due to higher conductivity of adsorbed water molecules, which takes more time to desorb. The gas sensitivity of polyaniline- SnO₂ materials to VOCs may be explained by the creation of positively charged depletion layer on the surface of the SnO₂, which could be formed owing to inter-particle electron migration from SnO₂ to polyaniline at the p-n heterojunctions. This would cause a lowering of the activation energy and enthalpy of physisorption for vapors with good electron-donating characteristics [1, 2]. For all the four VOCs the response time observed is less than recovery time.

Figure 8 shows the sensitivities versus the amount of VOCs exposure. It shows that the sensitivity of the sensing material is more for ethanol than the other three VOCs.

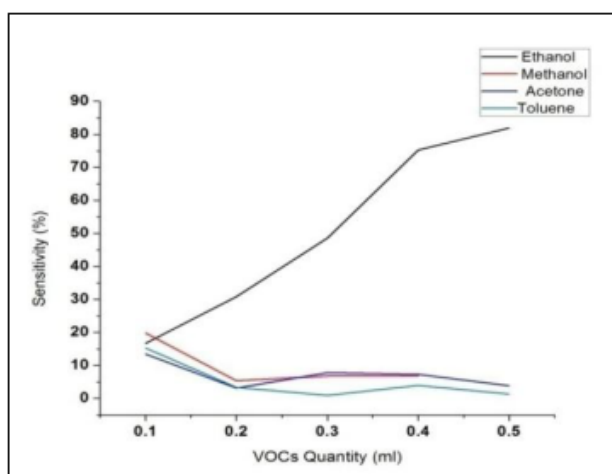


Figure 8: Sensitivities of ethanol, methanol, acetone and toluene to polyaniline- SnO₂ nanocomposite film

Because ethanol consumes six O-ads, methanol consumes three O-ads for complete oxidation. Acetone consumes four O-ads. But surface reactivity of acetone and toluene is less as compared to ethanol and methanol. The surface reactivity depends on functional groups involved in the reaction. The average sensitivity to the VOCs is in the order-ethanol (50.68%) > methanol (9.74%) > acetone (7.22%) > toluene (4.99%).

CONCLUSION

The sensitivity values of polyaniline- SnO₂ composite to the four organic vapors (VOCs) increases in the order of ethanol > methanol > acetone > toluene. Among these, the sensitivity increases with increasing number of methyl groups involved, suggesting that the sensitivity corresponds to the amount of oxygen adsorbed or the amount of surface lattice oxygen atoms consumed for the complete oxidation per alcohol molecule for total reducibility. The low sensitivity to toluene may be due to absence of oxygen atom in toluene. Acetone has no particular H atoms or groups which are easily dissociated, therefore less dissociative adsorption of oxygen on SnO₂ surface and therefore relatively less sensitivity as compared to ethanol and methanol is seen.

Conflicts of interest: The authors stated that no conflicts of interest.

REFERENCES

1. [Http://www.figaro.co.jp/en](http://www.figaro.co.jp/en)
2. Ulrich Hofer, Joachim Frank, Maximilian Fleischher, High temperature Ga₂O₃ gas sensor and SnO₂ gas sensor : A comparison - Sensor and Actuator, 2001, B 78: 6-11.
3. GENG Li-na, Gas sensitivity /SnO₂ hybrids to volatile organic compounds, Trans , Nanoferrous Met. Soc. China, 2009, 19: S678-S683.
4. Gong H, Wang YJ , Teo SC, Huang L, Interaction between thin-film tin oxide sensor and five organic vapors, Sensors and Actuators, 1999, B54: 232-235
5. Min-Hyun Seo, et al., Sensors and Actuators, 2011, B 154: 251-256.
6. Anjali A thole, Bhagwat SV, Prachi P Katre "Nanocomposite of Pd- polyaniline as a selective methanol sensor ", Sensors and actuators, 2006, B 144: 263-267.
7. Inyawilert K et al. Sensors and Actuators, 2014, B 192: 745-754 .
8. Kondawar SB, et al., Adv. Mat. Lett. 2012, 3(5):393-398.
9. Wei Chen, et al. *J Mater Sci* , 2008, 43:5291-5299.
10. Matnishyan AA et. al, Journal of Contemporary Physics, 2010, 45(5):246-250.

Band Gap Energy of $\text{Ni}_{1-x}\text{Cd}_x\text{Y}_y\text{Fe}_{2-y}\text{O}_4$ by Sol-gel Method

Bhise RB¹ and Rathod SM²

¹Department of Physics, B.J. College, Ale, Tal: Junnar, Dist: Pune, 412411, India,

²Nanomaterials and Laser Research Laboratory, Abasaheb Garware College, Pune, 411004, India

Email: bhiseramesh@gmail.com

Manuscript Details

Available online on <http://www.irjse.in>
ISSN: 2322-0015

Editor: Dr. Arvind Chavhan

Cite this article as:

Bhise RB and Rathod SM. Band Gap Energy of $\text{Ni}_{1-x}\text{Cd}_x\text{Y}_y\text{Fe}_{2-y}\text{O}_4$ by Sol-gel Method, *Int. Res. Journal of Science & Engineering*, December 2017; Special Issue A1 : 123-127.

© The Author(s). 2017 Open Access

This article is distributed under the terms
of the Creative Commons Attribution
4.0 International License

(<http://creativecommons.org/licenses/by/4.0/>),
which permits unrestricted use, distribution, and
reproduction in any medium, provided you give
appropriate credit to the original author(s) and
the source, provide a link to the Creative
Commons license, and indicate if changes were
made.

ABSTRACT

Nanoparticles of Y^{3+} substituted $\text{Ni}_{1-x}\text{Cd}_x\text{Y}_y\text{Fe}_{2-y}\text{O}_4$ (where $x = 0, 0.2, 0.4, 0.6$ and $y = 0, 0.075$) were synthesized using sol-gel autocombustion method. The investigation of optical properties was carried out for the synthesized samples using Fourier transform infrared spectroscopy (FTIR) and Ultraviolet visible spectrophotometer (UV-Vis). XRD revealed that the structure of these nanoparticles is spinel with average grain size lies in the range between 12.5 to 34.8 nm. Lattice parameter was found to increase with Ni-Cd concentration and this may be due to the larger ionic radius of the Y^{3+} ion. The energy band gap was calculated using Tauc method for samples with different ratio and average band gap energy was found to be 1.6294 eV. The substitution resulted in slight increase in the lattice constant and that sequentially may lead to the slightly increased in the energy gap.

Keywords: Autocombustion Method, Band Gap, Optical Property.

INTRODUCTION

Material technology associates the knowledge from the fields of physical science, chemical science, and Engineering. The wide applications of nanoparticles are in electronic, mechanical, optical, and magnetic devices, tissue engineering, magnetic storage systems and magnetic resonance imaging [1-2]. Material technology is new technique for processing manipulation and assembly using atoms, molecules or macromolecules for the

intelligent design of functional materials, components and systems with attractive qualities and functions [3-4]. Magnetic nanomaterials intensively studied as a recording media due to their superior physical properties. These properties make ferrites an ideal candidate for technical applications such as magnetic resonance imaging enhancement, catalysis, sensors and pigments [5]. Combined spinel ferrites have been studied intensively over the last few years due to their potential applications. Spinel ferrites have the chemical formula MFe_2O_4 in which M can be any divalent metal cations. In spinel ferrite, oxygen forms face centre cubic (FCC) lattice with divalent cations at tetrahedral (A) and/or octahedral (B) sites. Magnesium ferrite ($MgFe_2O_4$) has an inverse spinel structure with the preference of Mg^{2+} cations mainly on octahedral sites [6-9], while Zinc ferrite ($ZnFe_2O_4$) has normal spinel structure, in which Zn^{2+} cations mainly occupy tetrahedral sites [6-10]. The small scale size of the well-known spinel ferrites has opened up the door for intensive research to utilize their properties for biomedical applications [11-13]. Numerous methods were reported in literature showing the possibilities of producing particle size in the range of 2 - 100 nm [14-15]. In this work, $Ni_{1-x}Cd_xY_yFe_{2-y}O_4$ (where $x = 0, 0.2, 0.4, 0.6$ and $y = 0, 0.075$) were synthesized using co-precipitation methods. X-ray diffraction was used to investigate the structural and Ultraviolet visible spectrometer and Fourier Transform Infrared Spectroscopy were used to investigate the optical properties of crystallite nanoparticles.

METHODOLOGY

The Y^{3+} doped in Ni-Cd ferrite powders were synthesized by sol-gel autocombustion method at low temperatures for different compositions of $Ni_{1-x}Cd_xY_yFe_{2-y}O_4$ (where $x = 0, 0.2, 0.4, 0.6$ and $y = 0, 0.075$). The AR grade nitrate of Merck company (purity of 99%) are used in the experiments such as Yttrium nitrate ($Y(NO_3)_3 \cdot 6H_2O$), Nickel nitrate ($Ni(NO_3)_2 \cdot 6H_2O$), Cadmium nitrate ($Cd(NO_3)_2 \cdot 6H_2O$), Ferric nitrate ($Fe(NO_3)_3 \cdot 9H_2O$). These nitrates and citric acid are using stoichiometric ratio proportion to obtain the final product and the citric acid ($C_6H_8O_7$) is used as a fuel in the ratio 1:3. The proportion of each

reagent was defined according to its respective molar amounts [16]. All chemicals are dissolved in distilled water and were stirred till to obtain the homogeneous solution. To maintain pH equal to 7 by adding drop by drop ammonium hydroxide (NH_4OH) during the stirring process. This solution was stirred continuously with $80^\circ C$ for about 4-5 hours to obtain sol. After 4-5 hours, gel converts into ash and ash convert into powder. Finally get fine powder of $Ni_{1-x}Cd_xY_yFe_{2-y}O_4$ ferrite nanoparticles after auto combustion. The powder was sintered at $400^\circ C$ for 2 hours.

The structural characterization was done using XRD analysis. The X-ray diffractometer with Cu-K α radiation of wavelength 1.5405 \AA at 40 kV performed a scanning from 20 to 80 degree at a step size of 0.02 degree per second for each prepared sample and determined crystal structure, lattice parameter and crystallite size. The optical characteristics was studied using Fourier Transformation Infrared spectroscopy (FTIR) of Bruker 3000 Hyperion microscope with vertex 80 single point detector performing images resolution ranging between 7500 to 450 cm^{-1} and UV-Visible spectroscopy. Further investigations of the optical properties are under way to elucidate the effective role of inter particle interactions in these samples.

RESULTS AND DISCUSSION

3.1 Structural Studies;

XRD analysis: The resulting powder $Ni_{1-x}Cd_xY_yFe_{2-y}O_4$ (where $x = 0, 0.2, 0.4, 0.6$ and $y = 0, 0.075$) nanocrystals were characterized by XRD pattern. The XRD pattern of sintered Y^{3+} doped the nickel-magnesium-cadmium ferrite nano crystals as shown in figure-2. Obtained XRD pattern and crystalline phases were identified and it conformed the formation of a homogeneous well-defined spinal cubic structure with put any impurity. The broad peaks in the XRD pattern indicate a fine particle nature of the particles. The particle size was determined using Scherer's formula.

The average particle sizes of nanoparticles are given in Table-1. The particle size decreases as the

concentration of Y^{3+} increases. Lattice parameter obtained for prepared sample is ranging between 8.3399 to 8.3665 \AA and average grain size ranging between 12.5 to 34.8 nm. The deviation in lattice parameter can be attributed to the cations rearrangement in the nano sized prepared ferrites. Value of lattice constant for Ni-Cd doped Yttrium

ferrite shows the expansion of unit cell with rare earth doping when compared with pure Yttrium ferrite. This is expected due to substitution of large ionic radius of Y^{3+} ions (0.9\AA) with small ionic radius Fe^{3+} ions (0.645\AA). This result in Y^{3+} substituted ferrites to have higher thermal stability relative to Ni-Cd ferrite.

Table-1: The particle size of $Ni_{1-x}Cd_xY_yFe_{2-y}O_4$ by XRD

Composition	Average grain size (t) nm	Lattice constant (a) \AA
$NiFe_2O_4$	34.77	8.3399
$Ni_{0.8}Cd_{0.2}Fe_2O_4$	25.15	8.3455
$Ni_{0.8}Cd_{0.2}Y_{0.075}Fe_{1.925}O_4$	20.76	8.3591
$Ni_{0.6}Cd_{0.4}Y_{0.075}Fe_{1.925}O_4$	16.05	8.3635
$Ni_{0.4}Cd_{0.6}Y_{0.075}Fe_{1.925}O_4$	12.49	8.3665

Table-2: The band gap energy of $Ni_{1-x}Cd_xY_yFe_{2-y}O_4$ by UV- Visible spectroscopy

Composition	Wavelength (nm)	Band gap energy (eV)	
		Tangent Method	Tauc Method
$x=0.2, y=0$	751.25	1.6505	1.6382
$x=0.2, y=0.075$	762.1	1.6270	1.6603
$x=0.4, y=0.075$	770.9	1.6085	1.6789
$x=0.6, y=0.075$	760	1.6315	1.6774
Average Value		1.6294	1.6637

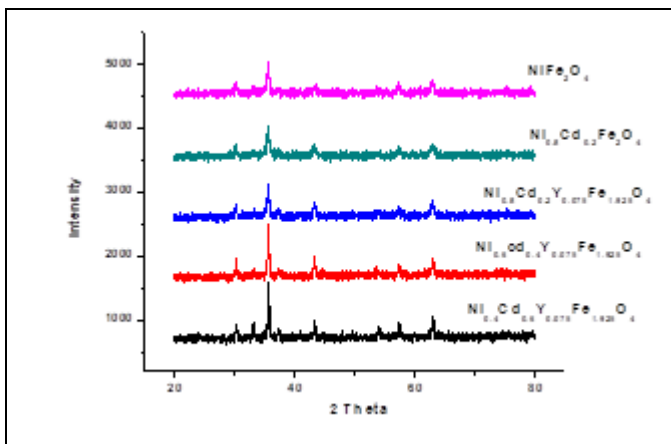


Figure 2: XRD pattern of $Ni_{1-x}Cd_xY_yFe_{2-y}O_4$

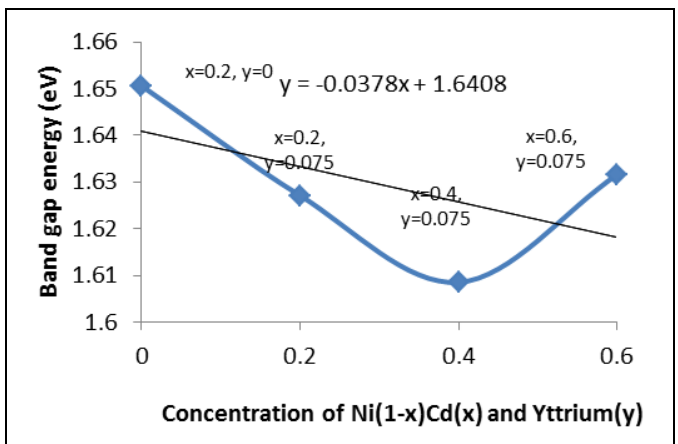


Figure 3: Variation of Band gap energy of $Ni_{1-x}Cd_xY_yFe_{2-y}O_4$ ferrite system with yttrium content(y)

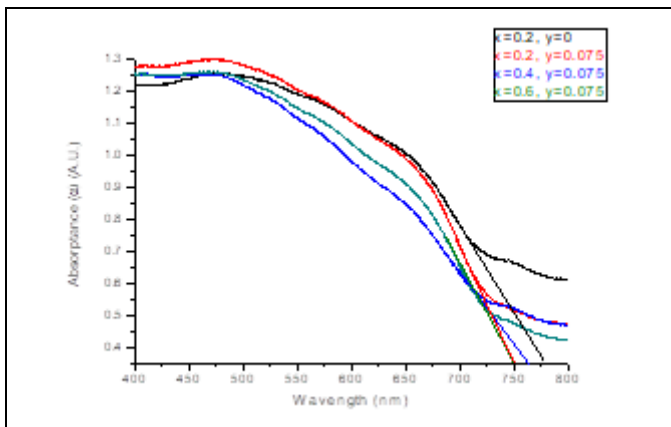


Figure 4: UV-Visible spectra of $Ni_{1-x}Cd_xY_yFe_{2-y}O_4$ nanoferrites

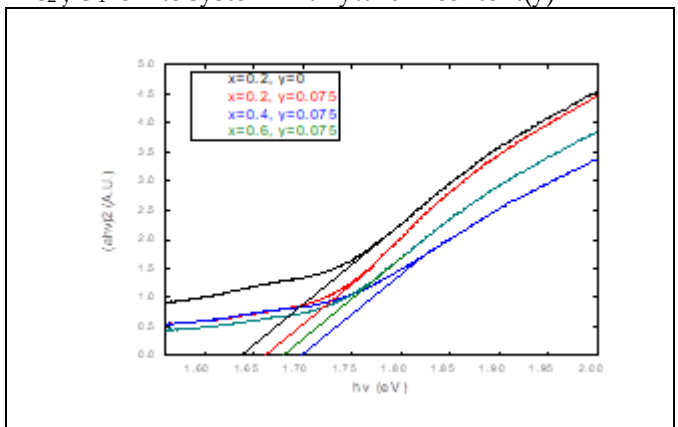


Figure 5: Band gap energy of $Ni_{1-x}Cd_xY_yFe_{2-y}O_4$ nanoferrites using Tauc method

3.2 Optical Studies:

a) UV Visible Analysis:

The figure-3 shows optical properties were studied from UV-Visible spectroscopy to calculate the band gap energy. In the absorption molecules of non-bonding electrons can absorb the energy in the form of ultraviolet or visible light to excite this electron to higher or anti-bonding molecular orbit. The energy band gap was calculated for samples. Energy band gap was found to be 1.6505, 1.6270, 1.6085 and 1.6315 eV. The substitution was resulted in slight increase in the lattice constant and that sequentially may lead to the slightly decrease in the energy gap. The average Band gap of prepared sample is 1.6294 eV and wavelength absorb by 761.06 nm. It is in the range of semiconductor materials.

The energy band gap was also determined by Tauc method for samples. It is 1.6505, 1.6270, 1.6085 and 1.6315 eV. The substitution was resulted in slightly decrease in the energy gap and the average Band gap is 1.6294 eV. It is also in the range of semiconductor materials.

b) FTIR Analysis: In order to investigate the chemical functional groups on the synthesized Ni_{1-x}

$Cd_x Y_y Fe_{2-y} O_4$, FTIR spectroscopy are performed. The FTIR spectra of the prepared $Ni_{0.6} Cd_{0.4} Y_{0.075} Fe_{1.925} O_4$ are shown in figure 6 to know the bonding characteristics of the materials. The peaks at 476.71 cm^{-1} and 559.97 cm^{-1} are the peaks of Fe-O bond in Y doped Ni-Cd ferrite and it is arises due to the lattice vibrations of the oxide ions against cations. The peak at 1383.62 cm^{-1} indicates the presence of O-H bond due to bending vibration. The broad peak at 3431.91 cm^{-1} gives presence of hydroxyl group in the material and indicates that the material absorbed moisture from atmosphere during analysis.

The intense absorption bond is observed at 559.97 cm^{-1} which shows the characteristic bond of spinel structure which may due to presence of Fe-O and Y-O bonds or crystalline nature of Y doped Ni-Cd ferrite. Hence, FTIR analysis supports the observation of XRD analysis and confirms the crystalline nature of ferrite. So, the peaks at 476.71 cm^{-1} and 1032.57 cm^{-1} confirms the presence of yttrium doped in Ni-Cd ferrite. Finally, the doping of Y^{3+} on Ni-Cd ferrite was confirmed by different pattern of the plots and the difference in relative position and intensity of the peaks appeared in the FTIR plots of the prepared samples.

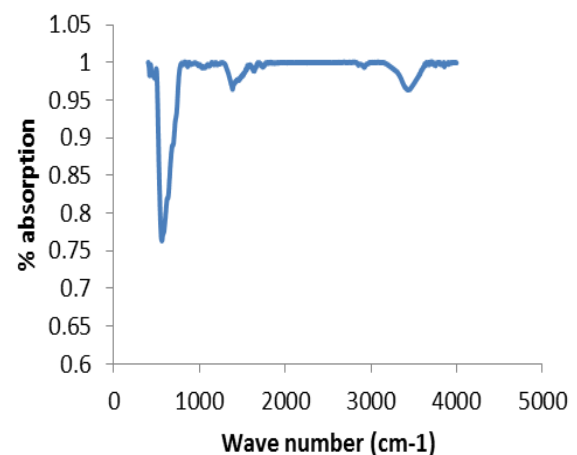
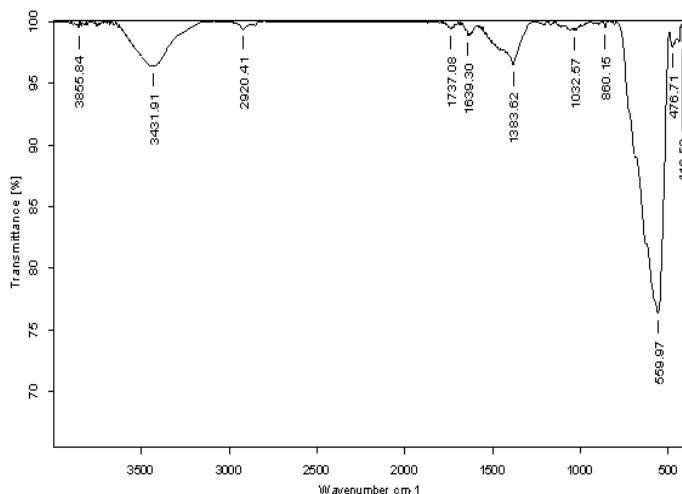


Figure 6: IR spectrum of $Ni_{0.6} Cd_{0.4} Y_{0.075} Fe_{1.925} O_4$ nanoferrites **Figure 7:** Absorption spectra of $Ni_{0.6} Cd_{0.4} Y_{0.075} Fe_{1.925} O_4$ ferrites

CONCLUSION

The $\text{Ni}_{1-x}\text{Cd}_x\text{Y}_y\text{Fe}_{2-y}\text{O}_4$ nanoferrites were synthesized using sol-gel autocombustion method. The increase in the Y^{3+} concentration gives the significant changes in the particle size and magnetic properties of the composition $\text{Ni}_{1-x}\text{Cd}_x\text{Y}_y\text{Fe}_{2-y}\text{O}_4$ (where $x = 0, 0.2, 0.4, 0.6$ and $y = 0, 0.075$). The prepared samples were characterized by XRD and shows that nanoparticles decrease with the increase in Y^{3+} content. The powders without Y^{3+} and Cd^{2+} presented small quantities of a second phase hematite (AFe_2O_4). The FTIR spectroscopy study shows two main metal oxygen bands in the range of $416.50 - 559.97 \text{ cm}^{-1}$ confirming the formation of cubic spinel phase structure of Y^{3+} substitute in Ni-Cd ferrite. The synthesis of nanoparticles with crystalline size decreases and lattice constant increases as the concentration increases and is in the range of 12.5 to 34.8 nm for 400°C . The UV-Visible analysis shows band gap energy increases with increase in Y^{3+} concentration and shows average band gap energy is 1.6294 eV at absorbed wavelength 549 nm. It is in the range of semiconductor materials. So that synthesized samples is in the nature of semiconductor materials.

REFERENCES

- Flores-Acosta, M., Sotelo-Lerma, M., Arizpe-Chavez, H., Castillon-Barraza, F.F. and Ramirez-Bon, R.J. Excitonic Absorption of Spherical PbS Nanoparticles in Zeolite A. *Solid State Communications*. 2003;128:407-411.
- Pulisova, P., Kovac, J., Voigt, A. and Raschman, P. Structure and Magnetic Properties of Co and Ni Nano-Ferrites Prepared by a Two Step Direct Microemulsions Synthesis. *Journal of Magnetism and Magnetic Materials*. 2013;341: 93-99.
- Lodhi, M.Y., et al.. New $\text{Mg}_{0.5}\text{Co}_x\text{Zn}_{0.5-x}\text{Fe}_2\text{O}_4$ Nano-Ferrites: Structural Elucidation and Electromagnetic Behavior Evaluation. *Current Applied Physics*. 2014;14, 716-720.
- Jan, L.S., Radiman, S., Siddig, M.A., Muniandy, S.V., Hamid, M.A. and Jamali, H.D. Preparation of Nanoparticles of Polystyrene and Polyaniline by γ -Irradiation in Lyotropic Liquid Crystal. *Colloids and Surfaces A: Physicochemical and Engineering Aspects*. 2004;251: 43-52.
- Mathew DS and Juang RS. An Overview of the Structure and Magnetism of Spinel Ferrite Nanoparticles and Their Synthesis in Micro Emulsions. *Chemi. Engi. Journal*. 2007; 129:51-65.
- Rahman S, et al. Structural and Magnetic Properties of ZnMg-Ferrite Nanoparticles Prepared Using the Co-Precipitation Method. *Ceramics International*. 2013; 39: 5235-5239.
- Pradeep A, Priyadharsini P and Chandrasekaran G. Sol-Gel Route of Synthesis of Nanoparticles of MgFe_2O_4 and XRD, FTIR and VSM Study. *Journal of Magnetism and Magnetic Materials*. 2008;320:2774-2779.
- Greenwood NN and Earnshaw A. Chemistry of the Elements; Pergamon Press Ltd., Oxford. 1984;279.
- Ichiyanagi Y, Kubota M., Moritake S, Kanazawa Y, Yamada T and Uehashi T. Magnetic Properties of Mg-Ferrite Nanoparticles. *Journal of Magnetism and Magnetic Materials*. 2007; 310: 2378-2380.
- Thummer KP, Chhantbar MC, Modi KB, Baldha GJ and Joshi HH Localized Canted Spin Behaviour in $\text{Zn}_x\text{Mg}_{1.5-x}\text{Mn}_{0.5}\text{Fe}_2\text{O}_4$ Spinel Ferrite System. *Journal of Magnetism and Magnetic Materials*. 2004;280:23-30.
- Kumara, C.S.S.R. and Mohammad F. Magnetic Nanomaterials for Hyperthermia-Based Therapy and Controlled Drug Delivery. *Advanced Drug Delivery Reviews*. 2011;63: 789-808.
- Giri J, Pradhan P, Somani V, Chelawat H, Chhatre S, Banerjee R and Bahadur D. Synthesis and Characterizations of Water-Based Ferrofluids of Substituted Ferrites [$\text{Fe}_{1-x}\text{B}_x\text{Fe}_2\text{O}_4$, B=Mn, Co ($x=0-1$)] for Biomedical Applications. *Journal of Magnetism & Magnetic Materials*. 2008;320: 724-730.
- Sharifi, I., Shokrollahi, H. and Amiri, S. Ferrite-Based Magnetic Nanofluids Used in Hyperthermia Applications. *Journal of Magnetism and Magnetic Materials*. 2012;324:903-915.
- Chen, Y., Ruan, M., Jiang, Y.F., Cheng, S.G. and Li, W. The Synthesis and Thermal Effect of CoFe_2O_4 Nanoparticles. *Journal of Alloys and Compounds*. 2010;493:L36-L38.
- Liu, Q., Sun, J.H., Long, H.R., Sun, X.Q., Zhong, X.J. and Xu, Z. Hydrothermal Synthesis of CoFe_2O_4 Nanoplatelets and Nanoparticles. *Materials Chemistry and Physics*. 2008;108:269-273.
- Bhise RB and Rathod SM. June. Synthesis of Nanosized Y^{3+} Doped Ni-Mg-Cd Ferrite Powders and their Structural, Magnetic properties by Sol-gel Auto Combustion Method. *Res. J. Material Sci.*, 2016; 4(5), 1-4.

Elemental and Compositional Studies on $Hg_xPb_{1-x}S$ Nanoparticle Films Grown from an Alkaline Chemical Bath

Chattarki AN,

Department of Physics, Anjuman Arts, Science & Commerce College, BIJAPUR, Karnataka
Corresponding author: dr.a.n.chattarki@gmail.com | Cell: +91 9448645263

FOR EDITOR USE ONLY

Manuscript Details

Available online on <http://www.irjse.in>
ISSN: 2322-0015

Editor: Dr. Arvind Chavhan

Cite this article as:

Chattarki AN. Elemental and Compositional Studies on $Hg_xPb_{1-x}S$ Nanoparticle Films Grown from an Alkaline Chemical Bath, *Int. Res. Journal of Science & Engineering*, December 2017; Special Issue A1 : 128-132.

© The Author(s). 2017 Open Access

This article is distributed under the terms of the Creative Commons Attribution 4.0 International License

(<http://creativecommons.org/licenses/by/4.0/>), which permits unrestricted use, distribution, and reproduction in any medium, provided you give appropriate credit to the original author(s) and the source, provide a link to the Creative Commons license, and indicate if changes were made.

ABSTRACT

An elemental and compositional study on $Hg_xPb_{1-x}S$ nanoparticle films grown on glass substrates under the optimized conditions ($0 \leq x \leq 0.2$) from an alkaline chemical bath is made in this paper

Keywords: $Hg_xPb_{1-x}S$ nanoparticle films.

INTRODUCTION

Technological advancement of modern society depends on the materials science and engineering community's ability to consider the novel materials with an extraordinary combination of physical, chemical and mechanical properties [1, 2]. Modern technology entails thin films for a variety of applications, which are thin material layers ranging from fraction of a nanometer to few micrometers in thickness. The semiconductor devices and optical coatings are the main applications benefiting from thin film fabrication. Some work is being done with ferromagnetic thin films for use in computer memory. Ceramic thin films are also in wide use. The relatively high hardness and inertness of ceramic materials make this type of thin film coatings of interest for protection of substrate materials against corrosion, oxidation and wear. In particular, the use of such coatings for cutting tools may extend the life of these items by several orders of magnitude. The engineering of thin films is intricated by the fact that their physics is, in some cases, not well understood. In particular, the problem of rewetting may be hard to solve, as there is ongoing debate and research into some processes by which this may occur.

Under such circumstances, a thin film is defined as a low dimensional material created by condensing, one by one, atomic /molecular /ionic species of the matter. The thickness is typically less than few microns. Films are said to be thin films if their layer thickness is $\leq 1\mu\text{m}$ on the substrate surface. The thin films without substrate are called foils. Thin film materials are the key elements of continued technological advances made in the fields of optoelectronics, photonic and magnetic devices. The processing of materials as the thin films allows easy integration into various types of devices. The properties of these materials significantly differ when analyzed. Most of the functional materials are rather employed in thin film form due to their specific electrical, magnetic and optical properties or wear resistances. Thin film technologies make use of the fact that the properties can significantly be controlled by the thickness parameter. Thin films are formed mostly by deposition, either by physical or chemical methods. Both crystalline and amorphous thin films have immense importance in this Hi-Tech. age. Thin film technology is a relatively younger and ever growing field in the physical and chemical sciences which is a confluence of the Materials Science, Surface Science, Applied Physics and Applied Chemistry. It has objectives in the provisions for scientific bases for the methods and materials used in thin film electronics. Additionally, it provides a sufficient data in the area of applications to permit for understanding of those aspects of the subject that might still be termed an 'art'. Thin film of metals was probably first prepared in a systematic manner by Michael Faraday using an electrochemical method. In general, thin films have a variety of applications such as in A.R. coatings, solar energy conversion, transistors, coating technology, interference filters, polarizers, narrow band filters, photoconductors, IR detectors, wave guide coatings, temperature controlled aerospace devices, photothermal solar coatings [3,4] (such as black chrome, nickel, cobalt), etc. Magnetic films in recording devices, superconducting films, thin films in microelectronics, diamond films and high wear coatings are used for engineering applications, corrosion resistive and decorative thin film coatings. The enormous flexibility offered by the thin film growth processes allows the fabrication of desired geometrical, topographical, physically crystallogra-

phic and metallurgical microstructures into two or lesser dimensions and to study the structure sensitive properties [3, 4]. In this paper therefore, the reaction mechanism and growth kinetics of PbS and $\text{Hg}_x\text{Pb}_{1-x}\text{S}$ ($0 \leq x \leq 0.2$) thin films deposited by a well set chemical bath deposition are presented elsewhere.

Deposition of the PbS and $\text{Hg}_x\text{Pb}_{1-x}\text{S}$ thin films

The substrates used for deposition were non conducting glass micro slides and conducting stainless steel strips of the dimensions mentioned earlier. A series of the $\text{Hg}_x\text{Pb}_{1-x}\text{S}$ ($0 \leq x \leq 0.2$) thin films were obtained onto the optically plane and meticulously cleaned glass and mirror polished stainless steel substrates [11-13]. For the deposition, solutions of lead acetate [$\text{Pb}(\text{CH}_3\text{COO})_2 \cdot 3\text{H}_2\text{O}$], mercuric chloride (HgCl_2) and thiourea [$(\text{H}_2\text{N})_2\text{CS}$], all 1 M, were used as the source materials for Pb^{2+} , Hg^{2+} and S^{2-} ions, respectively [11-13]. PbS and $\text{Hg}_x\text{Pb}_{1-x}\text{S}$ thin films were formed by the reaction between dissolved Pb^{2+} , Hg^{2+} and S^{2-} ions in an alkaline medium ($\text{pH} = 10.5 \pm 0.1$). An appropriate quantity of lead acetate (10 ml, 1M), TEA (1 ml), mercuric chloride (1 M) and thiourea (10 ml, 1 M) solutions were mixed in a 250 ml beaker. To this, distilled water was added to make the total volume of 200 ml and stirred well to form a homogeneous solution. The glass slides were mounted vertically on a specially designed substrate holder and kept rotating by an ac / dc constant gear motor at 70 ± 2 rpm, in the reaction bath. The deposition temperature was maintained at 80 ± 0.5 °C throughout the deposition. The reaction was allowed to take place for 1 hour. The deposition takes place via the condensation of metal and sulfide ions. After deposition, the films were detached from the solution bath and washed gently with a double distilled water to remove loosely bound PbS and $\text{Hg}_x\text{Pb}_{1-x}\text{S}$ powder. Finally, the films were dried in air and preserved in a dark desiccator before characterization.

The Elemental and Compositional Studies

Compositional analysis by an EDS

An energy dispersive X-ray analysis was conducted on both PbS and HgPbS samples to determine the qualitative measure of Hg^{2+} substitution. The analysis showed that Pb^{2+} from the PbS lattice has been replaced by Hg^{2+} ions and that the content of Hg went

on increasing when Hg-content in the chemical bath was increased [5-7]. Correspondingly, Pb-content decreased, whereas S-content remained almost constant throughout the composition range. Table I

shows the contents of Pb, Hg and S in pure PbS and the composite $Hg_xPb_{1-x}S$ thin films. Fig.1 shows the EDS micrographs of various thin films under investigation.

Table I The contents of Pb, S and Hg in PbS and $Hg_xPb_{1-x}S$ ($0 \leq x \leq 0.2$) thin films as revealed by the EDS and XPS

Compositio n x	Atomic %								Ratio, $\frac{Pb}{S}$		Ratio, $\frac{Pb}{Pb+Hg}$	
	EDS			XPS					EDS	XPS	EDS	XPS
	Pb	S	Hg	C 1s	O 1s	Pb 4f	S 2p	Hg d				
0	54.63	45.37	-	72.61	17.42	5.29	4.68	-	1.2	1.13	1	1
0.035	49.41	41.93	8.66	71.19	18.68	4.89	4.39	0.85	1.18	1.11	0.851	0.85
0.2	39.49	41.66	18.85	68.96	21.62	3.42	4.17	1.83	0.95	0.82	0.677	0.65

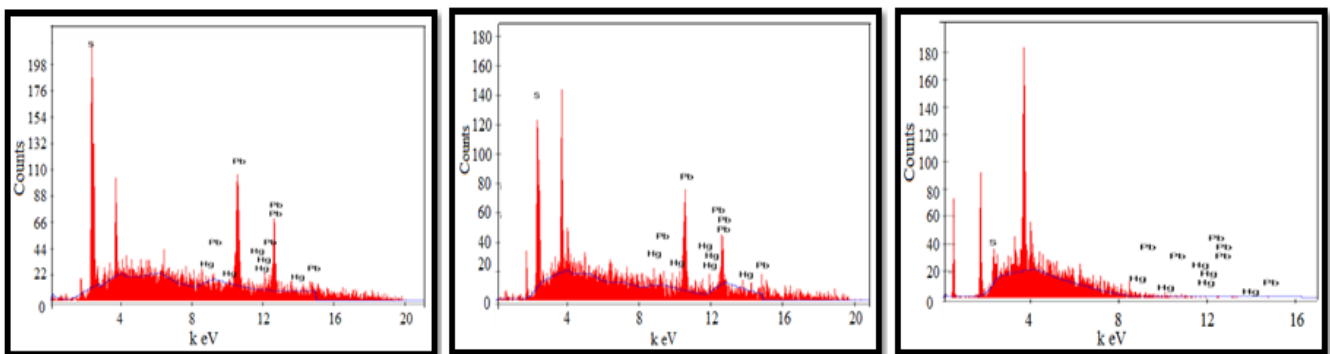


Fig1. ED's micrographs of PbS and HgPbS thin films.

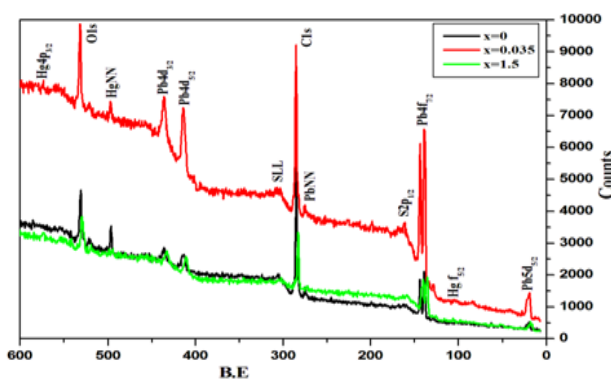


Fig2. XPS survey graphs of typical samples with: $x=0$, $x=0.035$ and $x=0.15$.

Compositional analysis by an XPS

An X-ray photoelectron spectroscopy (XPS) is widely used for the characterization of surfaces of the materials, e.g. nanoscale advanced materials, electrodes of fuel cells, photo catalysts, etc. For both conductive and nonconductive samples, XPS can meet the strong requirement for chemical state analysis. The measurement of the thickness of a surface film is also a common requirement met with XPS [22].

The development and characterization of the materials therefore received considerable attention. One desire for the analysis of these materials is the elemental depth profiles within these thin films. For this analysis, the maximum entropy method (MEM) has been explored to estimate the depth distribution. This is done by angle-resolved XPS (ARXPS) [18-26]. The estimation of the background generated by energy loss of the electrons from the photoelectron peak has also been applied if the thickness of the thin film is sufficiently less than approximately 3 times the inelastic mean free path of the observed photoelectron peak [27]. When the thickness of a thin film on a substrate approaches this thickness, a sputter etching method is generally applied to evaluate the elemental composition profile and ideally the chemical state of these elements. Table I shows the contents of Pb and S in PbS and Pb, Hg and S in composite $Hg_xPb_{1-x}S$ thin films. Fig.2 and fig.3 shows the XPS micrographs for three typical compositions.

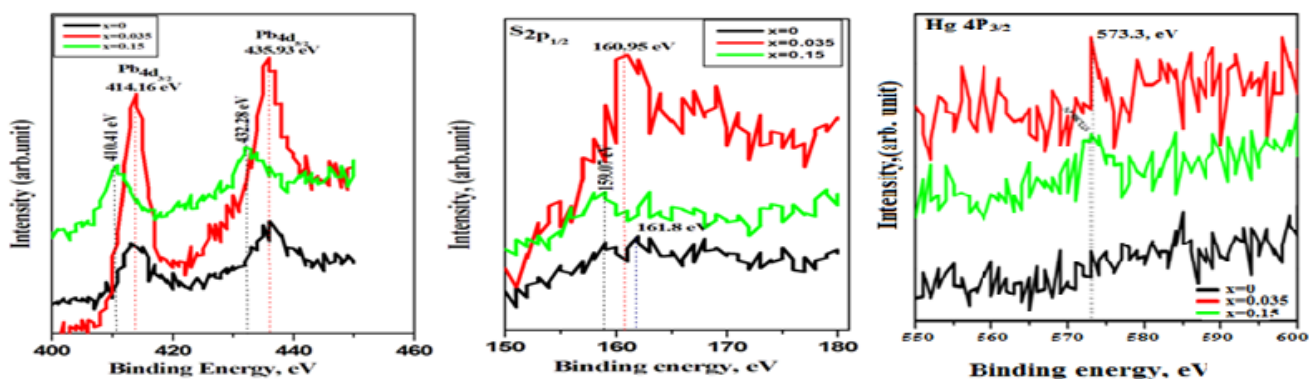


Fig.3 High-resolution XPS spectra for: (a) Pb $4d_{3/2}$, (b) S $2p_{1/2}$ and (c) Hg $4p_{3/2}$ regions for HgPbS thin films.

Survey scans (Fig.2) were carried out and showed the presence of Pb_{4d} , Pb_{5d} , Pb_{4f} , S_{2p} , and Hg_{4p} , Hg_{5f} core level signals. High-resolution XPS (HRXPS) (Fig.3) spectra of $Pb_{4d(3/2,5/2)}$, $S_{2p(1/2)}$, and $Hg_{4p(3/2)}$, $Hg_{5f(5/2)}$ levels of HgPbS nanoparticles are shown in fig.3 and the FWHM for the signals are less than 1 eV for all the signals and the binding energies (BEs) have been referenced to C1s.

The Pb_{4d} spectrum has a double feature due to spin orbit coupling resulting in $4d_{3/2}$ and $4d_{5/2}$ signals at 414.16 eV and 435.93 eV, respectively. A peak separation of 21.77 eV is an indicative of Pb (II). The signal observed at 160.95 eV is due to $S_{2p(1/2)}$ binding energy and that observed at 573.3 eV is due to $Hg_{4p(3/2)}$. XPS investigations on α -HgS and β -HgS have shown that the two forms show similar binding energies [28] and it is not possible to differentiate them based on XPS. The binding energies reported for Hg, Pb and S in these studies are in consonance with those reported earlier within 1 eV [29]. Measurements of the Pb_{4d} , Hg_{4p} and S_{2p} peak areas showed the ratio of Pb to S as 1.11 (for $x = 0.035$), which is very close to the ratio determined from EDS measurements (1:18). Our results are very similar to the results of Yang et al [28] for $CuInSe_2$ material as far as percentages of the constituents are considered and referred to C1s and O1s. These observations are in close consonance with that of the expected stoichiometry (1:1). No peaks corresponding to the impurities such as those of oxides or metallic lead (Pb) and mercury (Hg) are observed in the spectrum indicating high purity of the HgPbS product.

CONCLUSION

Among the various methods available to deposit PbS and $Hg_xPb_{1-x}S$ thin films, our indigenously developed chemical bath deposition (CBD) process must be ranked conceptually the simplest, easiest and having meaningless consumption. The various preparative parameters like deposition temperature, pH of the reaction mixture, deposition time and speed of the substrate rotation can easily be manipulated and optimized to obtain excellent quality thin, relatively uniform, smooth, and physically adherent and diffusively reflecting thin films. The binary and multi component homogeneous layers of controlled composition can be made feasible with this technique.

Conflicts of interest: The authors stated that no conflicts of interest.

REFERENCES

1. Glocker, I. Shah (eds), "Handbook of Thin Film Process Technology", in: A. R. West, Institute of Physics, John Willy & Sons, Singapore, 1&2(2002).
2. Bach, Hans, Dieter Krause, "Thin Films on Glass" in: Bach, Hans, Dieter Krause (eds), Springer-Verlag, (2003).
3. Glaser, Hans Joachim, Large Area Glass Coating, in: Von Ardenne (eds), Anlagentechnik GmbH, (2000).
4. Chopra KL and Das SR, in Thin Film Solar Cells, Plenum press, N.Y., (1983).
5. Chattarki AN, Kamble SM, Deshmukh LP, *Mater. lett.*, 2010,3: 39.

6. Chattarki AN, Deshmukh LP, *J. Rare Metal Mater. Engg.*, 2012,41:28.
7. Chattarki AN, Maldar NN, Deshmukh LP, *J. Alloys and Compds.*, 2014, 597: 223.
8. Sharma NC, Pandya DK, Sehgal HK, Chopra KL, *Thin Solid Films*, 1977, 32: 383.
9. Nair PK, Nair MTS, A. Fernandez and M. Ocampo, "Prospects of chemically deposited metal chalcogenide thin films for solar control applications, *J. Phys. ED Appl. Phys.*, 1989, Vol. 22:829.
10. Hodes G, *Physical Chem. Chemical Phys.*, 2007,9: 2181.
11. Deshmukh LP, Sutrave DS, *J. Mater. Chem. Phys.*, 1990, 55: 30.
12. Deshmukh LP, Palwe AB, Sawant VS, *Solar cells*, 1990, 28:1.
13. Deshmukh LP, Zipre KV, Palwe AB, Rane BP, Hankare PP, Manikshete AH, *Sol. Ener. Mater. and Solar cells*, 1992, 28: 249.
14. Deshmukh LP, More BM, Holikatti SG, *Bull. Mater. Sci.*, 1994, 17: 455.
15. Kainthla RC, Pandya DK, Chopra KL, *J. Electrochim. Soc.*, 1990, 127: 227.
16. Surayanarayana CV, Lakshman AS, Subryamaniam V, Kumar RK, *Bull. Electrochem.*, 1986, 2: 57.
17. Gosain DP, Shimizu T, Ohmura M, Suzuki M, Bando T., Okano S, *Mater. Sci.*, 1991, 26: 3271.
18. Das SN, Choi JH, Kar JP, Myong JM, *Appl. Surf. Sci.*, 2009, 255: 7219.
19. Sun CH, Gonzalez A, Linn NC, Jiang P, Jiang B, *Appl. Phys. Lett.*, 2008, 92: 05117.
20. Mozalev A, Habazaki H, J. Hubalek, *Electrochim. Acta*, 2012, 5: 241.
21. Wang SD, Luo SS, *Appl. Surf. Sci.*, 2012, 258: 5443.
22. Fadley CS, *J. Electron Spectrosc. Relat. Phenom.*, 1974, 4: 93.
23. Kato H, *Appl. Surf. Sci.*, 2002, 39: 190.
24. Smith GD, Firth S, Clark RJH, *J. Appl. Phys.*, 2002, 92: 4375.
25. Mozalev A, Habazaki H, Hubalek J, *Electrochim. Acta*, 2012, 5: 241.
26. ISO 18115: Surface Chemical Analysis- Vocabulary, (International Organization for Standardization, Genève, Switzerland) 2001, ASTM E673-95a, Standard terminology relating to surface analysis.
27. Sanada N, Yamamoto A, Oiwa R, Ohashi Y, *Surf. Interface Anal.* 2004, 36: 280.
28. J. Yang, Z. Jin, T. Liu, Chengjie Li, Yong Shi, *Sol. Ener. Mater. & Sol. Cells*, 2008, 92: 621.
29. Zhu JJ, Liu SW, Chen S, Palchik O, Koltypin Y, Gedanken A, *J. Solid State Chem.*, 2000, 153: 342.

Empirical mathematical model based on Moisture Diffusion and its Activation Energy in nAg/PVP nanocomposite

Mahapure Poonam D¹, Gangal SA², Aiyer RC³ and Gosavi SW¹

¹Department of Physics, Savitribai Phule Pune University, Pune 411007, India, | ²Department of Electronic, Savitribai Phule Pune University, Pune 411007, India, | ³Center for Sensor Studies, Savitribai Phule Pune University, Pune 411007, India | Corresponding Author: rcaiye1979@gmail.com

Manuscript Details

Available online on <http://www.irjse.in>
 ISSN: 2322-0015

Editor: Dr. Arvind Chavhan

Cite this article as:

Mahapure Poonam D, Gangal SA, Aiyer RC and Gosavi SW. Empirical mathematical model based on Moisture Diffusion and its Activation Energy in nAg/PVP nanocomposite, *Int. Res. Journal of Science & Engineering*, December 2017; Special Issue A1: 133-142.

© The Author(s). 2017 Open Access

This article is distributed under the terms of the Creative Commons Attribution 4.0 International License

(<http://creativecommons.org/licenses/by/4.0/>), which permits unrestricted use, distribution, and reproduction in any medium, provided you give appropriate credit to the original author(s) and the source, provide a link to the Creative Commons license, and indicate if changes were made.

ABSTRACT

An empirical relation to determine effective diffusivity and the activation energy of moisture in nano silver metal/ PVP composite (nAg/PVP) on the cylindrical alumina substrate is reported. nAg/PVP of size 55±10 nm composite is synthesized by in situ chemical reduction AgNO₃ in the presence of 0.001 wt% of PVP matrix. The film of nano composite is coated by drop casting of 2 µl solutions of nAg/PVP. 10, 18, 26, 33, 41 and 49 µm with ±2 µm thicknesses are obtained by layer by layer coating which named as A1, A2, A3, A4, A5 and A6 respectively. To determine the amount of water content, as a function of exposure time, which is essential for determining the effective diffusivity, the resistance is measured as a function of exposure time. A Strobe's formula is used to convert resistance into moisture content, which in turn relates diffusion time to moisture content. Resistance as a function of the diffusion time gives a 3rd order exponential decay. When the decay is divided into 3 terms, the constant shown in the strobe's formula in each region is calculated by measuring water content along with resistance at the center point of each region. The resistance values related to the corresponding moisture content are converted into moisture ratio (MR). The slope of ln (MR) vs. diffusion time gives effective diffusivity. The experiments were carried out at three different temperatures in the range 22-38°C. Activation energy is obtained as a slope of effective diffusivity as a function of (1/ (Temperature)). The activation energies are in different in three different regions of moisture diffusion suggesting three diffusion rates in three different regions. A model is suggested on the bases of these three diffusion rates. The activation energies go on increasing with thickness to a certain extent and then it's saturate.

Keywords: nAg/PVP nanocomposite, effective diffusivity, activation energy and empirical mathematical model.

INTRODUCTION

The reported polymeric resistive humidity sensors are based on either polyelectrolyte or conjugated polymers [1-4]. It is reported that conjugated polymers and their derivatives, when doped with proper dopant, however become sensitive to humidity. Their response is poor, at the most one order of magnitude change in the conductivity, due to their weak hygroscopic nature [5-11]. Therefore, research on polyelectrolytes doped with a particular dopant to enhance the sensitivity becomes a challenging work [12, 13]. Here PVP matrix doped with nAg particles are used.

In humidity sensing, the transfer of moisture is an important factor [14], therefore effective diffusivity value (D_e) and activation energy during drying [15-21] is used to describe the rate of moisture movement. Most of the research related to transfer of moisture is reported on vegetables and fruits for finding effective diffusivity value (D_e) and activation energy during drying [15-21]. A humidity sensor should have high diffusivity and high drying rate for quick response and recovery. The knowledge of water activity (effective diffusivity) and equations that describe their relationship, as a function of moisture content and temperature are important for modeling and predicting film barrier efficiency.

The present paper reports thickness and temperature dependent resistive properties of nAg/PVP nanocomposite as a humidity sensor. To understand the water transport mechanism in the present film a successful attempt is made to explain three different diffusion processes by measuring the effective diffusivity and activation energy as a function of time at a constant humidity. For measurement of effective diffusivity of moisture in the film, it is necessary to know the amount of diffusion of moisture in the film at the particular diffusion time, but it is found to be a very complicated job to measure accurate moisture content in the film with diffusion time by gravimetric method. To overcome above limitation, we tried to use Strobe empirical formula reported by Strobe et. al 2002 [22, 23] for our films by modifying constant.

METHODOLOGY

Synthesis of nAg/PVP composites and film Fabrication

In situ nAg/PVP composite is synthesized by chemical reduction of silver salt [24] in the presence of PVP polymer. The aqueous solution of PVP having concentration of 0.001 wt% of the polymer is prepared in double distilled water. The procedure for synthesis of nAg/PVP nanocomposite is already explained in ref. [24]. The reaction is stopped when a colorless solution becomes pale yellow (≈ 45 min), which is an evidence of formation of Ag nanoparticles [24, 25].

For fabrication of a film, Ceramic rods (length=0.3 cm and Diameter =1.50 mm) with nicrome cap for contact purpose are used. nAg/PVP nanocomposite is coated on a ceramic rod by drop casting of 2 μ l solutions and uniformity in the coated film was trying to achieve by using hand spinning. Further the film dried at room temperature of 32°C. The thickness of film is increased by successive deposition of 2 μ l solution per layer.

Material characterization

Structural, micro structural and electrical characterization of the synthesized nanocomposites was carried out using UV-vis spectroscopy (UV-Vis) and Transmission electron microscopy (TEM) techniques. Absorption spectra of the synthesized nanocomposites were recorded using UV- Vis spectrometer model HP 8452 with a resolution of 1nm and a required quartz cell. The particle size and morphology of nAg nanoparticles were analyzed by using transmission electron microscope (TEM; TECNAI G2 20-TWIN (FEI-NETHERLANDS)). The % water content in films was measured by using an electronic balance (accuracy 0.0001g).

System for studying diffusion of moisture in humidity sensing film

A system used to study the diffusion of moisture in humidity sensing film is shown in Fig.1. The system is same as the one used in our previous work [24]. It consists of a testing glass chamber with a small neck mounted on the glass sheet. The sensing film and the commercially available humidity sensor ((48-EU-05) to monitor/calibrate the chamber humidity) are kept neatly in the chamber.

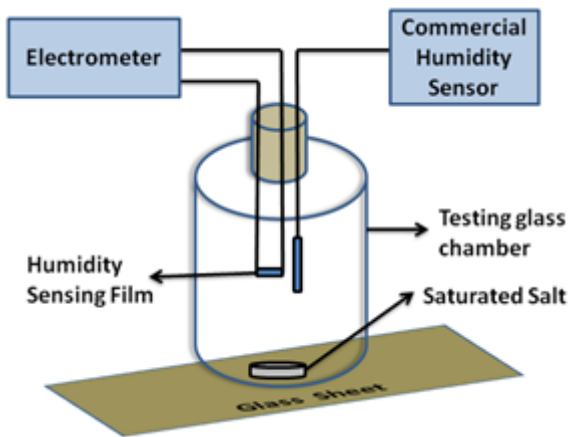


Fig.1. System for diffusion of moisture in humidity sensing film

The resistance of the film was measured using an electrometer (6517B, Keithley, $V = 20V$, $I=200nA$) [24]. For the present work, relative humidity of 95%RH was created in a glass chamber by using KNO_3 saturated salt [26] and make air tight by modeling clay, % RH is continually monitored by commercially available humidity sensors. A dry environment of 1-5%RH is created by using P_2O_5 salt. The film is kept for overnight in a dry environment and then exposed to 95%RH, by introducing it in a glass chamber from the upper neck side then make it air tight. The resistance of film with diffusion time is recorded. This data is used for further analysis of effective diffusivity and activation energy of film with thickness.

Data collection for modeling of RH sensor

The main part of the experimentation relates to the collection of data for diffusion of moisture in the film under study by surface/ bulk diffusion under various conditions via thickness of film, temperature (T), % RH to which film is exposed, with diffusion time (t). To measure moisture content (M) in film continuously as a function of diffusion time, under various conditions, by gravimetric method will be a very tedious job. However, it is easy to measure resistance as a function of exposure time. We have therefore devised a new method by using Strobe's empirical mathematical formula which relates moisture content to resistance. It has a constant term [22, 23]. This strobe's formula is used to convert resistance into moisture content, which in turn relates diffusion time to moisture content. The procedure is as follows,

- 1) The Film is exposed to relative humidity and change in resistance with diffusion time is measured.
- 2) An empirical formula reported by Strobe et. al 2002 [22, 23] for moisture adsorption in wood species, exposed to specific %RH at a given temperature for converting the corresponding resistance into moisture content is available and used here.

$$\text{Log}_{10}(\text{Moisture content}) = C - 2.113(\text{Log}_{10}(\text{Log}_{10}(R))) \quad \text{Eq.(1)}$$

Where: moisture content is the mass ratio in percentage (%) and R is the Ohmic resistance during the corresponding diffusion time in ohm (Ω). The empirical constant C in eq.1 is material dependent and 2.113 might be liquid (water) dependent.

Therefore, we determined the empirical constant C experimentally for nAg/PVP nanocomposite. The following procedure is adapted to determine the constant C.

- 2.1 The data on Resistance vs. Diffusion time is calculated at a specific humidity at a specific temperature for each film. A graph of Resistance vs. Diffusion time tried fitted for exponential relation up to three terms. The data is also subdivided into three regions and corresponding constants (C) are determined separately for three regions to minimize error.
- 2.2 Once the regions are fixed then to calculate constant C, 1st the dry film of weight (M_0) is exposed to specific humidity (say 95%RH) under isothermal environment (at $T= 22.2/ 28.3/ 38.8$ ° C) for a particular diffusion time, which is decided from regions and is weighed again (M_t) by using an electronic balance (accuracy 0.0001g). By knowing the values of M_t and M_0 , the moisture content at any time (time = t sec) was determined from Eq. 2 [27]

$$\text{Moisture content (\%)} = \left(\frac{M_t - M_0}{M_0} \right) \times 100 \quad \text{Eq.(2)}$$

- 2.3 For the same time (t sec), the resistance is also measured under the same isothermal environment at specific %RH. Knowing the value of moisture content and resistance at time (t sec), the empirical constant is determined by using Eq.1 (constant = C for nAg/PVP). Once the constant

(C) is decided for a particular region than resistance in particular region is converted into moisture content by using constant (C) for that region using eq.1.

- 2.4 The same procedure is repeated for every film three times at three different temperatures (22.20, 28.30 and 38.80°C). The constant is dependent on material thickness and environmental temperature (T) and not on time.
- 2.5 To verify the applicability of the above relation, water content at different diffusion times are carefully measured by gravimetric method and these experimental values are compared to the values determined by the above empirical relation with corresponding C (Eq.1). C may be different for different temperatures and different regions of sensitivity curves; hence these variations were studied to minimize error.
- 3) Once all resistance values converted into water content, then the water content is converted into the moisture ratio (MR) by using following equation eq.(3),

$$\text{Moisture ratio (MR)} = \left(\frac{M_t}{M_\infty} \right) \quad \text{Eq. (3)}$$

Where, $M_t = M_t$ is the mass of the moisture after absorption time t , $M_\infty =$ Saturated mass at specific RH.

The saturated mass is different for different region. For 1st and 2nd region, the time for saturated mass is decided from the region length. Approximately the last reading is considered as a saturated mass for the 1st and 2nd region. And for 3rd region saturated mass (M_∞) is the mass at the response time of the sensor where sensor achieves a stable resistance value (≈ 1 to 6 min according to the thickness of the film).

- 4) Once the MR is decided then effective diffusivity (De) and activation energy (Ea) are determined.

RESULTS AND DISCUSSION

1. UV-Visible and TEM analysis

Synthesis of nAg/PVP composite is carried out for 3-4 times and representative results are given here. When solution became pale yellow, then it was collected for study on diffusion of moisture. The UV-Visible peak around 400 nm is the confirmation for formation of

nAg particles. The solutions show same peak position around ≈ 425 nm (Fig.2). In order to find the size and morphology of nAg particles TEM images are taken. TEM image of nanocomposites is shown in insert of Fig. (2).The particle size is found to be of around 50 ± 5 nm with average spherical geometry.

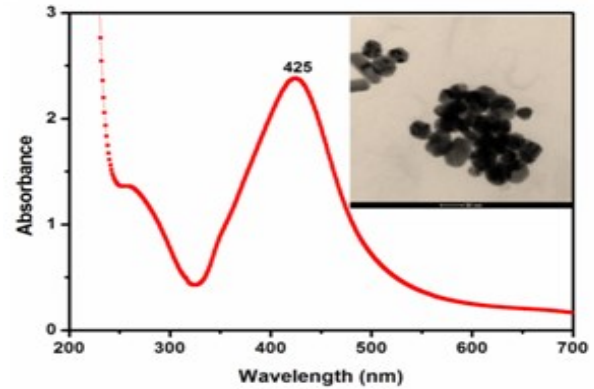


Fig.2. UV-Vis spectra of nAg/PVP nanocomposite

2. Relating measured Resistance to moisture content through mathematical model

Data collection for change in resistance with diffusion time

The change in resistances with diffusion time is measured for various thicknesses (10, 18, 26, 33, 41 and 49 μm). Data on two films of each thickness was taken. The data were also taken at three different temperatures (22.2, 28.3 and 38.8°C) for all the films. All the films showed similar exponential decay for a resistance Vs diffusion time. Representative data for film of thickness 26 μm (film A3) taken at three different temperatures is shown in Fig. 3.

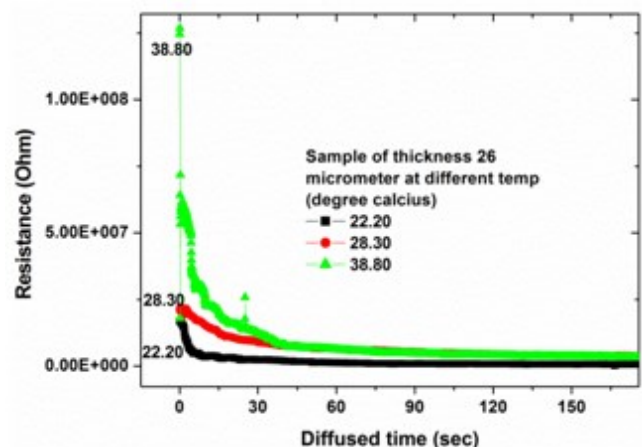


Fig.3. Resistance Vs. diffusion time at 94 %RH for Film A3

As can be seen from Fig.3, there is a slight decrease in resistance with an increase in temperature. This is seen in all the films. This data is used for calculation of activation energy in films required diffusion of moisture.

Curve fitting and Model generation

In this research paper, we tried 1 term, 2 terms and 3terms exponential model fitting to analyse the experimental data of Resistance vs. Diffusion time taken for all the films [28]. Fig.4 shows the representative data for film C at 22.2°C. When one term exponential equation is tried to fit, then regression coefficient is $R^2=0.923$, for two term exponential equation, it is ≈ 0.9482 and for the three term exponential equation is 0.96525 (Fig. 4). The three term exponential decay fitting is carried out for all films having different thicknesses at different temperatures having regression coefficient in the range 0.98-0.99.

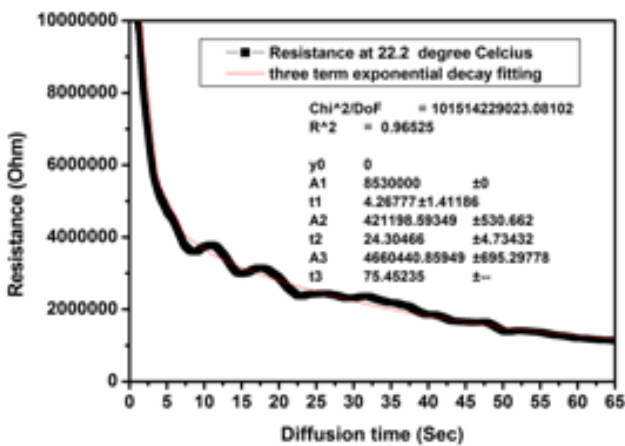


Fig.4. Three term exponential decay equation fitting for resistance vs. diffusion time for the A3 film Curve fitting expression is given in Eq. 4.

$$y = y_0 + A_1 e^{-\frac{x}{t_1}} + A_2 e^{-\frac{x}{t_2}} + A_3 e^{-\frac{x}{t_3}} \quad \text{Eq. (4)}$$

Eq. 4 consists of three different exponential terms having their own different time constants t_1 , t_2 and t_3 with coefficients of exponential terms, i.e A_1 , A_2 and A_3 having unit Ohm/sec. Where, each term corresponds to a different diffusion process. y_0 is the constant which comes out to be zero for the fitted curves where ($R^2=0.98$ to 0.99 for all the curves).

Relating resistance to the moisture content

From fig. 4 and Eq. 4, it can be inferred that, there are three different diffusion rates [29], represented by three different diffusion time regions. The regions are divided in such a way that, the values of exponential coefficient (A) and time constant (t) remain approximately the same as observed in Fig.4. These regions are shown in Fig. 5(a,b,c). Values of A and t are indicated in corresponding figures.

Further recorded resistance as a function of diffusion time is converted into moisture content by using eq. 1 (see section 2.4). The value of constant C in Eq. 1 is calculated for three different regions as explained below. For this conversion, the constant (C) in eq.1, has to be decided for each region separately by using following procedure.

1. To decide the constant for the 1st region in the A3 film Fig.5a, %moisture content (using eq.2) at midpoint of time interval (6 sec) of 1st region is measured by gravimetric method and taken as reference.
2. At the same time the resistance is taken which was measured by using an electrometer under the same temperature (22.2°C).
3. Now substituting the values of resistance and % moisture content in eq.4, constant (C) was determined and taken as constant for whole region, which comes out to be 0.89003 for the 1st region in A3 film at 22.2°C.
4. After getting the constant (C) for that particular region, all the resistances in that region were converted into moisture content by using the empirical relation in Eq. (1).

Next, separation of data (Resistance Vs Diffusion time) into three regions also helps to minimize the error in moisture content. The figure 6, give converted moisture content at three different temperatures for A3 film and their corresponding resistance at same temperature was given in Fig.3. Comparison between fig. 3 and Fig.6 shows that, at low temperature film has high moisture content and their corresponding resistance is also low.

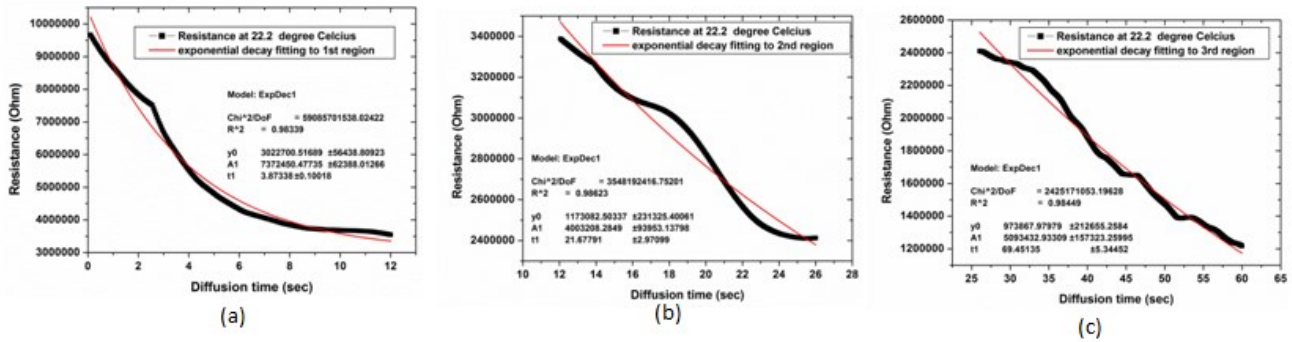


Fig.5. Selection of (a) 1st, (b) 2nd and (c) 3rd region for A3 film at 22.2°C

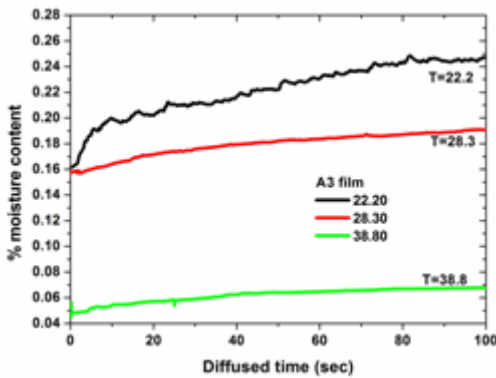


Fig.6. Theoretical % moisture content vs. diffusion time at 95 %RH for a A3 film

To verify the correctness of the theoretical calculated % moisture content from eq.1, the % moisture content at different time (other than mid time) which measured gravimetrically from eq.2 is compared with theoretical % moisture content (Fig.6) and it is given in fig.7.

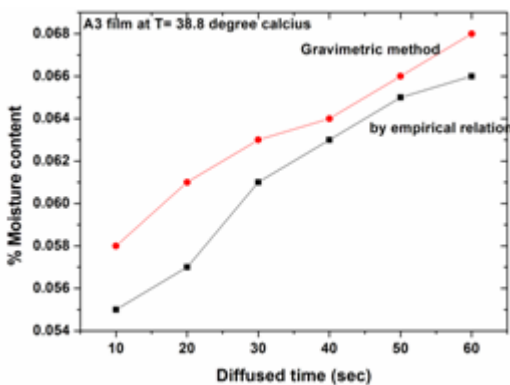


Fig.7. Comparison of % moisture content by empirical relation and gravimetric method at 95 %RH, T= 38.8 °C for A3 film

The comparison shows the correctness of our process, for use in calculating empirical values for that particular region. There is not much of difference in % moisture content by gravimetric (eq.2) and empirical relation (eq.1) though empirical curve shows slightly less moisture content. The maximum error in moisture content is about 5-6% when compared by gravimetric and empirical method.

Once % moisture content with diffusion time is obtained, the effective diffusivity and activation energy can be determined by using further theory.

3. Determination of effective diffusivity and activation energy (step7 of section 2.3)

The mathematical approach to calculate effective diffusion and activation energy is given. To predict the moisture content during the diffusion rate, mathematical models have been proposed using 2nd law of Fickian’s diffusion, as shown in Eq. (5). Here we considered that our film is like an infinite rectangular slab where it has thickness of about 11-49 μm as compared to length of film 0.01m. [30-33, 34]

$$\frac{\partial M}{\partial t} = \nabla[D_e(\nabla M)] \quad \text{Eq. (5)}$$

Where: D_e is the effective moisture diffusivity in m^2/s , t is time in second and M is moisture content in kg.

The calculated data of % moisture content Vs diffusion time follow the Fickian’s law, only when the mass uptake (moisture content) has a linear relation to the square root of diffusion time. The fig. 8 of %Moisture content Vs diffusion time shows linearity with regression coefficient $R^2 = 0.98771$. This shows nAg/PVP films follows the Fickian’s law.

The above expression is integrated over the thickness for the diffusion of moisture in thin film and the solution became [32, 34],

$$\frac{M_t}{M_\infty} = 1 - \frac{8}{\pi^2} \sum_{n=0}^{\infty} \frac{1}{(2n+1)^2} e^{-\frac{D_e(2n+1)^2\pi^2 t}{4L^2}} \quad \text{Eq. (6)}$$

Where, M_t is the mass of moisture after absorption time t , and M_∞ is the mass of moisture saturated film, D_e is the effective water diffusion coefficient in (m^2/s), t is the diffusion time, and L is the length of the film in meter.

In order to determine Fickian's coefficient (effective diffusivity) of diffusion, initial stage of Fickian's equation is simplified with ($n=0$) [31, 32, 33, 35]. There is not large variation in effective diffusivity when we considered next order ($n=1$). So we continued with $n=0$ [35]. Therefore Eq.6 becomes,

$$\frac{M_t}{M_\infty} = 1 - \frac{8}{\pi^2} e^{-\frac{D_e t \pi^2}{4L^2}} \quad \text{Eq. (7)}$$

Here $\frac{M_t}{M_\infty} = MR$ (moisture ratio), then taking the log on both sides of Eq.7. The effective diffusivity of moisture (D_e) is determined from following eq.8 [35]

$$\frac{\ln(MR)}{t} = \frac{\pi^2 D_e}{4L^2} \quad \text{Eq. (8)}$$

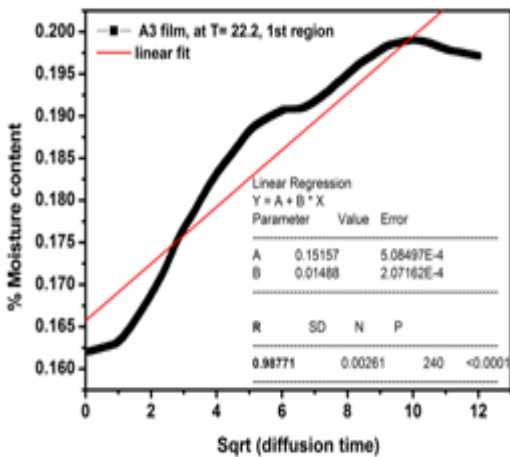


Fig.8. Moisture content Vs sqrt (diffusion time) at 95 %RH, T= 22.2 °C for A3 film

The effective diffusivity is determined from the slope of $\ln(MR)$ vs. diffusion time from simplifying equation. (6),

$$\text{slope of } \ln(MR) \text{ Vs. Diffusion time} = \frac{D_e \pi^2}{4L^2} \quad \text{Eq. (9)}$$

From moisture content, MR is calculated (Equation 5). The effective diffusion diffusivity is determined by plotting $\ln(MR)$ vs. Time (t) (Equation. (8)). Table 1, gives a brief idea about effective diffusivity (D_e) with temperature and thickness. Here D_1 is the effective diffusivity in region1, D_2 is the effective diffusivity in region2 and D_3 is the effective diffusivity in region3.

From table 1, Effective diffusivity of moisture decreases as the diffusion time increases in nAg/PVP. The dependence of the effective diffusivity on temperature can be described by the Arrhenius equation [31, 33]

$$D_e = D_0 e^{-\frac{E_a}{RT}} \quad \text{Eq. (10)}$$

Here, the effective diffusivity is D_e , D_0 diffusion constant = a^2v = product of the square of lattice constant and vibration frequency. It produces the same effect on effective diffusive of film at a particular temperature. So for the sake of simplicity, we neglect it. Our aim is to see trend in activation energy with diffusion time and thickness. E_a is the activation energy in KJ/mol and T is the absolute temperature of the chamber in Kelvin. $K = 1.38 \times 10^{-23}$ J/K is the Boltzmann's constant [32]. The activation energy can be determined from the slope of the Arrhenius plot, $\ln(D_e)$ vs. $1/T$ simplifying eq. (11)

$$\frac{\ln(D_e)}{1/T} = \frac{-E_a}{K} \quad \text{Eq. (11)}$$

The slope of the $\ln(D_e)$ Vs ($1/T$) segments will yield the activation energy for a particular region of diffusion.

From eq.11, Arrhenius plot between effective diffusivity and absolute temperature ($1/T$) gives nearly straight lines and regression parameters show good correlation with R^2 whose values ranging from 0.96 to 0.99 (Fig. 9a and 9b for thickness 26 μm), The slope of the $\ln(D_e)$ Vs $1/T$ plots gives activation energy in each region. The straight line nature and the high R^2 justify the application of the Arrhenius equation [16]. In Fig 9b, the constant B, represent the slope of region 3 for the A3 film. The product of slope and K (Boltzmann's constant) gives activation energy in Joule. For region 1 of A3 film, the activation energy was found to be 7.914×10^{-20} J or 0.49 eV. The same procedure is used for other films. According to Schmidt (1968) activation energy of approximately

0.17-0.22 eV may be assumed for the motion of hydrated ions in bulk water [36]. Table 2, gives a brief idea about activation energy of moisture during diffusion in eV.

Table.1. Effective diffusivity at different thickness and temperature

Thickness (μm)	Temperature (K)	Effective Diffusion (m ² /s)		
		D ₁	D ₂	D ₃
10	295.2	1.12E-7	2.28E-8	5.59E-9
	301.3	8.05E-7	7.69E-8	8.30E-9
	311.8	8.96E-7	1.48E-7	1.18E-8
18	295.2	4.19E-7	4.09E-8	7.48E-9
	301.3	5.42E-7	5.83E-8	9.48E-9
	311.8	1.57E-6	6.23E-8	1.28E-8
26	295.2	1.26E-7	1.39E-8	3.85E-9
	301.3	1.44E-7	1.58E-8	4.85E-9
	311.8	1.56E-7	2.54E-8	6.72E-9
33	295.2	1.26E-7	4.03E-9	7.93E-9
	301.3	1.44E-7	1.58E-8	8.90E-9
	311.8	1.56E-7	2.54E-8	1.39E-8
41	295.2	8.54E-8	1.82E-9	1.72E-9
	301.3	1.22E-7	9.84E-9	2.13E-9
	311.8	1.30E-7	1.02E-8	2.75E-9
49	295.2	3.28E-7	4.13E-8	1.17E-8
	301.3	3.59E-7	1.55E-8	1.24E-8
	311.8	4.94E-7	1.60E-8	2.15E-8

From table 2, E₁ is the activation energy during the sharp fall of resistance due to high adsorption of moisture in Fig.2, E₂ is the activation energy where resistance tries to achieve saturation which is time dependent region and E₃ is the activation energy during which resistance achieved saturation or time independent region (Fig.5). E₂ is higher than E₁ and E₃ i.e. E₃ < E₁ < E₂.

Table: 2. Change in activation energy with thickness and regions

Thickness (μm)	Activation energy (eV)		
	E ₁	E ₂	E ₃
10	0.58	1.20	0.21
18	0.48	1.26	0.25
26	0.49	1.26	0.25
33	0.59	1.31	0.32
41	0.60	1.08	0.25
49	0.24	1	0.20

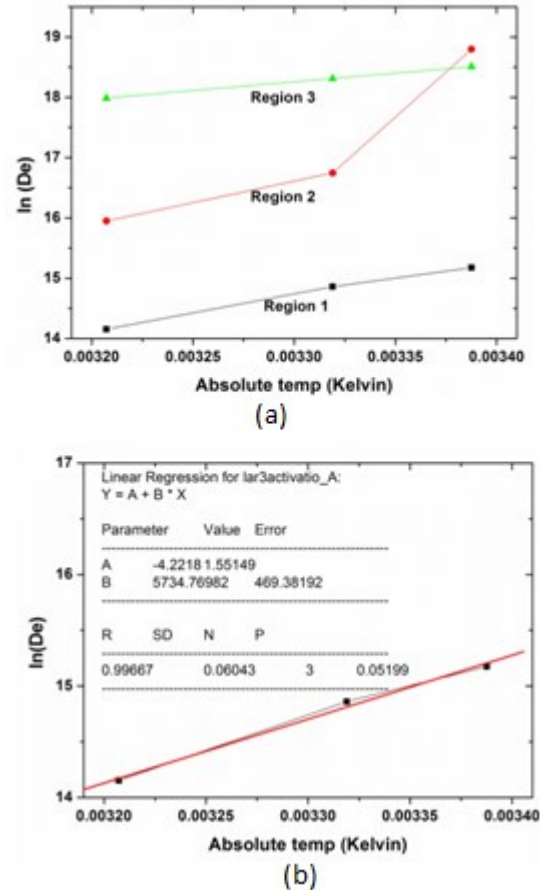


Fig.9. (a) Plot of ln (De) Vs. absolute temperature (1/T) for A3 film with each separate region (b) Linear fit with regression coefficient for the 3rd region to find activation energy

At the initial stages when film is exposed to moisture, resistance of the film falls sharply. With further increase in diffusion time, fall in resistance tends to achieve saturation. At the initial stages when film is exposed to moisture, moisture content in the film is low which increases with increase in diffusion time and achieved saturation [32] (Fig.6). The sharp fall in resistance during 1st region is due to more unsaturated sorption sites available for moisture adsorption. As the diffusion time increased, the sites become occupied, resulting in the reduction of the material capacity to absorb water. As the number of sites becomes fully occupied the moisture content approaches equilibrium [27]. So with the increase in diffusion time, there is a decrease in the diffusion of moisture which is verified by the table. 1. From above results, the diffusivity of moisture taking place in three successive steps. The effective diffusivity decreases continuously with an increase in diffusion

time. The comparison shows that inter Grain Diffusivity > Surface Diffusivity > Volume Diffusivity [34]. If we compared above comparison between grain, surface and volume diffusivity with table 2, then region 1 for surface diffusion, region 2 for the inter grain diffusion and 3rd region for volume diffusion.

When film is exposed to humidity, then sensor surface is the 1st part which comes in contact with humidity (surface diffusivity), as the diffusion time increases the moisture diffusion on the surface will start penetrating inside the film (grain diffusivity). Once all active sites are occupied, then the moisture tends to reach saturation (volume diffusivity). The correlation between effective diffusivity and activation energy shows that, the 3rd region, i.e. volume diffusion requires less amount of energy (0.20-0.32 eV) as compared to 1st and 2nd region. 2nd region, i.e. internal diffusion (grain diffusion) required more energy (1.08 - 6.21 eV) as compared to the energy in the other two regions. The amount of energy required for surface diffusion is an intermediate between intergrain and volume diffusion.

There is an increase in activation energy up to particular thickness, with further increase in thickness, the activation energy decreases. For these, thickness dependent behavior of activation energy, need to be studied further about the surface morphology of the film.

CONCLUSION

The diffusion mechanism of moisture in a nAg/PVP film is studied. It offers an exponential response of resistance as a function of diffusion time. An empirical model is suggested to fit to the data obtained for diffusion. The three orders exponential curve is fitted to data of resistance Vs diffusion time, offering three different rates of diffusion. These three terms exponential equations represent three different diffusion rates via surface, inter grain and volume diffusion. The activation energy needed for the three different diffusion rates is successfully calculated. The effective diffusivity of moisture decreases with increase in diffusion time and each region has its specific trend in activation energies with diffusion

time due to different diffusion rates. The activation energy required for inter grain diffusion is greater than surface and volume diffusion.

Conflicts of interest: The authors stated that no conflicts of interest.

REFERENCES

1. Lee CW, Kim OY, and Gong MS, *J. Appl. Polym. Sci.*, 2003, 89: 1062.
2. Gong MS, Lee CW, Joo SW and Choi BK. *J. Mater. Sci.*, 2002, 37: 4615.
3. Young-Min Jeon and Myoung-Seon Gong, *Macromolecular Research*, 2009, 17 No 4:227-231
4. Kulwicki BM. *J. Am. Ceram. Soc.*,1991,74: 697.
5. Casalbore-Miceli G, Camaioni N, Yang MJ, Zhen M, Zhan WX, Aprano AD. *Solid State Ionics*,1997, 100: 217
6. Casalbore-Miceli G, Camaioni N, Yang MJ, Zhen M, Zhan WX, Aprano AD. *Solid State Ionics*, 1997,100: 217
7. Rezlescu N, Doroftei C, Popa PD, Rom. *Journ, Phys.*, 2007, Vol.52, Nos. 3-4: 353-360.
8. Nechtschein M, Santier C, Travers JP, J. Chroboczek, A. Alix, and M. Ripert, *Synth. Metals*, 1987,18: 311.
9. Chiang JC and MacDiarmid AG, *Synth. Metals*, 1986, 13: 193.
10. Angelopoulos M, Ray A, and Mcdiarmid AG, *Synth. Metals*,1987, 21
11. Travers JP and Nechtschein M, *Synth. Metals*, 1987,21:135 .
12. Tonosaki T, Oho T, Isomura K, and Ogura K. *J. Electroanal.Chem.*,2002, 520, 89.
13. Lopez A, Virseda P, Abril J. *Drying Technology*, 1995,13(8&9) :2181-2190
14. Sakai Y, Sadaoka Y and Matsuguchi M, *Sens & Actuators* ,1996, B, 35: 85
15. Sharma M, Yashonath S, *Diffusion Fundamentals*, 2007,7: 11.1 - 11.15
16. Alakali JS, Ariaahu CC and Kucha EI, *American Journal of Food Technology*,2009, 4(3) :119-125
17. Lin YC, Xu Chen, *Chemical Physics Letters* 2005,412: 322-326
18. Wright JS, Lima W, Gilaa BP, Peartona SJ, J. L. Johnsonb, A. Ural F. Renc, *Sensors and Actuators*, 2009,B 140: 196-199
19. Hassini L, Azzouz S and Belghith A, *Drying* 2004 - Proceedings of the 14th International Drying

- Symposium (IDS 2004) São Paulo, Brazil, 22-25 August 2004, vol. B, pp. 1488-1495
20. Addo, A. Bart-Plange, *ARPN Journal of Agricultural and Biological Science*, 2009, Vol. 4, No. 6
21. Giraldo-Zuniga, Arevalo-Pinedo, Rodrigues, R.M. Lima, Feitosta, A.C., *Cienc. Tecnol. Aliment*, 2006., 5(2):89-92
22. Guillard V, Broyart B, Bonazzi C, Guilbert S, Gontard N. *Cereal Chem.* 81(6): 767-771
23. Straube J, Onysko D, Schumacher C. *Journal of Thermal Env. & Bldg. Sci.*,2002, 26 (2): 123-151
24. Laboratory Calibration and Field Results of Wood Resistance Humidity Sensors, Kohta Ueno, Building Science Corporation, John Straube, Ph.D., P.Eng., University of Waterloo
25. Poonam D. Mahapure, R.C. Aiyer and S.W. Gosavi, Proceedings of the 2015 2nd International Symposium on Physics and Technology of Sensors 978-1-4673-8018-8/15, 2015 IEEE
26. Shan Shan Tang, Chang Lu Shao , Shou Zhu Li, *Chinese Chemical Letters*,2007, 18 465-468.
27. Teng Fei, Hongran Zhao, Kai Jiang, Xing Zhou, Tong Zhang, *J. Appl. Polym. Sci.* 2013, DOI: 10.1002/APP.39400
28. Mu-Rong Yang, Ko-Shao Chen, *Sens and Actuators*,1998,B 49: 240-247
29. Shyamali AK, Jayaweera HHE and Ariyaratne TR, Proceedings of the Technical Sessions, 2009,25 :36-44
30. E. Meisami-asl, S. Rafiee, A. Keyhani and A. Tabatabaefar, *Peeters online journals*,2010, 3(3): 97-102
31. Shirring M.H, Fan X.J, Michel B, IMAPS 2008-41st international symposium on microelectronics
32. Mirzaee E, Rafiee S, Keyhani A, Emam-Djomeh Z., *Research in Agriculture Engineering*, 55, 2009 (3) 114-120
33. Yi He and Xuejun Fan, Electronic Components and Technology Conference, 1-4244-0985-3/07/2007 IEEE
34. Hassini L, Azzouz S and Belghith A, Drying 2004 - Proceedings of the 14th International Drying Symposium (IDS 2004), São Paulo, Brazil, 22-25 August 2004, vol. B, pp. 1488-1495
35. Ferda SEYHAN-G.RTAP, M. Mehmet AK, E. .zg.l EVRANUZ, *Turk J Agric For* ,2001,25: 297-304
36. Modeling Effective Moisture Diffusivity of Orange Slice (Thompson Cv.), Shahin Rafieea; Mohammad Sharifia; Alireza Keyhani; Mahmoud Omid; Ali Jafari; Seyed Saei, Mohtasebi; Hossain Mobli, *International Journal of Food Properties*,2010,13:32-40.
37. MSE 2090: Introduction to Materials Science Chapter 5, Diffusion.

AUTHOR INDEX

- Aiyer RC, 133
 Atram RG, 109
 Babrekar MK, 73
 Bhise RB, 123
 Bhoraskar SV, 64
 Bhosale Amarsinh, 44,
 Bhosale BB, 99
 Bhosale SE, 55,
 Bulakhe RN, 91
 Chabukswar VV, 1
 Chaskar MG, 1
 Chattarki AN, 128
 Chaudhari ND, 8
 Chaudhari Sharmila, 29
 Chaudhari SR, 1
 Chavan Apparao R, 73,
 Chilwar Rahul R, 73
 Deshmukh SS, 77
 Dighe Pradeep, 64,
 Ekar SU, 1
 Ekar SU, 81,
 Gaikwad SV, 39
 Gandhe Shrikant64,
 Gangal SA117,
 Gangal SA133,
 Garje Anil29
 Ghule BG81,
 Gijare Medha29,
 Giri SD103,
 Gosavi SW133
 Humbe Ashok77,
 Jadhav KM73
 Jadhav KM77
 Jadhav SS81,
 Jadhav VV81,
 Jare SK91,
 Kalange AE35
 Kale RD35
 Kale Sanjay R87
 Kangude BU1,
 Karmakar Sanjib15
 Karnik R21
 Kathare RV, 91
 Kaushik Baishya, 15
 Keche Atul77,
 Kharat Prashant B73,
 Khater MS21,
 Kholam YB1
 Kholam YB81
 Kokare MK64
 Kolhe RK99
 Kulkarni GR21,
 Kumar Dinesh59
 Lagad SB39
 Mahapure Poonam D133,
 Maldar PS103,
 Mane AA103,
 Mane RS81
 Mohite VR55
 Mohite VS103,
 Moholkar AV103
 More RM8,
 More SD77,
 Mulani Parvin44,
 Nakate UT81,
 Nikam SS103,
 Nirmal Sangeeta A109,
 Pandey Anand95
 Patekar Panchratna44
 Patil Manisha77,
 Pawar Sunil44,
 Pingale PC35,
 Rathod SM123
 Rathod SM64
 Raut SD81,
 Sali Nitin64,
 Sapkal RT55
 Sarkar A103,
 Shaha Swarali44
 Shaikh SF81,
 Shaligram AD117
 Shelke PN1,
 Shinde PV81,
 Shinde TB55,
 Shukla SJ77
 Singh KY59
 Singh Lalit Mohan59,
 Somvanshi Sandeep B73,
 Sonavane DK91,
 Sonawane MR109
 Suryawanshi RV91,
 Talathi P21
 Thube Dilip R87
 Tiwari KP95
 Varade PS117,
 Vasambekar PN8
 Waghmode JV55,
 Wani PN1,
 Wani PN81,

IRJSE INSTRUCTION FOR PREPARING THE MANUSCRIPT:

International Research Journal of Sciences & Engineering (IRJSE) publish research papers, case studies and short communications containing original research work of good standard and review papers of contemporary relevance from all over the world. Following types of contributions are considered for publication:

RESEARCH PAPERS (Full Length - Maximum of 12 pages-A/4 size).
CASE STUDIES, SHORT COMMUNICATIONS, REVIEW PAPERS including Mini Reviews

AUTHORISATION AND DECLARATION

Authors must accept full responsibility for the content of their articles. The Members of the Editorial Board and the Publisher of the journal are not responsible for the statements and opinions expressed by the authors in their articles/write-up published in the journal. To use the copyrighted material (for example table, figure etc.), the author/s must seek the permission from the Author/s and Publisher of the material and send the copy of the permission letters via e-mail to the Administrative Editor for records. In case, if it is not possible than do not use that material.

While submitting the paper the author (s) must give a declaration that "the article has not been published or sent for publication elsewhere".

Article Preparation Guidelines

Manuscript title: The title should be limited to 25 words or less and should not contain abbreviations. The title should be a brief phrase describing the contents of the paper.

Author Information: Complete names and affiliation of all authors, including contact details of corresponding author (Telephone, Fax and E-mail address).

Abstract: The abstract should be informative and completely self-explanatory, briefly present the topic, state the scope of the experiments, indicate significant data, and point out major findings and conclusions. The abstract should summarize the manuscript content in 300 words or less. Standard nomenclature should be used and abbreviations should be avoided. The preferable format should accommodate a description of the study background, methods, results and conclusion. Following the abstract, a list of keywords (3-10) and abbreviations should be included.

Text:

Introduction: The introduction should set the tone of the paper by providing a clear statement of the study, the relevant literature on the study subject and the proposed approach or solution. The introduction should be general enough to attract a reader's attention from a broad range of scientific disciplines.

Materials and Methods: This section should provide a complete overview of the design of the study. Detailed descriptions of materials or participants, comparisons, interventions and types of analysis should be mentioned. However, only new procedures should be described in detail; previously published procedures should be cited and important modifications of published procedures should be mentioned briefly. Capitalize trade names and include the manufacturer's name and address.

Results: The results section should provide complete details of the experiment that are required to support the conclusion of the study. The results should be written in the past tense when describing findings in the authors'experiments. Previously published findings should be written in the present tense. Results and discussion may be combined or in a separate section. Speculation and detailed interpretation of data should not be included in the results but should be put into the discussion section.

Acknowledgment: This section includes acknowledgment of people, grant details, funds, etc.

Note: If an author fails to submit his/her work as per the above instructions, they are pleased to maintain clear titles namely headings, subheading.

References:

Only published or accepted manuscripts should be included in the reference list. Meetings abstracts, conference talks, or papers that have been submitted but not yet accepted should not be cited. All personal communications should be supported by a letter from the relevant authors.

IRJSE uses the numbered citation (citation-sequence) method. References are listed and numbered in the order that they appear in the text. In the text, citations should be indicated by the reference number in brackets. Multiple citations within a single set of brackets should be separated by commas. When there are three or more sequential citations, they should be given as a range. Example: "... now enable biologists to simultaneously monitor the expression of thousands of genes in a single experiment [1,5-7,28]". Make sure the parts of the manuscript are in the correct order for the relevant journal before ordering the citations. Figure captions and tables should be at the end of the manuscript.

Authors are requested to provide at least one online link for each reference as following (preferably PubMed).

Because all references will be linked electronically as much as possible to the papers they cite, proper formatting of the references is crucial. Please use the following style for the reference list:

Examples:

Published Papers:

- 1.Laemmli UK. Cleavage of structural proteins during the assembly of the head of bacteriophage T4. *Nature*, 1970 227: 680-685.
 2. Brusic V, Rudy G, Honeyman G, Hammer J, Harrison L. Prediction of MHC class II- binding peptides using an evolutionary algorithm and artificial neural network. *Bioinformatics*, 1998; 14: 121-130.
- Note: Please list the first five authors and then add "et al." if there are additional authors.

Electronic Journal Articles Entrez Programming Utilities

1. <https://www.ncbi.nlm.nih.gov/books/NBK25500/>

Books:

- 1.Baggot JD. Principles of drug disposition in domestic animals: The basis of Veterinary Clinical Pharmacology. (1stedn), W.B. Saunders Company, Philadelphia, London, Toronto, 1999.
- 2.Zhang Z. Bioinformatics tools for differential analysis of proteomic expression profiling data from clinical samples. Taylor & Francis CRC Press. 2006.

Conferences:

- 1.Hofmann T. The Cluster-Abstraction Model: unsupervised learning of topic hierarchies from text data. Proceedings of the International Joint Conference on Artificial Intelligence. 1999.

Tables:

These should be used at a minimum and designed as simple as possible. We strongly encourage authors to submit tables as .doc format. Tables are to be typed double-spaced throughout, including headings and footnotes. Each table should be on a separate page, numbered consecutively in Arabic numerals and supplied with a heading and a legend. Tables should be self-explanatory without reference to the text. Preferably, the details of the methods used in the experiments should be described in the legend instead of in the text. The same data should not be presented in both table and graph form or repeated in the text. Cells can be copied from an Excel spreadsheet and pasted into a word document, but Excel files should not be embedded as objects.

Note: If the submission is in PDF format, the author is requested to retain the same in .doc format in order to aid in completion of process successfully.

Figures:

The preferred file formats for photographic images are .doc, TIFF and JPEG. If you have created images with separate components on different layers, please send us the Photoshop files.

All images must be at or above intended display size, with the following image resolutions: Line Art 800 dpi, Combination (Line Art + Halftone) 600 dpi, Halftone 300 dpi. See the Image quality specifications chart for details. Image files also must be cropped as close to the actual image as possible.

ISSN: 2322-0015

Journal home page : www.irjse.in

Contact : +91-997 055 9438

+91-942 077 5527

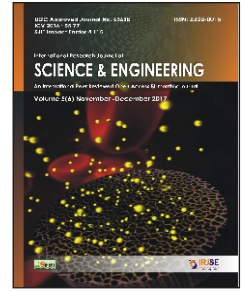


INTERNATIONAL RESEARCH JOURNAL OF SCIENCES & ENGINEERING

An international Peer Reviewed Open Access Refereed Journal

UGC Approved Journal No. 63628

46, Guruwandan, Jawahar Nagar, VMV Road,
Amravati- 444604



Membership form

The Editor,

I wish to be a member of **International Research Journal of Sciences & Engineering (IRJSE)** and agree to abide by the rules setup by you. The filled in proforma is:

- (1) Full Name (in block letters) :
- (2) Gender :
- (3) Nationality :
- (4) Working status and Department :
- (5) Field of Research :
- (6) Mailing Address :
- (7) City:.....State: Country:..... Pin:.....
- (8) Phone (O):..... (R):..... (M):.....
- (9) E-mail :
- (10) Nature of Subscription: Annual / Life / Fellow Membership.

MEMBERSHIP	ANNUAL		LIFE		FELLOW	
	Indian	Overseas	Indian	Overseas	Indian	Overseas
Individual :	INR. 3,500/-	US \$ 250	INR. 15,000/-	US \$ 550	INR. 25,000/-	US \$ 850
Institutional :	INR. 4,500/-	US \$ 350	INR. 25,000/-	US \$ 850	INR. 35,000/-	US \$ 1700

Mode of Payment

INRs./US\$/Euro can be remitted by online payment/E-Money Transfer/Western Union Money Transfer/Cash mentioning Receipt No. and date.

DETAIL OF TRANSFER PROCESS IS AS FOLLOWS:

A/C NAME : **Pallavi Deorao Rathod** MICR Code : **431240102**
 A/c No. : **50100219657932** Branch Code : **001016**
 IFS Code : **HDFC0001016**

Branch Address : **HDFC BANK LTD. BARARA TOWERS, DOCTOR LANE, NANDED MS, India**

[For E-money transfer, please add INRs. 125/- (US\$ 10) extra towards collection / service charges.

Payments should be made in the name of "**ARVIND CHAVHAN**" "**My WU# #: 761786640**"]

Detail about Western Union Money Transfer Services is as follows:

Full Name of Receiver ARVIND BHIMRAO CHAVHAN

Date: / /20

Signature:

Name :

Email this Membership form along with Scan copy of Fees deposit receipt to editorirjse@gmail.com